



**HAL**  
open science

# Fracture, Surface, and Structure of Silicate Glasses: Insights from Atomistic Computer Simulations

Zhen Zhang

► **To cite this version:**

Zhen Zhang. Fracture, Surface, and Structure of Silicate Glasses: Insights from Atomistic Computer Simulations. Physics [physics]. Université de Montpellier; Laboratoire Charles Coulomb, 2020. English. NNT: . tel-02902601

**HAL Id: tel-02902601**

**<https://hal.science/tel-02902601>**

Submitted on 20 Jul 2020

**HAL** is a multi-disciplinary open access archive for the deposit and dissemination of scientific research documents, whether they are published or not. The documents may come from teaching and research institutions in France or abroad, or from public or private research centers.

L'archive ouverte pluridisciplinaire **HAL**, est destinée au dépôt et à la diffusion de documents scientifiques de niveau recherche, publiés ou non, émanant des établissements d'enseignement et de recherche français ou étrangers, des laboratoires publics ou privés.

# THÈSE POUR OBTENIR LE GRADE DE DOCTEUR DE L'UNIVERSITÉ DE MONTPELLIER

En Physique

École doctorale: Information Structures Systèmes (I2S)

Unité de recherche: Laboratoire Charles Coulomb

## Fracture, Surface, and Structure of Silicate Glasses: Insights from Atomistic Computer Simulations

Présentée par Zhen ZHANG

Le 13 mai 2020

Sous la direction de Walter KOB  
et Simona ISPAS

Devant le jury composé de

Walter KOB, Professeur, Université de Montpellier

Simona ISPAS, Maître de Conférences, Université de Montpellier

Matteo CICCOTTI, Professeur, ESPCI Paris

Alfonso PEDONE, Professeur, Università degli studi di Modena e Reggio Emilia

Jürgen HORBACH, Professeur, Heinrich-Heine-Universität Düsseldorf

Tanguy ROUXEL, Professeur, Université de Rennes 1

Benoit RUFFLÉ, Professeur, Université de Montpellier

Directeur de thèse

Co-directrice de thèse

Rapporteur

Rapporteur

Examineur

Examineur

Examineur



UNIVERSITÉ  
DE MONTPELLIER



# Acknowledgements

The whole story began in the summer of 2015, when I was still a second year graduate student and felt anxious about my future career. One of the options that came to my mind was to do a Ph.D. study abroad. I contacted to Walter and he welcomed the idea and readily agreed to provide support. Luckily I got the scholarship from the China Scholarship Council (CSC) and eventually I landed on France in the fall of 2016. I am very grateful for the financial support from CSC, without which the trajectory of my life would probably look very different from the current one.

I wish to express my sincere gratitude to my thesis supervisor Simona. I would like to mention that the reason why I contacted Walter in the first place is because of a paper she and Walter co-authored about first-principles study of a silicate glass-former [Phys. Rev. B 91, 134201 (2015). Yes you should take a look at it!]. I soon realized that she is one of the experts who apply first-principles simulations to understand disordered materials. I am very thankful for her guidance and for sharing with me her expertises. Over the past three and a half years, I have benefited from her not only scientifically but also many aspects of my daily life; her constant help and concern have made my life much easier and also made me feel warm during some tough moments.

I am also deeply grateful to my thesis supervisor Walter for offering me the opportunity of conducting my Ph.D. work under his supervision. Working with him has been a very enriching experience for me. Scientifically, he is the one who can always propose interesting ideas and insights which bring our research to a new height. In life, his easygoing personality and kindness have had a very positive influence on me. I thank him for being available, patient, and supportive about my work. I am particularly thankful to him for all the confidence and encouragements he has given to me over the years.

I would like to thank the members of my thesis annual committee Daniele Coslovich, Domenico Truzzolillo, and Benoit Rufflé for their precious time and many insightful comments on my work. I thank Daniele also because of his assistance in administrative procedures of the university (about registration and taking French courses) and for his instructions on scientific programing. I also want to sincerely thank Matteo Ciccotti, Alfonso Pedone, Jürgen Horbach, Tanguy Rouxel, and Benoit Rufflé for agreeing to be

## ACKNOWLEDGEMENTS

---

member of the committee of my Ph.D. defense.

A special word of thanks goes to the colleagues and friends who have spent some time with me in the lab or outside the lab: Dimitrios, Andrea, Camille, Qinyi, Benjamin, Misaki, Daniel, Chris, Joris, Murari, Yoshihiko, Anshul, Valerio, Ludovic, Norbert, Marouane, Coralie, Ramon, Tianling, Cong, Miao, Manyuan. I enjoyed our conversions and spending time with you. I am also grateful to the help and suggestions that I have received from you concerning my research work or about life.

My particular thanks are due to my families and friends back in China. Without your understanding and support, finishing my Ph.D. study would not have been possible.

Lastly, I want to thank you, the reader, for picking up this thesis, and I hope you can find something interesting in this text.

*Montepllier, January 2020*

Zhen Zhang

# Abstract

Understanding the structure and mechanical behavior of materials on the microscopic scales is crucial for the design of products with desired properties. This thesis focuses on obtaining microscopic insights into the properties, notably fracture, of oxide glasses which are among the most widely used materials in the world. To this end, we use state-of-the-art atomistic simulation techniques to investigate silica and sodium silicates, i.e., the prototypical compositions for many oxide glasses. Using large-scale molecular dynamics simulations, the dynamic fracture of the glasses is studied in depth. We show that the mechanical properties of the glasses are considerably more sensitive to the used interaction potential and simulation protocol than the structural properties. Fracture of silica glass is found to be pure bond rupturing at the crack tip, whereas fracture of Na-rich glasses is accompanied by the growth and coalescence of cavities. We also reveal that the nonaffine atomic displacement is the microscopic reason for the composition-induced transition behavior in the stiffness of these glasses. It is found that the surfaces generated by the fracture are considerably rougher than the melt-formed surfaces and exhibit logarithmic-scaling at the nanoscale ( $\leq 10$  nm). By using first-principles simulations, the vibrational and electronic signatures of some structural units that are abundant on the glass surface are identified. In addition, the ionicity and strength of various types of bonds are inferred from these simulations. Finally, we introduce a novel method to characterize the structure in liquids and glasses. Our analysis shows that these systems have a three-dimensional structure that is surprisingly ordered.

**Keywords:** Oxide glasses, silica, sodium silicate, deformation, fracture, surface, atomistic computer simulations, molecular dynamics, first-principle calculations, chemical bonding, structural order



# Résumé

La compréhension de la structure et du comportement mécanique des matériaux à l'échelle microscopique est cruciale pour la conception de nouveaux produits aux propriétés spécifiques. Cette thèse vise à obtenir des informations microscopiques sur les propriétés, notamment celles de la fracture, des verres d'oxydes qui sont parmi les matériaux les plus utilisés au monde. À cette fin, nous utilisons des techniques de simulation atomistique de pointe pour étudier la silice et des silicates de sodium, c'est-à-dire les compositions représentatives pour de nombreux verres d'oxydes. À l'aide de simulations de dynamique moléculaire à grande échelle, la fracture dynamique des verres est étudiée de manière approfondie. Nous montrons que les propriétés mécaniques des verres sont considérablement plus sensibles au potentiel d'interaction et au protocole de simulation utilisés qu'à leurs propriétés structurelles. La fracture du verre de silice est due aux ruptures de liaisons en pointe de fissure, tandis que la fracture des verres riches en Na s'accompagne d'une croissance et d'une coalescence des cavités. Nous montrons également que l'origine microscopique du comportement transitoire présenté par la rigidité des verres en fonction de leur composition se trouve dans les déplacements atomiques non affines des atomes constituants. On constate que les surfaces générées suite à la fracture sont considérablement plus rugueuses que les surfaces formées par fusion et présentent un comportement en loi logarithmique à l'échelle nanométrique ( $\leq 10$  nm). En utilisant des simulations premiers principes, les signatures vibrationnelles et électroniques de certaines unités structurales, abondantes sur la surface du verre, sont identifiées. De plus, l'ionicité et la force de divers types de liaisons sont extraites à partir de ces simulations. Enfin, nous introduisons une méthode nouvelle pour caractériser la structure des liquides et des verres. Notre analyse montre que ces systèmes ont une structure tridimensionnelle étonnamment ordonnée.

**Mots clés:** Verres d'oxydes, silice, silicate de sodium, déformation, fracture, surface, simulations atomistiques, dynamique moléculaire, calculs premiers principes, liaison chimique, ordre structurel





## Abbreviations

AFM	Atomic force microscopy
AIMD	<i>Ab initio</i> molecular dynamics
BAD	Bond angle distribution
BLJM	Binary Lennard-Jones mixture
BO	Bridging oxygen
CN	Coordination number
csBO	Corner-sharing bridging oxygen
csSi	Corner-sharing silicon
DFT	Density functional theory
DT	Delaunay triangulation
EDF	Electronic degrees of freedom
eDOS	Electronic density of states
ELF	Electron localization function
esBO	Edge-sharing bridging oxygen
esSi	Edge-sharing silicon
FO	Free oxygen
FS	Fracture surface
GGA	Generalized gradient approximation
LDA	Local density approximation
LJ	Lennard-Jones
MD	Molecular dynamics
MS	Melt-formed surface

MSD	Mean squared displacement
NBO	Non-bridging oxygen
NSx	Na <sub>2</sub> O-xSiO <sub>2</sub> (Sodium silicate)
PBCs	Periodic boundary conditions
PDF	Probability distribution function
PS	Phase separation
RDF	Radial distribution function
SCL	Supercooled liquid
TBO	Threefold coordinated oxygen
VDOS	Vibrational density of states
2D	Two-dimensional
2M	Two-membered
3D	Three-dimensional

## Conversion of units

Length	$1 \text{ \AA} = 1 \times 10^{-1} \text{ nm} = 1 \times 10^{-10} \text{ m}$
Time	$1 \text{ fs} = 1 \times 10^{-3} \text{ ps} = 1 \times 10^{-6} \text{ ns} = 1 \times 10^{-15} \text{ s}$
Pressure	$1 \text{ GPa} = 1 \times 10^9 \text{ Pa} = 1 \times 10^9 \text{ N/m}^2$
Energy	$1 \text{ eV} = 1.602 \times 10^{-19} \text{ J} = 3.829 \times 10^{-20} \text{ cal (th)}$
Frequency	$1 \text{ cm}^{-1} = 2.998 \times 10^{10} \text{ Hz}$
Viscosity	$1 \text{ Pa}\cdot\text{s} = 10 \text{ poise}$

# Contents

<b>Acknowledgements</b>	<b>i</b>
<b>Abstract</b>	<b>iii</b>
<b>Abbreviations &amp; Conversion of units</b>	<b>vii</b>
<b>1 Introduction</b>	<b>1</b>
1.1 Motivation . . . . .	1
1.2 Objectives . . . . .	3
1.3 Facets of glass forming systems . . . . .	4
1.4 Structure . . . . .	6
1.5 Mechanics . . . . .	9
1.5.1 Stress-strain curve . . . . .	9
1.5.2 Strength and toughness of silicate glasses . . . . .	11
1.6 Fracture of oxide glasses: State of the art . . . . .	12
1.6.1 The setup . . . . .	13
1.6.2 Key results and open questions . . . . .	15
1.7 Basics of computer simulations . . . . .	18
1.7.1 Classical molecular dynamics . . . . .	19
1.7.2 <i>Ab initio</i> molecular dynamics . . . . .	24
1.7.3 Property calculation . . . . .	27
<b>2 On the critical role of interaction potential and simulation protocol</b>	<b>29</b>
2.1 Interatomic potentials . . . . .	30
2.2 Simulation methods . . . . .	32

2.3	Dynamical and structural properties . . . . .	34
2.4	Mechanical properties . . . . .	40
2.4.1	System-size dependence . . . . .	40
2.4.2	Fracture behavior and elastic moduli . . . . .	41
2.5	Summary . . . . .	45
<b>3</b>	<b>Fracture of sodium silicate glasses: Classical MD simulations</b>	<b>47</b>
3.1	Simulation protocol . . . . .	47
3.2	The big picture: Stress-strain behavior . . . . .	50
3.2.1	Effects of cooling rate and strain rate . . . . .	50
3.2.2	Effects of sample geometry and size . . . . .	54
3.2.3	Effect of notch geometry . . . . .	56
3.2.4	Effect of temperature . . . . .	57
3.2.5	Effect of glass composition . . . . .	58
3.2.6	Crack velocity . . . . .	63
3.3	Microscopic insights . . . . .	67
3.3.1	Cavitation . . . . .	67
3.3.2	Local properties . . . . .	71
3.4	Summary . . . . .	84
<b>4</b>	<b>Melt-formed and fracture surfaces: Classical MD simulations</b>	<b>87</b>
4.1	Construction of the geometric surface . . . . .	88
4.2	Surface composition and structure . . . . .	90
4.3	Surface morphology and roughness . . . . .	96
4.4	On the nature of glass surfaces: Scaling properties . . . . .	101
4.5	Temperature dependence of surface properties . . . . .	106
4.6	Summary . . . . .	107
<b>5</b>	<b>Surfaces of sodium silicate glasses: First principles calculations</b>	<b>109</b>
5.1	Models and simulation details . . . . .	109
5.2	Defining the surface region . . . . .	111
5.3	Dynamics of the liquids . . . . .	113

---

5.4	Structure: Surface vs. interior . . . . .	115
5.5	Vibrational properties . . . . .	120
5.6	Electronic properties . . . . .	125
5.6.1	Electronic density of states . . . . .	125
5.6.2	Atomic charge and bond character . . . . .	128
5.6.3	Electron localization function . . . . .	132
5.7	Summary . . . . .	138
<b>6</b>	<b>Uncovering hidden order in liquids and glasses</b>	<b>141</b>
6.1	Simulation details . . . . .	142
6.2	Model construction . . . . .	143
6.3	Radial distribution function . . . . .	144
6.4	Three dimensional distribution of particles . . . . .	146
6.5	Quantitative characterization . . . . .	149
6.6	Summary . . . . .	159
	<b>Summary and outlook</b>	<b>161</b>
	<b>Résumé en français</b>	<b>165</b>
	<b>Bibliography</b>	<b>171</b>
	<b>Curriculum Vitae</b>	<b>191</b>



# Chapter 1

## Introduction

### 1.1 Motivation

The presence of glasses in nature and technology is very common [1–3]. Glassy products such as window panes, tableware and optical fibers are well integrated in our everyday life. Sometimes we do not even notice their presence because of their transparency. The mentioned examples are glasses based on the chemical compound silica ( $\text{SiO}_2$ ), which are the most familiar and historically the oldest types of glasses. Mechanical reliability is a crucial requirement that underlies the diverse uses of modern glass products. Failure of brittle materials like oxide glasses is most often seen through the spreading of cracks. Understanding the fracture behavior of glass is thus of fundamental importance for designing glass products with improved mechanical performance.

The complexity of cracking in oxide glasses lies primarily in the fact that fracture is a multiscale phenomenon, i.e., different mechanisms operate across a large range of length scales, see Fig. 1.1. The breakdown of a material can be traced down to the breaking of chemical bonds at the nanometer and Ångstrom scales. Classical fracture mechanics, pioneered by Griffith [4] and Irwin [5], has shown great success in describing the stability and the slow growth of flaws within materials, particularly at the macro- and meso-scales. However, it fails to describe fast crack propagation and on the microscopic scales where the material can not be treated as a continuum [6]. Fundamental understanding of the latter requires insights from the atomic scale. This is the first motivation of the thesis.

Fracture of glass is complex also due to the fact the mechanisms that underlie cracking depend on the speed at which a crack forms as well as the type of loading (e.g., tension or shear) to which a material is subjected. Taking the crack velocity  $v_c$  as an example, as a crack radiates outwards from a flaw at the fracture origin,  $v_c$  increases rapidly (in microseconds) from nearly zero to  $10^3$  m/s [7, 8]. This process is accom-



panied by a progressive roughening of the fracture surface, which is often examined in experiments to infer the causes and mechanisms related to glass failure [7]. The aforementioned factors may partially account for the seemingly contradicting results that one finds in the literature regarding the fracture behavior of oxide glasses [9–11]. Glass breaks when a flaw meets tension. We aim to understand this primary failure mode and this becomes the second motivation of the current work.

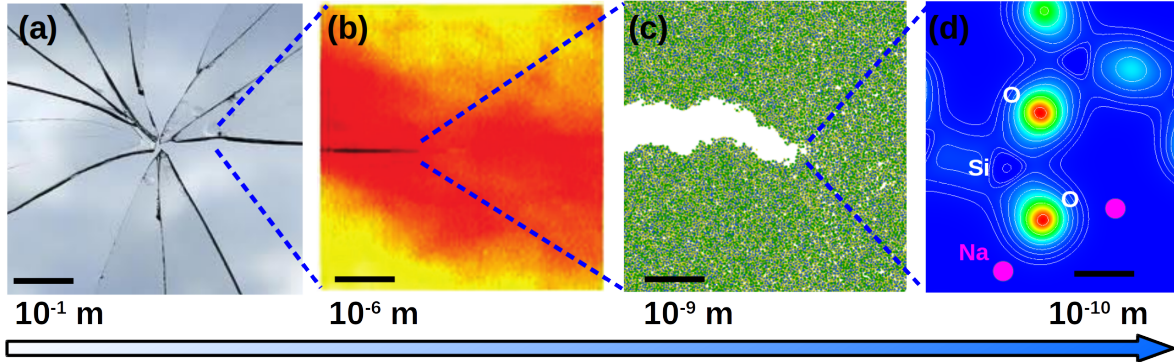


**Figure 1.1:** Multiscale fracture of glass. Crack spreading in brittle solids such as oxide glasses involves mechanisms that span a vast range of scales. (a) Macroscopic cracking of a window glass caused by impact. (b) Micrometer scale evolution of a crack as measured by atomic force microscopy. Image adapted from Pallares *et al.* [12]. (c) Nanometer scale details of the crack geometry as obtained by atomistic modeling (this work). (d) Ångstrom scale visualization of the volume charge density around broken Si-O bonds (this work).

The third aspect that contributes to the complexity of glass fracture is, not surprisingly, due to its non-crystalline structure. Unlike crystals which are homogeneous materials, glass exhibits inhomogeneities in structure and other properties on different length scales. Understanding the interplay between a fast-moving (dynamic) crack and heterogeneities at the microscopic scale is a very challenging task yet of practical importance in the design of toughening strategies for glassy products. This constitutes the third motivation of the present work.

An additional motivation of this thesis concerns a deeper understanding of the structure of glass, and disordered systems in general. In both experimental and computer simulation studies, the structure of liquids and glasses is mostly characterized by two-point correlation functions such as the static structure factor and radial distribution function [3, 13, 14]. However, this type of structural measure is far from adequate to provide a full spectrum of the structural features of these systems. We were thus motivated to propose new approaches for obtaining more insights into the structure of these disordered systems.

## 1.2 Objectives

This thesis aims to obtain a fundamental understanding of the structure and fracture behavior of oxide glasses on the microscopic scales. To this end, we combine atomistic computer simulation techniques with different capabilities. The systems of primary interest are silica and sodium silicate, both of which are prototypical compositions for oxide glasses. In light of these global objectives, this thesis seeks answers for the following questions:

- **Interatomic potential:** How sensitive is the mechanical behavior of glass to the interaction potential? How does the simulation protocol affect the conclusions regarding the nature of fracture? These questions will be addressed in Chapter 2.
- **Cracking process:** How the global stress-strain behavior of a glass depends on the production history, loading condition and composition? How fast does a dynamic crack propagate? Is fracture caused by cavitation on the nanometer scale? To which extent are glass properties inhomogeneous on the microscopic scales? Are these local properties correlated with each other? Does the crack propagate along regions rich in network modifier? We will provide insights into these questions in Chapter 3.
- **Surface characteristics:** How does melt-formed surface compare with fracture surface? How do the surface structure and composition compare with the ones of the bulk? How rough are the surfaces? What kind of scaling behavior do the surfaces exhibit on the nanometer scale? Answers to these questions can be found in Chapter 4.
- **Chemical bonding:** What is special about the structure of glass surface? What are the vibrational and electronic signatures of the structural units on the surface? How does the presence of Na influence the nature of chemical bonding and bond strength? We will clarify these questions in Chapter 5 based on the results from first principles calculations.
- **Structural order:** Are there nontrivial structural orders beyond short-range distances in liquids and glasses? How can we characterize the structure of disordered system by taking into account also angular dependence, i.e., using higher order correlation functions? These questions will be addressed in Chapter 6.

The rest of the thesis is organized as follows. In the remaining of Chapter 1, we give a brief introduction of the properties of oxide glasses and the basics of atomistic

computer simulations. In Chapters 2-6, we present the results concerning the aforementioned questions. Finally, we summarize the thesis and provide a outlook for the future.

### 1.3 Facets of glass forming systems

The term glass, in popular usage, refers mainly to silicate glass, which is made of silica ( $\text{SiO}_2$ ) and other metal oxides such as sodium oxide ( $\text{Na}_2\text{O}$ ) and calcium oxide ( $\text{CaO}$ ). These types of material are familiar to us as window panels and glass bottles. In a broader sense, glasses can be made of a range of different kinds of materials other than silica: metallic alloys, polymers, organic molecules, etc. Glass properties vary depending mainly on the chemical composition and production history.

But what is a “glass”? A bit surprisingly, although humans have been producing glasses for thousands of years, a consensus concerning the definition of glass has yet to be reached [15–17]. Nevertheless, there are at least two features that most people agree about glass: having a non-crystalline structure and exhibiting a glass transition. The first feature is relatively easy to understand. Crystals have a structure defined by a periodic arrangement of atoms or molecules (left panel of Fig. 1.2), i.e., the same local structural order extends to infinitely large distances. Non-crystalline structure therefore means that no such long range ordering exists. However, this does not mean that the structure of glass is completely random since short-range (local) ordering is usually present. (A closer look at the disordered packing of oranges, right panel of Fig. 1.2, one may still find a well preserved local icosahedral (fivefold) symmetry). Usually, glass structure represents a less efficient packing of atoms or molecules relative to their crystalline counterparts. Take silica as an example, the stable crystalline phase of silica  $\alpha$ -quartz has a density of  $2.65 \text{ g/cm}^3$ , whereas silica glass has a density of  $2.20 \text{ g/cm}^3$ .



**Figure 1.2:** Order versus disorder. The analog of packing oranges.

Glass transition, on the other hand, can be considered as a phenomenon of a liq-

uid that is cooled [18]. In the usual case, if a liquid is cooled down to its melting temperature  $T_m$ , it crystallizes and a sudden change (i.e., a discontinuity) of volume or enthalpy can be observed, see Fig. 1.3(a). This process is a standard first-order phase transition. However, if one cools the liquid fast enough, crystallization at  $T_m$  can be avoided and the liquid becomes supercooled. In the supercooled liquid (SCL) region, the volume follows the liquid line and the relaxation time for atomic/molecular rearrangements increases rapidly. The glass transition occurs when the relaxation time scale and the experimental time scale of observation cross [19], and this process lasts over a temperature range. As temperature is further decreased below  $T_g$ , called the *glass transition temperature*, the SCL becomes a glass. ( $T_g$  is basically defined as the middle point of this transformation  $T$  range). In practice,  $T_g$  can be defined as the temperature corresponding to the inflection point in the  $T$ -dependence of properties such as the (volumetric) thermal expansion coefficient

$$\alpha_V = \frac{1}{V} \left( \frac{\partial V}{\partial T} \right)_P \quad (1.1)$$

and heat capacity

$$C_P = \left( \frac{\partial H}{\partial T} \right)_P, \quad (1.2)$$

where  $V$  and  $H$  are the volume and enthalpy under constant pressure. In calorimetry experiments,  $T_g$  is often measured on heating. For this case,  $T_g$  is usually assigned to be the peak temperature of the  $C_P$  curve.

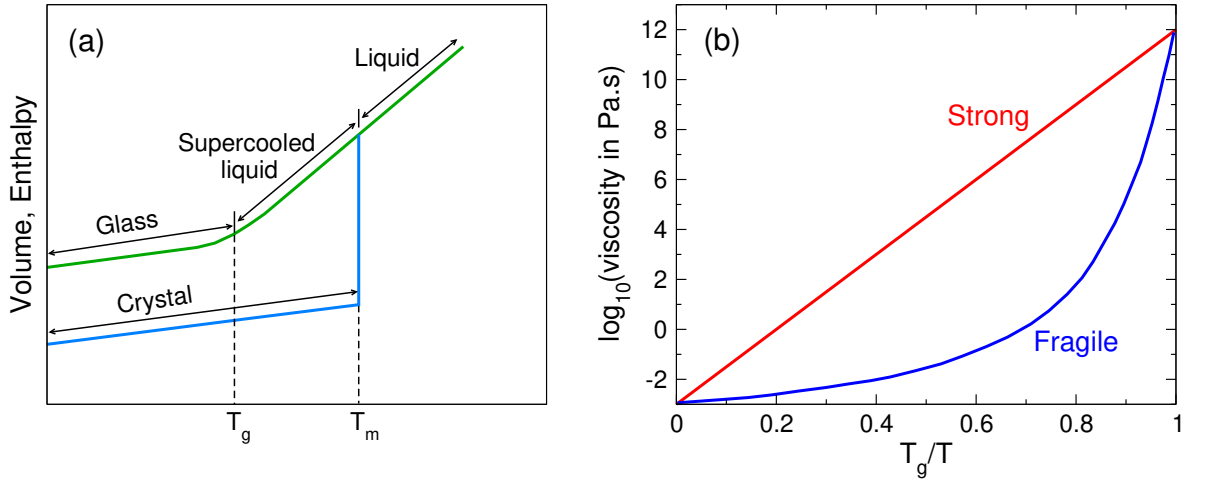


**Figure 1.3:** (a) Temperature dependence of a liquid’s volume or enthalpy at constant pressure, respectively.  $T_m$  is the melting temperature and  $T_g$  is the glass transition temperature. (b) Liquid viscosity as a function of scaled temperature  $T_g/T$ , showing Angell’s strong-fragile pattern. The structural relaxation time  $\tau_\alpha$  has nearly the same  $T$ -dependence as the shear viscosity.

It is important to note that the glass transition is primarily a kinetic phenomenon. On cooling, the atomic motion becomes increasingly sluggish and the SCL becomes

too viscous to flow at  $T_g$ . For nonpolymeric glass formers, the shear viscosity  $\eta$  at  $T_g$  is typically around  $10^{12}$  Pa·s. This viscosity value is sometimes used to define  $T_g$ , see Fig. 1.3(b). As the viscosity has such a large magnitude, the glassy state is essentially a solid state at human time scale.

Another relevant quantity which may cause confusion with  $T_g$  is the *fictive temperature*  $T_f$ , which can be defined as the temperature at which the supercooled liquid has a structure similar to that of the relaxing glass [20, 21]. The fictive temperature is usually measured on heating and is determined as the intersection of the glass line and the extended liquid line. Due to aging of the glass,  $T_f$  is usually smaller than  $T_g$ . Both  $T_g$  and  $T_f$  depend on the thermal history.

The viscosities of glass forming liquids may show very different  $T$ -dependence. Within Angell's concept of fragility, liquids can be classified into strong and fragile glass formers. For strong glass formers,  $\eta$  increases in an Arrhenius manner as temperature decreases, i.e.,

$$\eta = \eta_0 \exp\left(\frac{E}{k_B T}\right), \quad (1.3)$$

where  $\eta_0$  is a constant,  $k_B$  is the Boltzmann constant, and  $E$  is an activation energy. For strong liquids,  $E$  is (nearly)  $T$ -independent, whereas for fragile liquids it increases significantly with temperature on approaching  $T_g$  (i.e., a "super Arrhenius" behavior). Network oxides such as  $\text{SiO}_2$  are typical examples of strong glass formers. Organic compounds such as *o*-Terphenyl ( $\text{C}_{18}\text{H}_{14}$ ) can be classified as fragile glass formers [22]. Notice that even strong liquids will show some non-Arrhenius behavior at temperature near their  $T_g$ , but it is more dramatic for fragile liquids [23].

## 1.4 Structure

**Phase diagram of the  $\text{Na}_2\text{O-SiO}_2$  system.** As the binary sodium silicate ( $\text{Na}_2\text{O-SiO}_2$ ) system is of particular interest of this thesis, here we give a brief introduction for the phase diagram of the  $\text{Na}_2\text{O-SiO}_2$  system, see Fig. 1.4. For pure silica, as the melt is cooled, it crystallizes in three varieties, cristobalite, tridymite, and quartz at 1713, 1470 and 867 °C, respectively. (Quartz has  $\alpha$ - and  $\beta$ -forms. The inversion temperature is at 573 °C, below which  $\alpha$ -quartz is the stable phase). The first eutectic point, between the disilicate ( $\text{Na}_2\text{Si}_2\text{O}_5$ ) and quartz, appears at 793 °C when 24.5% of  $\text{Na}_2\text{O}$  is added. With further increasing  $\text{Na}_2\text{O}$  concentration, the second eutectic point between  $\text{Na}_2\text{Si}_2\text{O}_5$  and  $\text{Na}_2\text{SiO}_3$  (sodium metasilicate) shows up at 37.9%  $\text{Na}_2\text{O}$  and 846 °C. The melting points of  $\text{Na}_2\text{Si}_2\text{O}_5$  and  $\text{Na}_2\text{SiO}_3$  were determined at 874 and 1089 °C, respectively [24].

Another important feature of the  $\text{Na}_2\text{O-SiO}_2$  system is the phenomenon of phase

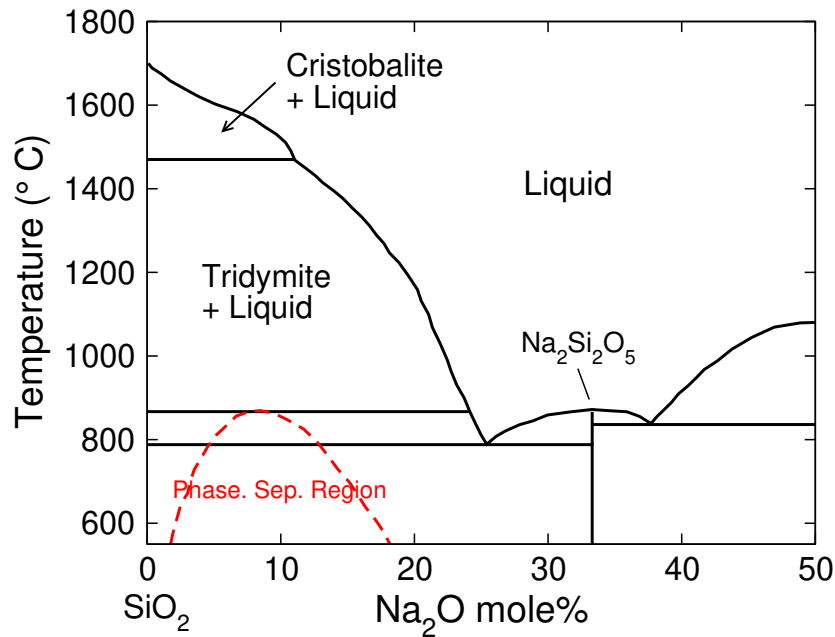


**Figure 1.4:** Phase diagram of the  $\text{Na}_2\text{SiO}_3\text{-SiO}_2$  system at the atmospheric pressure (Adapted from Kracek [24]). The mole percent of  $\text{Na}_2\text{O}$  varies from 0 to 50%.

separation (PS). It should be noted that the occurrence of PS in silica-based glasses is the norm rather than the exception [2]. The temperature at which PS occurs,  $T_c$ , is determined by the thermodynamics of regular solutions (see the dashed line in Fig. 1.4), whereas the extent of PS can range from the microscopic level to the macroscopic level, depending on the kinetics. For the  $\text{Na}_2\text{O-SiO}_2$  system, the PS is said to be *metastable*<sup>1</sup> since it occurs in the sub-liquidus region [2]. This usually means that the process of separation into two co-existing phases will be slow so that the scale of the microstructure may be undetectable by the naked eye. We note that the experimental  $T_g$  of the  $\text{Na}_2\text{O-SiO}_2$  system containing 5%-20% of  $\text{Na}_2\text{O}$  is about 430-480 °C, i.e., lower than  $T_c$  [25]. Despite this, the viscosity of the melt below  $T_c$  is already high so that PS only occurs on a small scale<sup>2</sup> in the final glass [2]. In computer simulations, the  $T_g$  for the aforementioned compositions are actually higher than  $T_c$ , due to the relatively fast quenching. Therefore, even microscopic PS is unlikely to happen.

**Structural models for sodium silicate glasses.** A number of models exist for describing the structure of silicate glasses. The most commonly used models are based on the idea of Zachariasen [26], and are referred by the term *random network theory* [2]. For the case of *vitreous silica*, the silicon-oxygen tetrahedron with a coordination number of four, i.e.,  $[\text{SiO}_4]$ , serves as the basic building block for the network. The short

<sup>1</sup>The term *metastable* or *stable* is attributed to the stability of the liquid phase in the phase separation region.

<sup>2</sup>Generally, this means that the glass looks homogeneous to the naked eye and optical microscope.

range order of the glass is preserved since these tetrahedra have a high degree of local ordering (even in the liquid state). A continuous, three-dimensional network is formed through the linkage of these  $[\text{SiO}_4]$  units at all four corners (i.e., corner-sharing). Disorder in the structure is obtained by allowing the variability of the SiOSi angle connecting adjacent tetrahedra, and the rotation of the tetrahedra. A two-dimensional (2D) representation of such a structure is shown in Fig. 1.5(a).

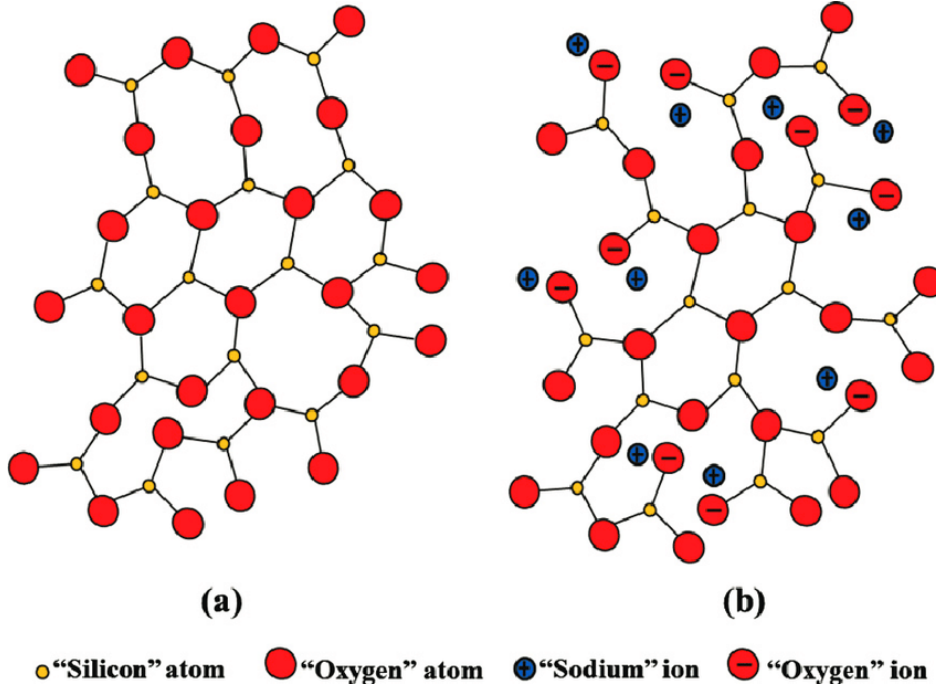


**Figure 1.5:** Schematic two-dimensional glass structures: (a) silica; (b) sodium silicate. After Hasanuzzaman *et al.* [27]

The addition of alkali oxides, e.g.,  $\text{Na}_2\text{O}$ , to silica results in breaking of the network connectivity by creating non-bridging oxygens (NBO, bonded to only one Si). Each NBO is in principle associated with a nearby alkali ions, e.g.,  $\text{Na}^+$  to maintain local charge neutrality. Glass density increases with increasing alkali oxide concentration due to the increase in atomic packing density. A 2D drawing of such a structure for sodium silicate is shown in Fig. 1.5(b).

An additional point to be noted regarding the structure is the formation of Na pockets or channels in sodosilicate glasses. Since the earlier 80's, there have been some speculations about the existence of preferential ion conducting pathways in a Si-O network [28, 29]. At present, there is certainly evidence from both experimental studies and computer simulations to support such models [30, 31]. Figure 1.6(a) shows the partial structure factors  $S_{\alpha,\beta}(q)$  as obtained from MD simulations for sodium trisilicate (NS3) in liquid and glass states. A well-pronounced peak at  $q \approx 0.9 \text{ \AA}^{-1}$  corresponds to an inhomogeneous distribution of sodium ions on a length scale of 6-8  $\text{\AA}$ .

The snapshot, Fig. 1.6(b), illustrates clearly a network of Na channels that percolate through the Si-O network. (Note that the sizes of spheres do not mirror the real sizes of the three atomic species). It is also found that the formation of Na-rich channels is fairly unaffected by  $\text{Na}_2\text{O}$  concentration, by temperature, or by a change of the density in the melt [31]. These findings at the microscopic level give an explanation for the observation that the viscosity of the  $\text{Na}_2\text{O-SiO}_2$  system depends relatively weakly on the  $\text{Na}_2\text{O}$  concentration [25, 32]. It remains an open question how the presence of such Na-rich channels and the related fast dynamics of  $\text{Na}^+$  affect the material's response to a mechanical load [33].

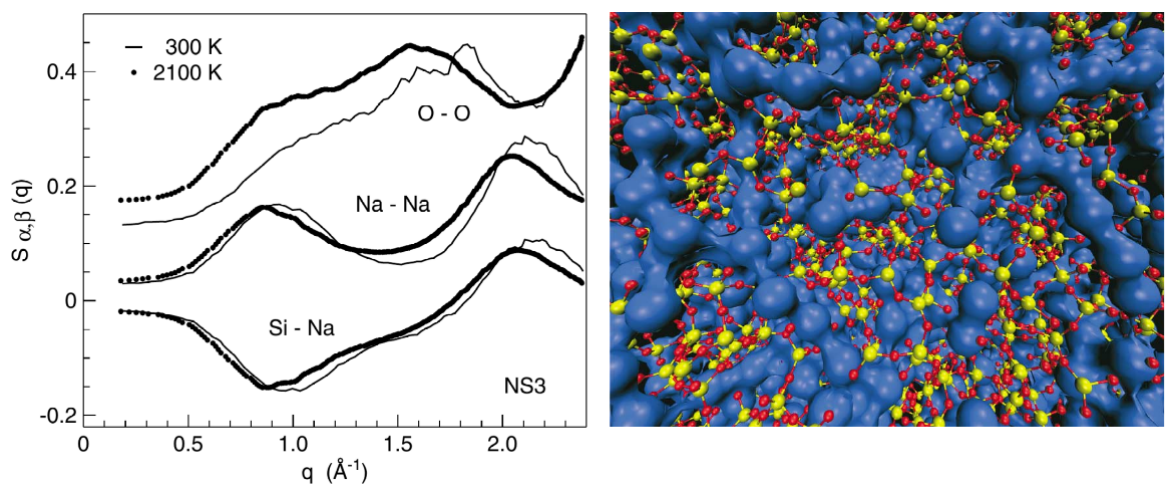


**Figure 1.6:** Formation of Na channels in sodium silicate glasses. (a) Partial structural factors  $S_{\alpha,\beta}(q)$  as obtained in molecular dynamics simulations in glassy and liquid sodium trisilicate (NS3) at experimental density.  $S_{O,O} + 0.1$  for clarity. (b) Snapshot of the structure of NS3 at 2100 K. The blue spheres that are connected to each other represent the Na atoms. The Si-O network is drawn by yellow (Si) and red (O) spheres that are connected to each other. After Meyer *et al.* [31].

## 1.5 Mechanics

### 1.5.1 Stress-strain curve

As fracture is of major concern in this thesis, we introduce here briefly the typical stress-strain ( $\sigma - \epsilon$ ) curve of a material under tensile loading. (Throughout the thesis, tensile stress are positive and compressive stresses are negative. The sign convention for strains is the same as that for stresses). Three characteristic points can be inferred from the stress-strain curve, Fig. 1.7(a). The first one is the *yield point* at which nonlinear (elastic+plastic) deformation begins. The *yield stress* (or *yield strength*) thus separates



elastic<sup>3</sup> and plastic behavior of material. The second point is the *failure point* where stress reaches a maximum. The stress at this point is thus called *failure stress* (or *maximum stress*). After the failure point the material fails and eventually reaches the *fracture point*, i.e., the point where the stress drops to zero rapidly. For ductile materials, one observes necking of the material before fracture. In contrast, brittle materials fracture without noticeable necking, i.e., the failure point is approximately the fracture point. For a perfectly brittle material the three characteristic points should coincide with each other [34]. The yield point and failure point can be easily identified from the slope of the stress-strain curve, i.e., the tangent modulus,

$$E_t = \frac{\partial \sigma}{\partial \epsilon}. \quad (1.4)$$

$E_t$  at  $\epsilon \rightarrow 0$  is known as the *elastic modulus* or *Young's modulus*  $E$ . In the linear elastic region,  $E_t$  is a constant and is equal to  $E$ , see Fig. 1.7(b). In contrast to the yield and failure points, the fracture point (for a ductile material in particular) is less easy to define if the material does not show a clean drop of stress after failure.

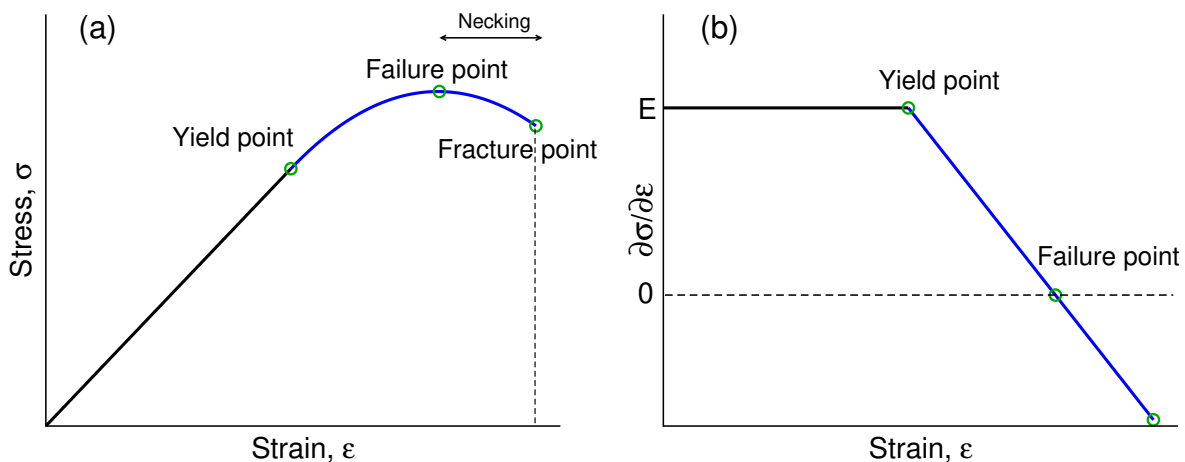


**Figure 1.7:** (a) Typical stress-strain curve for a material under tensile stress. The shown stress-strain curve is simply a combination of a linear and quadratic functions. (b) The corresponding tangent modulus curve. The open circles indicate the three characteristic points.

If  $E$  is large, then the material is said *stiff*. A less stiff material is also termed *flexible*. Another mechanical concept which might cause confusion with stiffness is *hardness*. *Soft* and *hard* are defined in mechanics with respect to yield strength, i.e., where plastic deformation begins. A material is said to be hard if it can withstand high applied stress before yielding. Therefore, mechanically speaking, it is possible to find a material that is stiff but soft.

<sup>3</sup>Elastic behavior is not always linear. Rubber under tension is a notable exception.

### 1.5.2 Strength and toughness of silicate glasses

Silicate glasses are prototypical strong yet brittle materials where cracks, once initiated, immediately propagate in an unstable, often catastrophic fashion. This brittle fracture behavior is considered as the main drawback of glasses for many modern applications [33, 35].

Silica-based glasses are among the intrinsically strongest man-made materials that can be produced on a large scale, see Fig. 1.8. For instance, a tensile strength of up to 26 GPa was measured for silica glass [36]. A theoretical strength of 32 GPa was also calculated for a typical silicate glass<sup>4</sup> [2]. (The theoretical strength is given by the force which must be applied to overcome the maximum restorative force between two atoms, and thus it should correspond to the failure stress as indicated in the  $\sigma - \epsilon$  curve). However, the practical strengths of glasses are usually far (orders of magnitude) less than their theoretical values mainly due to the presence of surface flaws [37]. These flaws act as stress concentrators which severely weaken the glass. Other factors affecting the strength of glass include composition, working environment, fatigue, etc.

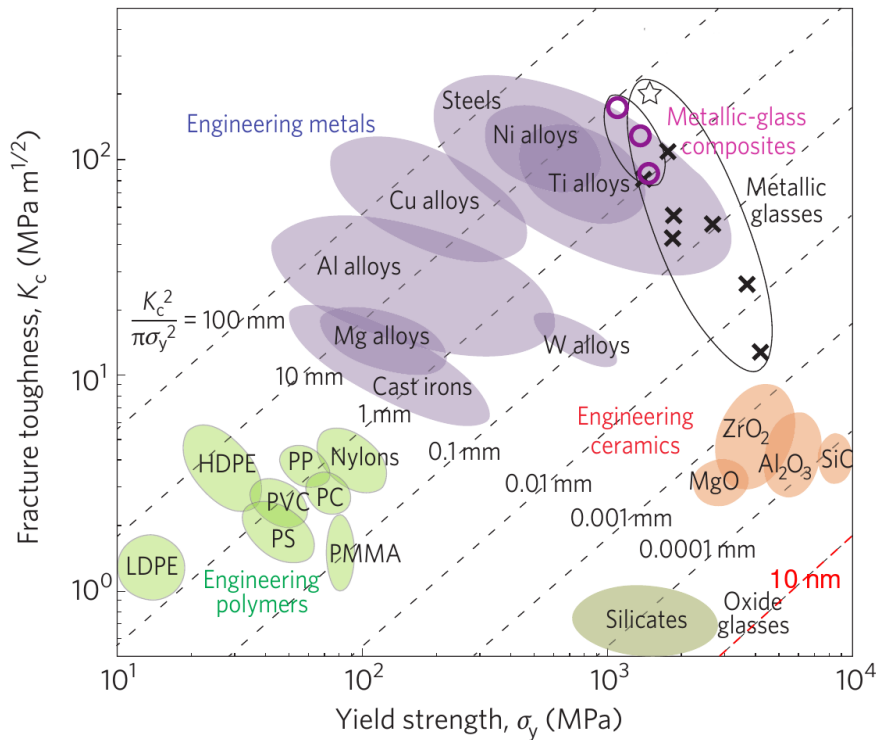


**Figure 1.8:** Strength-toughness relationship for engineering materials (figure adapted from Ritchie [38]). Yield strength data shown for oxide glasses represent ideal limits. Data for oxide glasses are from [39]. Diagonal lines (contours) correspond to values for the plastic-zone radius,  $K_c^2/\pi\sigma_y^2$ , where  $K_c$  is the fracture toughness and  $\sigma_y$  the yield strength.

<sup>4</sup>Exact composition unknown. We deduce that the glass should close to pure  $\text{SiO}_2$ , based on the given values of Young's modulus = 70 GPa and surface energy =  $3 \text{ J m}^{-2}$ .

While strength may correspond to any of the three characteristic points on the  $\sigma - \epsilon$  curve [2, 37, 38], toughness is a measure of a material's resistance to fracture. For the opening mode of fracture in experiments, toughness is the critical stress intensity factor  $K_{Ic}$ , which, according to continuum mechanics, can be determined by the expression [5]

$$K_{Ic} \propto \sigma_r \sqrt{a}, \quad (1.5)$$

where  $\sigma_r$  is the fracture stress of a sample with a pre-existing critical crack of length  $a$ .  $K_{Ic}$  as measured for silicate glasses are usually smaller than  $2 \text{ MPa}\cdot\sqrt{\text{m}}$ , which has been considered as an indication of brittleness [40]. In a more general sense, toughness is the energy needed (or absorbed) to cause fracture and is obtained by integrating the area under the stress-strain curve [41]. This definition of toughness is also called *work of fracture* [34].

It is generally true that harder (stronger) materials tend to be brittle, and lower strength materials which can deform more easily tend to be tougher (see Fig. 1.8). In other words, strength and toughness, two vital requirements for most structural materials, tend to be mutually exclusive [38].

For the search of materials that are not only strong but also tough, the conflict of strength versus toughness has to be resolved. Over the years, several toughening strategies have been put forward for increasing the damage resistance of glass products. Extrinsic toughening techniques such as thermal and chemical toughening create compress stress at the glass surface and thus effectively reduce (shield) the local stresses and strains actually experienced at the crack tip (surface flaws). Intrinsic toughening, on the other hand, is associated with making the cracking processes ahead of the crack tip more difficult. This can be achieved through, e.g., introducing a second phase and enlarging the plastic zone. Note that extrinsic toughening affects only the crack-growth toughness, whereas intrinsic toughening increases both the crack-initiation and crack-growth toughness. Extrinsic toughening is the primary source of toughening in brittle materials (e.g., oxide glasses), whereas intrinsic toughening is the major source of fracture resistance in ductile materials [33, 38].

## 1.6 Fracture of oxide glasses: State of the art

Fracture of glasses is a vast subject that has been studied for centuries. To give a comprehensive review of this topic would be impossible in the thesis. There are, however, several good review articles providing more detailed description of various aspects of this subject [42–46]. In this section, we instead give a comparative review of some recent studies of glass fracture using both experimental and simulation approaches.

### 1.6.1 The setup

To start, we show in Fig. 1.9 a simple analog that helps the visualization of different modes of crack. Let us consider the spacing between the upper and lower beaks of the “goofy duck” as a crack, which is initially closed, see Fig. 1.9(a). Depending on how the duck moves its beaks, different modes of crack loading are generated, Fig. 1.9(b-d). The opening mode (mode I), panel (b), is caused by a loading that is perpendicular to the crack plane. The sliding mode (mode II), panel (c), is produced by forces parallel to the crack plane and normal to the crack line. The tearing mode (mode III), panel (d), is caused by forces parallel to the crack surface and to the crack line. The opening mode of crack loading is the primary mode of experimental interest, and it will also be the focus of this thesis.

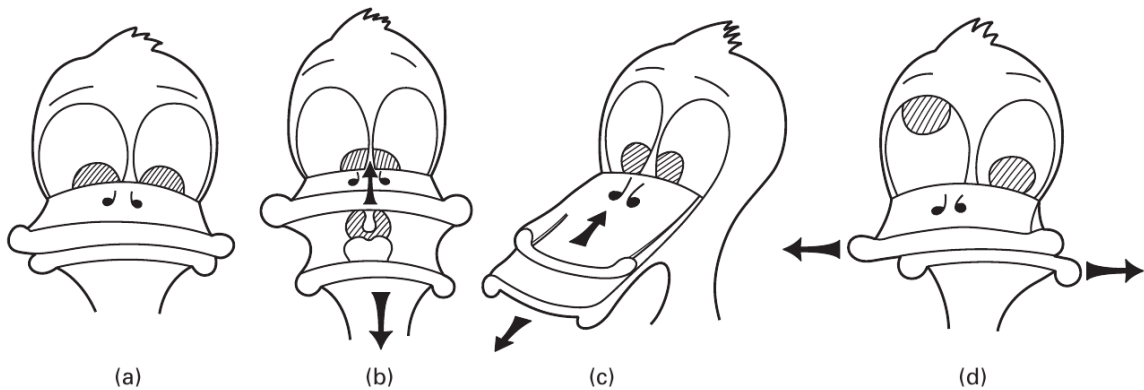


**Figure 1.9:** “Goofy duck” analog for the three modes of crack loading. (a) Crack/beak closed. (b) Opening mode. (c) Sliding mode. (d) Tearing mode. (Courtesy of M. H. Meyers [34].)

A comparison between two experimental results is meaningful only if they have been obtained under comparable conditions. The same rule applies to the comparison between experimental and simulation studies. Before discussing the results from previous studies, we briefly introduce the experimental and simulation setups usually used for investigating glass fracture, in particular fracture under tension. Some key parameters will also be mentioned.

**Experiments.** In experiments, fracture of glass can either be investigated by direct examination of the crack tip *in situ* or by post-mortem analysis of the fracture surface. For both approaches, atomic force microscopy (AFM) is the experimental technique that has become increasingly popular in recent years [47]. The measurement capability (or resolution) of AFM can reach  $\approx 0.05$  nm in the direction perpendicular to the surface and 1-10 nm in the direction parallel to the surface [45]. With this technique, fracture study is often conducted in a stress-corrosive environment, i.e., water

comes into play (different levels of humidities are maintained during the experiments). The crack velocity  $v_c$  can be controlled over a wide range (as low as  $10^{-13}$  m/s [47]) but usually has a small magnitude ( $< 10$  m/s [48]). To achieve slow (or subcritical<sup>5</sup>) crack growth, one usually initiates a crack by applying an uniaxial compressive stress, and then holds the load constant. The crack will propagate slowly due to the corrosive action of water [10, 47] (a phenomenon also known as *static fatigue* [2]). It is worth noting that, whilst water vapor promotes failure through the chemical reaction  $\text{SiO}_2 + 2\text{H}_2\text{O} \rightarrow \text{Si}(\text{OH})_4$  (results in sharpening of the crack tip), liquid water actually lead to crack blunting and thus increase the resistance to fracture.

**Simulations.** Computer simulations have been applied to study glass fracture for decades. Atomistic simulations, among many simulation and modeling techniques, have been frequently used to gain insight into the evolution of atomic scale details of fracture, which is difficult to observe with most of the available experimental techniques. Here we focus mainly on the fracture studies by using atomistic simulation techniques, notably molecular dynamics.

There are in general two types of fracture simulation that can be found in the literature: Dynamic fracture and quasi-static fracture. The first approach takes into consideration the effect of thermal vibration, i.e., fracture at a given temperature. One usually applies an external strain to the whole system by scaling the positions of all the atoms every  $N$  time steps [50]. For  $N = 1$ , a tiny increment of strain is applied at each time step. This is the method of choice for the current study and it has the merit that it mimics the dynamic fracture of glass in experiments, e.g., testing the strength of a glass rod under uniform tension. Applying uniform expansion to the sample is ideal when using high strain rate since stress wave propagation can be avoid [51].

To meet a given strain increment, other methodologies do exist. For example, one can choose to displace only atoms in the boundary layers that are normal to the pulling direction. The system is allowed to relax for a certain duration at each step of increasing strain in order to reach an “equilibrium” at the current strain state [9, 52–54].

The tensile strain rates reported in the previous simulation studies are usually larger than 0.1/ns [50–59]. The resulting crack velocity, as reported for silica glass, is on the order of  $10^3$  m/s. Such information for sodium silicate glasses, to our knowledge, has not been reported yet.

In the second approach, i.e., quasi-static fracture, the thermal and dynamical effects are neglected. A step-wise deformation is firstly applied to the sample. After that, the sample (i.e., configuration) is subjected to an energy minimization which permits to find the configuration corresponding to the local minima of the potential energy

---

<sup>5</sup>Crack velocity smaller than the onset velocity of dynamic fracture. For silicate glasses, this critical velocity is usually smaller than  $10^{-2}$  m/s [49].

landscape [60, 61]. In this approach, the effective strain rate is zero. This approach seems to mimic the subcritical crack growth under a low-temperature environment (i.e., the thermal and dynamical effects are small).

Another important point to be mentioned is the control of the simulation environment or conditions. More specifically, it concerns the atmosphere (vacuum or humid), temperature and pressure in/at which the fracture simulation is performed. We note that while fracture of glass is often studied with the presence of water in experiments, such chemical-mechanical interactions are rarely studied in simulations. This is not so surprising, since the chemical reactions between water and the glass network require the description of the atomic interaction with quantum accuracy, which is computationally very demanding. To our knowledge, only very recently such simulations, i.e., water interacting with glass fracture, have been performed for silica with system sizes of  $10^4 \sim 10^5$  atoms [62–64]. However, we note that careful attention should be paid to the influence of simulation setup and sample geometry, which was often unmentioned in previous simulations of glass fracture. We will discuss this point in more details in chapter 2 and 3.

Also very important is the control of the ensemble used for the fracture simulation. In the literature, fracture of glass is carried out either at a constant volume or a constant pressure, which could lead to different conclusions regarding the fracture behavior. As first reported in an earlier study of silica [56], constant volume simulation leads to a more brittle fracture of the glass. To mimic the fracture of glass in experiments, a constant pressure simulation should be used.

## 1.6.2 Key results and open questions

**Is crack growth caused by cavitation?** Silicate glasses have long been considered as brittle materials. That is to say, fracture of glass (from a microscopic point of view) is due to sequential breaking of atomic bonds at the crack tip. This brittle nature of glass should exclude any possibility of cavitation, i.e., the growth and coalescence of small voids ahead of the crack tip. This conventional picture was challenged by Célarié *et al.* [10] in 2003 with a paper entitled “Glass Breaks like Metal, but at the Nanometer Scale”. Based on *in situ* AFM observations on the sample surface, the authors claimed the presence of nanoscale cavities ahead of the stress-corrosion crack tip of an aluminosilicate glass. The size of the damage cavities reported were 20 nm long and 5 nm deep. (The third dimension is missing since the observation was done only on the sample surface). Later on they also carried out similar studies for silica glass and found that the cavities have sizes of  $125 \text{ nm} \times 25 \text{ nm}$  [65, 66]. Based on these results, they claimed that the origin of such a nanoscale damage mode, i.e., cracks propagate by the nucleation, growth and coalescence of cavities, is inherent to the amorphous structure,

irrespective of glass composition. In 2004, Guin and Wiederhorn [11] questioned the observation by Célarié *et al.* in a paper entitled “Fracture of Silicate Glasses: Ductile or Brittle?”. They used a *different* experimental setup for investigating slow crack growth in silica and soda-lime silicate glasses. In their work, AFM was used to acquire the profiles of the post-mortem fracture surfaces, which were subsequently examined to check the possibility of cavity formation during fracture. The authors found that the opposing fracture surfaces matched very well (The fracture surfaces matched to a resolution of better than 0.3 nm normal to the surface and 5 nm parallel to the surface), again irrespective of the compositions. Notwithstanding, they did not exclude the possibility of cavities smaller than 5 nm. Note that in the work of Célarié *et al.* the cracks were initiated by compressive stress whereas in the study of Guin and Wiederhorn the cracks propagate due to pure tension.

On the other side, researchers have also tried to understand the damage mechanisms of silicate glasses through computer simulations. Simmons and coworkers started the fracture study of silica glass by using MD simulations in the early 80s [67]. Later on, they studied the fracture behavior of silica under tensile loading and found only voids with sizes smaller than 0.5 nm [50]. Rountree and coworkers [9, 68, 69] performed large scale MD simulations of fracture of silica glass under tension and concluded that crack propagation is accompanied by nucleation and growth of nanometer scale cavities up to 20 nm ahead of the crack tip. However, after a more careful reading of their papers one realizes that important factors such as the sample geometry and strain rate are missing or not fully explained. Later, fracture of more complex glass compositions were also studied, using different interaction potentials and simulation setups [52, 56, 57, 70]. In these simulation studies, the influence of glass composition on the fracture behavior of glass at the nanoscale has been highlighted. Voids (or some times called “critical voids”) were found with sizes around 0.5 nm, weakly depending on glass composition (silica, sodium silicate or calcium aluminosilicate). All the above mentioned simulations were performed in vacuum, i.e., without interacting with water.

As mentioned by Wiederhorn *et al.* [45], careful attention should be payed when comparing the results of stress-corrosive fracture with the simulation studies, considering the vast differences in crack velocities and chemical conditions in these two techniques. Nevertheless, from a simulation perspective, there is always room for improvement in the simulation setup (to approach real experiments) and the analysis of the simulation outputs. This is indeed what we aim to do in this thesis. We will present a detailed analysis of the cavitation during glass fracture in section 3.3 and hopefully provide some fresh insights on this question.

**How large is the nonlinear zone near the crack tip?** In experiments, the nonlinear zone, or plastic zone, is usually characterized by measuring the crack tip

opening displacement and comparing it with an linear elastic solutions. The early measurement by Célarié *et al.* [10] showed that the nonlinear zone in a silicate glass is on the order of 100 nm, but later this value has been proven to be inaccurate [45]. The experimental study by Han *et al.* [71], based on the surface displacement field, suggested that the nonlinear zone in silica glass should be smaller than 10 nm. Note that this value is just an upper limit based on experimental observation. To our knowledge, experimental measurements with better resolution and for other silicate compositions have not been reported.

Continuum models such as the Dugdale-Barenblatt model have also been used to estimate the size of the nonlinear zone. According to the Dugdale-Barenblatt model, the size of the plastic zone at a crack tip in a continuum is given by [72, 73]

$$R = \frac{\pi K_{IC}^2}{8 \sigma_y^2}, \quad (1.6)$$

where  $K_{IC}$  is the critical stress intensity factor, and  $\sigma_y$  is the yield strength of the glass. For brittle materials (e.g. silica glass) the  $\sigma_y$  is very close to the maximum tensile strength. For silica glass, the estimated nonlinear zone size is 1.6 nm [45, 74]. This is basically the minimum size of the nonlinear zone that can be estimated from the elastic model. In experiments, particularly with AFM, reaching the accuracy level of 1-2 nm is a very difficult task. It is worth mentioning that the validity of these models for glass fracture at the nanoscale (where continuum mechanics is not valid anymore) is not so clear [45].

In computer simulations, the estimation of the nonlinear zone during glass fracture was rarely reported. This is due to both the limited system size ( $< 10$  nm usually) and the lack of a rigorous definition of the interface between plastic and elastic deformation. To our knowledge, only very recently, sensible measurements of the inelastic zone of glass fracture have been made from simulations. Rimsza and coworkers [61] adopted a quasi-2D geometry to study the propagation of a slit crack in silica glass. Based on the estimation of stress fields and dissipation energies around the crack tip, they found that the inelastic region is around 3 nm. Very recently, Chowdhury *et al.* investigated quasi-2D crack propagation in silica glass under tension by using reactive force fields [54]. By comparing the various properties of the glass during loading and unloading, they concluded that there is no traceable inelastic process zone in front of the crack tip. Apparently, no consensus has been reached on this question so far. It is also unclear how the simulation setup and the criteria for defining the inelastic zone will affect the final conclusion regarding its size.

**The role of network modifiers during glass fracture.** Alkali atoms such as Na are well-known to be able to modify the silica network by breaking Si-O bonds. However, when the glass is put under mechanical load, the behavior of these network modifying



atoms (or ions) is not so clear. Since alkali ions can diffuse in glass when a stress gradient is present, some theories of failure have proposed that the stress gradient at the crack tip can result in the migration of ions to the crack tip [75, 76]. This stress-assisted diffusion of the ions effectively weakens the glass and can cause sub-critical crack growth. Wiederhorn *et al.* [77] studied fracture of different oxide glasses in vacuum and found that there is no direct connection between crack growth and the presence of Na. Also the activation energy of Na diffusion in glass, 15-35 kcal/mol, is much smaller than that observed for crack motion, 60 to 176 kcal/mol. Instead, they proposed that crack growth depends on the crack-tip structure in the glass.

Further insight into the behavior of alkali ions during glass fracture was achieved by analyzing the composition and structure of fracture surface. Kelso *et al.* [78] found that the fracture surfaces of an alkali-containing silicate glass show layered distribution of atomic species: Alkali atoms are in the outermost layer, followed by oxygen, while Si atoms are drawn into the inner layers of the bulk. They further suggested that bond breakage in these glasses is likely due to the cooperative rearrangements of atoms which occur in the top several Å of the surface (in the case of a running crack, this should mean several Å around the crack tip).

There are a couple of mechanisms (or driving forces) proposed for the rearrangement of structure/composition near the fracture surface: 1) Higher mobility of alkali species relative to the O and Si species; 2) Alkali ions move to the outermost surface layer for charge compensating the dangling Si-O<sup>-</sup> bonds; 3) The stress gradient near the crack tip drives the alkali ions from the process zone to the surface.

## 1.7 Basics of computer simulations

Computer simulations, notably atomistic simulations, have now been established as standard techniques for exploring phenomena on the microscopic scales. The application of computer simulations is vast, from fundamental scientific exploration to engineering designs. Simulations can act as a bridge connecting theoretical models and experimental results. By using simulations one can also explore physical conditions that are difficult or impossible to realize in real experiments, such as extreme temperature and pressure [14].

For exploring the mechanical response of a material, multiscale approaches have become increasingly popular over the past two decades [9, 79]. To make contact between atomic and continuum length scales, one can choose modeling either by (i) a full atomistic approach through simulating millions of atoms or more to approach the continuum limit, or (ii) a hybrid method which couples atomic-scale simulations with continuum-mechanics-based models. Clearly, atomistic simulations play a central role

in both approaches.

There are two main atomistic simulation techniques, namely molecular dynamics (MD) and Monte Carlo (MC) simulations [14]. MC does not have an intrinsic time scale and is well-suited to investigate equilibrium states of a system. In contrast, MD is more suitable for exploring nonequilibrium states (e.g. glass states) and time-dependent properties. These simulation techniques provide a direct route from the microscopic details of a system (e.g., atomic species and interaction between atoms) to macroscopic properties that are of experimental interest (e.g., thermal expansion and transport coefficients).

Since the first MD study of vitreous silica by Woodcock *et al.* [80], MD simulations have been widely used to understand and predict the properties of oxide glasses. In recent years, MD simulations, combined with empirical modeling, have been used to accelerate the design of functional glasses which can now be produced at an industrial scale [81]. It should be noted, however, that the main limitation of MD simulation is the relatively short time and length scales in comparison with real experiments. Nonetheless, these discrepancies are becoming smaller and smaller thanks to the rapid development of computer hardware and efficient numerical algorithms.

Here we introduce the basics of MD simulations which have been used throughout this thesis. We will start with classical MD simulations which use empirical potentials to describe the interaction between atoms. Then we move on to *ab initio* MD which treats the atomic interaction quantum mechanically and thus allows to explore properties that are inaccessible by classical simulations.

### 1.7.1 Classical molecular dynamics

**Equations of motion.** In atomistic simulations, the goal is to determine the trajectories of the atoms in the system, characterized by the atomic positions  $\mathbf{r}_i$ , the atomic velocities  $\mathbf{v}_i$ , and their accelerations  $\mathbf{a}_i$ . Each atom is considered as a classical particle that follows Newton's second law, i.e.,

$$m_i \frac{d^2 \mathbf{r}_i}{dt^2} = \mathbf{F}_i, \quad (1.7)$$

where  $m_i$  and  $\mathbf{r}_i$  denote the mass and position of particle  $i$  in a  $N$  particle system, respectively.  $\mathbf{F}_i$  is the total force acting on this particle. The total energy of such a system is

$$E = K + V \quad (1.8)$$

where  $K$  is the kinetic energy of the entire system and  $V$  the potential energy. The kinetic energy is given by

$$K = \frac{1}{2} \sum_{i=1}^N m_i \mathbf{v}_i^2, \quad (1.9)$$

and the total potential energy is

$$V(\mathbf{r}) = \sum_{i=1}^N V_i(\mathbf{r}). \quad (1.10)$$

Note that the potential energy of particle  $i$  depends on the position of itself  $\mathbf{r}_i$  and all other particles in the system, denoted as  $\mathbf{r} = \{\mathbf{r}_j\}$ , where  $j \in \{1, \dots, N\}$ . The forces can be determined from the gradient of the potential energy and hence the equations of motion can be written as

$$m_i \frac{d^2 \mathbf{r}_i}{dt^2} = -\nabla_i V(\mathbf{r}). \quad (1.11)$$

The exact solutions of Eqs. (1.11) are unknown when  $N > 2$ . In practice, the equations can be solved by discretizing them in time, i.e., by using numerical algorithms called integrators.

**Integration.** There exist many integration schemes that are frequently used in MD simulations. The basic strategy is to develop a stepping method that gives new positions and velocities from the old ones, i.e.,

$$\mathbf{r}_i(t_0) \rightarrow \mathbf{r}_i(t_0 + \Delta t) \rightarrow \mathbf{r}_i(t_0 + 2\Delta t) \dots \quad (1.12)$$

$\Delta t$  is the time step for the integration. The initial positions  $\mathbf{r}(t_0)$  are often taken from available crystallographic and structural data from the literature. The initial velocities  $\mathbf{v}(t_0)$  are usually chosen to satisfy the Maxwell-Boltzmann distribution corresponding to a prescribed temperature. Here we introduce a very popular integration scheme called velocity Verlet algorithm. In this algorithm, the positions and velocities are updated as

$$\mathbf{r}_i(t + \Delta t) = \mathbf{r}_i(t) + \mathbf{v}_i(t)\Delta t + \frac{1}{2}\mathbf{a}_i(t)\Delta t^2 + O(\Delta t^4) \quad (1.13)$$

$$\mathbf{v}_i(t + \Delta t) = \mathbf{v}_i(t) + \frac{1}{2}[\mathbf{a}(t) + \mathbf{a}(t + \Delta t)]\Delta t + O(\Delta t^3). \quad (1.14)$$

The corresponding errors for positions and velocities are of orders  $O(\Delta t^4)$  and  $O(\Delta t^3)$ , respectively. The time step  $\Delta t$  for the integration has to be chosen carefully. In principle, the smaller the time step the more accurate the solution to the equation of motion becomes. Also, a smaller time step is crucial for guaranteeing conservation of the total energy. In practice, however, small time step means that more computer time is required for a given simulation time span. The goal is thus to find a operational balance accuracy of the integration and computational cost. In this work we have

chosen  $\Delta t = 1.6$  fs which is small enough to ensure a negligible energy drift and fluctuation over a wide range of temperatures.

**Interaction potential.** It is evident from Eqs. (1.11) that the interatomic potential is at the core of a successful MD simulation. The potential energy may be decomposed into terms depending on the coordinates of individual atoms, pairs, triplets, etc. [14]:

$$V(\mathbf{r}) = \sum_i V_1(\mathbf{r}_i) + \sum_i \sum_{j>i} V_2(\mathbf{r}_i, \mathbf{r}_j) + \sum_i \sum_{j>i} \sum_{k>j} V_3(\mathbf{r}_i, \mathbf{r}_j, \mathbf{r}_k) + \dots \quad (1.15)$$

where the notation  $\sum_i \sum_{j>i}$  indicates a summation over all distinct pairs  $i$  and  $j$  without counting any pair twice. The first term,  $V_1(\mathbf{r}_i)$ , is the energy arising from the particle itself, which is normally zero, unless there is an external field acting on the system. The second term,  $V_2(\mathbf{r}_i, \mathbf{r}_j)$ , the pair potential, is the most important one. ( $V_2(\mathbf{r}_i, \mathbf{r}_j)$  can also be written as  $V(r_{ij})$ , where  $r_{ij} = |\mathbf{r}_i - \mathbf{r}_j|$ . That is, the pair potential depends only on the magnitude of the pair separation  $r_{ij}$ ). The  $V_3(\mathbf{r}_i, \mathbf{r}_j, \mathbf{r}_k)$  term represents three-body interactions between atoms. These three-body terms are rarely included in computer simulations, since the calculation of these interactions is usually very time-consuming and these terms contribute only a small proportion to the total potential energy. Higher order terms are also neglected for the same reasons.

In most cases, the pairwise approximation gives a remarkably good description of material properties since the effects of higher order interactions can partially be included by fitting an “effective” pair potential. In the following we introduce a few popular functional forms for these pair potentials that are widely used in the simulation of liquids and glasses.

Pair potentials can usually be decomposed into short- and long-rang contributions:

$$V(r_{ij}) = V_S(r_{ij}) + V_L(r_{ij}) \quad (1.16)$$

One of the simplest and idealized pair potentials commonly used in computer simulation is the Lennard-Jones (LJ) 12–6 potential

$$V^{LJ}(r_{ij}) = 4\epsilon \left[ \left( \frac{\sigma}{r_{ij}} \right)^{12} - \left( \frac{\sigma}{r_{ij}} \right)^6 \right], \quad (1.17)$$

where  $\epsilon$  and  $\sigma$  are two potential parameters. The potential has a long-range attractive tail of the form  $-1/r_{ij}^6$  and a steeply rising repulsive wall at short distances. If the parameters are properly chosen, the LJ potential can describe quite reasonably the properties of some simple systems such as argon. It is also a popular choice for investigating general properties of liquids, and for comparison with theory.

For ionic systems such as silicates, the long-range term of the pair potential represents Coulombic interaction due to the electrostatic forces. The long-range interaction

is thus given by

$$V_L(r_{ij}) = \frac{q_i q_j}{4\pi\epsilon_0 r_{ij}}, \quad (1.18)$$

where  $q_i, q_j$  are the charges on ions  $i$  and  $j$ , respectively, and  $\epsilon_0$  is the vacuum permittivity. Different functional forms for the short-range interaction can be found in the literature. Two of the most common choices are the Buckingham potential

$$V_S^{\text{Buck.}}(r_{ij}) = A_{ij}\exp(-B_{ij}r_{ij}) - \frac{C_{ij}}{r_{ij}^6}, \quad (1.19)$$

and the Morse potential

$$V_S^{\text{Morse}}(r_{ij}) = D_{ij}[1 - \exp(A_{ij}(r_{ij} - r_0))]^2, \quad (1.20)$$

where  $A_{ij}, B_{ij}, C_{ij}$  and  $r_0$  are the parameters of the potentials. The Buckingham terms are used in the SHIK potential [82–84], which will be the choice in this thesis for performing classical MD simulations. The Morse term is implemented in the Pedone potential which has been used to simulate silica-based systems [85].

In practice, one has to define a cutoff distance  $r_{cut}$ , beyond which the interaction between atoms are not counted. The choice of  $r_{cut}$  is again a balance between accuracy and computational cost. For simulations at high temperature and pressure, in order to avoid the unphysical fusion of atoms at small distances (due to the  $-C_{ij}/r_{ij}^6$  term), one usually adds to the potential a strong repulsive term of the type  $D_{ij}/r_{ij}^n$ , where  $n$  is usually fixed (e.g.,  $n = 24$  in the SHIK potential) and  $D_{ij}$  is a fitting parameter. Note that the presence of this repulsive term induces only negligible variations of the potential energy and thus of the forces acting on atoms.

Pairwise potentials are usually parameterized by fitting structural, mechanical and vibrational properties from experimental data or quantum mechanical calculations. Transferability may be a main drawback of these empirical potentials, since they usually perform well only under certain composition and physical conditions.

**Periodic boundary conditions.** Atomistic simulations are usually performed for a sample containing less than  $10^7$  atoms. This number is much smaller than the sizes of real physical systems (which are of the order of  $10^{23}$  atoms) that one usually encounters in real life. As the system size used in simulations is small the surface effects can be strong. The problem of surface effects can be overcome to some extent by implementing periodic boundary conditions (PBCs). The original (central) simulation box is replicated throughout space to form an infinitely large bulk sample. The atoms in the periodic image cells move in exactly the same way as the atoms in the original box. If an atom leaves the central box, one of its images will enter through the opposite side. The atoms do not feel the existence of any wall or free surfaces. A two-dimensional example of such a periodic system is shown in Fig. 1.10. The duplicate boxes are labeled A, B, C, etc.

The effects of PBC may depend on the interaction potential and the phenomenon under investigation. For instance, the interaction between the atoms in the central cell and replicate cells may have a stronger effect on mechanical behavior than structural properties. Therefore, even with PBCs applied, it is still important to test if the properties of a simulated system and those of the macroscopic system which it represents are the same.

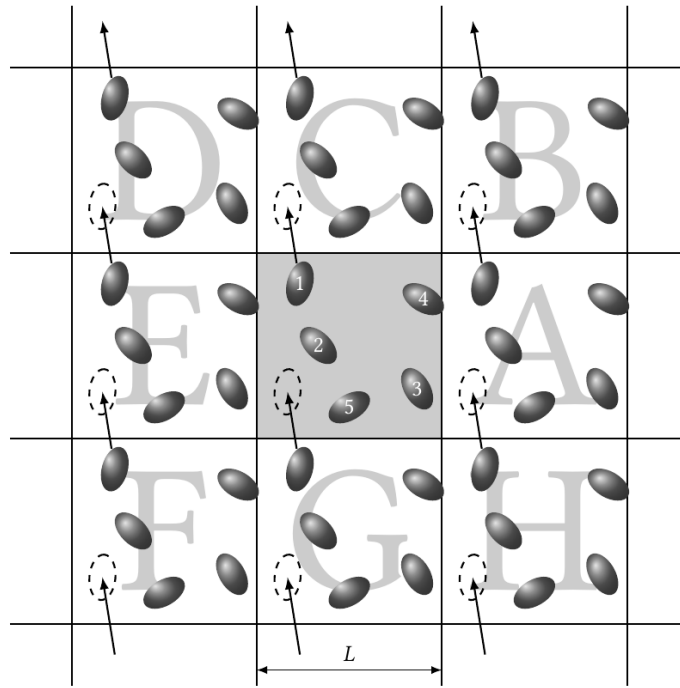


**Figure 1.10:** A two-dimensional periodic system. Molecules/atoms can enter and leave each box across each of the four edges. In a three-dimensional example, the four edges extend to six faces. After Allen and Tildesley [14].

**Statistical ensembles.** Statistical mechanics builds the bridge between microscopic states and macroscopic properties of a system. The central idea is the concept of the statistical (thermodynamic) ensembles. The ergodic hypothesis<sup>6</sup> states that for an isolated system of total energy  $E$ , the ensemble average of a property  $A$  is equivalent to the time average:

$$\langle A \rangle_{\text{Ensemble}} = \langle A \rangle_{\text{Time}} \quad (1.21)$$

where the symbol  $\langle \cdot \rangle$  denotes average. This relation allows the calculation of thermodynamical properties by simply averaging over sufficiently long time trajectories. The ensemble average of a property  $A$  is given by

$$\langle A \rangle_{\text{Time}} = \frac{1}{M} \sum_{i=1}^M A(\mathbf{p}, \mathbf{r}), \quad (1.22)$$

<sup>6</sup>The ergodic hypothesis is valid only for systems at equilibrium.

with  $\mathbf{p}_i = m_i \mathbf{v}_i$  as the linear momentum of particle  $i$ , and  $\mathbf{p} = \{\mathbf{p}_i\}$ , and  $M$  the number of measurements taken.

Different statistical ensembles are available in MD simulations, see Fig. 1.11 for a graphic representation. The microcanonical ensemble,  $NVE$ , is the “natural” ensemble in an MD simulation. This is due to the fact that the total energy  $E$  of the simulated system remains constant during the integration of the equations of motion (Eq. 1.11) for a system of  $N$  particles and a fixed volume  $V$ . In the  $NVE$  ensemble, the system evolves along a path of constant energy in the phase space. Other ensembles such as canonical ensemble,  $NVT$ , and isobaric-isothermal ensemble,  $NPT$ , are also frequently used in MD simulations. The  $NVT$  ensemble corresponds to a collection of thermodynamic states of the system characterized by a fixed number of particles  $N$  in a fixed volume  $V$  at a fixed temperature  $T$ . In contrast, the  $NPT$  ensemble is characterized by a fixed  $N$ , a fixed  $T$  and a constant pressure  $P$  (i.e., the volume becomes a dynamic variable). The  $NPT$  ensemble, in principle, is the closest to real experimental procedures.

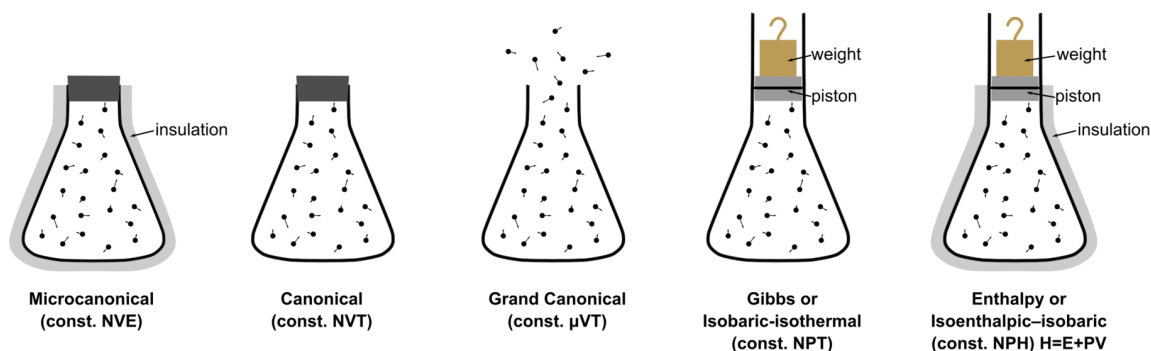


**Figure 1.11:** Visual representation of five statistical ensembles. (Image adapted from Wikipedia)

The usage of these thermodynamical ensembles often requires to control the temperature and pressure. In MD simulations, temperature is controlled through a thermostat which acts as a source of thermal energy and exchange heat with the coupled system whenever is necessary. Similarly, pressure is controlled by coupling the system to a barostat which usually acts as a “pressure bath”. Several approaches are available in MD simulations to maintain a target temperature and pressure [14]. In this thesis, the ones developed by Nosé [86, 87] and Hoover [88, 89] are used for performing simulation at constant temperature and pressure.

### 1.7.2 *Ab initio* molecular dynamics

In classical MD, the forces acting on atoms are obtained from an empirical potential with an fixed functional form and a set of parameters. The *ab initio* approach, by

contrast, requires no free parameters and the forces on the atoms are obtained from their electronic degrees of freedom (EDF).

Usually, within an *ab initio* approach, one solves the time-dependent Schrödinger equation which describes the EDF of the system and is given by

$$\mathcal{H}_e \Psi = E \Psi, \quad (1.23)$$

where the complex many-body wavefunction  $\Psi(\{\mathbf{r}_i\}; \{\mathbf{R}_I\})$  depends on the positions of the  $n$  electrons,  $\{\mathbf{r}_i\}$ , and the positions of the  $N$  nuclei,  $\{\mathbf{R}_I\}$  [90].  $E$  is the total energy, and the operator  $\mathcal{H}_e$  can be expressed as:

$$\mathcal{H}_e = - \sum_{i=1}^n \frac{1}{2} \nabla_i^2 + \sum_{i=1}^n \sum_{j>i}^n \frac{1}{|\mathbf{r}_i - \mathbf{r}_j|} - \sum_{i=1}^n \sum_{I=1}^N \frac{Z_I}{|\mathbf{r}_i - \mathbf{R}_I|}, \quad (1.24)$$

where  $Z_I$  denotes the charge of nucleus  $I$  which runs over the  $N$  nuclei. We note that this equation is written in atomic units, which means that Planck's constant, the charge and mass of electrons are set to unity. The Laplacian  $\nabla^2$  is given by  $\nabla^2 = \frac{\partial^2}{\partial x^2} + \frac{\partial^2}{\partial y^2} + \frac{\partial^2}{\partial z^2}$ . Equation (1.23) is called “Born-Oppenheimer” (or adiabatic) approximation, which treats quantum mechanically only the EDF and not the ones of the nuclei. This is quite reasonable since the mass of an electron is about 2000 times smaller than the lightest nucleus, i.e., the one of hydrogen. As the nuclei move much slower than the electrons, one thus assumes that the nuclei are clamped at fixed positions and the electrons are moving in the field of the nuclei.

To further reduce the computational complexity, one considers only the ground state solution of Eq. (1.23),  $\Psi_0$ , which correspond to the state of the lowest energy. The interaction potential between the nuclei is given by

$$\Phi(\{\mathbf{R}_J\}) = \langle \Psi_0 | \mathcal{H}_e | \Psi_0 \rangle + \sum_{J=1}^N \sum_{I>J}^N \frac{Z_I Z_J}{|\mathbf{R}_I - \mathbf{R}_J|}. \quad (1.25)$$

The force acting on particle  $I$  is thus expressed as [91]

$$\mathbf{F}_I = -\nabla_I \Phi(\{\mathbf{R}_J\}). \quad (1.26)$$

It is obvious from Eq. (1.25) that the key in the *ab initio* approach is to find the ground state solution  $\Psi_0$  of the Schrödinger equation. There are two main methods which can be used to achieve this goal. The first one is the quantum chemistry approach which starts from the Hartree-Fock method and factorizes the many-body wavefunction into one-particle wavefunction. One then has to search numerically for  $\Psi_0$  of this wavefunction.

The second method is the density functional theory (DFT) which exploits certain ground state properties of a many-electrons system in an external field. The current DFT formalism has been established in the early 60's by Hohenberg, Kohn and



Sham [92–94]. DFT replaces the many-body wavefunction  $\Psi(\{\mathbf{r}_i\})$  by the electronic density  $\rho(\mathbf{r})$ , effectively reducing the dimensionality of the problem from  $3 \times n$  (with  $n$  being the total number of electrons in the system) to three:

$$\rho(\mathbf{r}) = \int \dots \int d\mathbf{r}_2 \dots d\mathbf{r}_n \Psi_0^*(\mathbf{r}, \mathbf{r}_2, \dots, \mathbf{r}_n) \Psi_0(\mathbf{r}, \mathbf{r}_2, \dots, \mathbf{r}_n). \quad (1.27)$$

Within the Kohn-Sham approach, the total energy of the system can then be written as:

$$E_{\text{KS}}[\rho(\mathbf{r})] = -\frac{1}{2} \sum_{i=1}^n \int d\mathbf{r} \phi_i^*(\mathbf{r}) \nabla^2 \phi_i(\mathbf{r}) + \int d\mathbf{r} \rho(\mathbf{r}) \left[ \frac{1}{2} \int d\mathbf{r}' \frac{\rho(\mathbf{r}')}{|\mathbf{r} - \mathbf{r}'|} - \sum_{I=1}^N \frac{Z_I}{|\mathbf{r}_i - \mathbf{R}_I|} \right] + E_{\text{xc}}[\rho(\mathbf{r})]. \quad (1.28)$$

The first term represents the kinetic energy of a system of  $n$  non-interacting electrons having the same density as the real system exposed to the same external field. The second term is the Coulomb interaction between electron-electron and electron-nuclei. The third term denotes the exchange-correlation (XC) energy which accounts for all quantum many-body effects due to the Pauli exclusion principle. Since no exact expression exists for this term, approximations need to be made. Despite the fact that  $E_{\text{xc}}(\rho(\mathbf{r}))$  contributes much less than the other two terms to the total energy of the system, its determination may be crucial for chemically complex systems [95, 96].

The simplest approximation for  $E_{\text{xc}}[\rho(\mathbf{r})]$ , originally proposed by Kohn and Sham [93], is the local density approximation (LDA) which can be expressed as follows:

$$E_{\text{xc}}^{\text{LDA}}[\rho(\mathbf{r})] = \int d\mathbf{r} \rho(\mathbf{r}) \varepsilon_{\text{xc}}^{\text{LDA}}[\rho(\mathbf{r})] \quad (1.29)$$

where  $\varepsilon_{\text{xc}}[\rho(\mathbf{r})]$  denotes the exchange-correlation energy per particle of a uniform electron gas of density  $\rho(\mathbf{r})$ .

A more advanced approximation for  $E_{\text{xc}}[\rho(\mathbf{r})]$  is the generalized gradient approximation (GGA). GGA makes use of the density gradient of  $m$ th order and is given by

$$E_{\text{xc}}^{\text{GGA}}[\rho(\mathbf{r})] = \int d\mathbf{r} \rho(\mathbf{r}) \varepsilon_{\text{xc}}^{\text{GGA}}[\rho(\mathbf{r}); \nabla^m \rho(\mathbf{r})]. \quad (1.30)$$

The GGA functionals have been very successful in past two decades. Popular ones include PBE [97], BLYP [98], and PBEsol [99] (a revised version of the PBE functional and is used in this thesis).

However, it is not always the case that functionals with higher approximation predict more accurately than the predictions of the LDA functional. Hence one should choose the functional based on the properties of interest for a given system. It should be noted that the standard LDA and GGA functionals may fail in predicting some

material properties. A well-known problem is the underestimation of the band gap of semiconductors and insulators. To fix this deficiency, a third class of approximation for  $E_{\text{xc}}[\rho(\mathbf{r})]$ , hybrid functionals, were introduced [100, 101]. The hybrid functionals combine orbital-dependent Hartree-Fock with conventional GGA functionals in a linear manner (with a coefficient  $\alpha$  determines the amount of the mixing).

Further approximation are required in order to reduce the computational cost for calculating the forces on nuclei. As the chemical bonds between atoms are usually related to the outer valence electrons and depend only weakly on the core electrons, one can decouple the effects of core electrons with the ones of the valence electrons. Therefore, the core electrons of an atom are treated as an entity and their effects are replaced by an effectively potential, called “pseudo-potential”. The remaining valence electrons are described by a pseudo-wavefunction [90, 91].

For the *ab initio* approach within the framework of DFT, the equations of motion of the nuclei (particles) can be written as

$$M_I \frac{d^2 \mathbf{R}_I}{dt^2} = -\nabla_I E_{\text{KS},\text{min}}[\rho(\mathbf{r})], \quad (1.31)$$

where  $M_I$  and  $\mathbf{R}_I$  are respectively the mass and position of nucleus  $I$ , and  $E_{\text{KS},\text{min}}$  is the Kohn-Sham energy (Eq. (1.28)) for the system ground state. The nuclei are considered as classical particles and the integration scheme used in classical MD can be equally applied here to obtain the trajectories of the particles over time. As the particles move, the electronic structure changes. Therefore, in order to give a correct dynamics of the system in configuration space, one has to calculate the electronic ground state at each time step. This represents the Born-Oppenheimer molecular dynamics approach [14, 91], which is used in this thesis and is referred as *ab initio* molecular dynamics (AIMD) thereafter.

Explicit treatment of electronic degree of freedom makes AIMD computationally very expensive. Consequently, both the system size and time span that are accessible with AIMD are much smaller than in classical simulations. Notwithstanding, the merit of using this approach is obvious: The atomic interaction are described with quantum accuracy and one can obtain information that are inaccessible in classical simulations, notably chemical bonding [102].

### 1.7.3 Property calculation

Many properties of experimental interest can be calculated from computer simulations. Here we give a few examples. Other quantities concerning the structure, dynamics, and mechanical properties of the simulated system will be defined once encountered later in the thesis.

**Temperature.** According to the equipartition theorem, the temperature  $T$  of a system with  $N$  atoms is proportional to its kinetic energy  $K$ :

$$T = \frac{2\langle K \rangle}{3Nk_B}, \quad (1.32)$$

where  $k_B$  is the Boltzmann constant.

**Pressure.** The pressure is given by the virial theorem:

$$P = \frac{Nk_B T}{V} + \frac{1}{3V} \sum_{i=1}^{N-1} \sum_{j>i}^N \mathbf{F}(\mathbf{r}_{ij}) \cdot \mathbf{r}_{ij}. \quad (1.33)$$

The first term arises from the kinetic contributions and the second term stems from the interatomic forces.

**Pair distribution function.** This function, denoted as  $g(r)$ , is the simplest and is widely used for characterizing the structure of a liquid or a glass. It gives the probability of finding a pair of particles separated by a distance  $r$ , relative to the probability for a completely random distribution at the same density.  $g(r)$  is usually obtained by an ensemble average over pairs [14]

$$g(\mathbf{r}) = \frac{V}{N^2} \left\langle \sum_i^{N-1} \sum_{j>i}^N \delta(\mathbf{r} - \mathbf{r}_{ij}) \right\rangle, \quad (1.34)$$

where  $\mathbf{r}_{ij} = \mathbf{r} - \mathbf{r}_j$ . For an isotropic system the result depends only on  $r = |\mathbf{r}|$ .

**Mean squared displacement.** This quantity is often used to characterize the dynamics in a liquid. The mean squared displacement (MSD) at time  $t$  is defined as

$$r^2(t) = \frac{1}{N} \sum_{i=1}^N |\mathbf{r}_i(t) - \mathbf{r}_i(0)|^2, \quad (1.35)$$

where  $N$  is the number of particles to be averaged,  $r_i(0)$  and  $r_i(t)$  are respectively the reference position and the position at time  $t$  of the  $i$ th particle.

From the MSD at long times and the Einstein relation, one can obtain the diffusion constant  $D$  which is given by

$$D = \lim_{t \rightarrow \infty} \frac{r^2(t)}{6t}. \quad (1.36)$$

## Chapter 2

# On the critical role of interaction potential and simulation protocol

The reliability of the interaction potential is at the core of a successful computer simulation. There are two possibilities to describe these interactions: The *ab initio* approach and the classical approach based on the use of effective potential. In the first approach the interactions are calculated directly from the electronic structure of the system, a procedure that is very accurate (although not exact) but computationally very expensive [91]. We have used this approach to study the structural, vibrational and electronic properties of glass surface, and the results will be detailed in chapter 5. In the second approach, effective potentials allow to access significantly larger systems and longer times, but with compromised accuracy and transferability. Despite the aforementioned drawbacks, many numerical investigations are done with effective potentials since for many studies one needs to have systems that are relatively large to avoid finite size effects, e.g. to probe the mechanical properties of glasses.

In this work, we will use classical MD method to study the structure and mechanical properties of glasses. Thus it is of great importance to use a potential that is reliable for the investigated system (sodo-silicate) and the properties of interest (notably the mechanical behavior of glass). As we will see later, a realistic description of the fracture behavior of sodium silicate glass requires a system size of  $\approx 10^5$  atoms<sup>1</sup> and a relatively small cooling rate (e.g., 1 K/ps). These requirements make many-body interaction potentials and reactive force fields computationally too expensive to use. Therefore, here we will only focus on evaluating the performance of two-body effective potentials, in particular the ones that have often been used in the past for the simulation of sodo-silicate system.

---

<sup>1</sup>This number is only valid for bulk sample. For producing glass samples with free surfaces, the required system size may be ten times larger.

It is found that while most structural quantities show a relatively mild dependence on the used potential, the mechanical properties such as the failure stress and strain as well as the elastic moduli depend very strongly on the potential. Across the range of properties examined, the best performance is achieved with the SHIK potential, which will be our choice for the subsequent large scale simulations of sodo-silicate glasses.

## 2.1 Interatomic potentials

The compositions of concern are  $\text{SiO}_2$  and  $\text{Na}_2\text{O}-3\text{SiO}_2$  (NS3), both of which are representatives of oxide glass former. We consider several pairwise potentials, all of which have the same functional form given by

$$V(r_{ij}) = \frac{q_i q_j e^2}{4\pi\epsilon_0 r_{ij}} + A_{ij} e^{-r_{ij}/B_{ij}} - \frac{C_{ij}}{r_{ij}^6} \quad , \quad (2.1)$$

i.e., the sum of a Coulomb and Buckingham term. (Here  $r_{ij}$  is the distance between atoms  $i$  and  $j$ .) Thus the differences between the potentials are just the values for the various parameters of the potential, i.e.,  $q_i$ ,  $A_{ij}$  etc. For  $\text{SiO}_2$  and NS3, we considered the potentials proposed by Habasaki and Okada (HO) [103], by Teter *et al.* [104], by Guillot and Sator (GS) [105], and by Sundararaman *et al.* (SHIK) [83, 84]. For the SHIK potential, a version in its earlier development (unpublished), hereafter called SHIK<sub>0</sub> is also evaluated. We will show that these two versions of the SHIK potential give very similar results for the sodo-silicate in both liquid and glass states. For silica alone we also considered the potential by van Beest *et al.* (BKS) [106] since it is one the most used empirical potentials for the simulation of silica. The parameters of various potentials used in the present work are given in Table 2.1.

The presence of the Coulomb term in Eq. (2.1) makes the use of such potentials computationally expensive since the Coulomb interaction has to be evaluated by means of approaches like the Ewald summation [14]. One possibility to avoid this problem is to use the approach proposed by Wolf *et al.* [107, 108], in which the Coulomb term is replaced by

$$\frac{q_i q_j e^2}{4\pi\epsilon_0 r_{ij}} \rightarrow \begin{cases} \frac{q_i q_j e^2}{4\pi\epsilon_0} \left[ \left( \frac{1}{r_{ij}} - \frac{1}{r_c} \right) + \frac{r_{ij} - r_c}{r_c^2} \right] & r < r_c \\ 0 & r \geq r_c \end{cases} \quad , \quad (2.2)$$

where  $r_c$  is a cutoff distance. In this form the potential becomes thus short ranged and hence computationally much more efficient. The SHIK potential was originally developed by using the expression given by Eq. (2.2) as a substitution for the Coulomb term. However, we note that the potential can predict equally well the properties of

Parameters	BKS	GS	Teter	HO	SHIK	SHIK <sub>0</sub>
$A_{\text{SiO}}$ [eV]	1388.773	9022.853	1844.746	1742.1231	1120.529	1120.529
$A_{\text{OO}}$	18003.76	50306.43	13702.91	10631.499	23107.85	23107.85
$A_{\text{SiSi}}$	0.0000	0.0000	0.0000	865032008	2797.979	2797.979
$A_{\text{NaO}}$		120304.6	4383.756	1854.3947	1127566	1146444
$A_{\text{SiNa}}$		0.0000	0.0000	81407.619	495653	542345.9
$A_{\text{NaNa}}$		0.0000	0.0000	2558.6814	1476.9	1401.567
$B_{\text{SiO}}$ [ $\text{\AA}$ ]	0.3623	0.2650	0.3436	0.3513	0.3457	0.3457
$B_{\text{OO}}$	0.2052	0.1610	0.1938	0.2085	0.1962	0.1962
$B_{\text{SiSi}}$	1.0000	1.0000	1.0000	0.0657	0.2269	0.2269
$B_{\text{NaO}}$		0.1700	0.2438	0.2603	0.1450	0.1423
$B_{\text{SiNa}}$		1.0000	1.0000	0.1175	0.1847	0.1869
$B_{\text{NaNa}}$		1.0000	1.0000	0.1692	0.2935	0.2979
$C_{\text{SiO}}$ [ $\text{eV}\cdot\text{\AA}^6$ ]	175.0000	85.0927	192.580	212.9333	26.1321	26.1321
$C_{\text{OO}}$	133.5381	46.2981	54.6810	69.9590	139.6948	139.6948
$C_{\text{SiSi}}$	0.0000	0.0000	0.0000	23.1044	0.0000	0.0000
$C_{\text{NaO}}$		0.0000	30.7000	0.0000	40.5620	38.2298
$C_{\text{SiNa}}$		0.0000	0.0000	0.0000	0.0000	0.0000
$C_{\text{NaNa}}$		0.0000	0.0000	0.0000	0.0000	0.0000
$q_{\text{Si}}$ [e]	2.4	1.89	2.4	2.4	1.7755	1.7755
$q_{\text{Na}}$ [e]		0.4725	0.6	0.88	0.6018	0.5497
$q_{\text{O}}$ [e]	-1.2	-0.945	-1.2	-1.28*	-0.9328*	-0.9180*
$R_{\text{cut}}$ [ $\text{\AA}$ ]	5.5/12.0	11.0/12.0	8.0/12.0	8.0/12.0	8.0/10.0	8.0/10.0

**Table 2.1:** Parameters for the various potentials. The oxygen charges for the HO and SHIK potentials are given for the NS3 composition (see text for details). For silica, the oxygen charge is  $-q_{\text{Si}}/2$ . Also included are the cutoff distances  $R_{\text{cut}}$  for evaluating the short range/long range parts of the potentials.

the sodo-silicate system when switching back to the Coulomb interaction (Eq. (2.1)), see Ref. [109].

Due to the van der Waals term in Eq. (2.1), the potentials have a singularity at short distances. To prevent that particles fuse together in a unphysical manner, we added to the potentials a short range repulsive term [84, 110]. We note that this modification does not affect at all the properties of the system at intermediate and low temperatures and hence can be considered to be just a computational trick to avoid this singularity.

Finally we mention that for the HO and SHIK potentials, the charge of the oxygen atoms depends on composition. To maintain charge neutrality of the system, one thus

determines the charge of O by

$$q_{\text{O}} = \frac{(1 - y) q_{\text{Si}} + 2y q_{\text{Na}}}{2 - y}, \quad (2.3)$$

where  $y$  is the mole concentration of  $\text{Na}_2\text{O}$  [84, 103]. The oxygen charges reported in Table 2.1 were calculated for  $y = 0.25$ , which corresponds to the sodo-silicate composition (NS3) studied in the this chapter.

In Fig. 2.1 we plot the potential energy and the forces for the potentials considered. These graphs demonstrate that the different potentials and forces depend strongly on the chosen set of parameters which give thus a first indication that the predicted glass properties will depend on the used potential.

## 2.2 Simulation methods

The systems we consider are pure silica and a sodium silicate with composition  $\text{Na}_2\text{O}-3\text{SiO}_2$  corresponding to a  $\text{Na}_2\text{O}$  molar concentration of 25 %. The glass samples were produced by using the conventional melt-quench method. We used cubic boxes (periodic boundary conditions) that contained between 5000 and 600,000 particles, which corresponds to sizes between 4 and 20 nm at room temperature. For the long-range Coulomb interaction, the Wolf truncation method (see Eq. (2.2)) was employed only when using the SHIK potential, while for the other potentials this interaction was evaluated with the particle-particle particle-mesh (PPPM) solver algorithm [111] with an accuracy of  $5 \times 10^{-5}$  (desired relative error in forces).

The samples were first equilibrated at a high temperature in the canonical ensemble ( $NVT$ ) using a fixed volume that corresponds to the experimental value of the density of the glass at room temperature, i.e.,  $2.20 \text{ g/cm}^3$  for silica and  $2.43 \text{ g/cm}^3$  for NS3 [112]. These  $NVT$  runs were done at 3600 K for silica and 3000 K for NS3, both for about 300 ps, a time that is sufficiently long to equilibrate the samples completely. These liquids were subsequently equilibrated in the  $NPT$  ensemble (constant number of atoms, pressure, and temperature) at the same temperatures and at zero pressure. The lengths of these  $NPT$  runs depended on the potential considered and were sufficiently long to equilibrate the samples, i.e. the mean squared displacement of the particles was more than  $100 \text{ \AA}^2$  (see below). For the GS potential, the  $NPT$  equilibration of the NS3 liquid was done at 2100 K since for higher temperatures the samples became unstable because they were above the boiling point.

After equilibration, the liquid samples were quenched to 300 K in the  $NPT$  ensemble at zero pressure. The cooling rate was  $0.25 \text{ K/ps}$ , i.e. a value that is relatively small for MD simulations of sodium silicate glasses with a comparable system size. Previous

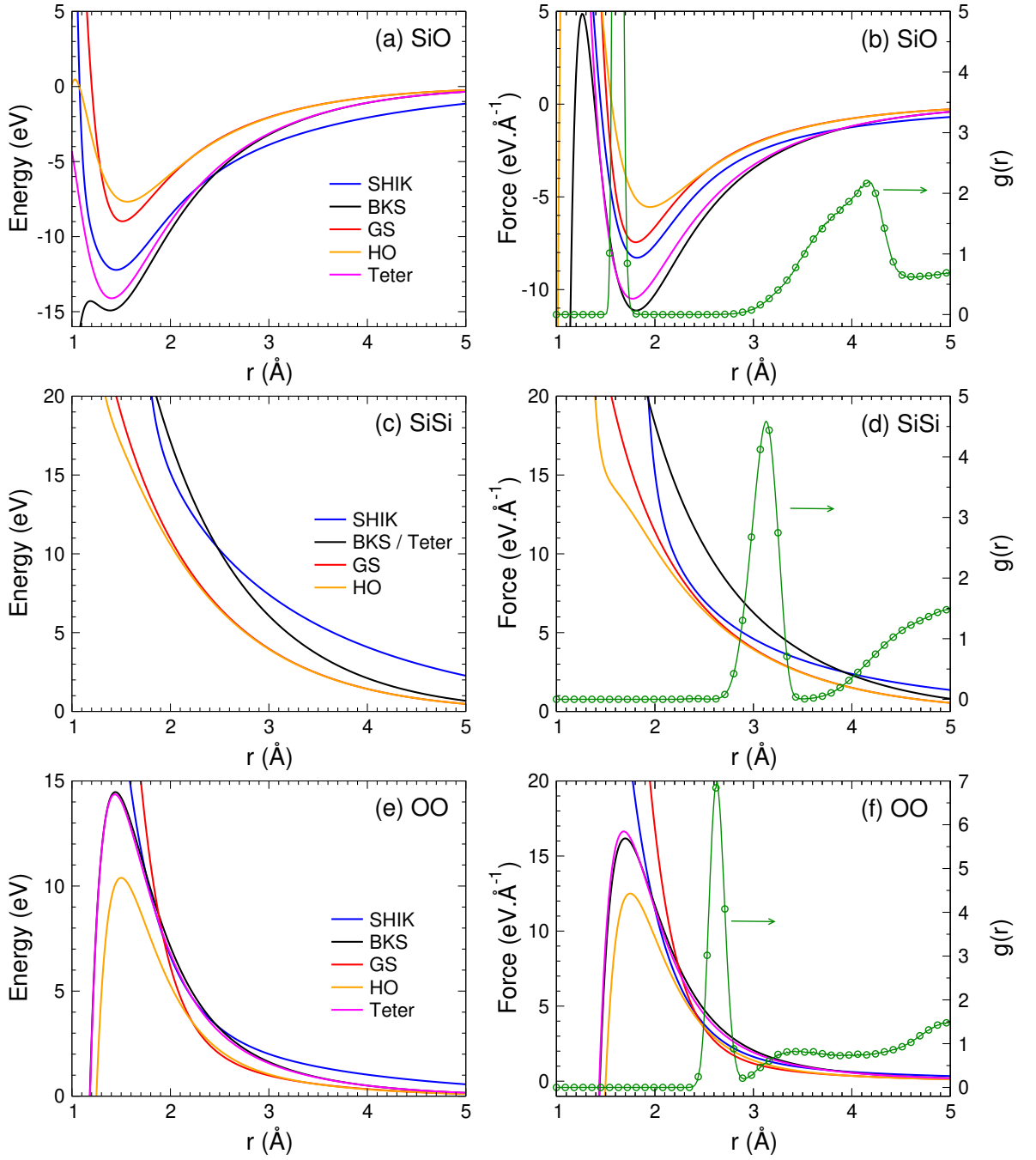


**Figure 2.1:** Distance dependence of the various interaction potentials [panels a), c), and e)] and their corresponding forces [panels b), d), and f)] for the SiO, SiSi and OO pairs, respectively. Also included in the right panels are the corresponding pair correlation function as predicted by the SHIK potential at 300 K (symbols).

simulation studies have shown that this cooling rate is small enough so that properties of the system do not depend on the cooling rate in a significant manner [110, 113, 114]. The glass samples at 300 K were then annealed in the  $NPT$  ensemble for 160 ps before being subjected to mechanical tests.



To determine the mechanical properties of the annealed glass samples we strained them in one direction using a strain rate of 0.5/ns. This value is sufficiently small to obtain results that do not depend in a significant manner on the rate, see Fig. 3.5. Mechanical loading for the glass was done both in the *NVT* and *NPT* ensembles. For the *NPT* simulation, the pressures in the directions orthogonal to the loading direction were set to zero and thus the corresponding box lengths were allowed to change. In contrast, for the *NVT* simulations, the two orthogonal directions were not allowed to change, i.e. the cross section was constant. From these simulations we can study the mechanical behavior, particularly the stress-strain behavior of the glass under uniaxial tension.

To calculate the stress-strain curve, we increased the dimension of the box in one direction linearly in time, i.e.,

$$L(t) = L_0(1 + \epsilon(t)), \quad (2.4)$$

where  $L_0$  is the original box length in the pulling direction and  $L(t)$  the length at time  $t$ . The strain  $\epsilon(t)$  is given by

$$\epsilon(t) = \dot{\epsilon}t, \quad (2.5)$$

where  $\dot{\epsilon}$  is the strain rate. The stress tensor is calculated by the virial theorem using the expression [115]

$$\boldsymbol{\sigma} = \frac{1}{V} \sum_{i=1}^N [m_i \mathbf{v}_i \otimes \mathbf{v}_i + \mathbf{r}_i \otimes \mathbf{f}_i], \quad (2.6)$$

where  $V$  and  $N$  are the volume and the total number of atoms of the simulation box, respectively, while  $m_i$  is the mass of atom  $i$ , and  $\mathbf{v}_i$ ,  $\mathbf{r}_i$  and  $\mathbf{f}_i$  are the velocity, position and force vector of atom  $i$ , respectively.

Temperature and pressure (for the *NPT* ensemble) were controlled using a Nosé-Hoover thermostat and barostat [87–89]. All simulations were carried out using the LAMMPS software [116] with a time step of 1.6 fs.

The results presented in the following sections have been obtained by using for each potential only one sample per composition. The results regarding the structural and dynamical properties were obtained by analyzing the samples containing 36,480 and 38,400 atoms for SiO<sub>2</sub> and NS3, respectively. These numbers correspond to box sizes around 8 nm at room temperature. These system sizes are sufficiently large to make sample-to-sample fluctuations small.

## 2.3 Dynamical and structural properties

Firstly, we investigate the dynamics of the liquids by calculating the mean squared displacement (MSD) (see Eq. (1.35)). In Fig. 2.2 we show the time dependence of the

MSD for Si, i.e., the species that moves the slowest. The temperatures are those at which we have equilibrated the samples in the  $NPT$  ensemble. It can be seen that at these temperatures, the dynamics is already somewhat glassy in that at intermediate times the MSD has a plateau [3]. These graphs also show that at long times the MSD is a linear function of time, i.e., that the particles have reached the diffusive regime, indicating that the system is equilibrated. In agreement with previous results [117], we find that the MSD at long times, and hence the diffusion constant, shows a very strong dependence on the potential (more than a factor of ten). Since it can be expected that the activation energy for the diffusion constant also depends on the potential considered, the diffusion constant at lower temperatures will differ even more. For NS3, panel (b), we note that the SHIK and SHIK<sub>0</sub> potentials give very similar results regarding the dynamics of the liquid.

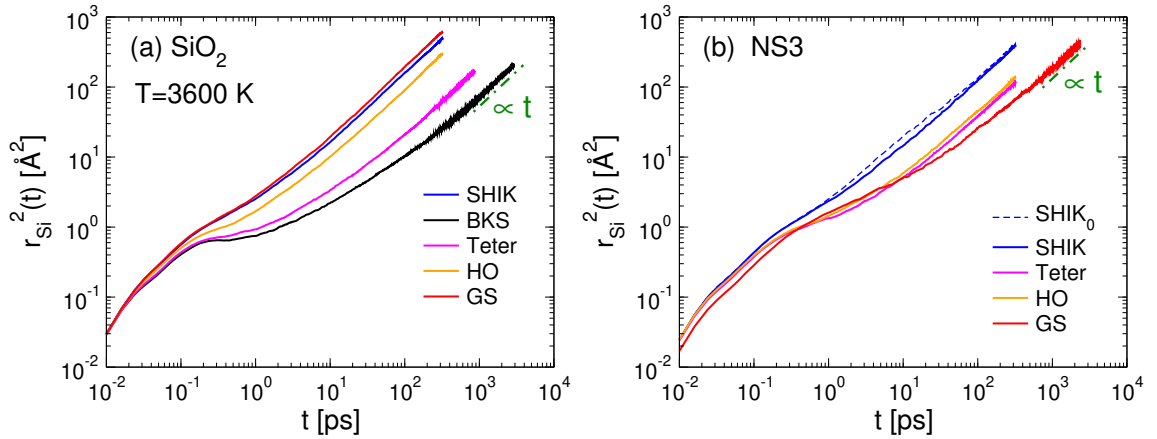


**Figure 2.2:** Mean squared displacement for silicon in the silica (a) and the NS3 (b) samples during the  $NPT$  equilibration at high temperatures and at zero pressure. The different curves correspond to the potentials used and the dashed line shows the diffusive behavior at long times. For  $\text{SiO}_2$  the temperature is 3600 K. For NS3 the temperature is 3000 K except for the GS curve which is for 2100 K.

A further interesting quantity to look at is the density of the sample during quenching. In Fig. 2.3 we show the temperature dependence of the density as predicted by the various potentials. The quenching was carried out at zero pressure from high temperatures to 0 K. These curves demonstrate that the  $T$ -dependence of the density depends significantly on the potential: Not only the absolute values differ but also the slope, i.e. the thermal expansion coefficient. For NS3 these slopes are larger than the ones for  $\text{SiO}_2$ , in agreement with the experimental findings [112].

Also included in the graphs are the experimental densities from room temperature (300 K, left most symbol) to higher temperatures. The densities at higher temperatures

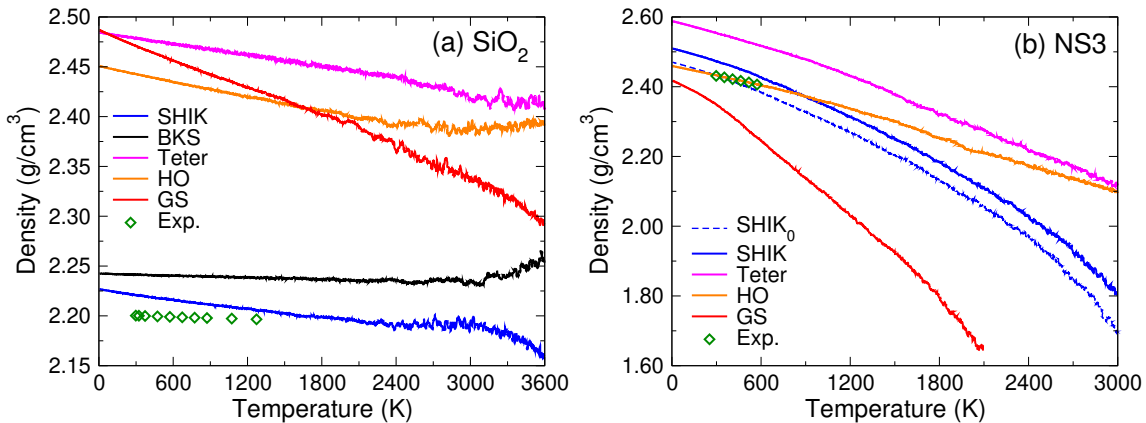


**Figure 2.3:** Temperature dependence of the density during the quench at zero pressure for silica and NS3, panels (a) and (b), respectively.

were calculated by using the formula

$$\rho = \frac{\rho_0}{1 + 3\alpha(T - T_0)}, \quad (2.7)$$

where  $\rho$  is the mass density at temperature  $T$ ,  $\rho_0$  is the density at room temperature  $T_0$ , and  $\alpha$  is the experimental thermal expansion coefficient [112]. For  $\text{SiO}_2$ , it can be seen that the Teter, HO, and GS potentials predict a density that is significantly too high. A good agreement with the experimental data is achieved by the BKS and SHIK potentials, not only at room temperature but also at higher temperatures. For NS3, it is notable that the HO potential predicts perfectly well the  $T$ -dependence of the density as given by the experimental data. The SHIK and SHIK<sub>0</sub> potentials are in fair agreement, whereas the GS and Teter potentials predict densities that are relatively far from the experimental ones.

We note that the density at room temperature is influenced by the cooling rate of the sample [110]. However, this dependence is relatively mild since the density is directly related to the fictive temperature which depends only logarithmically on the cooling rate. Thus the big discrepancy between the predicted density and the experimental value cannot be rationalized by a too high cooling rate but must instead be considered as a flaw of the used potential.

We now discuss the structural properties of the glasses. To start, we will look at the static structure factor (as seen in neutron scattering experiments) which is the weighted sum of the partial structure factors [3]:

$$S_{\text{tot}}(q) = \frac{N}{\sum_{\alpha=\text{Si,O,Na}} N_{\alpha} b_{\alpha}^2} \sum_{\alpha,\beta=\text{Si,O,Na}} b_{\alpha} b_{\beta} S_{\alpha\beta}(q) \quad . \quad (2.8)$$

Here  $q$  is the wave-vector,  $b_{\alpha}$  is the neutron scattering length [118] for species  $\alpha$  and the partial structure factor  $S_{\alpha\beta}(q)$  is defined as

$$S_{\alpha\beta}(q) = \frac{f_{\alpha\beta}}{N} \sum_{j=1}^{N_\alpha} \sum_{k=1}^{N_\beta} \langle \exp(i\mathbf{q} \cdot (\mathbf{r}_j - \mathbf{r}_k)) \rangle, \quad (2.9)$$

where  $\alpha, \beta = \text{Si, O, Na}$ , with  $f_{\alpha\beta} = 1$  for  $\alpha = \beta$  and  $f_{\alpha\beta} = 1/2$  otherwise, and  $N$  is the total number of atoms. As can be seen from Fig. 2.4(a), for the case of silica the two considered potentials agree very well with the experimental data. This is not that surprising since in most cases the parameters of such potentials have been optimized to reproduce the structure of the glass. Qualitatively the same conclusion can be drawn for the case of NS3, panel (b). There is, however, one exception: The GS potential shows a strong increase of the signal at small  $q$ . This behavior indicates the presence of a phase separation, in this case the formation of large domains of Na atoms, and a visual inspection of the sample shows that this is indeed the case, see Fig. 2.5. We note that this defect of the potential is not readily seen in the radial distribution functions and seems to have gone unnoticed so far, see Fig. 2.6.

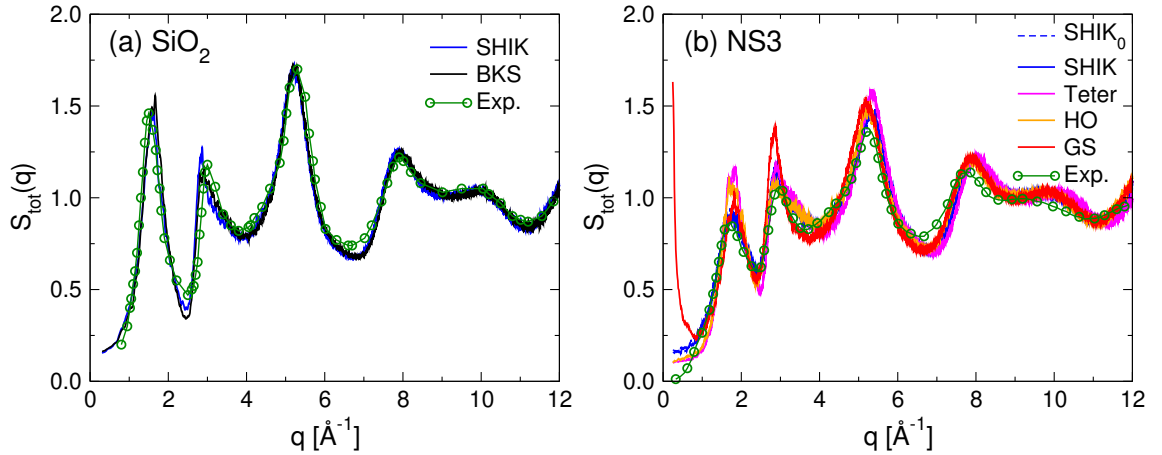


**Figure 2.4:** Static structure factor as seen in neutron scattering experiments for silica (a) and NS3 (b) glasses at 300 K. Experimental data for silica are taken from Ref. [119] and for NS3 from Ref. [120].

A further useful quantity to characterize the structure of silicate glasses is the bond angle distribution (BAD). Of particular interest is the inter-tetrahedral angle SiOSi since it gives information about the relative orientation of two neighboring tetrahedra. In Fig. 2.7 we show the BAD of SiOSi of the glasses produced by using various potentials. For the case of SiO<sub>2</sub>, panel (a), we recognize that both the BKS and SHIK potential predict a position of the maximum of the distribution that is compatible with the experimental estimate [121]. For NS3, panel (b), the BAD of SiOSi is basically independent of the potential used. The only exception is the data obtained from the Teter potential which peaks at a significantly larger angle.

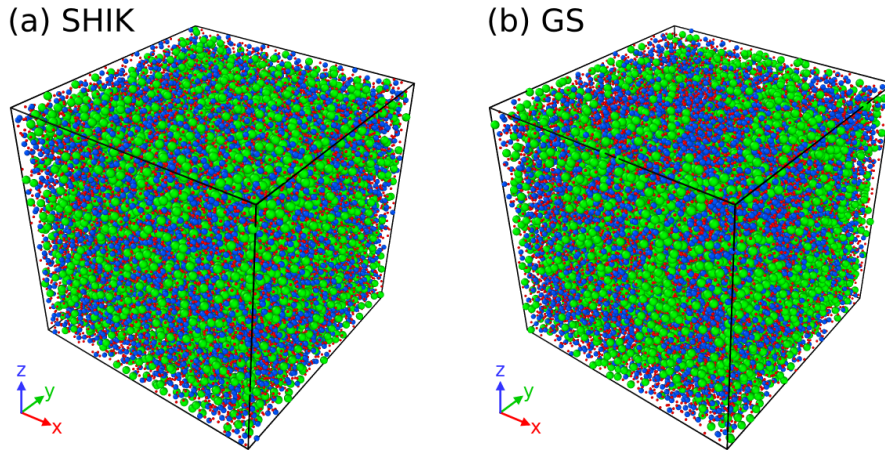


**Figure 2.5:** Atomic structure of the NS3 glasses produced by using the SHIK (a) and GS (b) potentials. O, Si and Na atoms correspond to red (small), blue (medium) and green (big) balls, respectively.

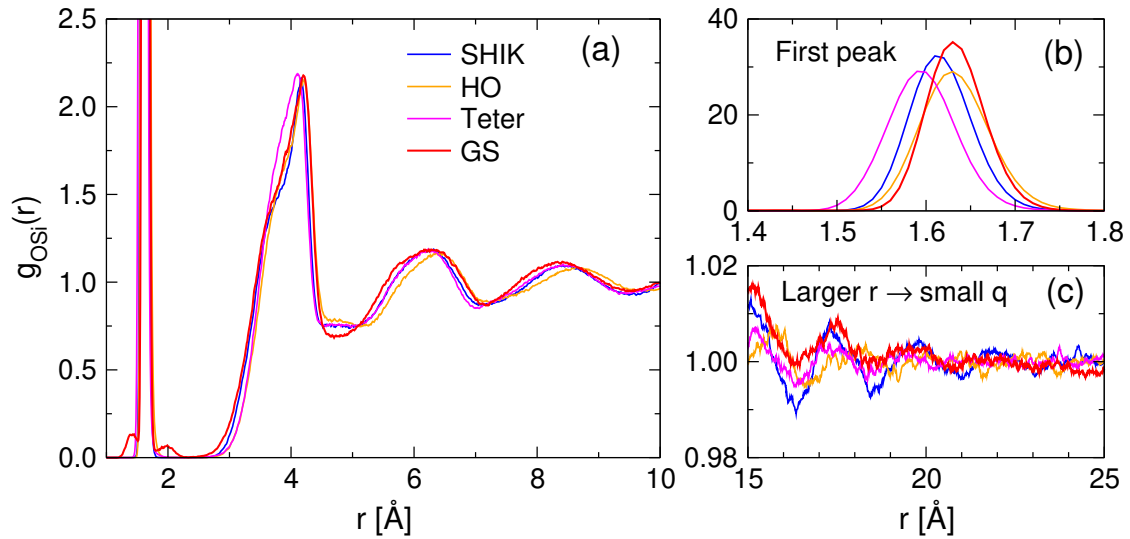


**Figure 2.6:** Radial distribution function for the Si-O pair of the NS3 glass at 300 K.

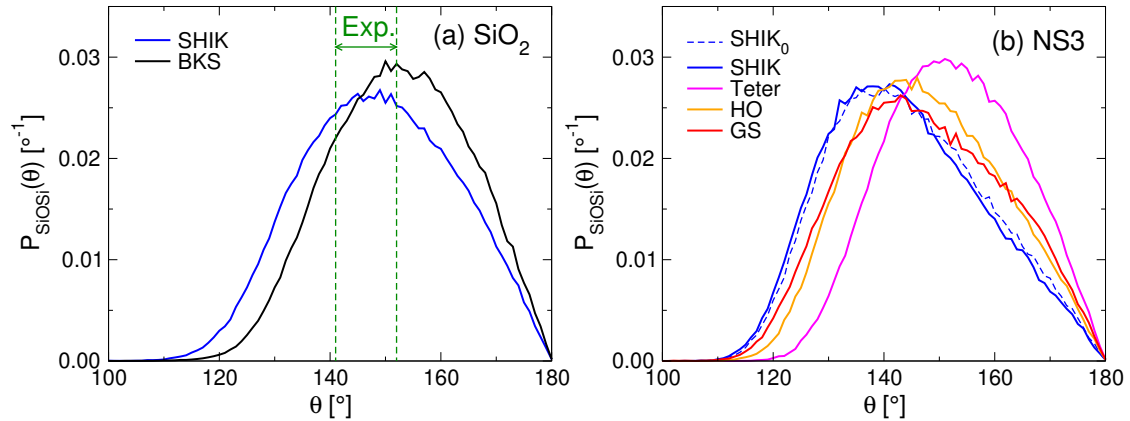


**Figure 2.7:** SiOSi angle distribution for silica (a) and NS3 (b) glasses. The vertical green lines indicate the range of most probable SiOSi angle extracted from previous experimental studies (see Ref. [121]).

The mean SiOSi angles are  $144.5^\circ$ ,  $143.7^\circ$ ,  $152.3^\circ$  and  $147.7^\circ$ , and  $147.2^\circ$  for the SHIK<sub>0</sub>, SHIK, Teter, HO and GS potentials, respectively. The prediction by the SHIK<sub>0</sub> and SHIK potentials are in good agreement with experimental measurements [122] which gives a mean SiOSi angle of  $141.7^\circ$ . In addition, previous *ab initio* simulations [123, 124] of very similar compositions predicted the peak positions of the BAD to be close to  $140^\circ$ . This value is compatible with the prediction of the SHIK, HO, and GS potentials, but not with the Teter potential.

Finally we discuss two local structural quantities that probe the local environment of an atom, namely the oxygen speciation and the distribution of the  $Q_n$  tetrahedral species in NS3. For the former we have used the first minimum in the radial distribution function of the Si-O pair to determine the number of silicon atoms in the nearest neighboring shell of a given oxygen atom,  $CN_O$ , and thus to determine whether the atom is free (FO,  $CN_O = 0$ ), non-bridging (NB,  $CN_O = 1$ ), bridging (BO,  $CN_O = 2$ ), or threefold coordinated (TBO,  $CN_O = 3$ ). Fig. 2.8(a) shows that the considered potentials all give the same distribution and it agrees very well with the experimental measurements [125]. Thus, one can conclude that this quantity is very robust or in other terms the oxygen speciation is not very useful indicator for testing the quality of a potential.

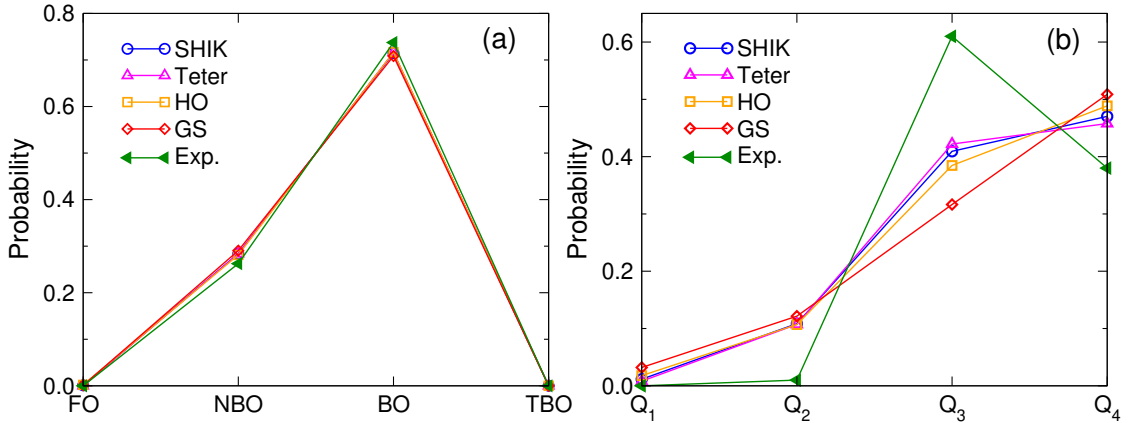


**Figure 2.8:** Distributions of oxygen speciations, panel (a), and  $Q_n$  species, panel (b), for the NS3 glass at 300 K. The experimental data in panels (a) and (b) is from Ref. [125], and Ref. [126], respectively.

Things are different for the  $Q_n$  species, i.e. the probability that a silicon atom is connected to exactly  $n$  bridging oxygens,  $n = 0, 1, 2, 3, 4$ . These probabilities are shown in Fig. 2.8(b) and one finds that the frequency of  $Q_3$  depends significantly on the potential. In particular, one observes that the GS potential gives a probability that is rather low relative to the other potentials and also to the experimental data. This observation indicates that the fraction of the  $Q_3$  units can be used as an indicator for evaluating the quality of a potential. In addition, we mention that the network

depolymerization depends also on the cooling rate: For sodosilicate glasses, it has been shown that the percentage of  $Q_3$  increases with decreasing quench rate while the  $Q_4$  one decreases, and hence improve the agreement with the experimental data [114].

## 2.4 Mechanical properties

### 2.4.1 System-size dependence

In computer simulations, it is important to check that the system studied is large enough to avoid boundary effects (or at least to maintain the effects at an insignificant level). Often, the finite size effects also depend on which property of the system one looks at. For example, structural properties of liquids and glasses can usually be studied from simulations with a system size of  $10^3 - 10^4$  atoms. In contrast, elasticity and fracture are associated with strongly non-local processes and hence finite size effects can be prominent, as we will see in the following.

Figure 2.9 shows the stress-strain curve for fracture simulations with different (cubic) box sizes. (These results are for the SHIK potential, but for the other force fields a similar behavior has been found.) For the case of silica, panel (a), one finds that the elastic regime is basically independent of  $L$ . However, once the failure point (i.e. the strain at which the stress has a maximum) has been attained there are very strong finite size effects in that the small systems break in a much gentler manner than the large ones. Only if  $L$  has reached 10 nm, which corresponds to around 75,000 atoms, the stress-strain curve becomes basically independent of the system size (see Refs. [127] and [57] for related studies).

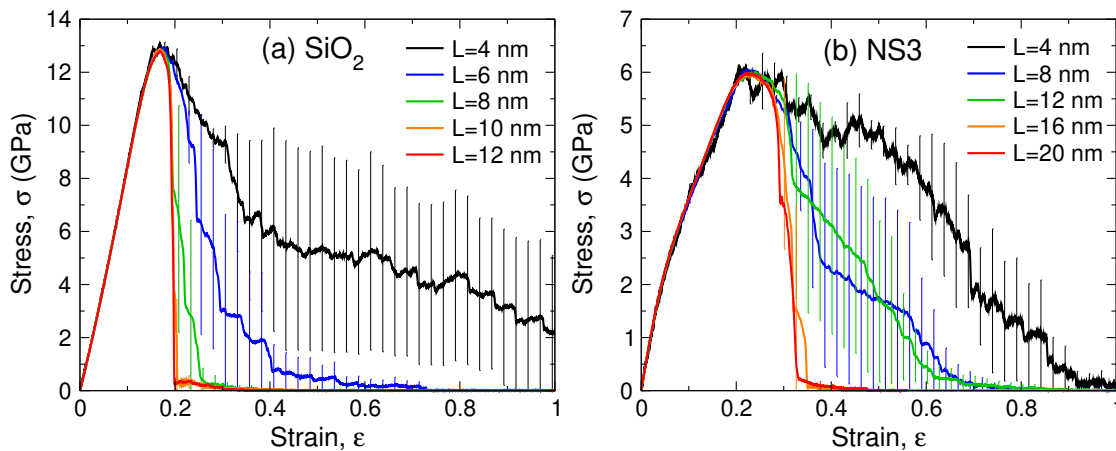


**Figure 2.9:** Dependence of stress-strain curve on the system size for the SHIK potential. (a) Silica and (b) NS3. The system size ranges from around 5000 to around 600,000 atoms, corresponding to a cubic box size from 4 nm to 20 nm at room temperature density, before starting to strain. The error bars were evaluated as the standard deviation of three samples.

For the case of NS3, panel (b), the system size dependence is more pronounced in that one has to use systems of about  $L = 16$  nm, corresponding to about 300,000 atoms, before the stress-strain curve converges. These stronger finite size effects are likely related to the presence of the Na atoms which make a more heterogeneous structure in the NS3 glass compared to that of  $\text{SiO}_2$  [29, 128]. Similar to the case of silica, we find that for the small-strain region (i.e., before the failure point) the curves superimpose quite nicely and thus this region depends only weakly on system size.

In order to make a fair comparison of the behavior predicted by the different potentials we have used in the following the same system size  $L = 8$  nm, which corresponds to  $N = 36480$  and  $N = 38400$  atoms for  $\text{SiO}_2$  and NS3, respectively. Although for this system size one still can observe finite size effects, they are minor and hence do not preclude to understand which potentials give rise to a realistic fracture behavior and which ones do not.

## 2.4.2 Fracture behavior and elastic moduli

We now discuss the fracture behavior and the elastic properties of the glasses. In Fig. 2.10 we show the stress-strain curves obtained in  $NPT$  ensemble by using the various potentials. For silica, panel (a), it can be seen that the BKS glass is stiffer and stronger than the SHIK glass, and it also breaks in a more ductile manner. Interestingly, however, both potentials predict the same failure strain  $\epsilon_f$  at  $\approx 0.17$ , in excellent agreement with the experimental value of 0.18 [129]. In addition, when compared with experimental data, we find that the SHIK potential gives excellent prediction not only for the stress-strain curve at small strains but also the fracture strength, whereas the BKS potential significantly overestimate these quantities. This is also demonstrated in panel (b) of Fig. 2.10, in which we compare the tangent modulus  $E_t$  predicted by the simulations with experimental results. The tangent modulus  $E_t$  is defined as

$$E_t = \frac{d\sigma}{d\epsilon} \quad , \quad (2.10)$$

where  $\sigma$  is the stress in the pulling direction and  $\epsilon$  the strain. From the  $NPT$  simulations, one can also obtain the Young's modulus, which is given by

$$E = \lim_{\epsilon \rightarrow 0} E_t^{NPT}(\epsilon) \quad , \quad (2.11)$$

Figure. 2.10(b) shows clearly that for all strains the BKS potential predict a tangent modulus that is significantly larger than the one predicted by the SHIK potential and the experimental data. The SHIK potential predicts for  $E$  a value  $\approx 72$  GPa, in very good agreement with the experimental value  $\approx 73$  GPa [112]. The BKS potential predicts a much larger value of  $\approx 86$  GPa, consistent with the findings from a previous



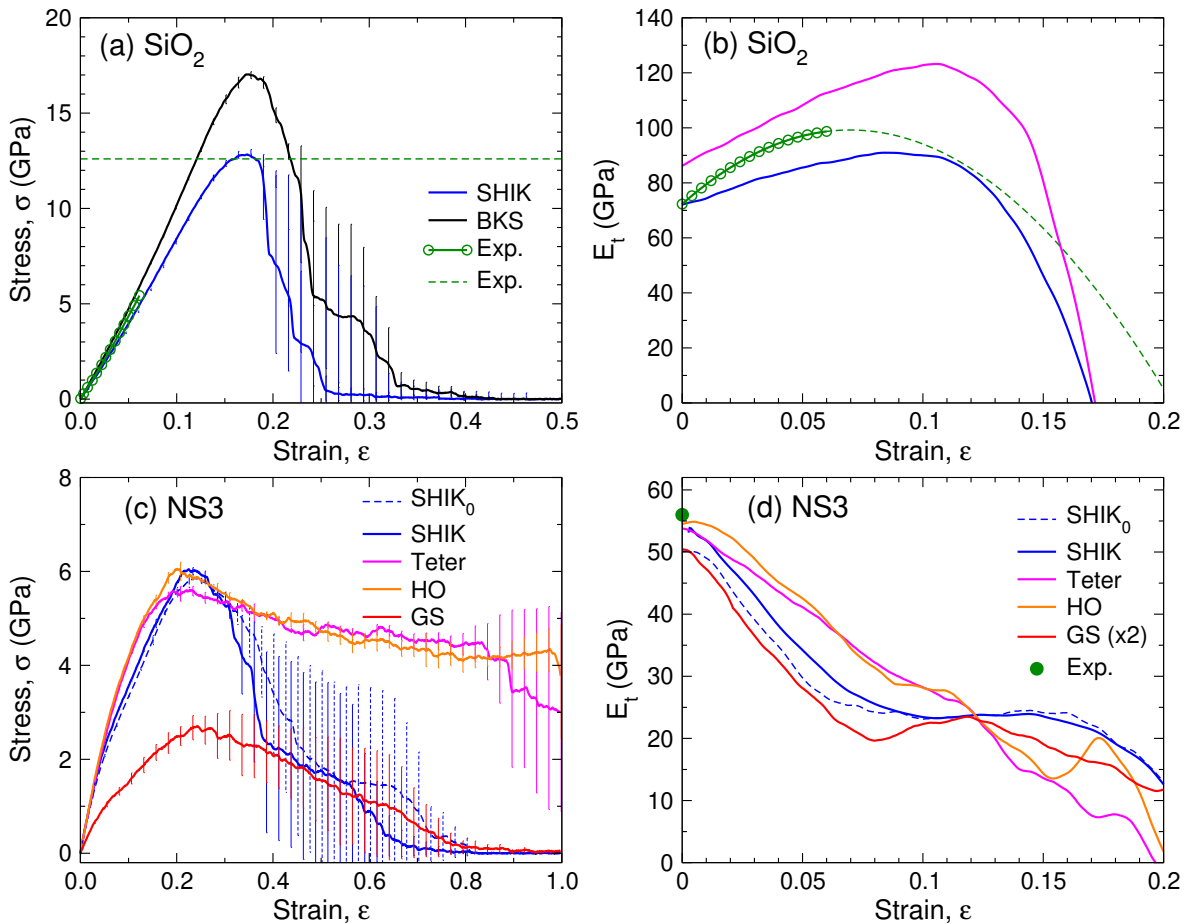


**Figure 2.10:** Mechanical responses of the glasses under uniaxial tension. Panels (a) and (b) show the stress-strain curve and the tangent modulus for silica, respectively. The green symbols are the experimental data from Ref. [130]. The green dashed line in panel (a) indicates the experimental strength of silica glass [129]. The green dashed line in panel (b) is the polynomial fit from Ref. [131] to experimental data and its extrapolation to large strains. Panels (c) and (d): Same quantities as in panels (a) and (b) for the case of NS3. The green symbol in (d) is the experimental data taken from Ref. [132].

study [127]. For the failure strength, the BKS and SHIK potentials predict 17.6 GPa and 12.8 GPa, respectively. The prediction of the SHIK potential is in excellent agreement with the experimental value of 12.6 GPa [129]. All these values are also given in Table 2.2.

The stress-strain curve of NS3 glass as predicted by the different potentials is shown in Fig. 2.10(c). Surprisingly we find that under *NPT* conditions the HO and Teter potentials show no sign of fracture even if the sample is stretched to 100%. This shows that these potentials have a serious flaw in that they strongly overestimate the ductile behavior of NS3. Also the stress-strain curve from the GS potential is not realistic in that the stiffness in the elastic regime is strongly underestimated, the failure stress is too small, and that the fracture is way too ductile. Hence we conclude that these

three potentials should not be used to study the fracture behavior of NS3. A much more reasonable stress-strain curves is found for the SHIK potential which shows a relatively brittle fracture. This brittleness is, however, less pronounced than the one found in SiO<sub>2</sub>, see panel (a), in agreement with the expectation that the addition of Na will make the glass more ductile. The failure stress for the SHIK potential is around 6 GPa (see Table 2.2 for exact values), which is close to the experimental values that are between 7.5 GPa and 11.7 GPa [133, 134] (this latter value is only an upper limit, see Ref. [133]).

The predicted Young's modulus of the NS3 glass is around 55 GPa by the SHIK, HO and Teter potentials, in good agreement with the experimental value of 56 GPa [112], while the GS potential predicts a value of only 26 GPa, thus way too small. A more notable difference between the various potentials is found for the strain dependence of the tangent modulus, shown in Fig. 2.10(d): While for the HO and Teter potentials,  $E_t$  decreases basically in a linear manner, the SHIK and GS potentials show at intermediate strain a plateau before they decrease to zero. (Note that the data for the GS potential has been multiplied by a factor of 2.0 in order to bring it on the same scale as the other curves.) This plateau is also directly visible in the stress-strain curves in that they show at around  $\epsilon = 0.07$  a marked bend, see panel (c). The microscopic origins of this rapid change in the effective stiffness of the sample will be discussed in more details in the next sections.

Quantity		E	C <sub>11</sub>	B	G	$\nu$	$\epsilon_f$	$\sigma_f$	$\rho$
Unit		GPa	GPa	GPa	GPa			GPa	g/cm <sup>3</sup>
Silica	SHIK	72.1	80.6	40.8	29.9	0.205	16.89	12.84	2.221
	BKS	85.8	99.0	52.3	35.0	0.226	17.18	17.65	2.241
	Exp.	72.9 <sup>a</sup>	78.0 <sup>a</sup>	36.3 <sup>a</sup>	31.3 <sup>a</sup>	0.165 <sup>a</sup>	18.00 <sup>b</sup>	12.6 <sup>b</sup> , 11-14 <sup>c</sup>	2.201 <sup>a</sup>
NS3	SHIK <sub>0</sub>	50.7	60.6	33.4	20.3	0.246	23.98	5.89	2.432
	SHIK	55.7	66.2	36.4	22.4	0.245	22.43	6.05	2.472
	HO	54.8	68.1	39.3	21.6	0.268	19.99	6.05	2.433
	Teter	54.5	66.7	37.8	21.7	0.259	22.03	5.66	2.555
	GS	25.9	31.4	17.5	10.4	0.252	25.09	2.72	2.348
	Exp.	56.0 <sup>f</sup>	69.5 <sup>a</sup>	37.2 <sup>a</sup>	24.3 <sup>a</sup>	0.250 <sup>f</sup>	20.85 <sup>d</sup>	11.71 <sup>d</sup> , 7.5 <sup>e</sup>	2.431 <sup>a</sup>

**Table 2.2:** Elastic constants (Young's modulus  $E$ , longitudinal modulus  $C_{11}$ , bulk modulus  $B$ , shear modulus  $G$ ), Poisson's ratio  $\nu$ , failure strain  $\epsilon_f$  and stress  $\sigma_f$ , and density  $\rho$  at 300 K, compared with experimental data. <sup>a</sup> Ref. [112]. <sup>b</sup> Ref. [129]. <sup>c</sup> Ref. [135]. <sup>d</sup> Ref. [133]. (at 77 K, strength is overestimated, see discussion section in Ref. [133]). <sup>e</sup> Ref. [134] (strength at 77 K). <sup>f</sup> Ref. [132].

The fact that neither the Teter nor the HO potential predict fracture of glass even if strained to 100% is astonishing since, from a structural point of view, these potentials

give reasonable predictions. Thus one might wonder whether this unrealistic behavior is related to the ensemble used during the tensile loading. In Fig. 2.11 we thus show the stress-strain curve predicted by the two potentials but now in the  $NVT$  ensemble, i.e. the sample size orthogonal to the pulling direction is fixed. It can be seen that the stress-strain curves obtained in the  $NVT$  ensemble are completely different from the ones obtained in the  $NPT$  ensemble: The glass becomes much more brittle when simulated in  $NVT$  ensemble. However, this enhanced brittleness is nothing else but an artifact from the  $NVT$  ensemble. Pedone *et al.* found similar ensemble effect for the case of silica [56]. For other potentials considered in this work, we also find that fracture simulation in the  $NVT$  ensemble makes the glass more brittle and for some potentials the glass will break at much smaller strain. Based on these results, we thus conclude the  $NVT$  ensemble should be avoided for investigating the fracture behavior of glass as it does not correspond to glass fracture in real experiments.

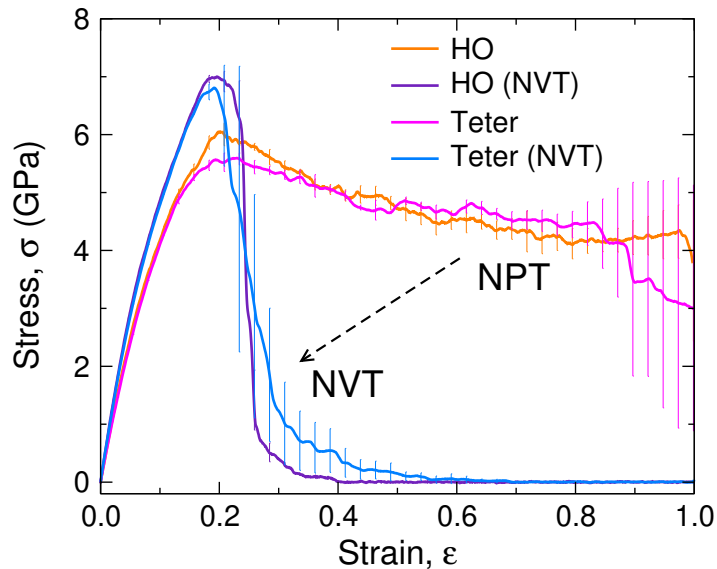


**Figure 2.11:** Influence of simulation ensemble on glass fracture. The orange and red curves are the same as in Fig. 2.10(c). The violet and blue curves are the data obtained in the  $NVT$  ensemble.

With the stress-strain curves from the  $NVT$  simulation, one can estimate the longitudinal modulus  $C_{11}$  by the expression

$$C_{11} = \lim_{\epsilon \rightarrow 0} E_t^{NVT}(\epsilon) \quad . \quad (2.12)$$

From  $E$  and  $C_{11}$  one can then obtain the bulk modulus  $B$ , the shear modulus  $G$ , and the Poisson's ratio  $\nu$  using the following relations [112, 136]:

$$E = \frac{9B(C_{11} - B)}{(3B + C_{11})} \quad (2.13)$$

$$G = \frac{3(C_{11} - B)}{4} \quad (2.14)$$

$$\nu = \frac{E}{2G} - 1 \quad . \quad (2.15)$$

The estimated elastic constants, together with the failure stress and failure strain and the glass density are summarized in Table 2.2. Overall, one can conclude that the SHIK potential is likely the most reliable potential. Note that this potential has the merit to be applicable not only to NS3 but, with the same set of parameters, also to SiO<sub>2</sub> and therefore also applicable for compositions in between the two systems [84]. We also note that the SHIK<sub>0</sub> potential performs almost as good as the SHIK potential, thus both of them are suitable for the simulation of glass fracture.

## 2.5 Summary

To summarize, we have investigated systematically the dependence of glass properties, in particular mechanical behavior of glass, on the used interaction potential. The simulations were set up to mimic the production and fracture of glass in real life, i.e., both of them should be conducted in constant pressure rather than constant volume. Firstly, we find that the dynamics of the liquid and the density during quenching show noticeable dependence on the potential. Secondly, it is found that the structural features of glass show a relatively mild dependence on the interaction potential. The only noticeable failure is found for the GS potential which predicts a phase separation into sodium rich/poor regions, as indicated by the divergence of  $S(q)$  at small  $q$ .

For the fracture behavior of glass, the SHIK potential clearly outperforms the other considered potentials in that it predicts for silica a stress-strain curve that is in excellent agreement with experiments and for NS3 the prediction is also reasonable. A further important result of this study is the system size dependence of the fracture behavior. It is found that while the small strain region (i.e., before failure) is basically independent of the system size, the fracture region (i.e., after the failure point) shows pronounced system size effect. An insufficient system size may lead to the conclusion that the glass is very ductile. Our results suggest that a reliable description of the fracture behavior requires a box size on the order of 10 nm for silica and 16 nm for NS3. Finally, we emphasize that close attention must be paid to the simulation ensemble. Fracture in the  $NPT$  ensemble is more realistic, whereas simulation in the  $NVT$  ensemble can result in artificial brittle fracture behavior.

## 2. ON THE CRITICAL ROLE OF INTERACTION POTENTIAL AND SIMULATION PROTOCOL

---

# Chapter 3

## Fracture of sodium silicate glasses: Classical MD simulations

In this chapter, we investigate dynamic fracture of sodosilicate glasses under tensile loading by using large scale molecular dynamics simulations. We introduce first the simulation setups which mimic the fracture of glass in real life, i.e., cracks initiate from surface flaws. We then explore the influence of various factors on the stress-strain behavior of glass. Based on the stress-strain curve, we estimate the toughness parameters and also the crack velocities for the glasses with varied compositions and at different temperatures.

To obtain a deeper understanding of glass fracture on the microscopic scales, we analyze first the cavitation process in silica and Na-rich glasses. Then, we explore various local properties of the glasses during deformation and monitor the evolution and quantified the correlations between different local quantities. We further analyze the distributions of various local properties and explain at microscopic scale for the transition behavior of the stiffness of the glasses as given by the tangent modulus. The results presented in this chapter shine new light on several important questions regarding the fracture behavior of oxide glasses on the microscopic scales.

### 3.1 Simulation protocol

We prepared two types of glass samples, namely bulk and sandwich (with free surface) glasses, for pure  $\text{SiO}_2$  and  $\text{Na}_2\text{O-xSiO}_2$  (NSx). As the simulation protocol for producing the bulk glasses has already been described in chapter 2, here we only provide a brief recap. The glasses were produced by using the conventional melt-quench procedure. The sample containing up to  $\sim 600,000$  atoms (corresponding to a cubic box of side length  $L \approx 20$  nm with experimental glass density at room temperature) was firstly

melted and equilibrated at a high temperature  $T_1$  (3600 K for silica and 3000 K for Na-containing compositions). Subsequently, the liquid sample was cooled down (linear ramp) to a low temperature  $T_3$  (usually 300 K) with a cooling rate  $\gamma$ . The glass sample was finally annealed at  $T_3$  for 160 ps. The entire simulation of glass production was performed in the  $NPT$  ensemble and at zero pressure, see Fig. 3.1(a).

In order to mimic glass fracture in real life, which usually starts from flaws and defects on the surface of glass, we produced a second kind of glass with a sandwich geometry. Two surfaces were firstly introduced by inserting free volumes on the top and bottom sides of the sample in the liquid state. The  $z$ -direction is normal to the two surfaces. The sample was subsequently equilibrated at a high temperature  $T_1$  for 1.6 ns, which is sufficiently long to ensure the reconstruction of the surface and hence to equilibrate the sample. Following that, the liquid sample was subjected to a two-stage quenching, with a slow cooling rate  $\gamma_1$  for the high- $T$  range and a relatively faster cooling rate  $\gamma_2$  ( $\gamma_2 = 3\gamma_1$ ) for the low- $T$  range. Finally the sample was annealed at  $T_3$  for 800 ps. The temperature  $T_2$  at which the cooling rate changes depends on composition.  $T_2$  is chosen to be at least 200 K below the simulation glass transition temperature  $T_g$  (see Fig. 3.2(a)). At  $T_2$  we also switched the simulation ensemble from  $NVT$  to  $NPT$ , see Fig. 3.1(b). Our simulation setup has the advantages that: 1) Fast cooling below  $T_g$  saves computational time while retaining statistically the same structure as slow cooling; 2)  $NVT$  simulation in the high- $T$  range helps to retain a regular shape of the sample. Below  $T_g$  the sample has more or less a fixed shape and switching to the  $NPT$  ensemble (for the two directions parallel to the surfaces only) allows to release internal stresses and facilitate local structural rearrangement. Sandwich samples containing up to  $\sim 2,300,000$  atoms were produced.

Once the glass sample was prepared, we put the sample under uniaxial tension with a constant strain rate, and monitor its changes in structural and mechanical properties, see Fig. 3.1(c). For the sandwich sample we introduced also a notch on the surface and then annealed the notched sample at an intermediate temperature (600-800 K, depending on the composition) for 160 ps before putting the sample under tension. During the mechanical loading, the glass sample is allowed to relax in the two directions perpendicular to the pulling direction. We note that the current simulation setup for the sandwich glass mimics the plane stress condition, i.e., a thin slab in the  $z$ -direction with the stress component  $\sigma_{\alpha z} = 0$ , for  $\alpha = x, y, z$ .

Throughout the simulations, we used the SHIK potential which has been introduced in chapter 2. Temperature and pressure (for the  $NPT$  ensemble) were controlled using a Nosé-Hoover thermostat and barostat [87–89]. All simulations were carried out using the LAMMPS software [116] with a time step of 1.6 fs.

Note that in this section we did not specify simulation parameters such as the

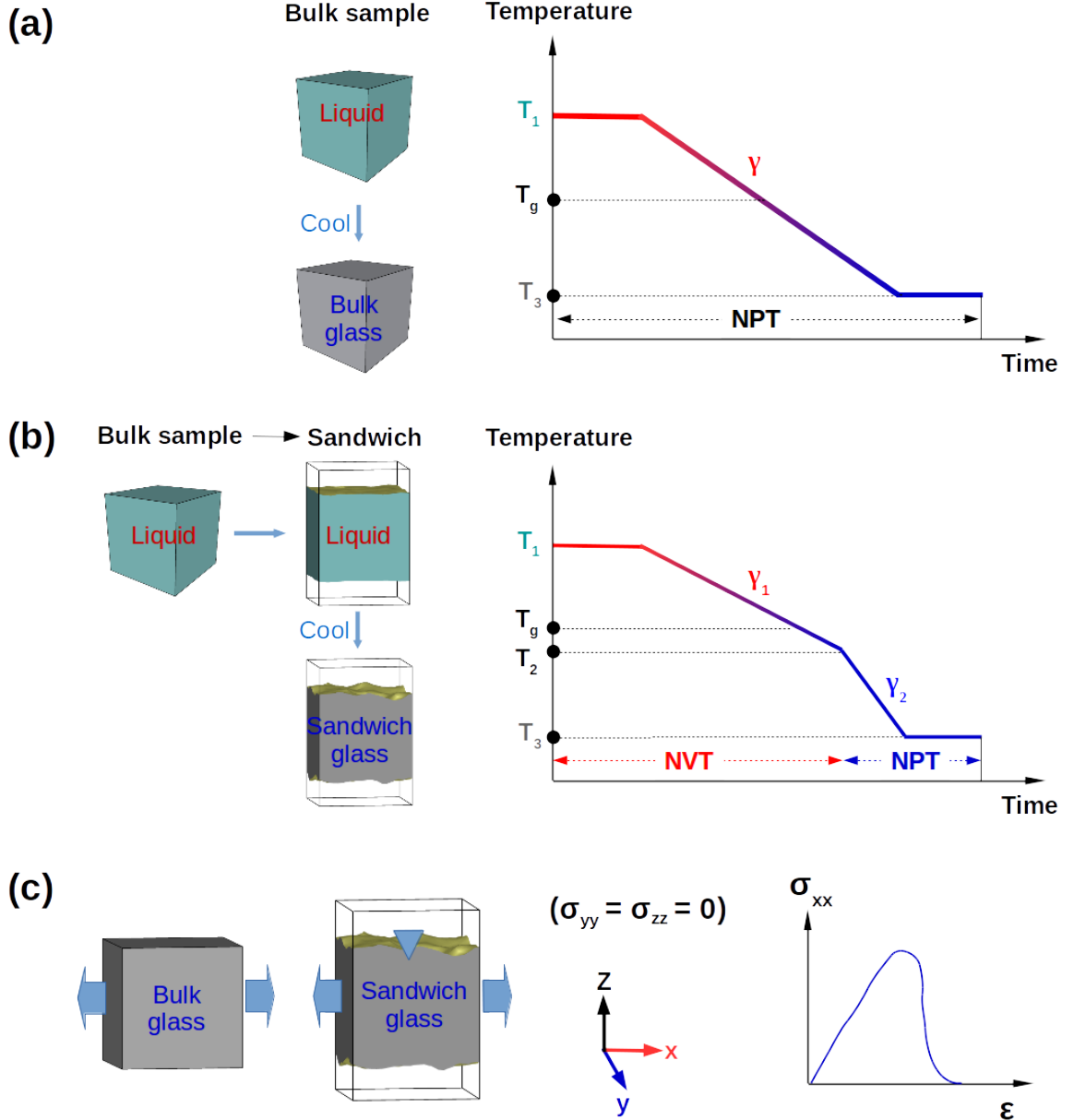


**Figure 3.1:** Schematic drawing of the simulation procedures. (a) Preparation of the bulk glass sample. (b) Preparation of the sandwich glass sample. (c) Glass fracture by uniaxial tension.  $T_1$  denotes the high temperature for equilibrating the sandwich sample in the liquid state.  $T_3$  represents the working temperature for deformation.  $T_2$  is the temperature at which we switch from slow cooling procedure (cooling rate  $\gamma_1$ ) to a relatively fast cooling (cooling rate  $\gamma_2$ ) in order to save computer time, and this temperature is chosen to be at least 200 K below the glass transition temperature ( $T_g$ ) (see Fig. 3.2).

dimensions of the sample, the cooling rate for glass production and the strain rate for fracture simulation. We will discuss the influence of these parameters in the next section in terms of stress-strain behavior, which is supposed to be much more sensitive to the simulation parameters than structural properties (see also the discussion in



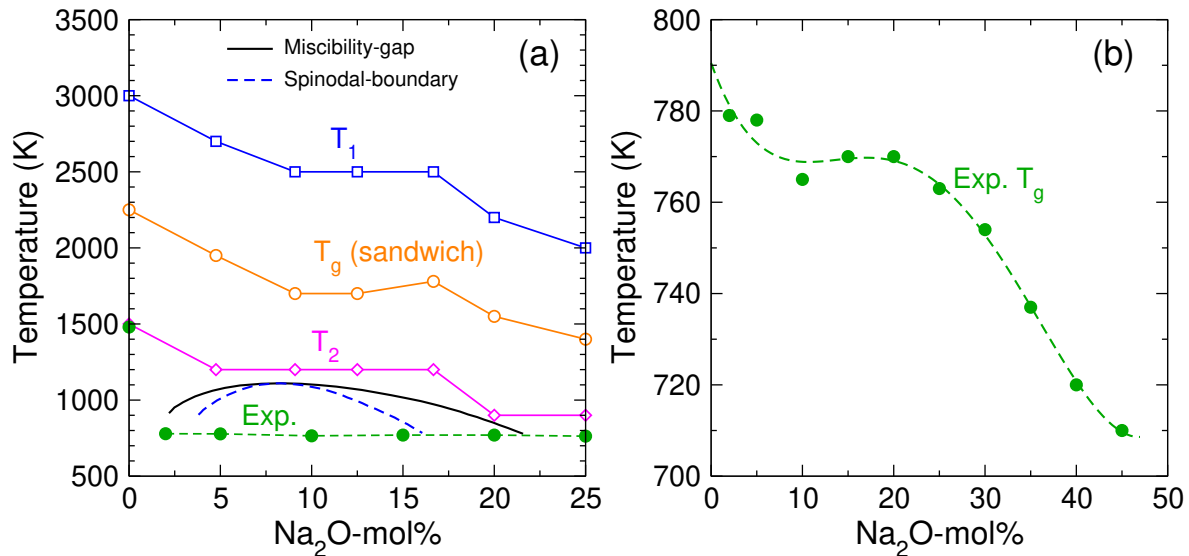


**Figure 3.2:** (a) Temperature profiles for the simulations. The  $T_g$  was estimated for the sandwich samples produced with a cooling rate  $\gamma_1 = 0.13$  K/ps. Total energy ( $U$ ) versus  $T$  was employed to measure  $T_g$ , i.e., the temperature at which the extrapolated liquid and glass lines across. The uncertainty of the  $T_g$  estimation is about  $\pm 50$  K. Also included in the graph are the experimental  $T_g$  (filled circles) measured by using calorimetric method for Na<sub>2</sub>O- $x$ SiO<sub>2</sub> [32] and for SiO<sub>2</sub> [139].  $\Delta T_g = \pm 3^\circ\text{C}$ . Black and blue lines are miscibility-gap and spinodal boundaries, respectively, calculated from modified regular-mixing equations [140]. (b) Re-plotting the experimental  $T_g$  for Na<sub>2</sub>O- $x$ SiO<sub>2</sub> as shown in (a) and the data are fitted with a fourth order polynomial function (dashed line).

chapter 2).

Figure 3.2(a) shows the various temperatures that are related to our simulations. For comparison, we included in the graph also the experimental  $T_g$  and the two lines associated with phase separation in sodium silicate system. In Fig. 3.2(b), we plot only the experimental  $T_g$  which shows that a plateau appears at  $\approx 10$  mole% of Na<sub>2</sub>O [32, 137, 138].

## 3.2 The big picture: Stress-strain behavior

### 3.2.1 Effects of cooling rate and strain rate

Firstly, we examine how the glass production history affects the fracture behavior of glass. Here we focus on one of the most important factors for glass production, the cooling rate  $\gamma$ . In Fig. 3.3 we show the stress-strain curves of bulk glasses produced with different  $\gamma$ . We note that these system sizes are large enough to avoid significant finite size effect (see Fig. 2.9). For both silica and NS3, faster cooling yields softer

glasses and more ductile fracture behavior. The graphs also demonstrate that once  $\gamma < 0.3$  K/ps, the stress-strain curves have more or less converged, i.e., the fracture behavior of the glass will no longer depend on  $\gamma$  in a significant manner. Therefore, we have chosen  $\gamma = 0.25$  K/ps and  $\gamma = 0.125$  K/ps for producing the bulk and sandwich glasses, respectively, otherwise specified. Taking into account the fact that surfaces have a faster dynamics than the bulk (thus require shorter relaxation time),  $\gamma_1 = 0.125$  K/ps allows the production of well-relaxed sandwich glasses.

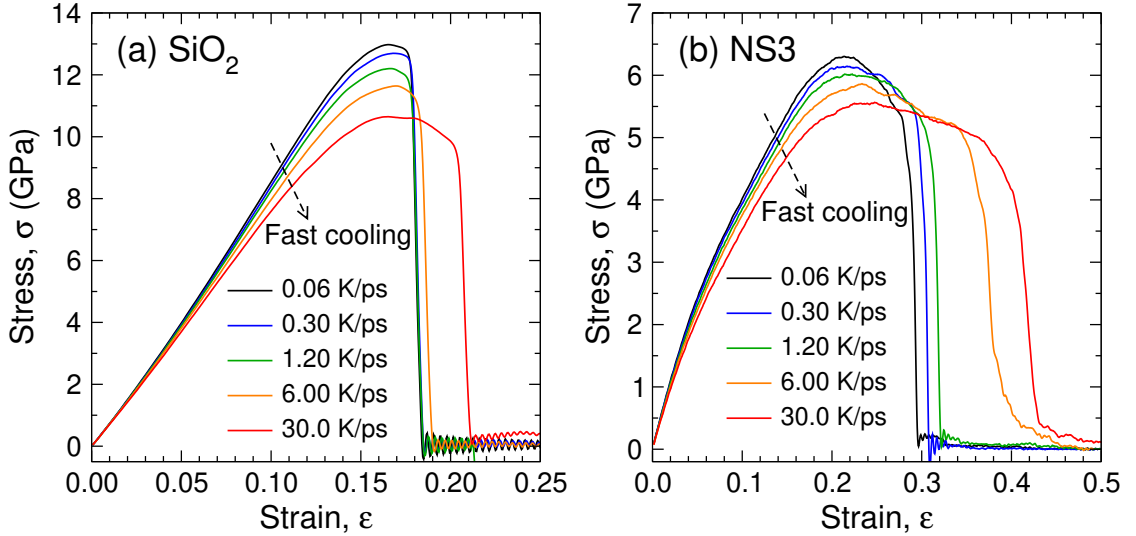


**Figure 3.3:** Cooling rate effect on the stress-strain behavior of bulk glasses at 300 K. (a) Silica with a cubic box size of  $L = 20$  nm. (b) NS3 with  $L = 20$  nm. Note that these bulk samples were produced using the same procedure for producing the sandwich glasses, i.e., consists of two cooling stages. The strain rate is 0.5/ns.

Nevertheless, in order to inspect visually what could happen if a fast cooling rate is applied for the production of sandwich glasses, we show in Fig. 3.4 the atomic layers close to the surfaces of the glass sample at 300 K. For the case of silica, it can be seen that there are many atoms present in the vacuum between the two surfaces. (As PBCs are applied, the two surfaces are actually facing each other in the direction normal to the surfaces). With a cooling rate of  $\gamma = 0.125$  K/ps only a few atoms are still remaining in the vacuum. For NS3 the structural changes are not obvious. However, the slow-quenched glass has larger remaining volume of the empty space, implying a more relaxed (thus more compact) structure of the glass. Note that here we show the results for two extreme compositions considered in this study, i.e., SiO<sub>2</sub> and NS3 (25 mole% Na<sub>2</sub>O). For the other compositions between them, the same cooling rate effect is seen.

For many materials, the stress-strain curves are sensitive to the strain rate  $\dot{\epsilon}$ . The tensile tests in experiments are usually conducted in the range  $10^{-4} \text{ s}^{-1} < \dot{\epsilon} < 10^{-2} \text{ s}^{-1}$  [34]. High-strain-rate tests are often utilized to obtain information on the

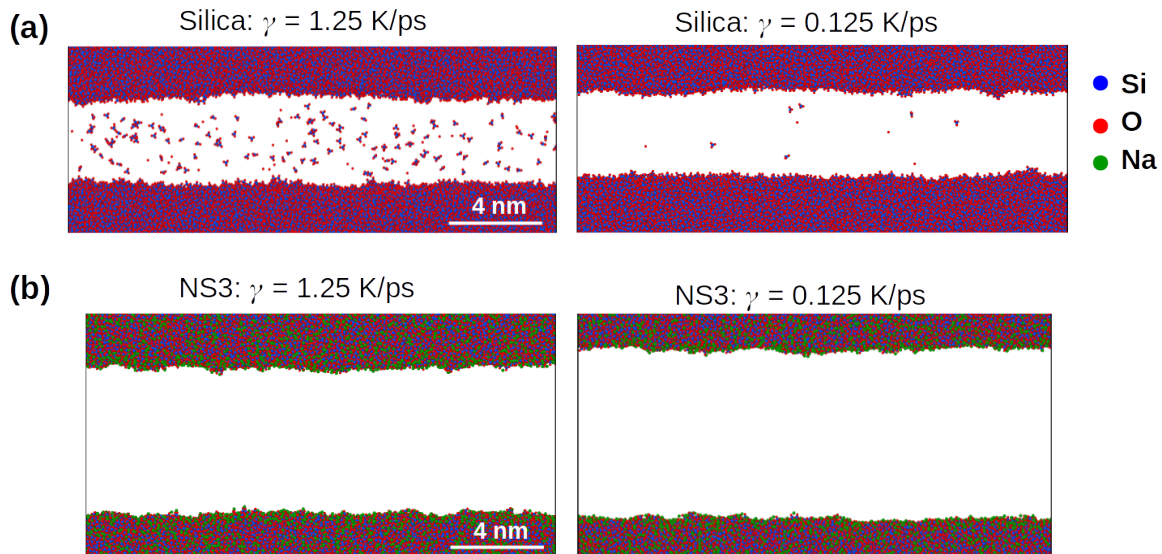


**Figure 3.4:** Cooling rate effect on the atomic structure near the surfaces of the sandwich glasses at 300 K.

performance of materials under dynamic impact condition. In computer simulations, high strain rates are often adopted for testing the mechanical response of materials (mainly due to the consideration of computational cost). Earlier simulation studies of silica glass found high sensitivity of the stress-strain behavior to the strain rate at  $2.0 \times 10^{11} \text{ s}^{-1} < \dot{\epsilon} < 4.0 \times 10^{11} \text{ s}^{-1}$  [51, 55]. A recent study, using reactive force field, investigated the stress-strain behavior of silica glass under tensile loading for strain rates  $2.3 \times 10^8 \text{ s}^{-1} < \dot{\epsilon} < 1.0 \times 10^{15} \text{ s}^{-1}$  [58]. A transition strain rate was identified at  $2.5 \times 10^{11} \text{ s}^{-1}$  (i.e., 250/ns), above which a drastic increase of elastic modulus and strength can be observed.

To examine the influence of strain rate on glass fracture, the bulk glasses at 300 K were elongated uniaxially using five strain rates, ranging from 12.5 /ns to 0.02 /ns. For both the silica and NS3 glasses, we observe that the strength of the glass decreases with slower strain rate, Fig. 3.5. This phenomenon was also observed in experiments for glasses and is known as *dynamic fatigue* [2]. If the loading rate is high, a higher stress will be reached before sufficient structural changes (stress relaxation) occur to cause failure. Amorphous materials such as oxide glasses show viscoelastic (or anelastic) behavior, i.e., their mechanical behavior depends on both temperature and time [34]. Lowering temperature reduces the thermal effects thus can help to decrease the fatigue rate.

In Fig. 3.5(c)-(d) we show the failure stress  $\sigma_f$  and strain  $\epsilon_f$  as a function of strain rate  $\dot{\epsilon}$ . The data are fitted using the expression:  $Y = A \cdot \ln(\dot{\epsilon}/\dot{\epsilon}_0)$ , where  $Y$  denotes  $\sigma_f$  or  $\epsilon_f$ ,  $A$  and  $\dot{\epsilon}_0$  are two fitting parameters. One recognizes from the graphs that both  $\sigma_f$  and  $\epsilon_f$  show an logarithmic dependence on  $\dot{\epsilon}$ . Also one notices that the failure point

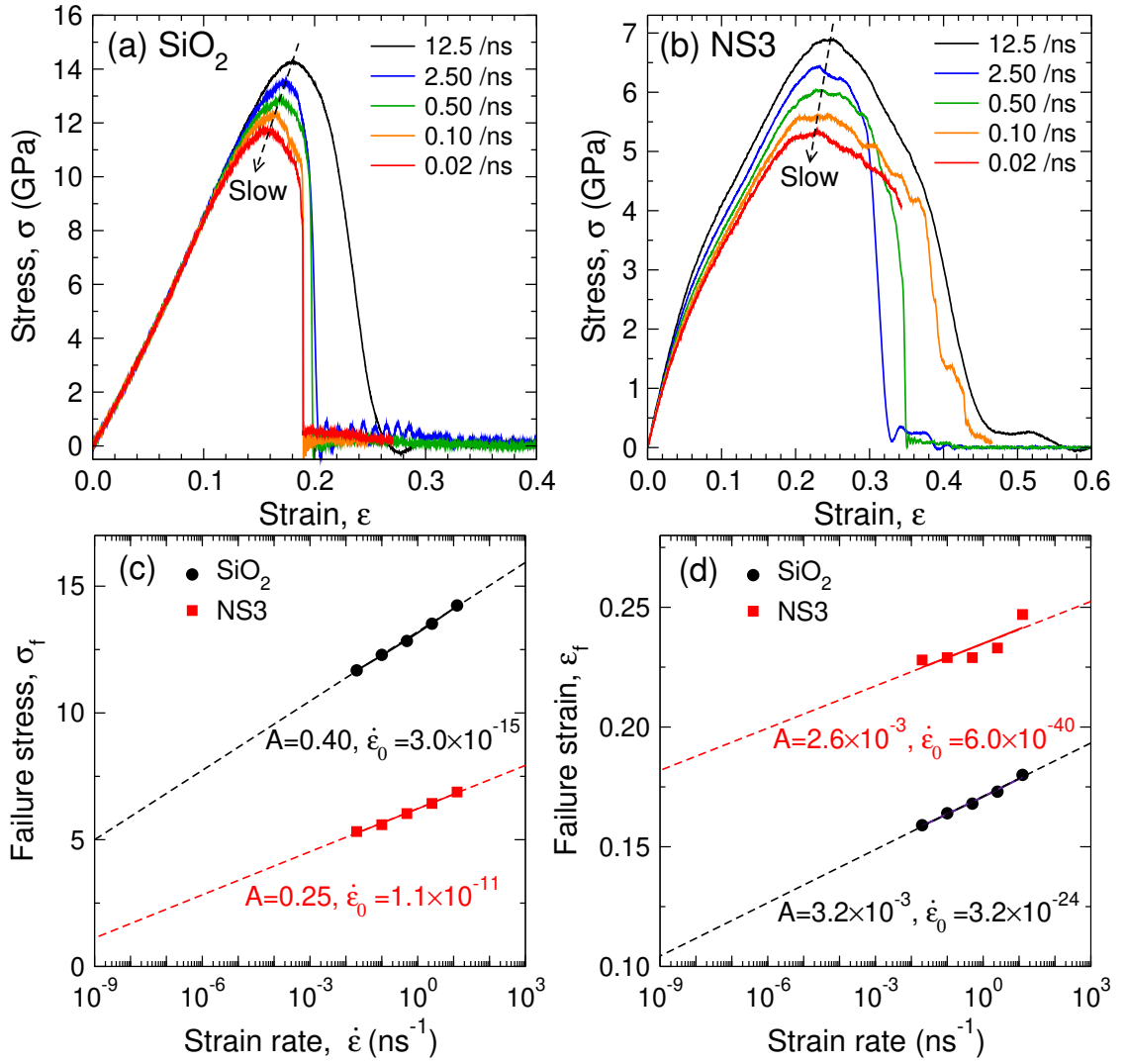


**Figure 3.5:** Influence of strain rate  $\dot{\epsilon}$  on the stress-strain behavior of the bulk glasses at 300 K. (a) Silica with a cubic box size of  $L = 12$  nm. (b) NS3 with  $L = 16$  nm. The cooling rate  $\gamma = 0.25$  K/ps. (c) and (d) are failure stress and strain versus strain rate, respectively. The dashed lines are logarithmic fits (with parameters  $A$  and  $\dot{\epsilon}_0$ ) to the data points and are extrapolated to small and large strain rates.

(for both the stress and strain) of the silica glass is more sensitive to strain rate than that of the Na-rich NS3 glass.

For the simulated glasses at 300 K, we observe no substantial difference in the stress-strain behavior (both before and after the failure point) with strain rate  $\leq 0.5$  /ns. Therefore, for the reason of computational efficiency, we choose a strain rate of 0.5 /ns for the production runs of the bulk and sandwich glasses (otherwise specified). It is worth mentioning that we did not explore higher strain rates since we aimed to reach a (more or less) convergence of the stress-strain behavior that is comparable to real experiments.

### 3.2.2 Effects of sample geometry and size

In many previous simulation studies of glass fracture, a quasi-2D sample geometry has been adopted, i.e., the dimension of the sample in one direction is much smaller than the other two directions (see for example Refs. [52, 54, 61, 141]). However, to which extent this quasi-2D fracture can be compared with 3D fracture (which is the case of glass fracture in real life) is not so clear. To better understand the effect of sample geometry, we have evaluated the fracture behavior of the sandwich glasses with different thickness (see Fig. 3.6). In practice, we have fixed the sample dimensions in two directions to be  $\approx 30$  nm and 50 nm. (Note that these two lengths are for the glass at zero strain. With increasing strain, these two dimensions will contract a bit and thus become shorter). Interestingly, we find that for silica the thickness of the glass does not affect the stress-strain behavior. The fracture of NS3, by contrast, depends strongly on the sample thickness in that the glass can withstand more deformation (i.e. it fails later and thus is tougher) with increasing the thickness of the sample. This result indicates that the quasi-2D geometry may allow only a qualitative description of glass fracture while quantitatively there is a strong dependence on glass composition.

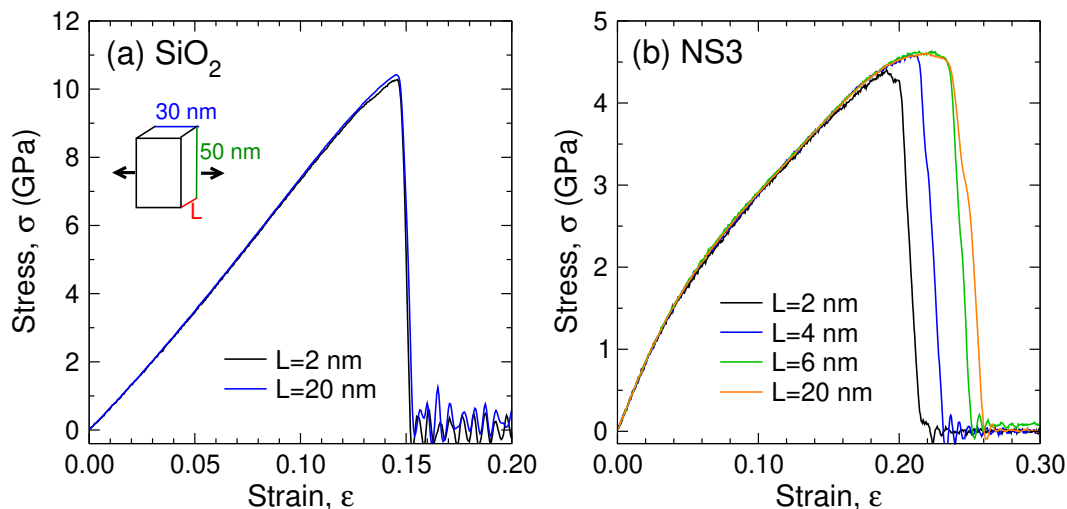


**Figure 3.6:** Effect of the sample thickness on the stress-strain behavior of the sandwich glasses at 300 K. The inset in (a) shows that the sample dimensions have been fixed at 30 nm and 50 nm in two directions. Note that these dimensions do not include the vacuum on the top and bottom sides of the sample.

We recall that the objective of this thesis is not only to investigate the stress-strain behavior, but also to obtain more insights into the fracture behavior and surface properties of the glasses. Apparently, the quasi-2D fracture does not allow to achieve the later. Therefore, we choose to study glass fracture using a 3D geometry, i.e., all the sample dimensions are comparable to each other. For silicate glasses, since the crack velocity during dynamic fracture is very high ( $\approx 10^3$  m/s), we choose a cuboid

geometry for the sample with dimension in the direction of crack propagation larger than the other two directions ( $L \times 1.5L \times 2.5L$ ). The free surfaces are introduced in the direction of the largest dimension.

In Sec. 2.4 we have shown the system size dependence of the fracture behavior of bulk sodium silicate glasses. We have concluded that for silica a cubic box with a side length  $L = 10$  nm is required to reach convergence of the stress-strain behavior, whereas for NS3 a cubic box with  $L = 16$  nm is needed, thus highlighting the compositional dependence of the system size dependence. In Fig. 3.7 we show the results for the glasses with sandwich geometry and a fixed ratio of its dimensions ( $L \times 1.5L \times 2.5L$ ). It can be seen from Fig. 3.7(a) that  $L = 8$  nm is enough to produce a brittle fracture behavior of silica. With increasing system size, the glass becomes slightly stiffer and fails at a bit smaller strain, but the overall fracture behavior remains unchanged. We note that these changes are mainly due to the presence of the free surfaces, whereas for the bulk glass they do not exist. In contrast, Fig. 3.7(b) demonstrates that for NS3, one has to use simulation box with  $L > 16$  nm to obtain a clean stress-strain behavior after the failure point (i.e., the point corresponds to maximum stress). It is worth noting that although the stress-strain response after glass failure shows very strong system size dependence, the small strain region, e.g.,  $\epsilon < 0.10$  is hardly affected by the system size, in agreement with the findings for bulk glasses (see Sec. 2.4). Finally, we note also that the fracture strength of the sandwich glasses are smaller than the ones of the bulk glasses ( $\approx 12.5$  GPa for silica and  $\approx 7$  GPa for NS3) due to the presence of free surfaces and thus more structural defects. This is consistent with the fact that glass usually has much smaller practical strength in comparison to its theoretical strength due to the presence of surface flaws [33, 41].

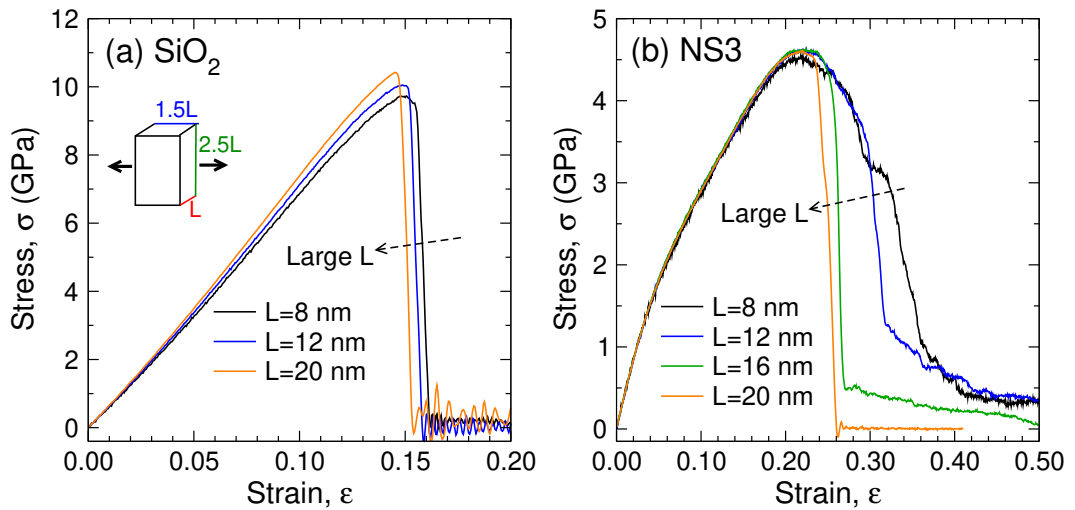


**Figure 3.7:** Influence of system size on the stress-strain behavior of the notch-free sandwich glasses at 300 K. The inset in (a) illustrates the rectangular cuboid geometry of the sample with  $L$  the smallest dimension.

Since we intended to investigate the deformation of glass both before and after failure, a large system size is desired in order to avoid (or at least minimize) the finite size effects. Therefore, in the following we will mainly discuss the deformation and fracture behavior of sandwich glasses with  $L = 20$  nm, unless otherwise specified.

### 3.2.3 Effect of notch geometry

In this section we examine the influence of introducing a surface notch on the stress-strain behavior of the sandwich glasses. We have fixed the shape of the notch to have an isosceles triangle as cross section and investigated the influence of the sharpness and depth of the notch on the stress-strain response. Figure 3.8(a) shows for the case of silica that at a fixed notch depth of  $a = 21$  Å increasing the sharpness (i.e., smaller  $b$ ) results in a slight reduction of the glass strength. This result indicates that within the range of  $b/a$  ratio examined, the notch sharpness has only a weak effect on the strength. The influence of the notch depth  $a$  is shown in Fig. 3.8(b). One recognizes that increasing  $a$  leads to a significant reduction of the glass strength. This effect is more pronounced when  $a$  is relatively small.

We emphasize that our motivation for introducing a notch on the free surface is to control the initiation of crack propagation. Therefore, based on the results discussed above, we have chosen for the production runs a notch geometry of  $a = 21$  Å and  $b = 31.5$  Å ( $b = 1.5a$ ). The size of the notch is about 1/10 and 1/25 of the sample dimensions in the pulling direction and the direction normal to the surfaces, respectively. Note that we discuss here only the results for silica, but similar effects of notch geometry are found for the Na-containing glasses.

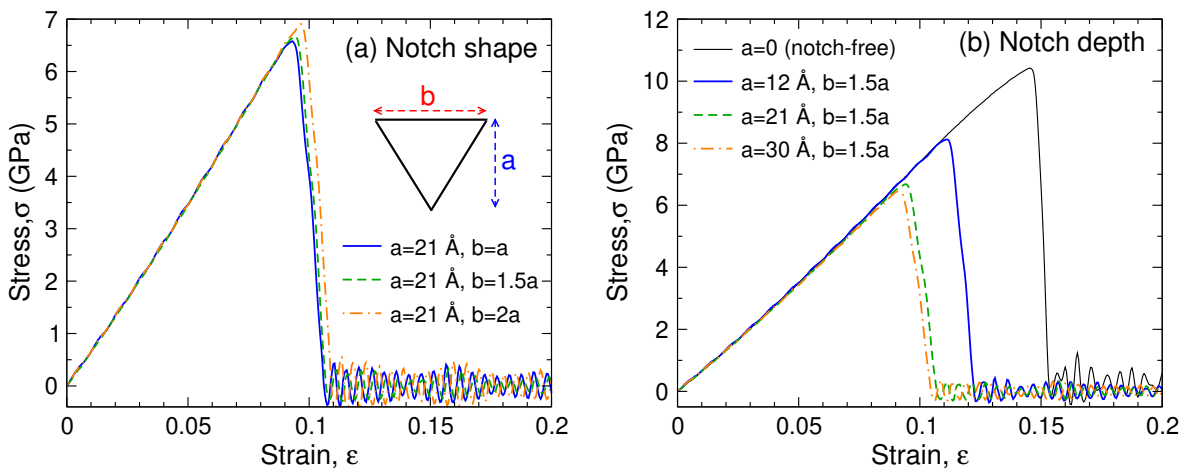


**Figure 3.8:** Influence of (a) the notch shape and (b) notch depth on the stress-strain behavior of the sandwich silica glass at 300 K. The inset in (a) illustrates the isosceles triangular cross section of the introduced notch on the glass surface. The parameters  $a$  and  $b$  control the geometry of the notch.

### 3.2.4 Effect of temperature

We now discuss the influence of another important factor on the fracture of materials, temperature  $T$ . As  $T$  increases, brittle materials can be transformed into ductile materials. In Fig. 3.9, we show the influence of  $T$  on the stress-strain behavior of the sandwich glasses. It can be seen from panel (a) that the strength of silica glass decreases with increasing  $T$  but that the glass remains brittle (i.e. stress drops to zero rapidly once the failure point is reached) if  $T$  is below 1600 K. With further increasing  $T$ , the sample becomes very ductile in that the stress decreases very slowly and the glass is able to withstand large strain before fracture. This behavior can be rationalized by considering the atomic movement and reorganization of the microstructure. We note that 2000 K is approaching the glass transition temperature for the sandwich glass (see Fig. 3.2). Atoms start to move very fast and are able to escape from their local constraints and therefore the sample is able to accommodate large deformation. For the NS3 glass, the  $T$ -dependence of the stress-strain behavior is more pronounced than the silica glass. With increasing  $T$ , the glass becomes softer, i.e., the slope of the curve at small strain region drops. The glass behaves very ductile when  $T$  is above 900 K, which is also approaching the glass transition temperature of the glass.

A further interesting result is found in the  $T$ -dependence of failure strain  $\epsilon_f$ , see panel (c). For silica, we find basically a monotonic decrease of failure strain with increasing  $T$ . (The only exception seems to be the point at 2000 K, a temperature that may induce pronounced viscous flow of the glass, and thus makes the sample more deformation-tolerant). A similar  $T$ -dependence of  $\epsilon_f$  is observed for the NS10 glass ( $\approx 9.1\%$  Na<sub>2</sub>O). However, as one further increases the Na concentration, e.g., for the NS3 glass ( $\approx 25\%$  Na<sub>2</sub>O), one recognizes that the  $T$ -dependence of  $\epsilon_f$  becomes non-monotonic: Increasing  $T$  results in larger  $\epsilon_f$  at the beginning, but when  $T$  is higher than  $\approx 300$  K, the failure strain decreases. The  $T$ -dependence of  $\epsilon_f$  for the Na-rich NS3 glass may be rationalized by considering two thermal activated effects: Local softening and global softening. As  $T$  is lower than a threshold value (around 300 K for NS3), increasing  $T$  mainly promotes local softening due to the activated motion of Na atoms. In this  $T$ -range the backbone of the glass, i.e., the Si-O network softens but the local softening is more pronounced thus the glass can accommodate more strains without failure. However, once  $T$  is higher than a critical value, the global softening of the network becomes more pronounced (also possibly the locally soft regions start to percolate) thus the glass structure tends to fail earlier, i.e., reach the failure point at a smaller strain.

Also of interest is the  $T$ -dependence of failure stress  $\sigma_f$ , see panel (d). We notice that all sets of data can be fitted very well by a linear function. The two exceptions are for the highest  $T$  examined for the silica and NS10 glass. This result suggests that



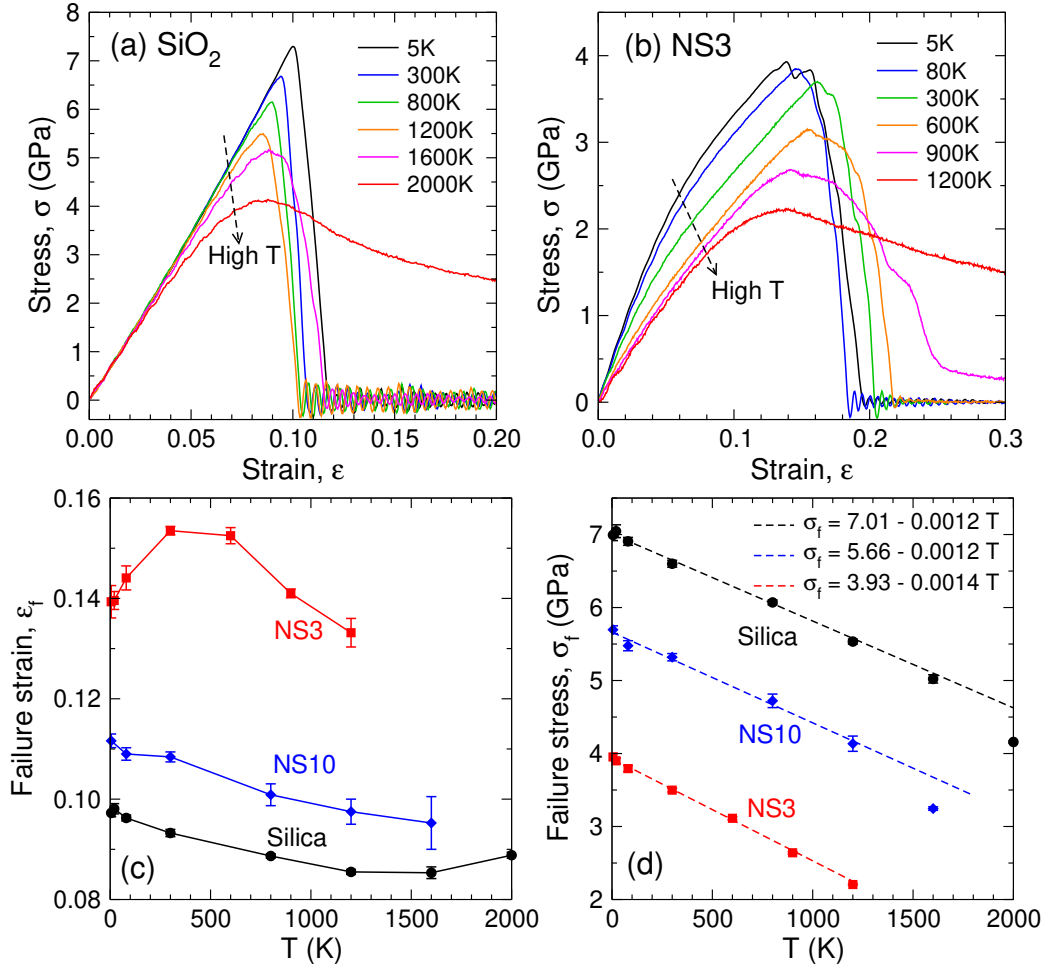


**Figure 3.9:** Influence of temperature on the stress-strain behavior of the sandwich glasses. Dashed lines in (d) are linear fits to the corresponding data sets. Error bars represent the standard error of the mean of six fracture samples.

$\sigma_f$  decreases linearly with temperature when  $T$  is well below  $T_g$ . Most surprisingly, the slopes of the three fitting lines are almost the same, implying that composition does not influence how fast the failure stress (i.e., the strength of the glass) changes with temperature.

### 3.2.5 Effect of glass composition

As glass fracture often happens at room temperature, we now fix the temperature of fracture simulation at 300 K, and investigate the compositional dependence of glass fracture. More specifically, we study how the fracture behavior of  $\text{Na}_2\text{O}-x\text{SiO}_2$  (NS $x$ ) glasses varies with sodium concentration.

In Fig. 3.10(a) we show the stress-strain behavior of the bulk glasses. It can be seen that silica shows characteristics of brittle fracture in that it reaches the failure

stress in almost a linear manner and the stress drops to zero very rapidly after failure. With increasing Na concentration, the glass becomes softer in that the slope of the curves at small strain decreased considerably. Also one observes that the failure stress shifts to lower value and the failure strain shifts to larger value, if more Na is added. At larger strain, i.e., after the failure point, there is also a noticeable compositional dependence. For the Na-poor compositions, i.e., from silica to NS10, the glasses remain brittle. However, for the Na-rich compositions the stress drops relatively slowly with increasing strain, implying that the crack is somehow arrested and thus advances only slowly. For the NS3 glass, the fracture point is at  $\epsilon \approx 30\%$  (i.e., after which the glass will break rapidly), and the region of necking (crack arresting) has a width of around 8% strain.

The compositional effect on the deformation behavior of the NSx glasses is also manifested in the tangent modulus ( $E_t$ , see Eq. 2.10) of the glasses, see panel (b). One recognizes an anomaly of silica in that  $E_t$  increases at the beginning and decreases after a critical strain at around 9% strain. This finding compares very well with experimental results (see the discussion in chapter 2). With increasing Na concentration, the absolute value of  $E_t$  decreases, indicating that the glass becomes softer. Also the behavior of the  $E_t(\epsilon)$  changes in that the overshooting of silica at small strain weakens and disappears for NS10. With even more Na added, one notices that a plateau in the  $E_t(\epsilon)$  curve shows up, and it becomes very pronounced for the Na-rich NS3 glass. We will show in the next section that the strain dependence of glass stiffness as given by  $E_t$  can be related to the nonaffine part of atomic displacement.

Figure 3.10(c-d) show the stress-strain behavior of the sandwich glasses for various Na concentrations. It can be seen that the sandwich glasses exhibit a similar compositional dependence as the bulk glasses. However, the sandwich glasses differ in that the glass strength is reduced and the glasses (notably for Na-rich compositions) seem more brittle due to the presence of notched surfaces. In panel (d), one observes again the bending behavior in the  $E_t - \epsilon$  curves, indicating that this feature is independent of the sample geometry.

Finally we show in Fig. 3.10(e-f) the failure strain and stress of the sandwich glasses. In panel (e), we include also the experimental results as measured for glass fibers by using two-point bending method [133]. It is found that the failure strain estimated for the bulk glasses compare very well with the experimental data. The only exception is the Na-poor region where our simulations do not show a minimum of failure strain at around 5% Na<sub>2</sub>O. (The origin of this local minimum may be related to the 2-point bending technique adopted in the experiments [133]. This technique creates a special stress gradient in the specimen that one does see in the case of tensile loading.) In panel (f), one recognizes that the strengths of the bulk glasses compare reasonably well

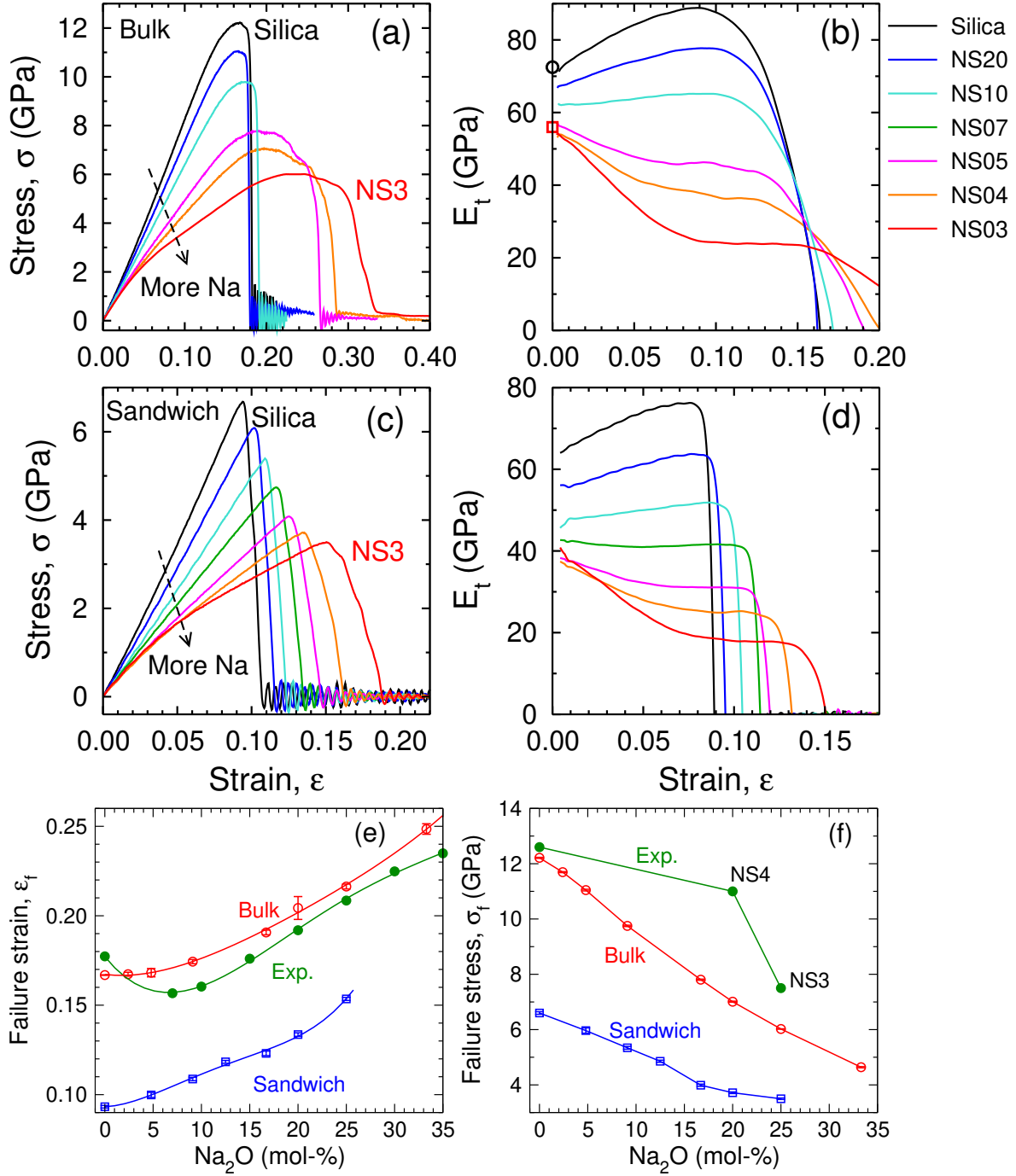


**Figure 3.10:** Effect of composition on the stress-strain behavior of NSx glasses. (a) and (b): Stress and tangent modulus of the bulk glasses at 300 K, respectively. In (b), the two open symbols (circle for silica and square for NS3) at zero strain are experimental data [112, 132]. (c) and (d): Stress and tangent modulus of the notched sandwich glasses at 300 K, respectively. (e) and (f) Failure strain and failure stress versus  $\text{Na}_2\text{O}$  concentration, respectively. The lines in panel (e) are fourth order polynomial fits to the data sets. The experimental data in (e) are from Ref. [133]. For panel (f), the experimental data are taken from Refs. [129], [133], [134] for silica, NS4 and NS3, respectively. Error bars are standard error of the mean of three and six fracture samples for the bulk and sandwich glasses, respectively.

with the experimental data. (The experimental data for NS4 may be overestimated due to the experimental setup, see the discussion in Ref. [133]). In addition, one also sees that the failure stress and strain show very similar compositional dependence as the bulk glasses, but the absolute values are much smaller due to the introduction of free surfaces and pre-notch.

From the stress-strain curves we have seen that the Na-rich glasses show a pronounced ductility relative to the Na-poor ones. A further step is thus to quantify the relative ductility of the glasses. Previous simulation studies, based on energetic approach, have defined a brittleness index by the expression [52, 61]:

$$B = \frac{G_c}{G_{el}}, \quad (3.1)$$

where  $G_c$  is the fracture energy (or critical energy release rate) and  $G_{el}$  is the elastic contribution to the fracture energy. The difference between the two energies  $G_c - G_{el}$  thus accounts for the energy dissipated due to any plastic (irreversible) deformation process.  $G_c$  and  $G_{el}$  are proportional to the area under the  $\sigma - \epsilon$  curve up to the failure point and the fracture point, respectively. Based on this idea, we used the stress-strain curve to define two toughness parameters: Fracture toughness  $\Pi_0$  and failure toughness  $\Pi_f$ . The parameter  $\Pi_0$  is given by integrating the area under the stress-strain curve, i.e.,

$$\Pi_0 = \int_0^\infty \sigma d\epsilon, \quad (3.2)$$

whereas  $\Pi_f$  is defined by integrating the stress-strain curve only up to the failure strain  $\epsilon_f$ , that is

$$\Pi_f = \int_0^{\epsilon_f} \sigma d\epsilon \quad (3.3)$$

The ratio between failure toughness and fracture toughness is an indicator of the brittleness of a material, and thus the brittleness index  $B$  is defined as

$$B = \frac{\Pi_f}{\Pi_0}. \quad (3.4)$$

$B = 1$  means that the fracture perfectly brittle. The smaller the value of  $B$  the more ductile the material is.

The two toughness parameters are shown for three different sample geometries in Figs. 3.11(a) and (b). For the bulk glasses, one recognizes that  $\Pi_0$  decreases first with the addition of Na and a minimum is reached at around 10% of  $\text{Na}_2\text{O}$ . Further increasing Na content leads to a greater value of  $\Pi_0$ , i.e., the glass becomes tougher. This increase in toughness can be attributed to the enhanced ductility. That is to say, the Na-rich glasses become softer (lower strength), but at the mean time can deform more easily to accommodate the applied load (i.e., the glass can survive at larger strain). The results for the notched sandwich glasses show similar trend but the

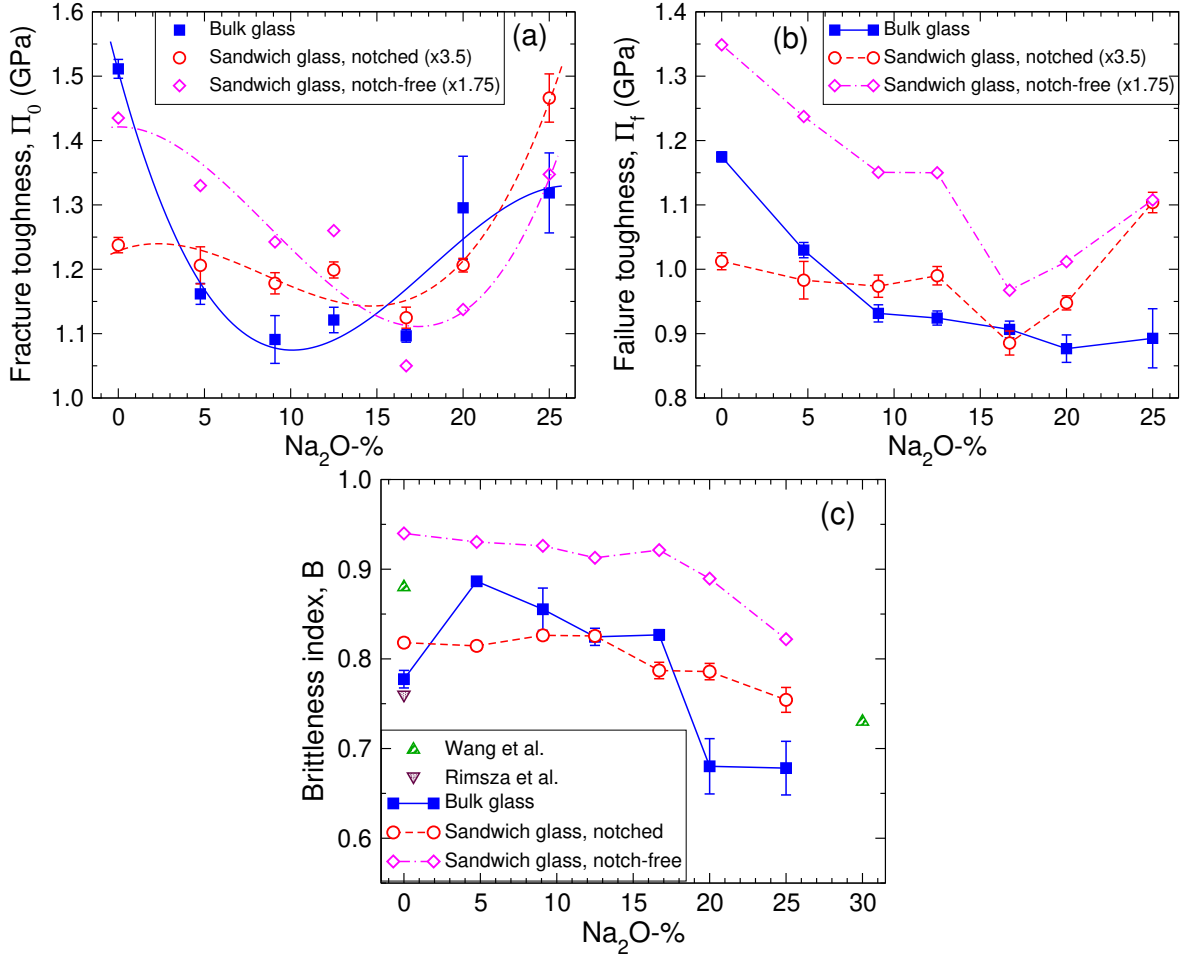


**Figure 3.11:** Composition dependence of the toughness and brittleness parameters of the glasses. (a) Fracture toughness  $\Pi_0$ . (b) Failure toughness  $\Pi_f$ . (c) Brittleness index  $B = \Pi_f / \Pi_0$ . The bulk and sandwich glasses correspond to the data shown in Fig. 3.10. In (a) and (b) the data for the notched and notch-free sandwich glasses have been multiplied by 3.5 and 1.75, respectively. The lines in (a) are third order polynomial fits of the three data sets. In (c), also included are the data from Wang *et al.* [52] and Rimsza *et al.* [61]. Error bars are standard error of the mean of three and six fracture samples for the bulk and notched sandwich glasses, respectively. For the notch-free sandwich glasses, only one fracture simulation was performed for each composition.

minimum location is shifted to a higher Na concentration (around 17% Na<sub>2</sub>O), which might be a consequence of the presence of notched surfaces. The data points for the notch-free sandwich glasses show similar dependence on the Na content as the notched sandwich samples.

The failure toughness  $\Pi_f$  of the bulk glass decreases with increasing Na content. Interestingly, it shows a noticeable slope change at around 10% Na<sub>2</sub>O, corresponding well to the location of the minimum in  $\Pi_0$ . Both the notch-free and notched sandwich glasses show a minimum in  $\Pi_f$  at around 17% Na<sub>2</sub>O.

Figure 3.11(c) shows the brittleness index estimated for the glasses together with the results from previous studies for comparison. Taking into account the fact that different potentials and simulation setups were used, our finding that  $B \approx 0.8$  for the bulk and notched sandwich silica is in reasonable agreement with previous studies, which have found a brittleness index of 0.88 [52] and 0.76 [61] for silica glass. For sodium silicate glasses, it was reported that  $B = 0.73$  for the glass with 30% of  $\text{Na}_2\text{O}$  [52]. Our results are comparable to this finding if the data is properly extrapolated. The data for the notch-free sandwich glasses are somehow larger than the values for the bulk and notched sandwich glasses. These results indicate that the absolute value of  $B$  depends somewhat on the sample geometry, but its dependence on composition seems unaffected. One also notices that the value of  $B$  is much less affected by the sample geometry than  $\Pi_0$  and  $\Pi_f$ . Finally, we note that the brittleness index may show a noticeable dependence on the strain rate as we will see a bit later.

### 3.2.6 Crack velocity

Based on the stress-strain behavior, we also estimated the crack velocity  $v_c$  during glass fracture by using the expression:

$$v_c = L_c / (t_0 - t_m), \quad (3.5)$$

where  $L_c$  denotes the total crack length and  $t_0 - t_m$  is the duration of crack propagation, i.e., stress drops from the maximum (at  $t_m$ ) to zero (at time  $t_0$ ). We note that this definition of  $v_c$  is sensible for the fracture of the sandwich glasses, since no noticeable regions of crack arresting can be observed after the failure point, i.e., the failure point can be considered as the fracture point.

As shown in Fig. 3.12(a), glass composition has a pronounced effect on  $v_c$ . With increasing Na concentration, we observe that  $v_c$  decreased from  $\approx 1800$  m/s for silica to  $\approx 650$  m/s for NS3. We also note that the dependence of  $v_c$  on Na concentration also changes, i.e., the slope of the curve also depends on composition. Figure 3.12(b) shows the influence of temperature on crack velocity. Overall, we observe that silica and NS3 exhibit similar  $T$ -dependence. With increasing  $T$ ,  $v_c$  increases firstly and then tends to decrease at higher temperature. This result suggests a temperature induced stiffening-to-softening transition of the fracture behavior.

Experimental studies have reported that the terminal crack velocity in  $\text{SiO}_2$ -based glasses ranges from 700 m/s to 2500 m/s, depending on composition and elastic properties [7]. The crack velocity generally decreases with decreasing  $\text{SiO}_2$  concentration. For soda-lime-silica (74 $\text{SiO}_2$ -13 $\text{Na}_2\text{O}$ -11 $\text{CaO}$ , wt%) glass, the terminal  $v_c$  was shown to be  $\approx 1500$  m/s [142]. It has also been suggested that the terminal  $v_c$  can be reached in the

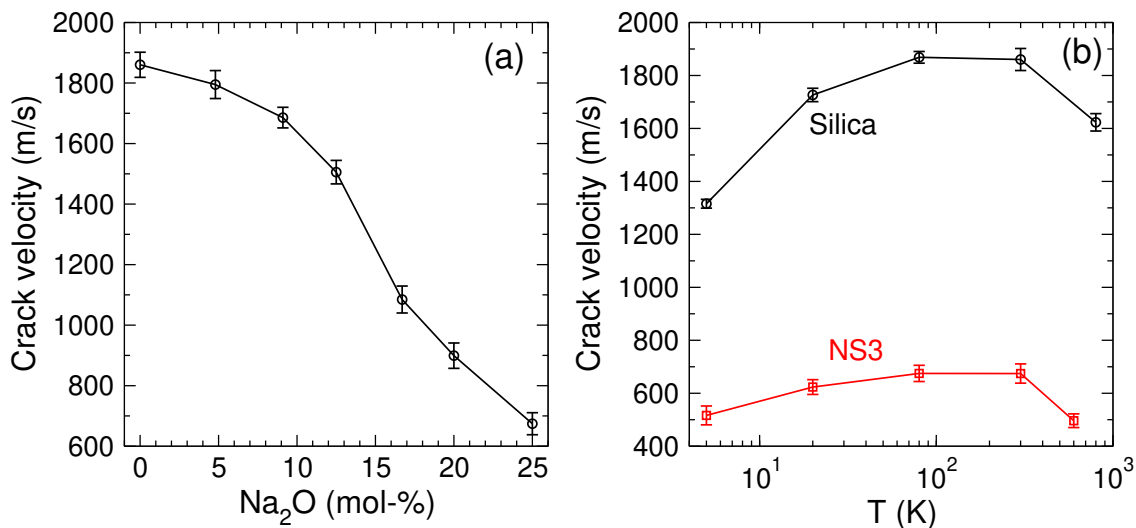


**Figure 3.12:** Crack velocity as a function of composition (a) and temperature (b). Crack velocity was measured for the notched sandwich glasses. Error bars are standard error of the mean of six fracture samples.

mirror region<sup>1</sup>, which is the region we focus on. The magnitude of  $v_c$  estimated from our simulations as well as its composition-dependence are in agreement with experimental results. We note that as cracks propagate with  $v_c \approx 1500$  m/s, it is impossible for our eyes to follow them. This is also the reason why computer simulations and more advanced experimental techniques are required to study the dynamic fracture of brittle materials such as oxide glasses.

Furthermore, we have investigated the influence of strain rate  $\dot{\epsilon}$  on  $v_c$ . We took from the fracture simulation with  $\dot{\epsilon} = 0.5/\text{ns}$  an atomic configuration before the failure point as a starting point, and then applied different strain rates to it. The resulting  $\sigma - \epsilon$  curves are shown in Fig. 3.13. One notices that the strain rate effect is more pronounced for the Na-rich NS3 glass than for the silica glass. A recent study of silica glass using reactive force fields as interaction potential found for the strain rate of  $5/\text{ns}$  a terminal  $v_c$  of  $\approx 2200$  m/s [54], a value that is comparable with the  $v_c$  estimated in our work. For sodium silicate glass, no such data was found in the literature. Additionally, we note that as the brittleness index  $B$  (Eq. 3.4) is very sensitive to the change of the  $\sigma - \epsilon$  curve, one would observe a noticeable increase of  $B$  with decreasing strain rate.

The theory of linear elastic fracture mechanics predicts that mode I (tensile) cracks propagating faster than the Rayleigh wave speed,  $v_R$ , is forbidden, since for this case the energy release rate would be negative [143]. To have an idea of how these crack velocities compare with  $v_R$ , we estimate for the sandwich glasses the  $v_R$  using the

<sup>1</sup>This region is close to the fracture origin and is relatively smooth.

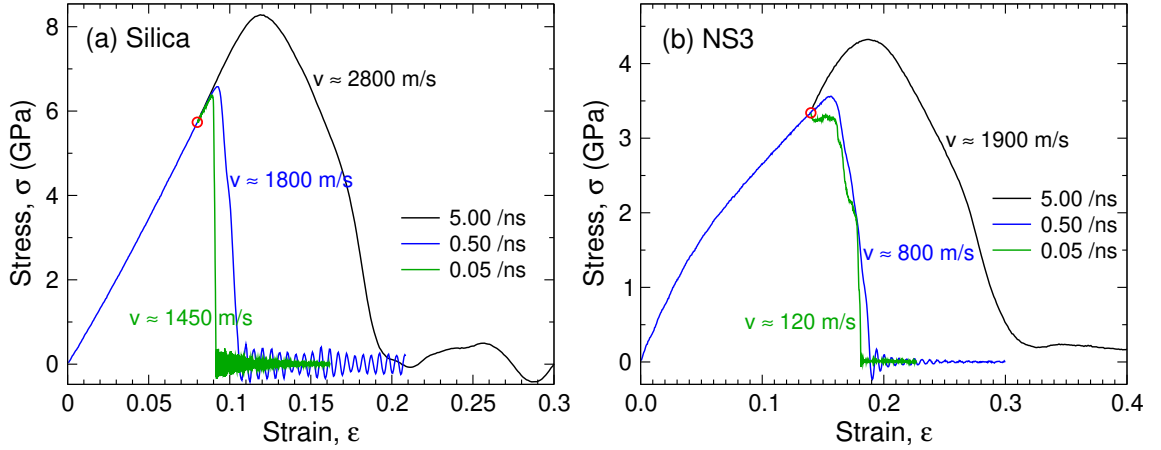


**Figure 3.13:** Strain rate dependence of the crack velocity for the sandwich glasses having dimensions of 20, 30, 50 nm. Strain rate changes during tensile loading. The circle in each graph indicates the point where the strain rate switches from a constant value of 0.5/ns to the values shown in the legend.

formula [144–147]

$$v_R = \frac{0.87 + 1.12\nu}{1 + \nu} \sqrt{\frac{G}{\rho}}, \quad (3.6)$$

where  $G$  is shear modulus,  $\nu$  is Poisson's ratio and  $\rho$  is density. For the sandwich glasses the estimated values for these various quantities are listed in Table 3.1.

Glass	Na <sub>2</sub> O (%)	$\nu$	$E$	$G$	$\rho$	$v_R$ (m/s)	$v_c$ (m/s)	$v_c/v_R$
Silica	0.0	0.200	63.0	26.3	2.20	3148	1860	0.59
NS20	4.8	0.195	54.5	22.8	2.26	2893	1795	0.62
NS10	9.1	0.185	47.2	19.9	2.28	2687	1686	0.63
NS07	12.5	0.205	42.9	17.8	2.31	2533	1506	0.59
NS05	16.7	0.210	39.3	16.2	2.35	2403	1085	0.45
NS04	20.0	0.215	38.2	15.7	2.38	2348	899	0.38
NS03	25.0	0.235	41.6	16.8	2.43	2418	672	0.28

**Table 3.1:** Na<sub>2</sub>O concentration (mole%), elastic properties (Poisson's ratio  $\nu$ , Young's modulus  $E$  (GPa), shear modulus  $G$ (GPa)), experimental density  $\rho$  (g/cm<sup>3</sup>) at room temperature, Rayleigh wave speed  $v_R$ , crack velocity  $v_c$  and the ratio between  $r_c$  and  $v_R$ . Sandwich glasses at 300 K.

In Fig. 3.14(a) we compare the crack velocities with the estimated Rayleigh wave speed, experimental transverse ( $v_T$ ) and longitudinal ( $v_L$ ) wave speeds<sup>2</sup> in sodium silicate glasses. Also included in the graph are the  $v_L$  and  $v_T$  calculated based on the

<sup>2</sup>Rayleigh waves are a type of surface wave that travel along the surface of solids, whereas transverse (shear) and longitudinal waves travel in the bulk.



elastic constants in Table 3.1 using the expressions [146–148]

$$v_L = \sqrt{\frac{E(1-\nu)}{\rho(1+\nu)(1-2\nu)}} \quad v_T = \sqrt{\frac{G}{\rho}}. \quad (3.7)$$

Overall we find that  $v_L > v_T > v_R > v_c$ . The transverse ( $v_L$ ) and longitudinal ( $v_T$ ) wave speeds estimated from the simulations are lower (might be related to the cooling rate) but do exhibit the same variation trend as the experimental ones. Figure 3.14(b) shows that the ratio between crack velocity ( $v_c$ ) and Rayleigh wave speed ( $v_R$ ) reaches a maximum at around 9% Na<sub>2</sub>O (NS10), i.e., the critical composition in the transition behavior of  $E_t$  (see Fig. 3.10). This finding implies that the mechanical responses before failure also have consequences for the fracture process. In addition, for the Na-poor compositions, i.e., Na<sub>2</sub>O% < 13%, the estimated  $v_c/v_R$  is compatible with the value of 0.5 ~ 0.6 that one usually finds in experimental measurements [7]. For the Na-rich glasses,  $v_c/v_R$  is considerably smaller. The reduction of  $v_c/v_R$  can be related to the fact that the local deviation of the crack front (crack arresting) is more pronounced in these glasses, which is also reflected in the surface morphology as we will see in the next chapter. Finally, we note that all the estimated  $v_c/v_R$  are smaller than the experimental upper bound of 0.66 found for inorganic glasses [149, 150].

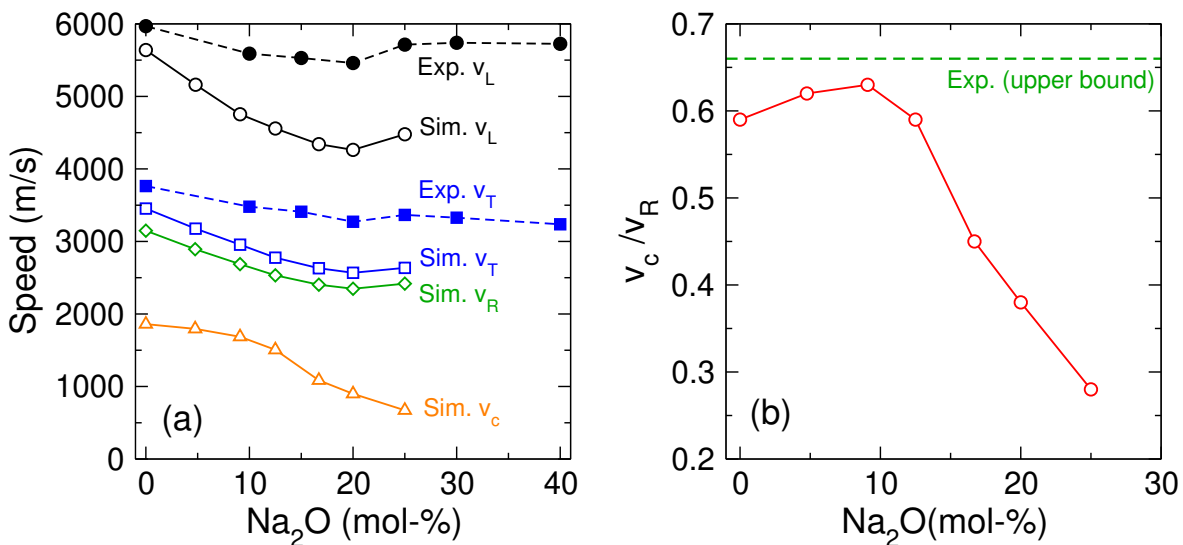


**Figure 3.14:** (a) Crack velocity  $v_c$  compared with various elastic wave speeds as estimated from our simulations and measured from experiments.  $v_c$  and  $v_R$  are also listed in Table 3.1. Experimental data were measured by using Brillouin light scattering at room temperature (The data for silica and sodo-silicate glasses are taken from Refs. [151] and [136], respectively). (b)  $v_c/v_R$  as a function of Na<sub>2</sub>O concentration. The dashed line indicate the experimental upper bound found in inorganic glasses [149, 150].

We have discussed in this section the influences of important factors for glass fracture in terms of the stress-strain behavior, which is rather a global picture of the

mechanical response of glass. Based on the  $\sigma - \epsilon$  curve, we also estimated the brittleness parameters and the crack velocities. In the next section we will explore the properties of the glasses on the microscopic scales, i.e., on the length scale of several Å. We will see that the mechanical behavior of glass at the macroscopic scales can indeed be better understood with the knowledge of structure, dynamics, and mechanics at the microscopic scales.

## 3.3 Microscopic insights

### 3.3.1 Cavitation

Previous studies have pointed out the critical role of compositional change on the stress-strain behavior of glass [52, 57]. However, a detailed analysis of the nanoscale cavitation process (i.e., the formation and growth of cavities during deformation of glass) is still missing. (A more detailed literature review can be found in chapter 1). To understand the deformation and fracture behavior of glasses on the microscopic scale, we explore first whether or not glass fracture is accompanied by the formation and growth of voids (or cavities).

Here we define voids as the regions where no atom can be found in a probing sphere with a radius  $R_c$ . All atoms are simply viewed as point-like objects, i.e., no volume is assigned to the atoms. The probing sphere moves over the whole sample and the regions where no atoms are contained in the sphere are thus defined as voids. In practice, a 3D grid with a unit size of 1.25 Å was used in the search of voids. Figure 3.15(a) shows that the number of voids ( $N_{\text{void}}$ ) in the unstrained glasses decreases in an exponential manner with increasing  $R_c$ . In Fig. 3.15(b), the void density,  $\rho_{\text{void}}$ , is plotted as a function of Na concentration. One observes that, for a chosen  $R_c$ ,  $\rho_{\text{void}}$  decreases exponentially with increasing Na<sub>2</sub>O content. Also interesting is the finding that  $\rho_{\text{void}}$  decreases faster for larger  $R_c$  (the absolute value of the exponent increases with  $R_c$ ).

As indicated by the intersection between the  $N_{\text{void}}$  curve and the green dashed line, panel (a), a probing sphere of size  $R_c \approx 4.0$  Å is required in order to exclude the free volumes in the glass samples been identified as voids for the glass samples considered. These results also demonstrate that voids with radius up to  $\approx 4.0$  Å are naturally present in the unstrained glasses. A previous study, using the same definition of void, found that the largest void in silica glass has a radius of  $\approx 3.5$  Å [50]. We suspect that the smaller value they have found might be a consequence of small system size they have studied (cubic boxes with size of  $\approx 37$  Å). (Small simulation box leads to insufficient statistics). As shown in Fig. 3.15,  $N_{\text{void}}$  at a given  $R_c$  depends on the composition, i.e., Na-rich compositions tend to have fewer voids. This finding is related

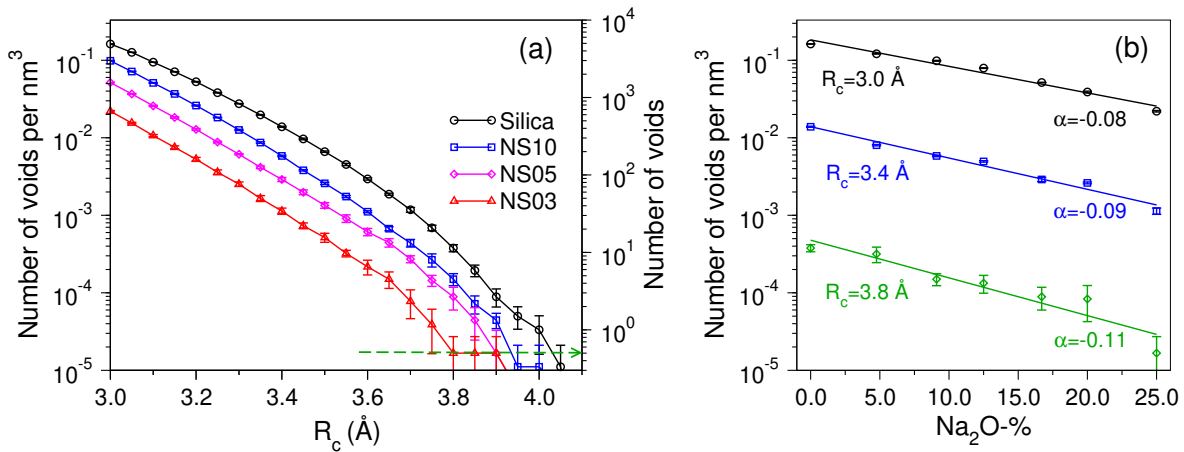


**Figure 3.15:** (a) Number of voids versus the radius of the probing sphere,  $R_c$ . In the search of voids, the examined samples are the sandwich glasses which have dimensions of  $20 \text{ nm} \times 30 \text{ nm} \times 50 \text{ nm}$ . The green dashed line points to  $N_{\text{void}}=0.5$ , i.e., with 50% probability to find only one void with size  $R_c$  in the unstrained sample. (b) Number of voids per  $\text{nm}^3$  versus  $\text{Na}_2\text{O}$  concentration. The lines are exponential fits to the data, and the exponents  $\alpha$  are shown in the graph as well. Error bars are standard error of the mean of six fracture samples.

to the fact that the atomic number density  $\rho_N$  of the glass increases with the addition of Na. The structure of sodium silicate glasses can be viewed as a network of  $[\text{SiO}_4]$  tetrahedra with occasional breaks in connectivity. The Na atoms occupy the interstices in the network, reducing the free volume of the structure. For the simulated glasses at 300 K,  $\rho_N$  is  $66.82 \text{ nm}^{-3}$  for silica and  $73.83 \text{ nm}^{-3}$  for NS3. However, all of these critical values are close to  $4.0 \text{ \AA}$ . Therefore, in the present analysis, a critical value of  $R_c = 4.0 \text{ \AA}$  was chosen for the search of voids during the deformation of the glasses.

With the threshold size of void determined, we now can characterize the fracture of glass in terms of cavitation. Firstly, we show in Fig. 3.16 some snapshot corresponding to specific strains during fracture of silica, panel (a), and NS3, panel (b). To associate these snapshots with the mechanical condition of the glass sample, we depict in panels (c) and (d) the stress-strain curves of the corresponding glasses.

For silica, by visual inspection we find that a few ( $< 5$ ) voids are present before reaching the maximum stress ( $\epsilon = 0.092$ ), and these voids only have a size of  $R \approx 4.0 \text{ \AA}$ . They are also unstable as they do not survive if the strain is changed by a few percents, i.e., their presence is due to the fluctuations of local structure and composition. Once the failure point is reached, the crack propagates very rapidly through the sample. During the entire fracture process, we did not observe growth and coalescence of the voids. Our finding is thus in accordance with the traditional picture that silica is brittle and the crack propagates by sequential rupturing of the atomic bonds at the crack tip.

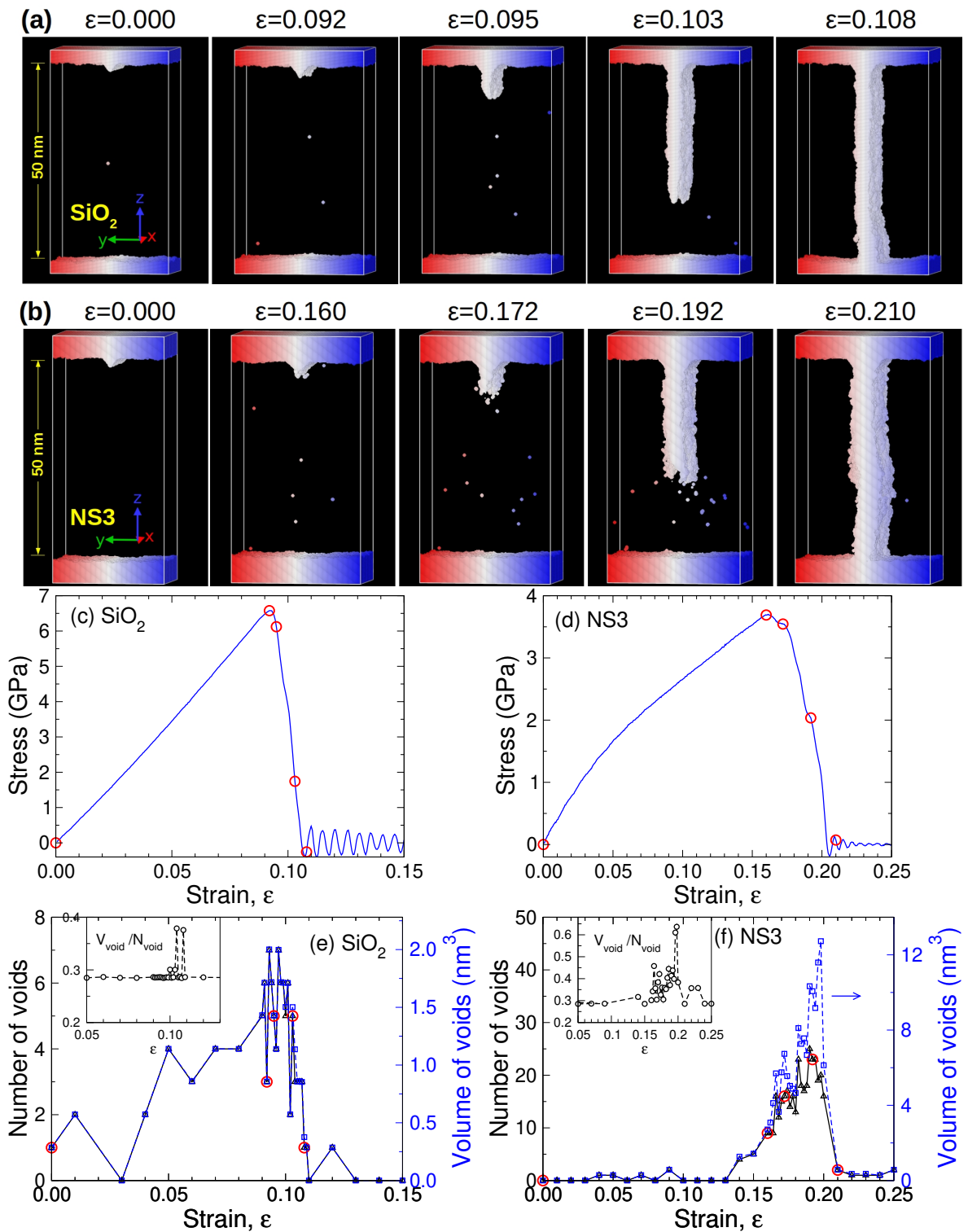


**Figure 3.16:** (a) and (b) Snapshots showing the empty volume during the fracture of the silica (a) and NS3 (b) glasses (sample size  $20 \times 30 \times 50$  nm). A notch was introduced on the top surface to initiate the fracture. Color coding is based on the coordinate in the  $y$ -direction. (c) and (d) Stress-strain curves correspond to the fracture of the two glasses. (e) and (f) The total number and volume of voids during fracture of the two glasses. The red circles in panels (c-f) highlight the specific strain points as shown in the snapshots. The insets in panels (e-f) show the ratio between the volume ( $\text{nm}^3$ ) and number of the voids.

Quantitatively, we show in panel (e) for silica the number of voids,  $N_{\text{void}}$  and their total volume  $V_{\text{void}}$  during the fracture of the glasses. We note that the curve showing the number of voids and the curve for volume of voids collapse onto each other almost perfectly. This is confirmed by the inset of panel (e), which shows that the ratio  $V_{\text{void}}/N_{\text{void}} \approx 0.286 \text{ nm}^3$  over the entire strain range. This ratio corresponds to void size  $R \approx 4.1 \text{ \AA}$ , thus indicating that all the voids have the same size, during the fracture process. The two noticeable jumps of the  $V_{\text{void}}/N_{\text{void}}$  at around 10% strain are just (unstable) fluctuations. These quantitative results confirm our observation from the snapshots, showing that silica breaks in a brittle manner and no growth and coalescence of voids can be detected. This observation agrees with the finding of a recent simulation study of the fracture of silica glass using reactive force fields [54], and also is consistent with the post-mortem analysis of fracture surfaces of silica glass by Guin and Wiederhorn [11].

For NS3, panel (b), we find again only a few unstable and small voids ( $R = 4.0 \text{ \AA}$ ) present before the failure point. However, once the crack starts to propagate, the situation shows noticeable differences from the fracture of silica. Firstly, we observe that the number of voids increases and at some specific points, e.g.,  $\epsilon = 0.172$ , small voids near the crack tip will grow and then merge with the crack front. Also very interestingly, we find that micro-branching of the crack may also show up at some points (e.g.,  $\epsilon = 0.192$ ) along the fracture path. But we note that the formation of microcracks is rather a minor and transitory event and eventually these microcracks will be invisible from the fracture surface.

From Fig. 3.16(f), we notice a drastic increase in the number of voids as the strain approaches the failure point, and this trend also continues during the crack propagation. As for the volume of voids, we find that the curve superimposes very nicely to the curve of the number of voids before the failure point (see also the inset in same graph). This result indicates that  $N_{\text{void}}$  increases with strain but each individual void is not growing before the failure point. Once the crack starts to advance, one notices that the volume of voids goes up faster than the number of voids, implying that some voids grow to bigger sizes and may merge with their neighboring voids. This is also reflected in the change of the ratio  $V_{\text{void}}/N_{\text{void}}$  (inset of panel(f)). All together, these results indicate that the fracture of NS3 glass is accompanied by the growth and coalescence of cavities. One also notices that  $V_{\text{void}}/N_{\text{void}}$  at its highest value is about twice the value of the initial plateau, suggesting that on average the voids can grow to twice as large as their initial size, i.e., reaching a size of  $R \approx 5.0 \text{ \AA}$  assuming the voids are spherical in shape.

However the assumption that voids are spheres may not be appropriate as the growth of voids might depend on the direction. In Fig. 3.17 we show an example of irregular voids that appear at  $\epsilon = 0.196$ . It can be seen that the biggest void has in the

$x$ -direction (parallel to the crack front) a dimension of  $\approx 3.5$  nm, while only a dimension of  $\approx 1.5$  nm in the  $y$ -direction (perpendicular to the fracture plane). This result clearly indicates that with increasing strain, some voids will grow and merge with others to form big voids with very irregular shapes. Taking into account the fact that the voids may shrink after fracture due to the reversible part of the surface displacements, the dimension of the voids in the out-of-plane direction (e.g. the  $y$ -direction) will become even smaller [66]. These two effects together may explain why no remnants of voids were detected by comparing postmortem fracture surfaces of soda-lime-silicate glass [11].

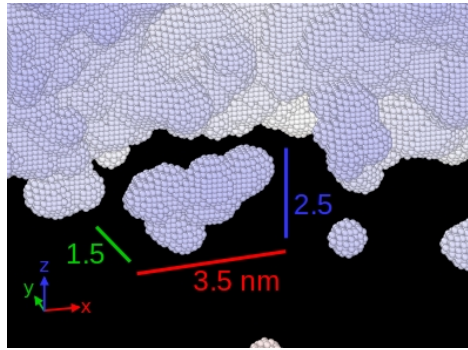


**Figure 3.17:** Enlarged view of the largest void found at  $\epsilon = 0.196$  for the fracture of the NS3 glass.

Finally, we note that one may average over the results of multiple fracture samples for small-strain region to improve the statistics. This operation will make smoother the curves shown in Fig. 3.16 but the conclusions would be the same as above since the glass sample is big enough to ensure only a negligible fluctuation in the small-strain range. However, once the glasses are approaching the failure strain, we find that one glass sample may fail and then break a bit earlier than the other samples (which is a normal sample-to-sample fluctuation). Since the stress-strain curve looks very steep during fracture, for a given strain in the fracture region (i.e., from the maximum stress to zero stress) the corresponding stress may vary largely for different samples (although the overall fracture behavior of different samples look qualitatively similar to each other). As a consequence, average over multiple samples in this range will lead to a large error bar in the  $y$ -axis. This could potentially wash out the true mechanisms of glass fracture as show in the voids analysis in Fig. 3.16 which is shown only for one representative sample.

### 3.3.2 Local properties

The mechanical behavior of glass on the macroscopic scale can be better understood by probing the properties of the glass at the microscopic scales. In this section, we

firstly quantify the local structural, dynamical and mechanical properties of the glasses under tension. Then we discuss the evolutions and correlations between various local properties.

First of all, let us give the definitions of the various local quantities that we explored:

- Mass density:  $\rho_m = m/V$ , where  $m$  is the mass and  $V$  the volume.
- Atomic number fraction:  $f_i = N_i/N_{tot}$ , where  $f_i$  is the number fraction of atom specie  $i$ .  $N_i$  and  $N_{tot}$  are the numbers of atoms of type  $i$  and all types, respectively. The stoichiometric atomic number fraction of Na is equal to 0.167 in NS3 glass, for example.
- Nonaffine displacement [152]:  $\mathbf{u}_i^{\text{na}} = \mathbf{r}_i - \mathbf{r}_i^{\text{aff}}$ , where  $\mathbf{r}_i$  stands for the current position of the particle  $i$  and  $\mathbf{r}_i^{\text{aff}}$  is the resulting position after the affine transformation under an imposed strain of  $\epsilon$ . For the transformation considered here we have  $\mathbf{r}_i^{\text{aff}} = (1 + \epsilon)\mathbf{r}_i^0$ , where  $\mathbf{r}_i^0$  denotes the reference (initial) position of particle  $i$ . In the following we use  $u$  to represent the norm of  $\mathbf{u}^{\text{na}}$ .
- Atomic shear strain: To quantify plastic deformation at the atomic level, here we use the atomic local shear strain  $\eta_i^{\text{Mises}}$  as first introduced by Shimizu *et al.* [153].  $\eta_i^{\text{Mises}}$  is a good measure of local plastic (or inelastic) deformation. Briefly, the  $\eta_i$  is calculated by the following steps:

1) Calculate the separation vector between atom  $i$  and  $j$  by

$$\mathbf{d}_{ij} = \mathbf{r}_j - \mathbf{r}_i, \quad (3.8a)$$

where atom  $j$  is one of atom  $i$ 's neighbors within a prescribed cutoff radius  $r_c$ .

2) Seek a local affine transformation matrix  $\mathbf{F}_i$  (also called deformation gradient tensor) that best maps

$$\{\mathbf{d}_{ij}^0\} \rightarrow \{\mathbf{d}_{ij}\}, \forall i \in N_i^0, \quad (3.8b)$$

where the superscript 0 means the reference configuration, and  $N_i^0$  is the total number of neighbors of atom  $i$  at the reference configuration.  $\mathbf{F}_i$  is determined by minimizing [154]

$$\sum_{j \in N_i^0} |\mathbf{d}_{ij}^0 \mathbf{F}_i - \mathbf{d}_{ij}|^2. \quad (3.8c)$$

3) Calculate the atomic Green-Lagrangian strain tensor by

$$\boldsymbol{\eta}_i = \frac{1}{2}(\mathbf{F}_i \mathbf{F}_i^T - \mathbf{I}). \quad (3.8d)$$

4) Based on the six components of  $\boldsymbol{\eta}_i$ , one can compute atom  $i$ 's local shear invariant as

$$\eta_i^{\text{Mises}} = \sqrt{\eta_{yz}^2 + \eta_{xz}^2 + \eta_{xy}^2 + \frac{(\eta_{yy} - \eta_{zz})^2 + (\eta_{xx} - \eta_{zz})^2 + (\eta_{xx} - \eta_{yy})^2}{6}}. \quad (3.8e)$$

$\eta_i^{\text{Mises}}$  is a measure of local inelastic deformation. The calculation of these atomic-level strain tensors was realized by using the OVITO software [155].

- Atomic stress: We compute the symmetric per-atom stress tensor for atom  $i$  using the following formula:

$$\sigma_i^{ab} = \frac{1}{V_i}(-m_i v_i^a v_i^b - W_i^{ab}), \quad (3.9a)$$

where  $a$  and  $b$  takes on values  $x, y, z$  to generate the 6 components of the stress tensor, and  $V_i$  is the volume assigned to atom  $i$ . In practice, this volume can be represented by the Voronoi volume around the atom. On the right hand side of Eq. (3.9a), the first term denotes a kinetic energy contribution for atom  $i$ , and the second term is the virial contribution which is given by

$$\begin{aligned} W_{ab} = & \frac{1}{2} \sum_{n=1}^{N_p} \sum_{m=1}^2 r_{ma} F_{mb} + \frac{1}{2} \sum_{n=1}^{N_b} \sum_{m=1}^2 r_{ma} F_{mb} \\ & + \frac{1}{3} \sum_{n=1}^{N_p} \sum_{m=1}^3 r_{ma} F_{mb} + \frac{1}{4} \sum_{n=1}^{N_d} \sum_{m=1}^4 r_{ma} F_{mb} \\ & + \frac{1}{4} \sum_{n=1}^{N_i} \sum_{m=1}^4 r_{ma} F_{mb} + f_{\text{Kspace}}. \end{aligned} \quad (3.9b)$$

The first, second, third, fourth and fifth terms are pairwise, bond, angle, dihedral and improper contributions for which atom  $i$  is part of, respectively. The last term is for the K-space contribution from long-range Coulombic interactions (For the SHIK potential with the Wolf approximation of Coulombic interactions, this term is not required). Note that the stress for each atom is due to its interaction with all other atoms in the simulation. More details concerning the computation of the virial for individual atoms can be found in Refs. [115, 156]. The diagonal components of the per-atom stress tensor are of particular interest in the present work. Note that the total pressure of the system can be calculated by the expression:

$$P = -\frac{1}{3V} \sum_{i=1}^N (\sigma_i^{xx} + \sigma_i^{yy} + \sigma_i^{zz}) V_i \quad (3.9c)$$

where  $N$  is the total number of atoms in the sample,  $V$  the total volume, and  $\sigma_i^{xx}$  the  $x$ -component of the atomic stress tensor for atom  $i$ . (Pressure is simply the negative of hydrostatic stress). The calculation of the per-atom stress tensor was realized by using the LAMMPS package [116].



- Local temperature: The temperature is calculated by

$$T = \frac{2}{3} \frac{E_k}{Nk_B}, \quad (3.10a)$$

where  $E_k$  is the total kinetic energy of a group of  $N$  atoms, i.e.

$$E_k = \sum_{i=1}^N \frac{1}{2} m_i v_i^2, \quad (3.10b)$$

$k_B$  is the Boltzmann constant and  $T$  the temperature associated with the group of  $N$  atoms. The limit of this local temperature is the per-atom temperature ( $T_i$ ), i.e., the temperature is calculated using only a single atom. Note that since “temperature” can only be a well defined concept for a large group of atoms, what we will be looking at is rather the instantaneous kinetic energy mapped to a temperature scale.

- Coordination number: We compute the coordination number of Si (i.e., the number of O in the nearest neighbor shell of a given Si) and also the coordination number of O (i.e., the number of Si in the nearest neighbor shell of a given O). The cutoff distance for the search of nearest neighbor is chosen as the first minimum in the radial correlation function of Si-O pair, i.e.,  $g_{\text{SiO}}(r)$ .
- Change of inter-tetrahedral angle  $\delta\theta$ :  $\delta\theta_i^\epsilon = \theta_i^\epsilon - \theta_i^0$ , where  $\theta_i^0$  is the SiOSi angle of O atom  $i$  in the initial configuration (0% strain),  $\theta_i^\epsilon$  is the SiOSi angle of the same O atom in the current configuration with  $\epsilon$  applied strain. Note that it is possible that a SiOSi connection at 0% strain does not exist anymore at strain  $\epsilon$ , since some bridging oxygens may become non-bridging oxygens. For this case, we simply assign  $\delta\theta_i^\epsilon = 0$ .

For all aforementioned local quantities, we have subsequently applied a coarse-graining procedure to obtain local maps. We have carefully examined the influence of the coarse-graining length-scale  $\omega$  and the weight function  $\phi(r)$  for assigning weight to each atom. We found that  $\omega = 8 \text{ \AA}$  and a Gaussian weight function  $\phi(r) = \exp(-r^2/(2\sigma^2))$ , with  $\sigma = \omega/\sqrt{2}$  performs reasonably well. We note that the chosen coarse-graining length is also the choice of previous simulation studies [60, 70].

To start, we show in Fig. 3.18 the distribution of mass density ( $\rho_m$ ) of the NS3 glass. For the unstrained glass ( $\epsilon = 0$ ), the  $\rho_m$  distribution has a Gaussian-like shape and peaks at  $\rho_m \approx 2.45 \text{ g/cm}^3$ , which is very close to the experimental density  $2.43 \text{ g/cm}^3$  at room temperature [112]. This agreement indicates that the analysis of glass properties at the atomic scale based on a group of atoms does make sense. With increasing strain, one observes that the distribution broadens and shifts to the left. This is simply due to the fact that the glass network become more and more diluted

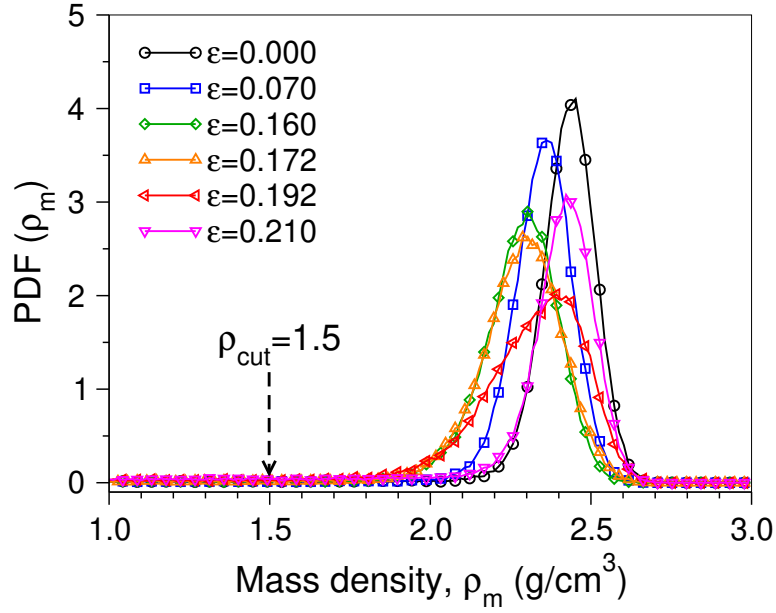


**Figure 3.18:** Distribution of mass density of a sandwich NS3 glass at various applied strain.  $\rho_{cut}$  is the threshold density that we used to exclude the empty spaces in the surrounding of the glass sample.

with increasing strain. Once the glass starts to fracture, i.e.,  $\epsilon > 0.16$ , the distribution will shift backwards, and eventually peaks at a position more or less the same as the unstrained sample. But the distribution of the fractured sample is still broader since the density near the two fracture surfaces will be smaller than the bulk density.

Note that the density distribution has a tail at  $\rho_m \rightarrow 0$  (not shown in the graph) which corresponds to the empty spaces on the two surface sides of the glass. In order to obtain a map that matches the glass matrix, it is preferred to get rid of the empty spaces. However, unambiguous determination of the glass-vacuum interface is certainly nontrivial. The strategy we applied here is to use a threshold density  $\rho_{cut} = 1.5 \text{ g/cm}^3$ . All regions with density smaller than  $\rho_{cut}$  will be considered as empty space and thus will be removed.

To justify the aforementioned strategy of approximation, we show in Fig. 3.19 snapshots of the glass network as well as the density map at various strains. It can be seen that with  $\rho_{cut} = 1.5 \text{ g/cm}^3$ , the local density maps indeed match the glass sample reasonably well at different applied strain. We emphasize that a slight adjustment of  $\rho_{cut}$  will not change the profile of the maps significantly.

**Distributions of local properties.** In Fig. 3.20 we show the maps of several local properties that are of interest during fracture of the NS3 glass. One clearly sees that the local compositional, structural, kinetic and mechanical quantities all show pronounced heterogeneity. To understand better these local properties, we first investigate the distributions of these quantities. Figure 3.21(a) shows the stress-strain curve (with

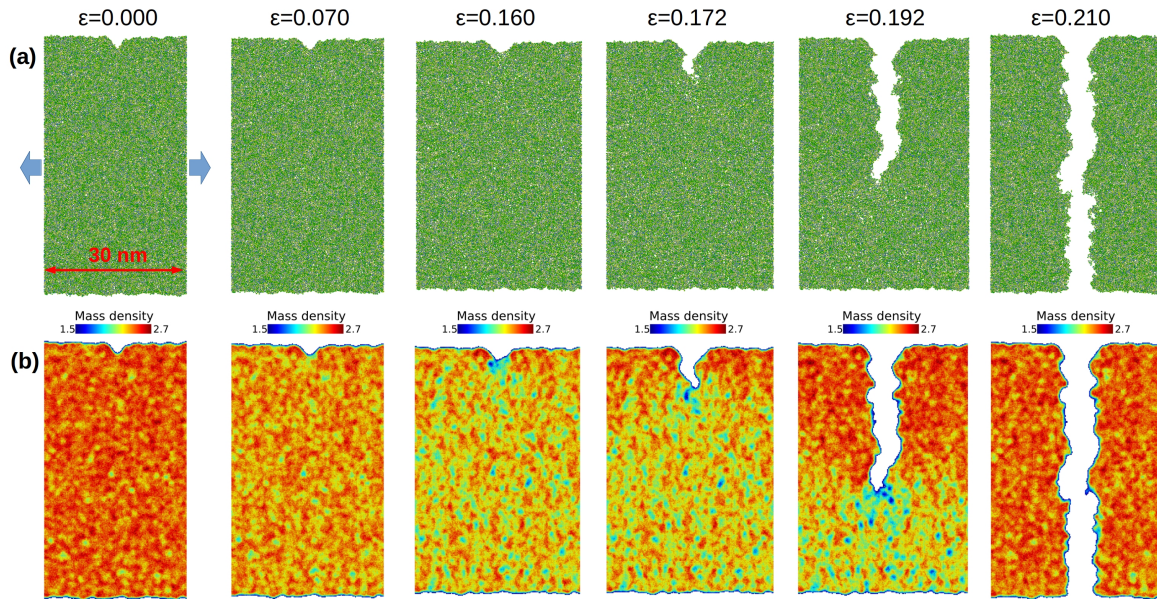


**Figure 3.19:** (a) Snapshots showing the evolution of a slice ( $10 \text{ \AA}$  in thickness) corresponding to the middle plane of the NS3 glass under uniaxial tension. (b) Local density ( $\text{g/cm}^3$ ) maps corresponding to the snapshots in panel (a). Regions with  $\rho_m < 1.5 \text{ g/cm}^3$  are removed.

specific strain points highlighted) which corresponds to the fracture of the Na-rich NS3 glass. Figure 3.21(b) shows the distribution of local  $T$  at various strains and one sees that the distribution remains unchanged before the failure point. Once the fracture starts, one notices that the peak position of the distribution shifts to lower  $T$  whereas the tails at large  $T$  raise. This result is consistent with the snapshots in Fig. 3.20 which show the local heating near the crack tip. Once the fracture is done, the sample will become again spatially homogeneous with respect to temperature. This corresponds to the drop of the tails at large  $T$  and the shifting of the peak position to the initial state, i.e., at  $\approx 300 \text{ K}$ . One also observes that the distribution of local  $T$  at  $\epsilon = 0.25$  is broader than the one at  $\epsilon = 0$ . This difference can be attributed to the fact that the sample has not yet reached the real steady state with a constant temperature.

Figure 3.21(c) shows that, for small  $\epsilon$ , the distribution of local shear strain  $\eta^{\text{Mise}}$  continuously shifts to larger value with increasing global strain, indicating that the inelastic part of the deformation is accumulating. Once the crack starts to advance, one sees that a tail appears at large  $\eta^{\text{Mise}}$  and it becomes increasingly pronounced with the advancing of the crack. This tail at large  $\eta^{\text{Mise}}$  arises from the fracture surfaces (see the snapshots in Fig. 3.20). Once the fracture is over, the tail in the distribution remains basically unchanged since the fracture surfaces are no more evolving.

In Fig. 3.21(d) we plot the distribution of local tensile stress at various global strains. With increasing global strain, one notes that the distribution shifts to larger stress and broadens, indicating that the glass is increasingly stressed and also the lo-

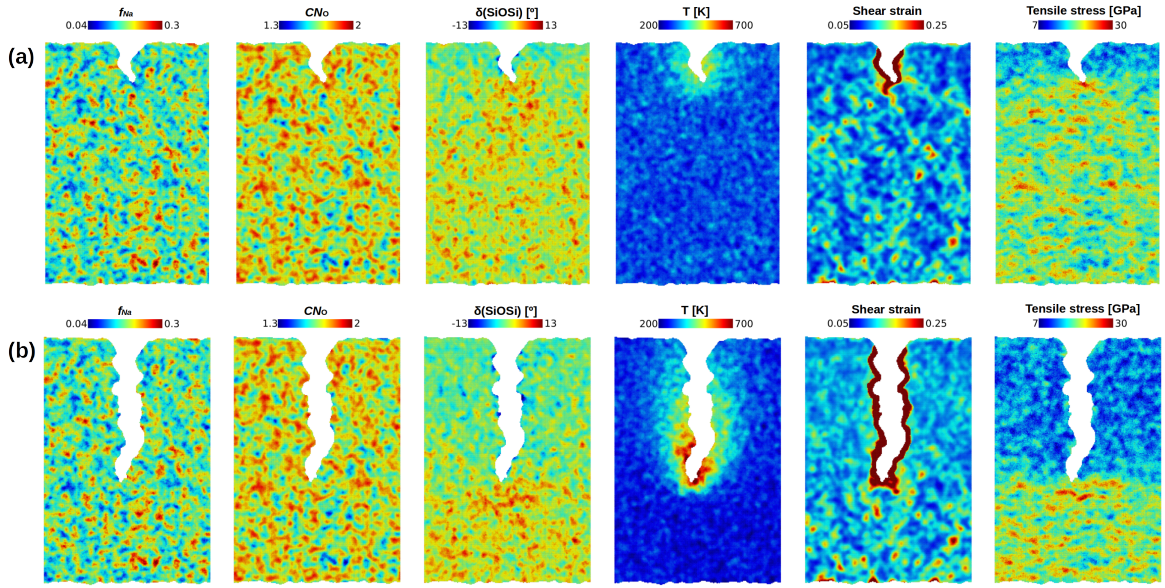


**Figure 3.20:** Maps of various local properties at (a)  $\epsilon = 0.172$  and (b)  $\epsilon = 0.192$  for the NS3 sandwich glass. See the text for the definition of each quantity. These maps are shown for the middle plane of the simulation box in the direction orthogonal to the crack front.

cal stress becomes more heterogeneous. Once the fracture begins, one observes that the peak position at large stress remains unchanged whereas the peak intensity decreases. As the crack advances, another peak at small stress arises and it becomes increasingly pronounced. Eventually the distribution looks like the one at  $\epsilon = 0$ , i.e., a globally stress-free state. All these evolutions of the local stress distribution reflect in a quantitatively manner the maps of local tensile stress as shown in Fig. 3.20.

**Correlations between local properties.** In addition to the distributions of these local properties, we also notice that they are correlated to each other. Therefore, a further step to understand these local maps is to quantify the correlations between them. We note that as we have explored more than 20 different local properties (taking into account the partials for each atomic species), the combinatorial possibilities are over 100. Therefore, we will focus on a few pairs that could be more instructive for understanding the deformation and fracture of sodium silicate glass at the microscopic scales. In Fig. 3.22 shows the correlations between various local properties at the failure point ( $\epsilon = 0.162$ ), panels (a-d), and during fracture  $\epsilon = 0.192$ , panels (e-f). Note that the correlation is evaluated for the whole sample, not just for the surroundings of the crack tip. One recognizes the correlation between local Na fraction and Si fraction (panel (a)) is very pronounced, whereas for the pair of local temperature and shear strain (panel (f)), one observes a bimodal distribution (see the ellipses in the graph).

To be more quantitative, here we rely on the Spearman's rank correlation coefficient,  $r_s$  [157], which is a measure of statistical dependence between the rankings of two

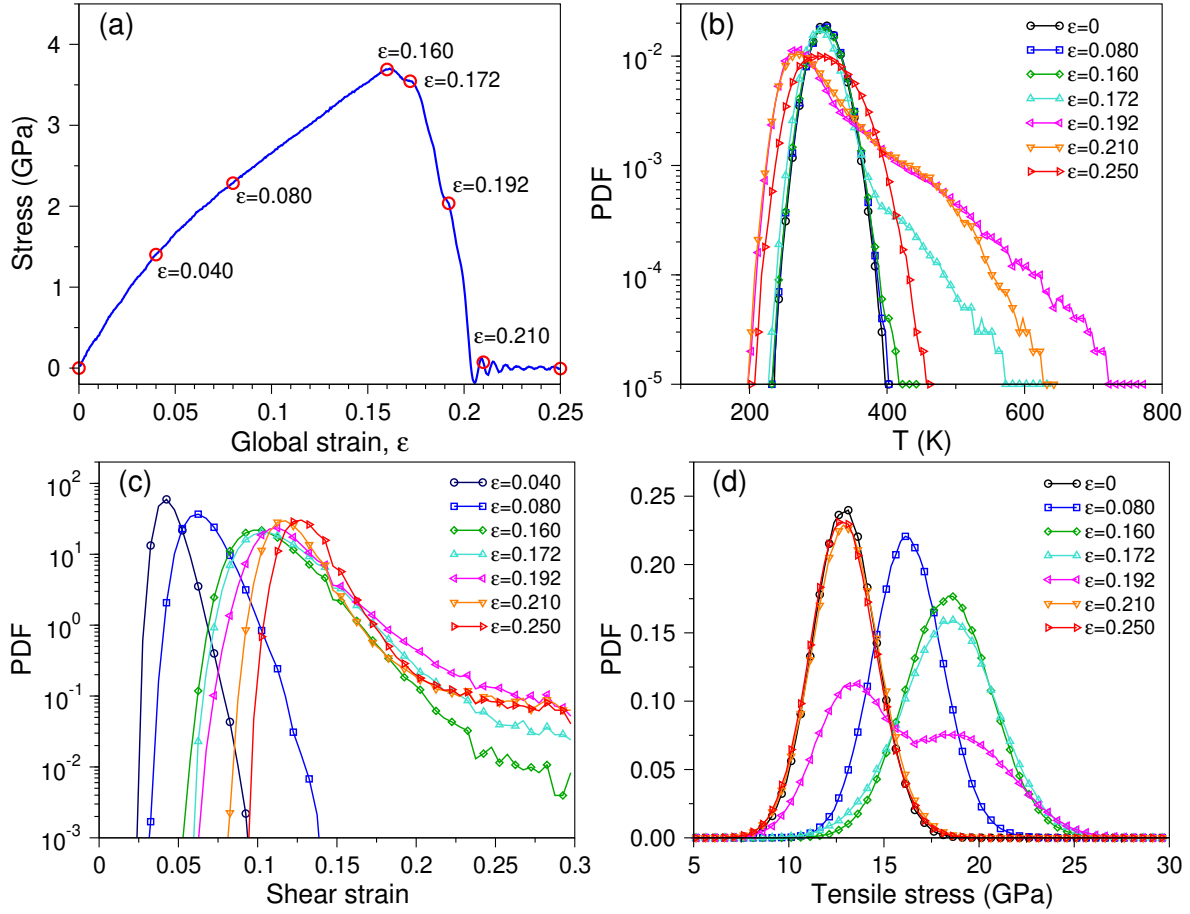


**Figure 3.21:** (a) Stress-strain curve of the NS3 sandwich glass at 300 K. (c-d): Distributions of local temperature, shear strain, and local tensile stress, respectively. Note that, for this analysis, the layers ( $\approx 2.5$  nm in thickness) near the free surfaces of the sandwich sample were removed. In panel (a), the red circles indicate the various global strains shown in panels (b-d).

variables. For a sample of size  $n$ , the  $i$ th observations of two variables  $X_i$  and  $Y_i$  are converted to ranks  $rg_{X_i}$  and  $rg_{Y_i}$ , and  $r_s$  is given by

$$r_s = \frac{\text{cov}(rg_X, rg_Y)}{\sigma_{rg_X} \sigma_{rg_Y}}, \quad (3.11)$$

where  $\text{cov}(rg_X, rg_Y)$  is the covariance of the rank variables,  $\sigma_{rg_X}$  is the standard deviation of the rank variable  $rg_X$ . If all  $n$  ranks are distinct integers, the coefficient  $r_s$  can be computed using the formula

$$r_s = 1 - \frac{6 \sum d_i^2}{n(n^2 - 1)}, \quad (3.12)$$

where  $d_i = rg_{X_i} - rg_{Y_i}$ , is the difference between the two ranks of the  $i$ th observations for the variables  $X$  and  $Y$ . The coefficient  $r_s$  is always in the range  $[-1, 1]$  and  $r_s > 0$  means positive correlation, i.e.,  $Y$  tends to increase when  $X$  increases and vice versa. In

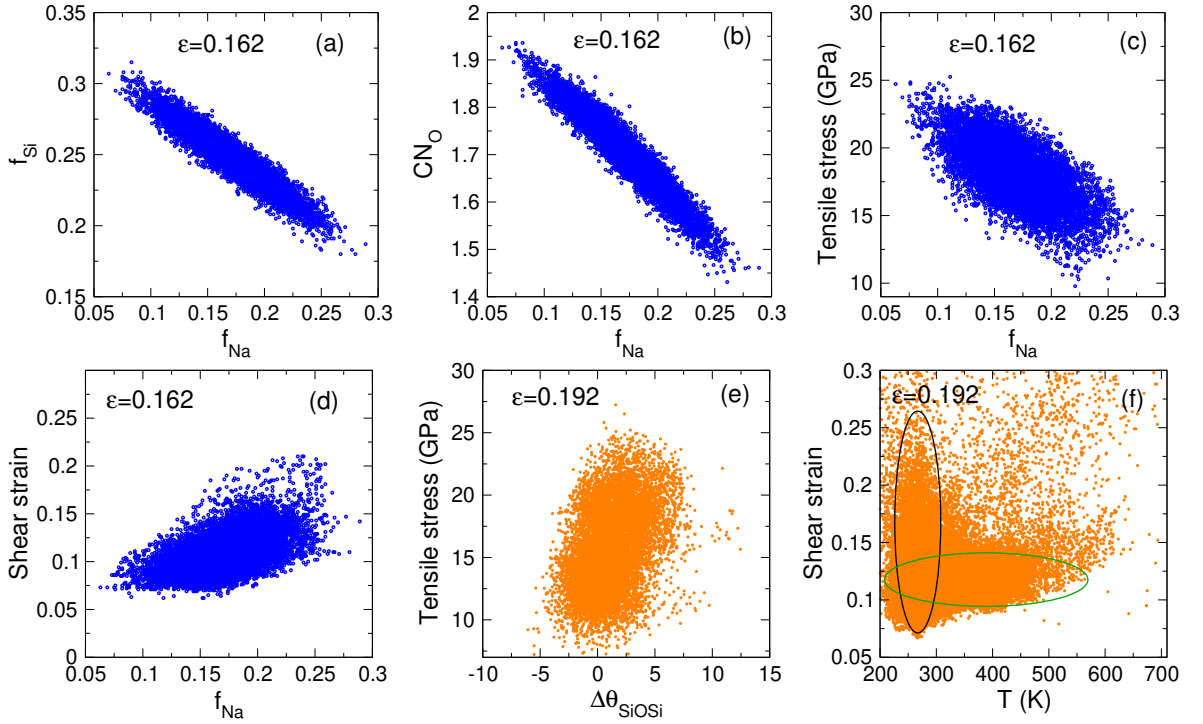


**Figure 3.22:** Correlation between several pairs of local properties. See the main text for the definition of each quantity. Note that in panels (a-d) the correlations are shown for  $\epsilon = 0.162$ , i.e., the failure point, whereas in panels (e-f)  $\epsilon = 0.192$ , i.e., during fracture (see also the lower panels in Fig. 3.20).

contrast,  $r_s < 0$  means anti-correlation, i.e., Y tends to decrease when X increases and vice versa. The magnitude of  $r_s$  indicates the degree of correlation, with  $r_s = 0$  means no correlation between the two variables. In contrast to the Pearson correlation, which only gives a perfect correlation when variables X and Y are related by a linear function, a perfect Spearman correlation results when X and Y are related by any monotonic function [158].

In Fig. 3.23, we show the correlations between various local quantities as functions of the applied strain. First of all, we recognize from panel (a) that the local atomic fractions are strongly correlated: Si and O are positively correlated with  $r_s(\text{Si}, \text{O}) \approx 0.75$ ; Si and Na are negatively correlated with  $r_s(\text{Si}, \text{Na}) \approx -0.94$ ; A strong anti-correlation is also found between O and Na with  $r_s(\text{O}, \text{Na}) \approx -0.90$ . These correlations are indeed what one would expect for soda-silicate glasses, in agreement with previous simulation work [60]. Moreover, we find that the correlation between the local compositions is basically independent of the applied strain. These results make sense since the glass structure is basically fixed at room temperature. It is unlikely to observe dramatic changes of local composition and structure even if the glass is under external tensile stress. This point is further confirmed by the correlation between local Na fraction,  $f_{\text{Na}}$ , and local coordination number of O,  $CN_{\text{O}}$ , in panel (b). It can be seen that

$f_{\text{Na}}$  and  $CN_{\text{O}}$  are strongly anti-correlated, and their correlation coefficient is nearly a constant. Their correlation suggests that Na-rich regions tend to have smaller  $CN_{\text{O}}$ , i.e., the glass network is less connected, in agreement with the local maps in Fig. 3.20.

Furthermore, one can also explore the correlation between local composition and local mechanical properties. As shown in panel (c), overall, we note that  $f_{\text{Na}}$  is positively correlated with local shear strain, while anti-correlated with local tensile stress. This results can be understood by recalling that Na-rich regions are more flexible due to the high mobility of Na and less connected network. Therefore, these regions can deform more easily and thus are able to accommodate more strain and also reduce stress. Very interestingly, the dependence of the correlations on the applied strain can be divided into 3 regions, namely before fracture, during fracture, and after fracture (as indicated by the dashed lines in the graphs). Before fracture (i.e., before the failure point), we notice that the correlation between  $f_{\text{Na}}$  and local stress and strain becomes increasingly pronounced with increasing strain and the maximum is reached at the failure point. These results imply that the glass becomes more and more heterogeneous in both composition and mechanics as it is deformed. Once the fracture starts, the correlations decrease. This result suggests that the propagation of the crack helps to release the constraints and heterogeneities that have been built before the failure point. Thus the degree of correlations between these quantities will soon return to a small value once the fracture is completed.

In panel (d), we show the correlations between shear strain and tensile stress. As expected, we observe that they are anti-correlated, i.e., zones with large shear strain tend to have small stress. We note that the largest correlation coefficient only has a value  $\approx 0.3$  (at the failure point). This might be due to the fact that shear deformation mainly happens at the vicinity of the crack tip. Averaging the correlation over the entire sample will inevitably hide the true level of correlation near the crack tip. Nevertheless, it is clear that shear strain and tensile stress are anti-correlated and their correlation shows a similar three-stage strain dependent as the ones in panel (c).

Also very interesting is the correlation between local stress and local structural changes, more specifically the change of the inter-tetrahedral angle. As can be seen from panel (e), the correlation is very weak before the fracture (only a slight increase of correlation can be noticed). Once the fracture starts,  $r_s$  soars, reaching a value of more than 0.5 in the middle of the fracture. The rationale is that upon elongating, the linkage between neighboring tetrahedra will likely be stretched and thus increasing the SiOSi angle. Therefore, the regions with larger  $\delta\theta$  (i.e., more stretched) tend to be under high stress. Once the fracture is done, the stress is released. Therefore, the correlation between them decreases considerably.

A final interesting result we discuss here is the correlation between local temperature

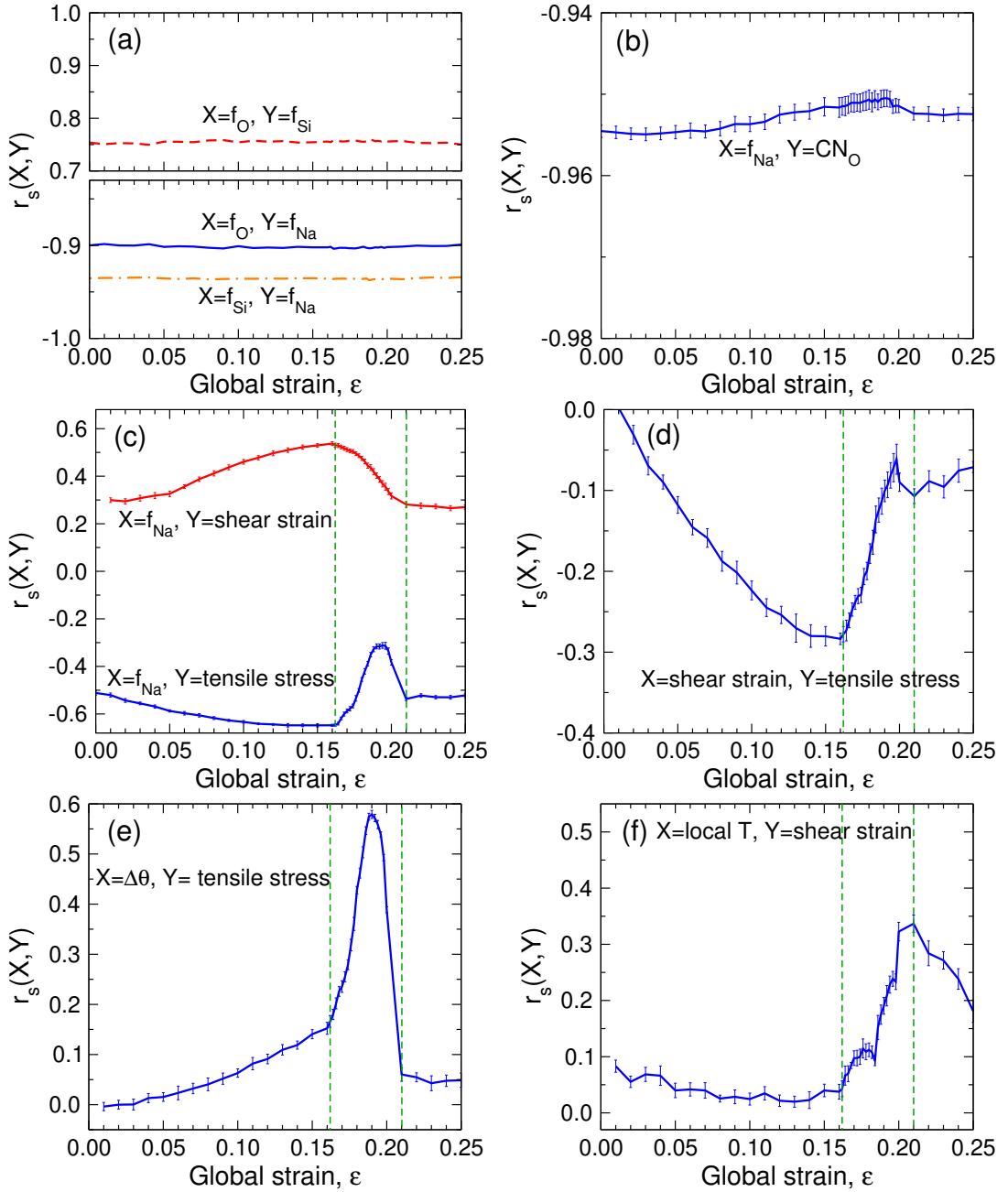


**Figure 3.23:** Spearman's correlation coefficient ( $r_s$ ) for various pairs of local quantities in the NS3 sandwich glass. (a) Correlation between local atomic fractions. (b) Correlation between local Na fraction and O coordination number. (c) Correlation between local Na fraction and local mechanical quantities. (d) Correlation between local tensile stress and shear strain. (e) Correlation between local SiOSi angular change and local stress. (f) Correlation between local temperature and shear strain. The layers ( $\approx 2.5$  nm in thickness) near the free surfaces of the glass sample were removed before the correlation analysis. The vertical dashed lines correspond to the failure point (i.e., at maximum stress) and the fracture point (i.e., at zero stress), respectively. Error bars are standard error of the mean of 10 slices orthogonal to the direction of the crack front.



and local shear strain. From the maps in Fig. 3.20 we have noticed that the local temperature and shear strain are positively correlated during glass fracture. Fig. 3.23(f) shows that  $r_s$  is nearly zero before failure. However, once the crack starts to propagate,  $r_s$  increases continuously until the fracture complete. The rationale for this result is that the breaking of the atomic bonds at the crack tip releases energy and thus results in local heating. As the crack passes through the glass, more and more energy are released and dissipated into the bulk, which then promotes plastic deformation of the sample. Once the fracture is done, the sample will gradually cool down thus  $r_s$  also declines and eventually reaches value close to the ones before fracture.

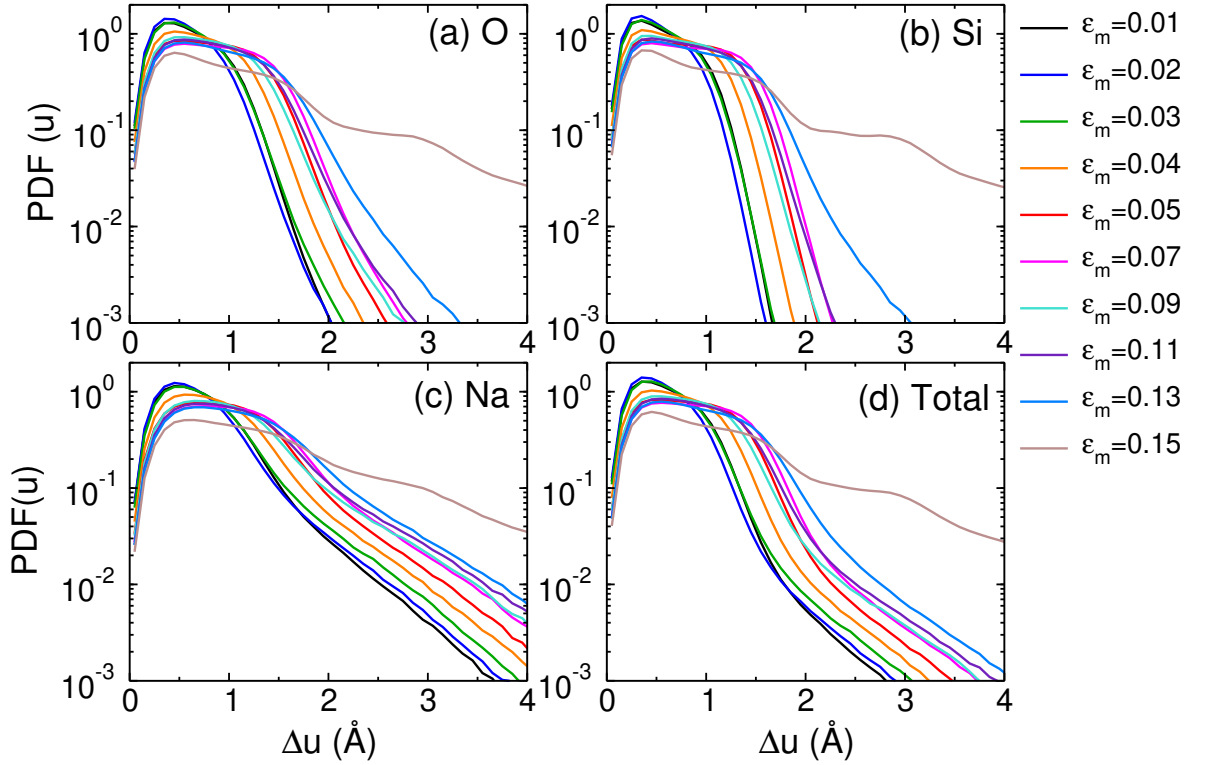
**Atomic-scale origin of glass stiffness.** We recall that, in Fig. 3.10, a composition-induced transition behavior in the tangent modulus has been revealed. Note that this transition behavior is independent of sample geometry, i.e., it appears for both the bulk and sandwich glasses. Below we will show that this transition behavior can be attributed to the atomic scale nonaffine displacement.

Figure 3.24 shows the incremental nonaffine displacement  $\Delta u$  for the Na-rich NS3 glass at different applied strain. To obtain  $\Delta u$ , a sliding reference configuration was used with the strain increment  $\Delta\epsilon$  fixed at 2%, i.e., if the current configuration is at strain  $\epsilon_c$  then the reference configuration is at  $\epsilon_c - 2\%$ . In Fig 3.24, the strain  $\epsilon_m$  corresponds to the mid-point between the reference and current configurations. By comparing the  $\Delta u$  of the three species, panels (a-c), one recognizes that the ones for Na are larger than the ones for Si and O (mainly in the tails of distributions). This is due to the fact that Na has the highest freedom in the glass matrix thus can displace more under deformation, whereas the motion of O and Si are largely constrained by the glass network.

Very interestingly, one observes that for the first peaks in the probability distribution functions (PDFs), all species show the same strain dependence: For  $\epsilon_f < 4\%$ , the peaks are basically independent of  $\epsilon_m$ . The peak intensity decreases considerably at 4% and then becomes a constant again for  $0.05 < \epsilon_f < 0.13$ . Further increasing of  $\epsilon_m$  leads to a noticeable decrease of the first peak and also a significant rise of the curve at large  $\Delta u$ . The observed strain dependence of  $\Delta u$  seem to coincide with the ones of the tangent modulus curve as shown in Fig. 3.10.

The results shown in Fig. 3.24 imply that the strain dependence of the nonaffine part of the atomic displacements might be the microscopic reason for the change in the macroscopic stiffness, as given by the tangent modulus. If this is the case, then one would expect that this quantity should also show a similar composition dependence as the tangent modulus curves.

Figure 3.25 shows the average incremental nonaffine displacement  $\langle \Delta u \rangle$  as a function of strain for the NSx bulk glasses. (The results for the sandwich glasses are similar



**Figure 3.24:** Incremental nonaffine displacement  $\Delta u$  for the NS3 sandwich glass.

to the bulk ones). Firstly, one recognizes that the total  $\langle \Delta u \rangle$  exhibits a compositional dependence that coincides very well with the behavior of the tangent modulus curves: For silica, one observe  $\langle \Delta u \rangle$  decreases with increasing Na%, meaning that the glass becomes less and less deformable. This corresponds to the finding that the glass stiffens (i.e.,  $E_t$  increases) with increasing strain. A minimum of  $\langle \Delta u \rangle$  is reached when  $\epsilon_m \approx 10\%$ , after which  $\langle \Delta u \rangle$  increases rapidly. This result is also consistent with the behavior of  $E_t$ . The critical compositions is found to be NS10, for which one observes that  $\langle \Delta u \rangle$  is essentially a constant in the small-strain range. For the Na-rich glasses, e.g., NS3,  $\langle \Delta u \rangle$  increases at small-strain range ( $\epsilon_m < 8\%$ ), and then a weaker dependence is found in the intermediate-strain range ( $8\% < \epsilon_m < 16\%$ ), after which a drastic increase of  $\langle \Delta u \rangle$  shows up. Based on all these observations, we conclude that the nonaffine part of the atomic displacements dictate the stiffness of the glass on the macroscopic scale.

A further interesting message from Fig. 3.25 is the behavior of the three partials, panels (b-d). While the  $\langle \Delta u \rangle$  of Si and O show basically the same behavior as the ones of the total  $\langle \Delta u \rangle$ , the ones for Na demonstrate very different behaviors. Firstly, one notices that the curves for the glasses with smaller Na content are higher than the ones for the Na-rich glasses, indicating that the mobility of Na decreases with increasing Na concentration. This result makes certainly sense as the addition of Na reduces the free volume in the glass network, and the Na atoms themselves can also

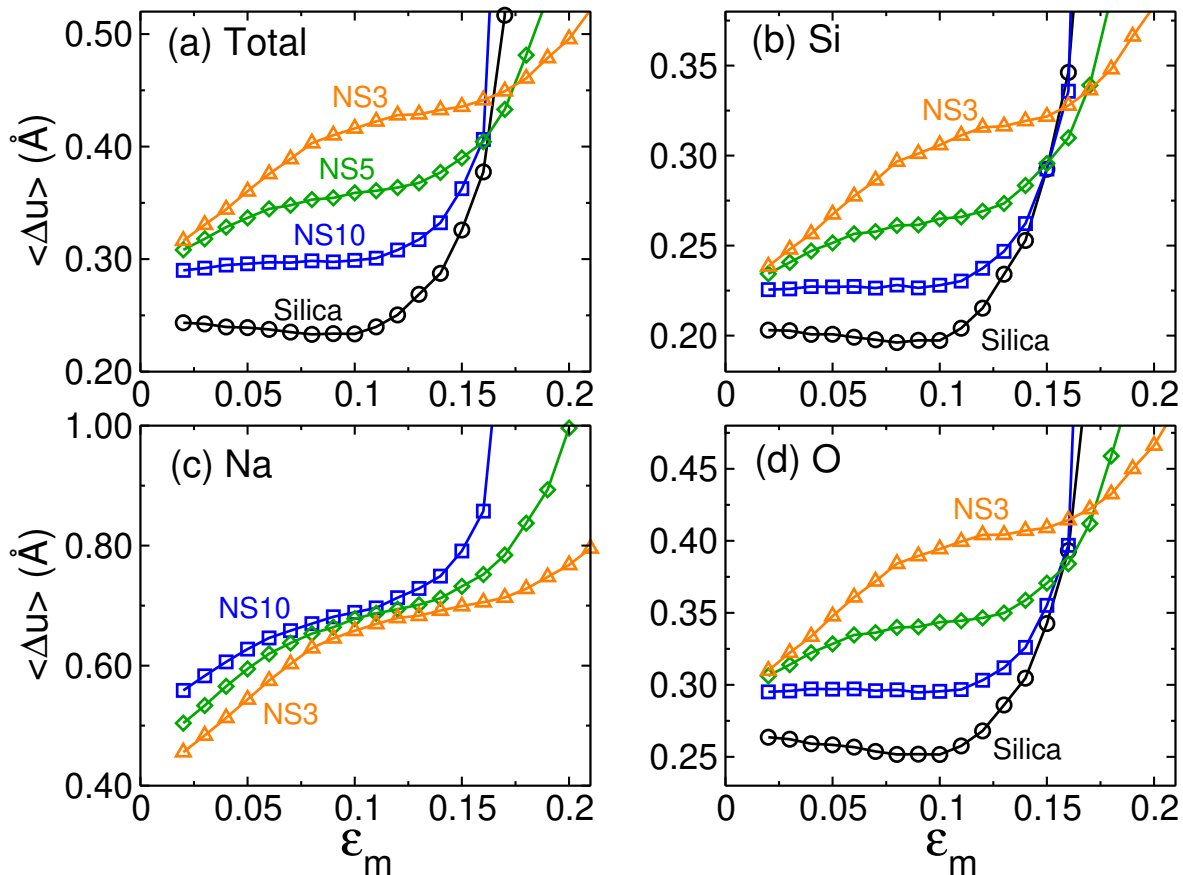


**Figure 3.25:** Per-atom incremental nonaffine displacement  $\Delta u$  versus strain  $\epsilon_m$  for the bulk NSx glasses. The increment of strain is 2% and  $\epsilon_m$  denotes the strain corresponding to the mid-point of the reference and current configurations.

hinder the movement of each other. The network atoms (i.e., Si and O), by contrast, becomes more mobile with increasing Na concentration due to the depolymerization of the network. Secondly, the strain dependence of the  $\langle \Delta u \rangle$  for Na does not show the transition behavior as seen in panels (a), (b) and (d). For all glass compositions,  $\langle \Delta u \rangle$  increases with increasing strain and a shoulder can be observed in the intermediate-strain range. We note that although Na atoms behave differently from the network atoms, in the end it is the total  $\langle \Delta u \rangle$  that matters for determining glass stiffness.

### 3.4 Summary

To summarize, we have investigated systematically the dynamic fracture of sodium silicate glasses under tension. We have adopted simulation protocols that mimic the fracture of glass in real experiments. Two sample symmetries were considered, i.e., bulk glass and sandwich glass (with free surfaces). We have shown that many factors (cooling rate, strain rate, temperature, composition, ...) can have a strong influence

on the tensile stress-strain behavior of the glass. The sodium rich glasses are generally more sensitive to the variation of these factors than silica. For the adopted simulation setups, it is found that a cooling rate  $\gamma \leq 0.3$  K/ps and a strain rate  $\dot{\epsilon} \leq 0.5$ /ns are required to reach a (more or less) convergence of the stress-strain behavior. In addition, we find that while the stress-strain behavior of silica is unaffected by the change in sample thickness, the Na-rich NS3 glass requires a thickness of  $\approx 6$  nm to reach a saturation. This result indicates that a quasi-2D sample geometry may not be sufficient to represent a realistic glass fracture and a 3D geometry is necessary. Furthermore, we have shown that the failure stress decreases linearly with increasing temperature (below  $T_g$ ), independent of glass composition. In contrast, the failure strain shows different  $T$ -dependence as the composition changes.

The compositional dependence of the stress-strain behavior and the tangent modulus curve exhibit an remarkable transition behavior at a critical  $\text{Na}_2\text{O}$  concentration of  $\approx 10\%$ , i.e., NS10. This behavior is also observed in the compositional dependence of  $v_c/v_R$ , i.e., the ratio between the crack velocity and the Rayleigh wave speed, thus indicating that the deformation behavior of the glass before failure also has consequences on the fracture process. The estimated crack velocities show reasonably good agreement with previous experimental and simulation works.

For obtaining insights on the microscopic scales, we have firstly probed the cavitation process during glass fracture. It is found that voids as large as  $R \approx 4$  Å can appear naturally in the unstrained glass, weakly depending on the composition. For silica, no growth and coalescence of voids can be observed, i.e., the glass breaks in a completely brittle manner. In contrast, the fracture of Na-rich NS3 glass shows some degrees of ductility, which is demonstrated by the fact that voids do emerge and grow ahead of the crack tip. Finally, we have found that, for the NS3 glass, the linear extent of big voids may be direction-dependent. And the largest dimension of the voids is found to be on the order of a few nanometers.

Furthermore, we have analyzed various local properties in the Na-rich NS3 glass and quantified the correlation between different properties. We have found that as long as local mechanical properties are concerned, the correlations can be divided into three stages, i.e., before fracture, during fracture, and after fracture. The results show that the correlations between Na concentration and local mechanical quantities (e.g., shear strain and tensile stress) increase with increasing strain and reach a maximum at the failure point, i.e., the pre-notch starts to propagate in the sandwich glass. As the fracture proceeds, the correlations decrease and eventually reach the same level as the ones in the unstrained state. Finally, we have found that the nonaffine atomic displacement seems to be the microscopic origin of the changes in the stiffness of the glass as indicated by the tangent modulus.



## Chapter 4

# Melt-formed and fracture surfaces: Classical MD simulations

A fundamental understanding of glass surfaces is important for many practical applications such as pharmaceutical packaging and displays. In recent years, spectroscopic techniques such as low-energy ion scattering (LEIS) and atomic force microscopy (AFM) have become popular choices for investigating the properties of glass surfaces in experiments. LEIS has a unique sensitivity to the topmost 1-2 atomic layers of a surface. Therefore, it has been used to probe the structure and composition of the surfaces of silicate glasses [78, 159–161]. However a notable limitation of this technique is the sputtering procedure that is usually performed to clean the surface (which could potentially remove parts of the true features of the surface). On the other side, AFM is mainly used to investigate the morphology and roughness of a surface. This technique can hardly provide reliable information on the length scale of a few nanometers due to instrumental noise [162]. Due to the limitations of these experimental techniques, a good understanding of glass surfaces on the microscopic scales is still lacking.

In the past decades, computer simulations have also been used to probe the microscopic (mostly atomic scale) features of glass surfaces. To characterize the surfaces, the conventional approach requires defining a surface layer, the thickness of which is usually several Å for example, based on properties such as the density profile in the orthogonal direction [163–166]. However, defining such a surface layer only allows to obtain averaged information near the surface, whereas, the characteristics of the true surface, which in principle should be a monolayer of atoms, are rarely reported. The objective of this chapter is thus to characterize and understand glass surfaces at the monolayer level with atomic resolution.

This chapter is a follow-up of the results discussed in the previous chapter. We present a comparative study of the characteristics of the melt-formed and fracture

surfaces of silica and sodo-silicate glasses as produced by using large-scale MD simulations. We introduce first the geometric method that was used for constructing the two kinds of surfaces. We then discuss the composition and structure of the monolayer surfaces as well as the depth profiles of these quantities with respect to the surface. After that, we present results regarding the topographical feature, i.e., roughness and height correlation of the surfaces. We mainly focus on compositional effect but the role of temperature will also be discussed. This study provides new insights toward a better understanding of the nature of these two types of glass surfaces at the nanometer scale.

## 4.1 Construction of the geometric surface

In Sec. 3.1 we have introduced the simulation protocol in details. Here a brief recap is given. A conventional melt-quench procedure was used in our computer simulations to produce glasses. We introduced empty spaces on the top and bottom of the liquid sample thus creating free surface on both sides. After equilibration we cooled down the sample to room temperature thus obtaining glasses with two free surfaces, which in the following we will refer as melt-formed surfaces (MS). After breaking the glass under uniaxial tension, a second type of glass surface is generated, i.e. fracture surface (FS). Figure. 4.1 shows a schematic representation of the simulation procedure. The glass samples considered in this chapter have dimensions of  $20 \text{ nm} \times 30 \text{ nm} \times 50 \text{ nm}$  ( $\approx 2,300,000$  atoms). For the MS and FS, two and six independent surfaces were averaged to obtain the results that will be presented below, respectively.

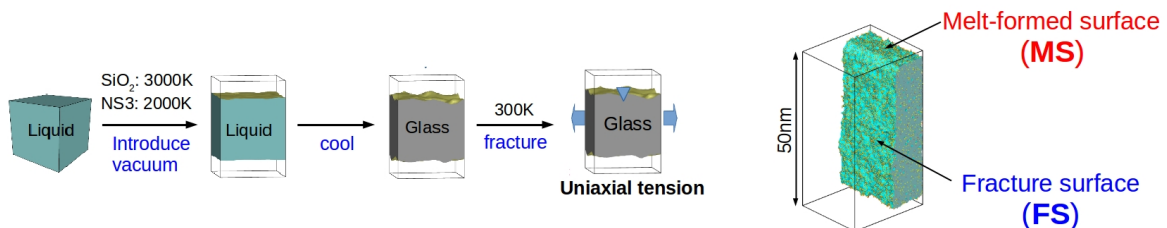


**Figure 4.1:** Schematics of the simulation procedure. Glass with free surfaces, i.e. melt-formed surface (MS) is fractured under uniaxial tension, resulting in fracture surfaces (FS).

In atomistic simulations, the atoms that constitute a solid are often modeled as point-like objects. Constructing the surface of a solid corresponds thus to construct the geometric boundaries of a set of points in space which allows to divide space into solid and open regions. In order to discern empty space in between a set of atomic points, a probe sphere is usually needed. The open region can then be defined as those parts of space that are accessible to the virtual probe sphere without touching any of the atomic points. The radius of the probe sphere  $R_\alpha$  is the length scale which

determines how many details and small features of the solid's geometric shape are resolved by the method.

The algorithm that we used for constructing the surface mesh is based on the alpha-shape method of Edelsbrunner and Mücke [167]. It starts with the Delaunay tetrahedrization (in 3D) of the input point set. To illustrate this geometrical method more clearly, we give an example for the 2D case, i.e., Delaunay triangulation (DT) [168], see Fig. 4.2. For a given set  $\mathbf{P}$  of discrete points, the triangulation  $DT(\mathbf{P})$  is done in such a way that no point in  $\mathbf{P}$  is inside the circumcircle of any triangle in  $DT(\mathbf{P})$ . For the 3D case, the circumcircle extends naturally to a circumscribed sphere, which touches each of the tetrahedron's vertices. From the resulting tetrahedra, all tessellation elements are then evaluated by comparing their circumspheres to the reference probe sphere, which has a radius of  $R_\alpha$ . These elements (with circumsphere radius  $R$ ) which satisfy  $R < R_\alpha$  are classified as solid, and the union of all solid Delaunay elements defines the geometric shape of the atomistic solid. A robust realization of this algorithm is implemented in OVITO [169].

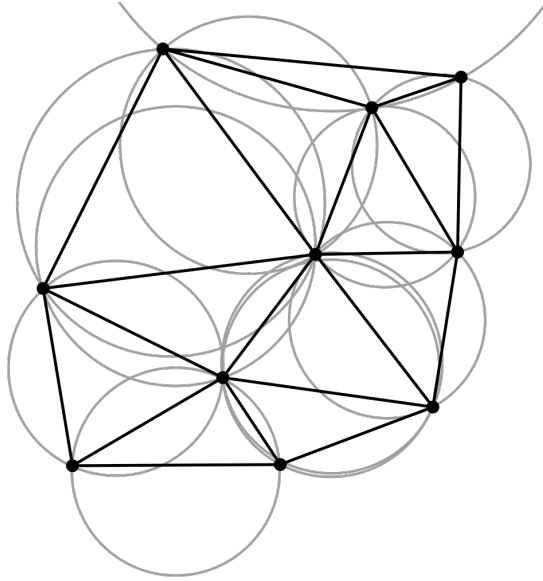


**Figure 4.2:** A Delaunay triangulation in the plane with circumcircles shown.

Once the geometric surface is constructed, i.e., the mesh points of the surface are identified, we first fit a plane to the set of mesh points using least squares fitting procedure. After that, the fitted plane and the set of points are rotated to horizontal, i.e., the  $x-y$ -plane. Finally, a linear interpolation is applied to the scattered triangular mesh to obtain an uniform grid. We conduct further analysis of surface morphology and roughness based on this interpolated surface. See Fig. 4.3 for schematic representations of the surface construction procedure.



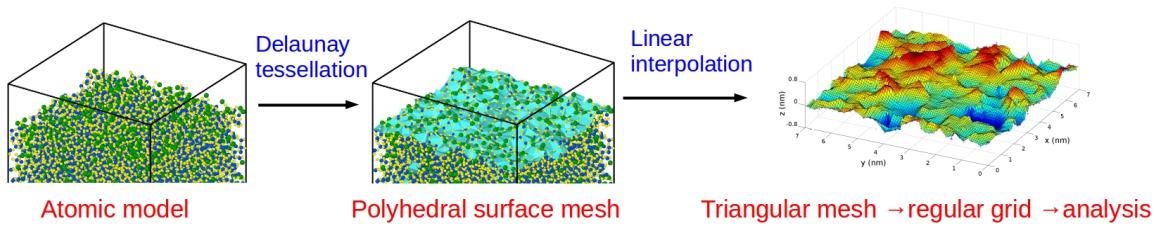


**Figure 4.3:** Schematics of the construction of the geometric surface. Left: Atomic model of the sandwich sample at 300 K. Middle: Constructing polyhedral surface mesh. The resulting surface, which consists of triangular faces, reflects the atomic steps that are typically present on the surfaces of a solid. The shown sample is NS10 and the constructed surface is a melt-formed surface. (The procedure for constructing the FS is similar. The main difference is that, for the FS, layers of width  $\approx 5$  nm below the MS are cut out to eliminate the influence of the MS.)

## 4.2 Surface composition and structure

One of the great advantages of the surface construction method that used here is that it allows to identify the surface atoms explicitly. The triangular mesh points which define the geometrical surface are actually the atoms on the outermost layer of the surface. Therefore, we can study the composition and structure of the monolayer glass surface.

Firstly, we examine how the surface composition depends on the choice of  $R_\alpha$ . Figure 4.4 shows the composition of the MS as a function of  $R_\alpha$ . For the case of silica, one recognizes that with increasing  $R_\alpha$ , the fraction of O increases and the one of Si decreases. The rationale for this finding is that more fine features on the surface are excluded with increasing  $R_\alpha$ , i.e., the surface becomes smoother. Consequently, both the numbers of O and Si on the surface decrease with increasing  $R_\alpha$ . However, since Si atoms contribute mainly to these fine details of the surface layer, increasing  $R_\alpha$  results in a larger fractional change of Si than that of O. As a result, the fraction of O increases while the one of Si decreases with increasing  $R_\alpha$ . For the Na-rich NS3 glass, one observes a less pronounced reduction of Si fraction and also a slight decrease of O content (in contrast to silica). As a consequence, the fraction of Na increases with larger  $R_\alpha$ . These results can be understood by recalling the fact that the Na atoms are more preferred to present on the outermost layer of the surface than the O and Si atoms. Reduction of the total number of atoms on the surface with increasing  $R_\alpha$  results in a larger relative changes of Si and O than that of Na. At the end, the fraction of Na increases with increasing  $R_\alpha$ .

As the effect of  $R_\alpha$  is clarified, in the following we choose to show the results obtained for  $R_\alpha = 3.2 \text{ \AA}$  (unless otherwise specified). We justify this choice by mentioning that: 1)  $\text{SiO}_4$ -tetrahedra form the backbone of the glass network, and  $3.2 \text{ \AA}$  approximately

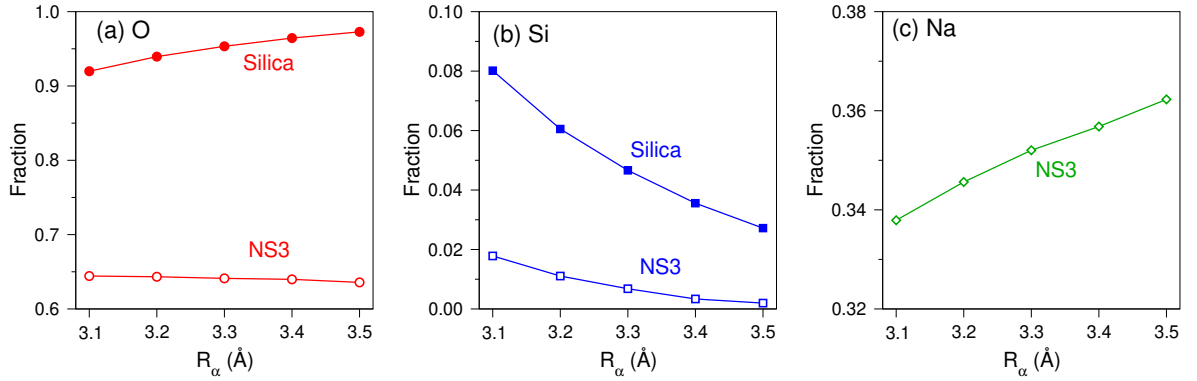


**Figure 4.4:** Influence of  $R_\alpha$  on the estimated surface composition. (a-c) are for O, Si, and Na, respectively. The data are for the melt-formed surfaces at 300 K. The errors are less than the size of the symbols.

equals to the first nearest neighboring distance between two Si atoms; 2) By visual inspection of the constructed surface, this value allows to resolve fine surface features and avoid artificial holes in the constructed surfaces.

In Fig. 4.5(a) we compare firstly the composition between glass surfaces and the bulk. (The bulk data are simply the stoichiometric results). Overall, it can be seen that glass surfaces are rich in Na and O. Notably, the enrichment of Na is more pronounced in the MS. The rationale is that MS is created at a relatively high temperature (in the liquid state) and equilibrate for a relatively long time (1.6 ns). Both factors promote the diffusion of Na from the near-surface region to the surface for the purpose of charge compensation (to the dangling SiO bond) thus reducing surface energy. Also included in the figure are experimental data for FS as measured by LEIS spectroscopy [160]. Also in that study, the enrichment of Na in the surface layer was observed, in agreement with our findings. The behavior of O is somewhat unclear due to the large error bar in the experiments.

Based on the elemental fraction, one can further calculate the per-atom atomic charge  $Q$ , which is given by

$$Q = \sum f_\alpha q_\alpha, \quad (4.1)$$

where  $f_\alpha$  and  $q_\alpha$  are the fraction and charge of atom species  $\alpha$  ( $\alpha \in \text{O, Si, Na}$ ). The charges for Si and Na are the same for all compositions, whereas the charge for O depends on composition in order to ensure charge neutrality (see the discussion in chapter 2 and Table 2.1). Figure 4.5(b) shows the per-atom atomic charge versus Na concentration for the two surfaces. Firstly, one recognizes that the surfaces are both negatively charged, and the negativity is more pronounced for the MS. Secondly, the surfaces become less negative with increasing Na content. For silica, one observes that the MS is much more negative than the FS. However, this difference in charge becomes smaller with the addition of Na, and eventually the two types of surfaces have charges

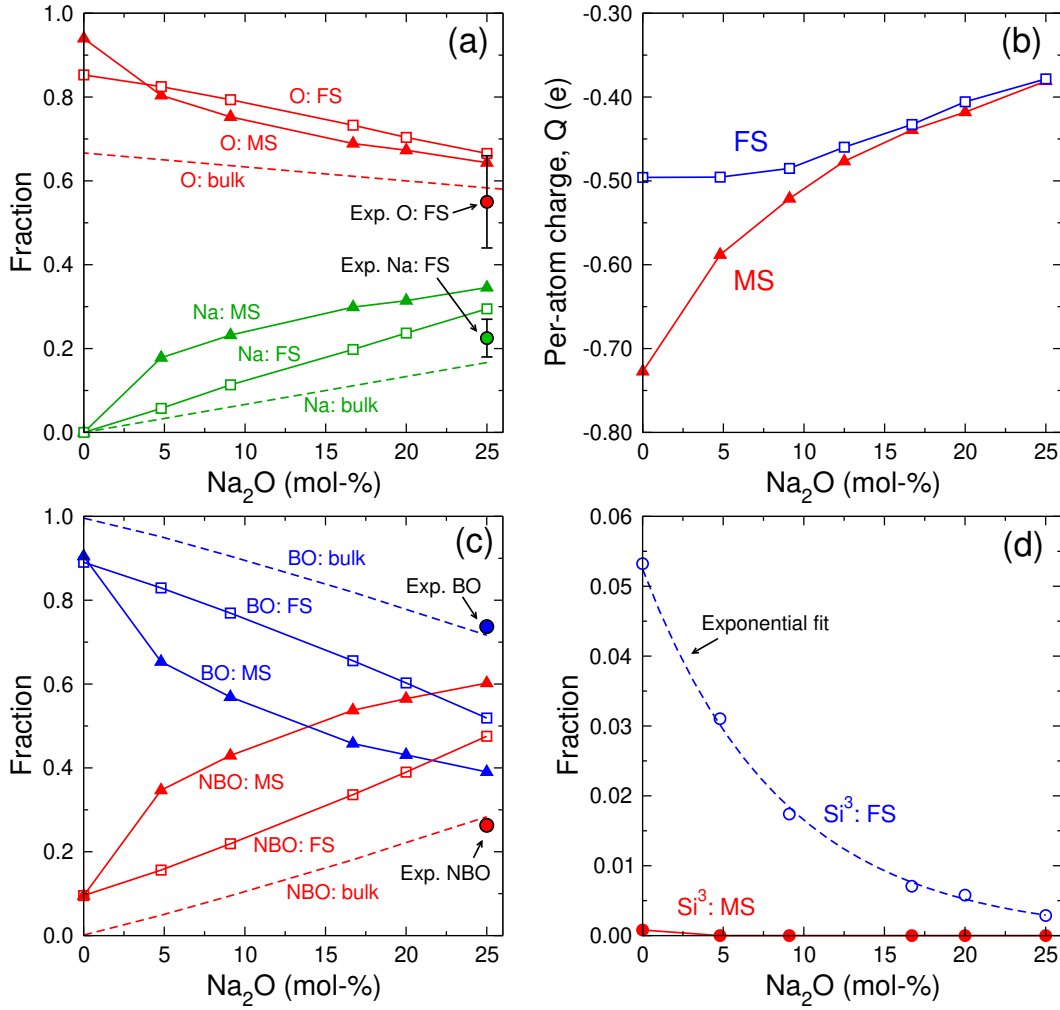


**Figure 4.5:** Surface composition and structure. (a) Fraction of different atomic species on the MS and FS. Experimental data are taken from Almeida *et al.* [160]. (b) Per-atom atomic charge on the surfaces. (c) Fraction of BO and NBO species on the surfaces. (d) Fraction of undercoordinated Si defects. Experimental data are taken from Nesbitt *et al.* [125]. Dashed line in (d) is an exponential fit to the FS data. Error bars are standard deviation and are smaller than the symbol size for all data points.

close to each other when Na<sub>2</sub>O% > 12%.

To characterize the surface atomic structure, we further decomposed O into bridging (BO) and nonbridging oxygen (NBO) and their fractions are depicted in Fig. 4.5(c). Noticeably, both surfaces are rich in NBO, with the MS been more abundant in NBO than the FS. The enrichment of NBO on the surface is directly related to the behavior of Na as shown in panel (a). More Na on the surface results in the breaking of SiOSi linkage thus creating more dangling bonds, i.e., more NBO.

Figure 4.5(d) shows the concentration of the under-coordinated (3-fold) Si, a typical structural defects for FS for the two types of surfaces. We observe that for MS, Si<sup>3+</sup> is nearly zero, whereas FS has a considerable amount of Si<sup>3+</sup> and its concentration strongly

depends on the composition. The presence of  $\text{Si}^3$  on the FS can be explained by the fact that the glass was fractured at room temperature with a very high velocity (see Fig. 3.12). Therefore, the damaged structure during fracture can hardly be healed, leaving some Si under-coordinated. The fact that the fraction of  $\text{Si}^3$  is dependent on the Na concentration demonstrates the critical role of Na in recovering the structural damages during fracture.

Previous experimental studies of trisilicate glass surfaces found that, for elevated temperatures, some atomic species (O and alkali, but not Si) will evaporate from the surface [159]. In our simulations we also monitored the number and fraction of different atomic species during the melt-quench process, and the results are shown in Fig. 4.6. From panel (a), it can be seen that the number of evaporated atoms remains nearly constant at the equilibration temperature (i.e., 2000 K) for the liquid. Upon cooling the evaporated atoms gradually return to the bulk and thus decreasing the density of atoms in the vapor. As temperature is reduced to  $\sim 1400$  K, no atom will leave the surface anymore. This temperature is very close to the glass transition temperature of the current sample, see Fig. 3.2.

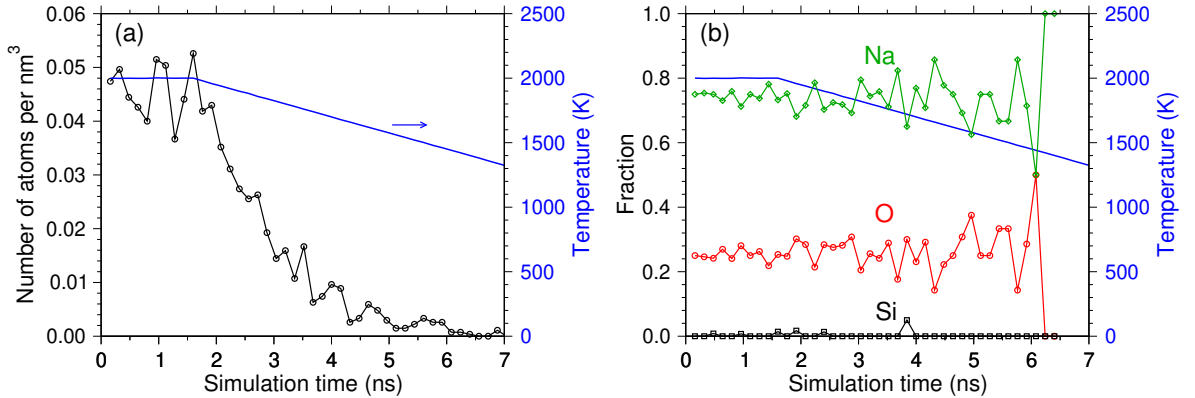


**Figure 4.6:** Total number and fraction of different atomic species in the vapor of NS3 sandwich sample during the melt-quench process.

Figure 4.6(b) shows the fraction of different atomic species in the vapor. In agreement with previous experimental observations by Kelso and Pantano [159], the main constituents of the vapor are O and Na, and the concentration of Si is negligible. Very interestingly, we find that the fraction of Na and O are almost constant in the vapor during the melt-quench process with a ratio of  $\sim 3$  between Na and O. This finding indicates that overall the vapor is a positively charged medium. On the other side, by analyzing the composition of the surface monolayer at room temperature, we found that both the MS and FS are negatively charged. This result means that after all Na in the vapor come back to the surface, it is still negatively charged. Therefore one can conclude that the near-surface region has negative charge throughout the simulation.

This non-neutrality of the surface could be another driving force for the diffusion of Na towards the surface.

Another interesting characterization of glass surface is the depth profiles of composition and structure normal to the glass surface. While most experimental studies have found difficulties in obtaining reliably such information, see for example Ref. [161], the simulations can explore this easily once the surface monolayer has been defined.

In Fig. 4.7(a-b), we compare the depth profiles of various species normal to the MS and FS of glasses. For both silica and NS3, the atomic fraction at  $r = 0$  corresponds to the composition of the surface monolayer, which has also been discussed in Fig. 4.5. For the atoms (by construction) below the surface, the distance  $r$  represents the length of the shortest path from a given atom to any atom on the surface.

Overall, we note that the curves for the FS and MS are very similar. Notable differences are mainly observed at small  $r$ , i.e., near the surface monolayer. For the case of silica, with increasing  $r$ , we notice a big drop of O concentration is accompanied by a huge jump of Si fraction, indicating that Si atoms dominate that atomic layer right below the surface monolayer, in agreement with the findings of previous simulation studies [164, 165]. With further increasing of  $r$ , we find alternating appearance of peaks for O and Si, indicating the heterogeneities (or segregation as noted in a previous experimental study [161]) in composition in the near-surface region. These fluctuations in atomic concentrations decay very quickly and become basically unnoticeable when  $r$  has reached  $\approx 2$  nm. For the case of NS3, panel (b), similar compositional changes as in silica are also observed for Si and O. Interestingly, one observes that the fluctuation of the atomic fraction of Na washes out faster than the network-related species (Si and O). The finding might be related to the high mobility of Na, which helps to disperse the compositional segregation below the surface.

Figures 4.7(c-d) show the per-atom atomic charge versus the distance from the surfaces. One recognizes that the surface monolayer is negatively charged, irrespective of composition and surface type. As  $r$  increases, one finds that alternating peaks/valleys show up, a result that is directly related to the variation of atomic fractions as shown panels (a-b). In addition, we notice that the charge fluctuations of NS3 seem to wash out faster than the ones of silica. This observation is similar to the behavior of the atomic fraction of Na.

Furthermore, in order to understand the decaying behavior of the atomic fraction and charge, we have replotted the data on semi-log (not shown) and log-log scales. It is found that for both the MS and FS, the atomic charge (also the atomic fraction) exhibits power law dependence on the distance from the surface, see panels (e-f). The straight line in panel (e) passes through most of the peaks and thus indicates how fast the charge for silica decays. In order to make a comparison with the decaying of the

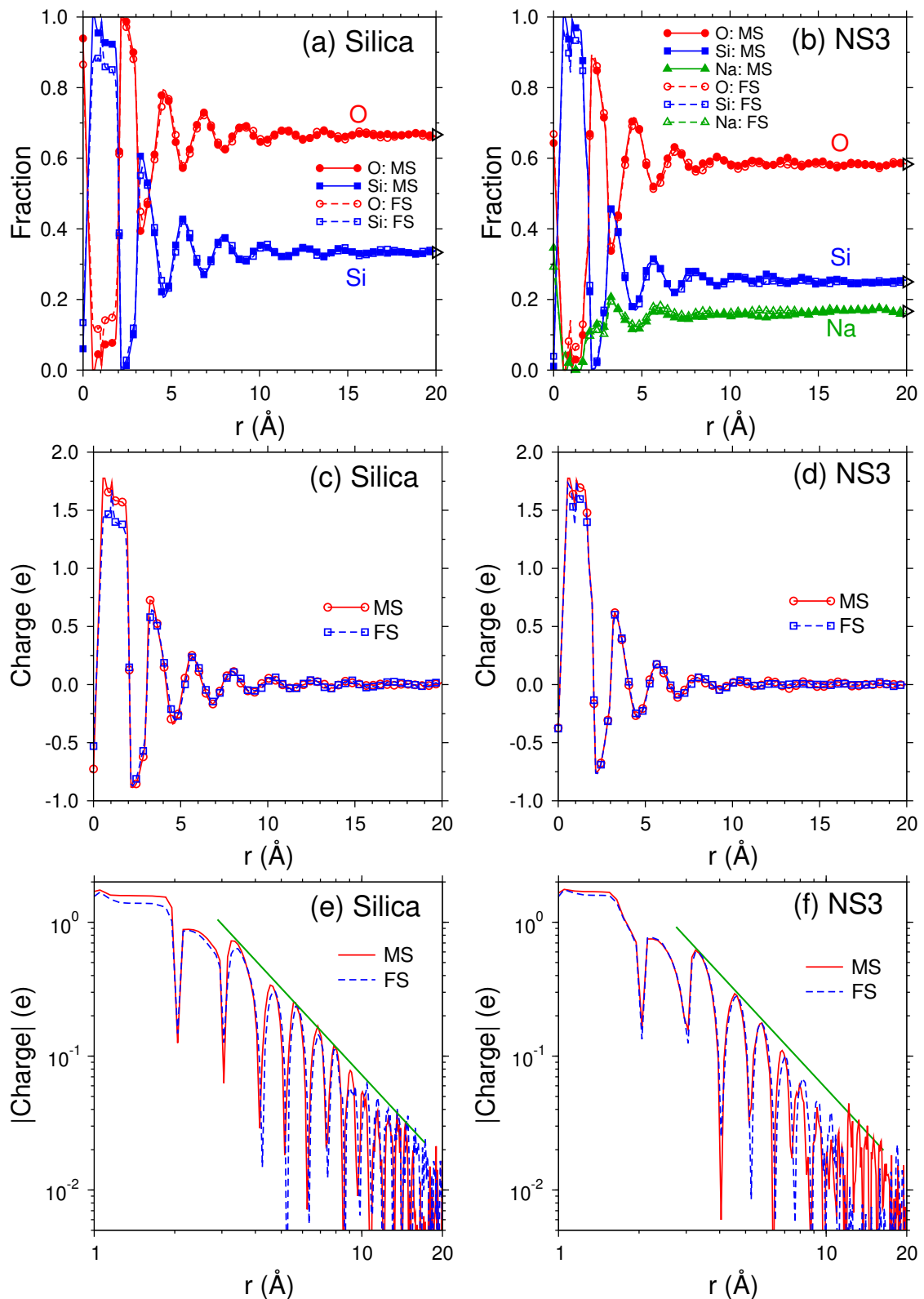


**Figure 4.7:** (a) and (b): Depth profiles of elemental concentrations with respect to the monolayer surfaces of the silica and NS3 glasses, respectively. In practice, the composition at distance  $r$  is the mean of a 1.1 Å thick layer. (c) and (d): Depth profiles of the per-atom atomic charge silica and NS3, respectively. (e) and (f): Log-log plots of the data in (c) and (d), respectively. Note that the atomic charge is now shown in absolute value. The green solid lines in the two graphs are guides to the eye and have the same slope.

charge for NS3, a straight line with the same slope is also shown in panel (f). One notices that the charge for NS3 indeed decays faster than the one for silica as evidenced by the gap between the charge and the straight line for  $6 < r < 11$  Å. The faster decaying of the charge (also the composition) of NS3 can be attributed to the structural role of Na as discussed earlier.

### 4.3 Surface morphology and roughness

The morphology and roughness of glass surface under different environments were studied in the past by using experimental techniques such as AFM. Gupta *et al.* reported a comparative study of MS and FS of silica and E-glass<sup>1</sup> [170]. The authors found that, for the case of silica, the root mean squared (RMS) roughness is  $\approx 0.18$  nm and  $0.34 - 0.40$  nm for the MS and FS, respectively. Note that the glass was broken by fast crack propagation under bending forces. It was also found that the MS of the E-glass is approximately the same as that of silica, whereas the FS of the E-glass is considerably rougher than the one of silica. Wiederhorn *et al.* investigated the roughness of fracture surfaces of silica and soda-lime-silica glass produced by sub-critical crack propagation [48]. It was found that, for silica, the RMS roughness decreases from  $\approx 0.5$  to  $\approx 0.35$  nm with decreasing crack velocity from  $10^{-10}$  to  $10$  m/s. The roughness of soda-lime-silica glass is larger than that of silica and shows also a decreasing trend with increasing crack velocity. A recent study by Pallares *et al.* looked again at the roughness of sub-critical fracture surfaces of oxide glasses [171]. They found that silica surface has a RMS roughness of  $\approx 0.4$  nm, and it weakly depends on the stress intensity factor  $K_I$  (proportional to the loading stress). In contrast, the roughness of a sodium silicate glass (25 wt% Na<sub>2</sub>O) shows a noticeable decreasing tendency with increasing  $K_I$ . All of the above mentioned studies used AFM to acquire surface profiles. In the latter two studies, the sub-critical fracture surfaces are also shown to be self-affine, a scaling property of glass surface that will be discussed in the next section.

Previous studies have attributed the roughness of the MS to the freezing of the capillary waves of the melt at the glass transition temperature [170, 172, 173], whereas the roughness of the FS has been related to the microscopic heterogeneities in structure and mechanical properties [48, 170, 171].

We now discuss of the geometric features of the glass surfaces obtained from our simulations. Figure 4.8 shows the morphology of the two types of glass surfaces at the nanometer scale with atomic resolution. For the MS, upper panels of Fig. 4.8, we observe no significant difference in the morphological feature and roughness between

---

<sup>1</sup>A low alkali glass with a typical nominal composition of SiO<sub>2</sub> 54%, Al<sub>2</sub>O<sub>3</sub> 14%, CaO+MgO 22%, B<sub>2</sub>O<sub>3</sub> 10% and Na<sub>2</sub>O+K<sub>2</sub>O less than 2% (wt%).

silica and NS3 surfaces. In contrast, in lower panels of Fig. 4.8 we notice that the NS3 surface has much larger fluctuations not only in the in-plane direction but also in the out-of-plane direction, i.e., variation of the surface height. These results suggest that the Na-rich NS3 composition has a rougher surface than silica. Therefore, we can conclude from the surface images that the morphology of glass surfaces depends on surface nature (FS or MS) as well as the composition.

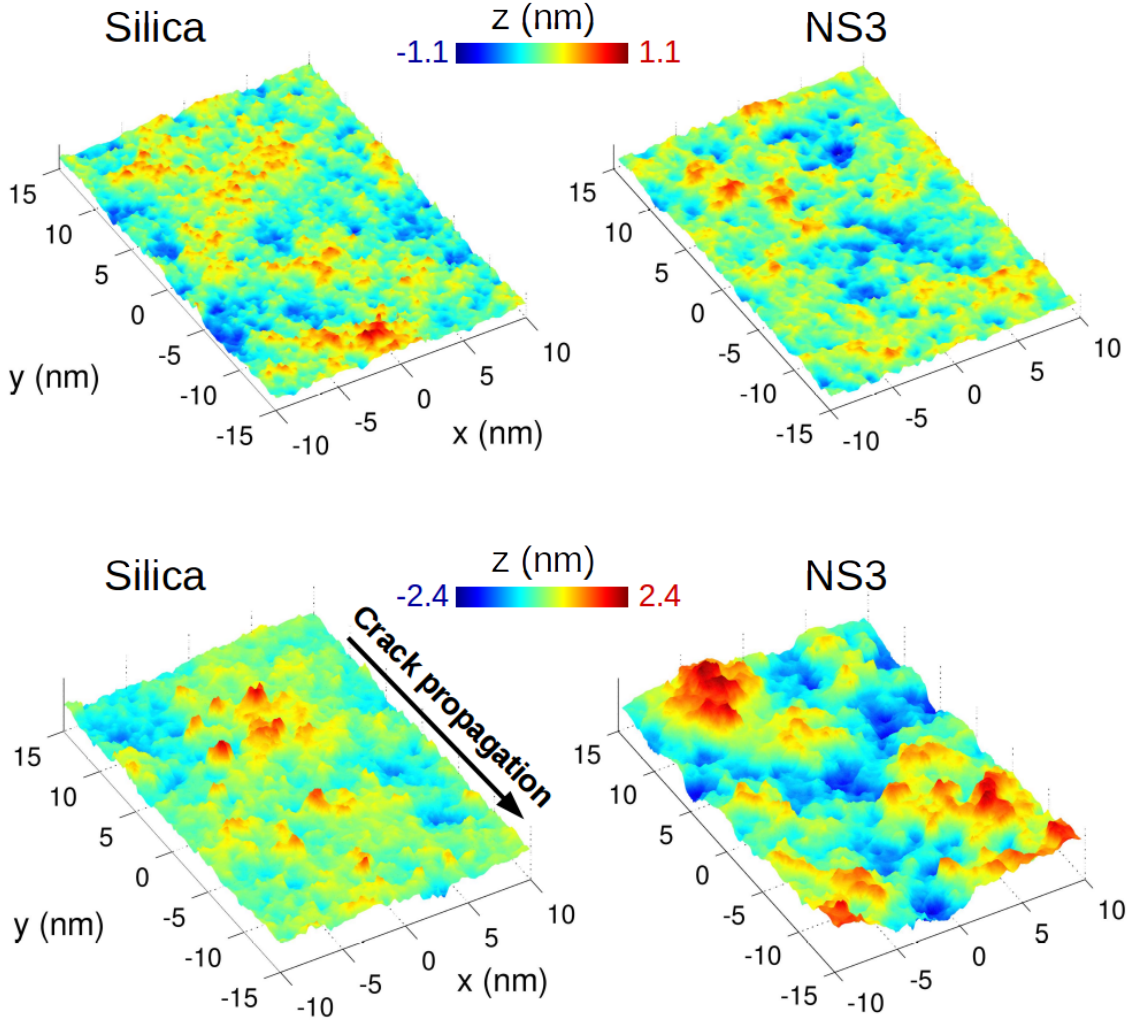


**Figure 4.8:** Surface morphology. Upper panel: Melt-formed surface (MS). Lower panel: Fracture surface (FS). Crack propagates along the negative  $y$ -direction.

A further step to characterize glass surfaces is to quantify their height fluctuation. The first quantity that we will look at is the root mean squared (RMS) roughness of the surface which is defined as

$$\sigma = \sqrt{\langle z^2 \rangle - \langle z \rangle^2}. \quad (4.2)$$

Experimentally, it has been observed that fracture surface becomes rougher as the crack length (i.e., the distance between the fracture origin and the crack tip) increases,



i.e., progressive roughening of fracture surface [7, 174]. With increasing distance from the fracture origin, the fracture surface of brittle solids is generally divided into mirror, mist and hackle regions [7]. The mirror region appears to be smooth when observed by optical microscopy. For silica glass, the mirror region size was estimated to be  $\approx 1$  mm [175], a value that is much larger than the length scales that can be accessed by atomistic simulations. Nevertheless, one would still wonder for our fracture samples whether or not the surface roughness depends on the crack length. For the FS, as illustrated in Fig. 4.9(a), the fracture surface is cut into four equal-sized segments along the direction of crack growth. Figure 4.9(c) shows that, for a given composition, the roughness of each segment (within the error bar) stays around a constant, indicating that the surface roughness is independent of crack length. Also one can notice from panel (c) that surface roughness depends on composition and this will be discussed later. That the simulated surface does not show this roughening feature can be attributed to the relatively small length scale, i.e., several tens of nanometers, that we have explored. These FS are produced at the very initial stage of crack propagation, and are thus belong to the smooth mirror region.

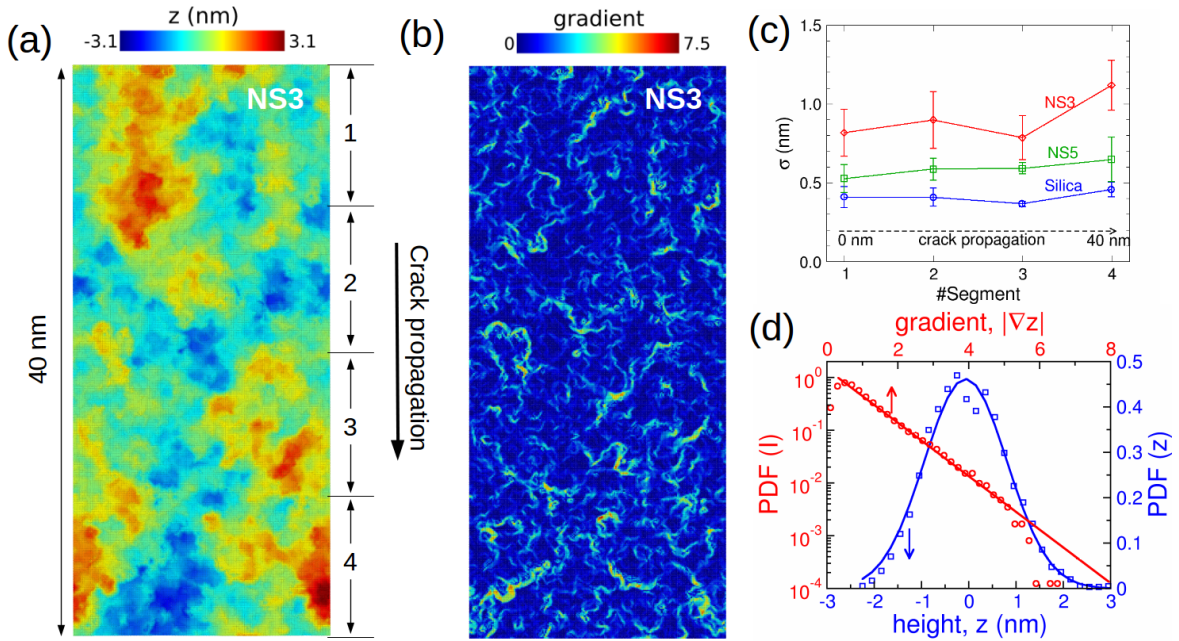


**Figure 4.9:** (a) Height map  $z(x, y)$  of a fracture surface of the NS3 glass. The surface is divided into 4 equal segments along the crack propagation direction. (b) Gradient map  $|\nabla z|$  corresponding to the surface image in (a). (c) RMS roughness of the surface segments along the crack propagation direction. (d) Distributions of surface height  $z$  and gradient  $|\nabla z|$ . The blue line is a Gaussian fit and the red line is an exponential fit for the data up to  $|\nabla z| = 6$ .

In addition, it has been shown experimentally that there is a strong (positive) correlation between surface appearance (and also roughness) with crack velocity [8, 174]. Since we observe no significant changes of surface roughness as fracture proceeds,

we can make the hypothesis that the crack velocity remains almost a constant during fracture. We thus can estimate the crack velocity based on the crack length and fracture time (see Fig. 3.12).

For the FS of the NS3 glass, we show in Fig. 4.9(b) the map of surface height gradient  $|\nabla z|$ , which is calculated via

$$|\nabla z| = \sqrt{\left(\frac{\partial z}{\partial x}\right)^2 + \left(\frac{\partial z}{\partial y}\right)^2}. \quad (4.3)$$

The bright regions of the map indicate the presence of cliffs, i.e., drastic change of surface height. In Fig. 4.9(d) the distributions of surface height  $z$  and gradient amplitude  $|\nabla z|$  are depicted. It can be seen that the distribution of  $z$  looks like a Gaussian, whereas for  $|\nabla z|$  the distribution exhibits at large  $|\nabla z|$  an exponential decay.

We now compare the MS and FS in a more quantitative manner. Firstly from their surface height distributions, Fig. 4.10(a) and (b), one can see that the MS is basically independent of glass composition, whereas the FS exhibits a strong compositional dependence. For the FS, with increasing Na content, the height distribution broadens, suggesting that the surface becomes rougher.

More quantitatively, in Fig. 4.10(c) we show the standard deviation (i.e., RMS roughness) of the height distributions. It can be seen that the roughness of the MS of silica has a relatively small value of  $\sim 0.25$  nm, and shows a slight decreasing trend with increasing Na concentration. For the FS, the RMS roughness is considerably larger and its value increases from  $\sim 0.4$  nm for silica to  $\sim 0.8$  nm for NS3 (25% Na<sub>2</sub>O). Included in the same graph are the experimental data measured by using AFM [170]. One observes that the surfaces generated in our simulations seem rougher but still comparable to the experimental values. The most probable reason that accounts for the differences is the resolution of the acquired surface profiles. This factor affects also the surface scaling property of the surface as we will see in the next section.

Very interesting is the finding that the roughness of the MS of silica is in excellent agreement with the intrinsic roughness predicted by frozen capillary waves of the melt at the glass transition temperature [170, 172]. According to this theory, the RMS roughness of a pristine melt-formed surface can be expressed as

$$\sigma \approx \sqrt{\frac{k_B T_g}{\gamma_0}}, \quad (4.4)$$

where  $k_B$  is Boltzmann's constant and  $\gamma_0$  is the surface tension at the glass transition temperature  $T_g$ . Plugging in the experimental data of  $T_g \approx 1500$  K and  $\gamma_0 \approx 0.29$  J/m<sup>2</sup> [176], one obtains a roughness value of  $\approx 0.26$  nm for the MS of silica [170]. The good agreement between our result and the theoretical prediction indicates that

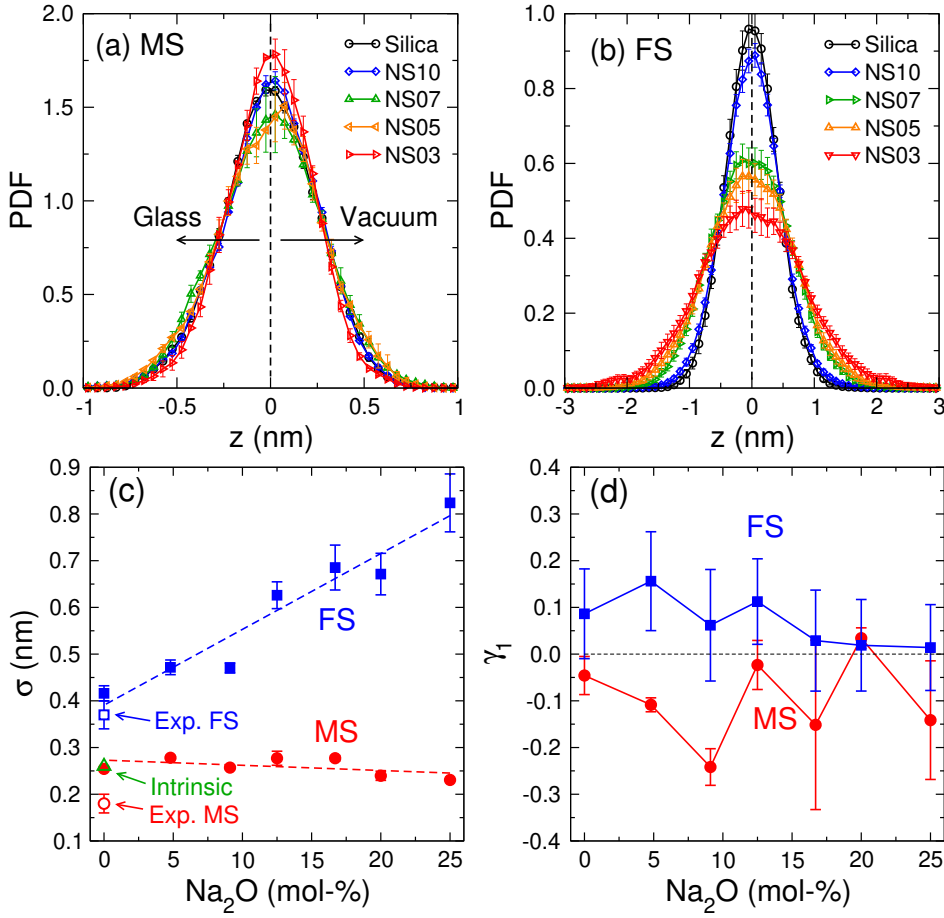


**Figure 4.10:** (a) and (b): Surface height distribution as a function of composition. The mean surface height  $\langle z \rangle$  is equal to zero. The surface side with  $z > 0$  is facing the vacuum, while the side with  $z < 0$  is facing the bulk. (c) RMS roughness of the surfaces. The dashed lines are linear fits to the data sets. Experimental data were obtained for AFM images with size  $1 \mu\text{m} \times 1 \mu\text{m}$  [170]. The triangle corresponds to the intrinsic roughness of silica surface as estimated from the theory of frozen capillary waves. (d) Skewness of the surface height distribution.

the assumption that capillary waves freeze at the  $T_g$  is a reasonable approximation to account for the roughness of pristine melt-formed glass surface. We note also that all the quantitative results in panel (c) are consistent with the observation from the surface images. The distinct compositional dependence of the MS and FS implies that their formation are due to different mechanisms. We will discuss this aspect in more details later.

Another feature of great interest to explore is the symmetric property of the surfaces. In other words, the question to be answered here is whether or not the two sides of the surface (one side facing the vacuum and another side facing the glass) are statistically the same. For this we consider the skewness,  $\gamma_1$ , of surface height

distribution

$$\gamma_1 = \frac{\langle z^3 \rangle}{\sigma^3}. \quad (4.5)$$

Skewness is a measure of the asymmetry of a probability distribution. For a unimodal distribution (e.g., normal distribution),  $\gamma_1 < 0$  commonly indicates that the tail is on the left side of the distribution, and  $\gamma_1 > 0$  indicates that the tail is on the right. The parameter  $\gamma_1$  for the two types of surfaces are shown in Fig. 4.10(d). It can be seen that, for the FS,  $\gamma_1 > 0$  and for MS  $\gamma_1 < 0$  and not clear compositional dependence can be inferred. This results indicate that the MS and FS have different asymmetric property. For the MS, the tail of surface height distribution is on the glass side, implying that more deep holes present on the melt-formed surface. For the FS, the distribution tail is on the vacuum side, indicating more high peaks appear on the fracture surface. Again, these asymmetric properties of the surfaces are related to their mechanisms of formation.

## 4.4 On the nature of glass surfaces: Scaling properties

The RMS roughness  $\sigma$  discussed above is a height parameter for characterizing the surface. More insights can be obtained by considering also the height-height correlation, which is defined as [177]

$$\Delta z(r) = \sqrt{\langle [z(r+x) - z(r)]^2 \rangle_x} \quad (4.6)$$

in one dimension, where  $\Delta z$  is the height difference between two points separated by a distance  $r$ , and  $x$  denotes the direction of the evaluated line profile. With this quantity one can also explore the surface height correlation in different directions.

Since the pioneer work by Mandelbrot *et al.* [178], it has been reported for a wide range of materials that fracture surface exhibits self-affine fractal property, i.e.,

$$\Delta z \propto r^\zeta, \quad (4.7)$$

where  $\zeta$  is called roughness exponent. Therefore for a self-affine surface one would thus expect a power law dependence of  $\Delta z$  on  $r$ . For melt-formed surface, the theory of capillary wave predicts a logarithmic dependence of  $(\Delta z)^2$  on  $r$  [172, 173], i.e.,

$$(\Delta z)^2 = \frac{k_B T}{\pi \gamma} \ln \left( \frac{r}{\lambda_m} \right), \quad (4.8)$$

where  $k_B$  is Boltzmann's constant,  $\gamma$  is the surface tension and  $\lambda_m$  denotes the lower spatial cutoff of the capillary wave. For silicate glasses,  $\lambda_m$  is usually taken as the length scale of a  $[\text{SiO}_4]$  tetrahedron which is around 0.5 nm.

Figures 4.11(a-b) show the 1D height-height correlation function for the MS and FS, respectively. For the MS, one notices that the two curves corresponding to two different directions collapse onto each other very well, indicating that the MS is isotropic. One can also notice that the curves for silica and NS3 are close to each other, indicating that they have nearly the same roughness. In contrast to this, for the case of the FS, the curves for the two orthogonal directions show a pronounced difference, indicating that the FS is, as expected, anisotropic. The curve for  $x$ -direction (i.e., parallel to the crack front) is not only higher but also steeper than the one for  $y$ -direction (direction of the crack growth), suggesting that the direction parallel to crack front is rougher than the direction of crack propagation. These results are consistent with the finding of an experimental study of the fracture surface of silica glass [179]. From panel (b), one recognizes that the curves for NS3 are much higher than the ones for silica, in accordance with the finding that the FS becomes rougher with the addition of Na.

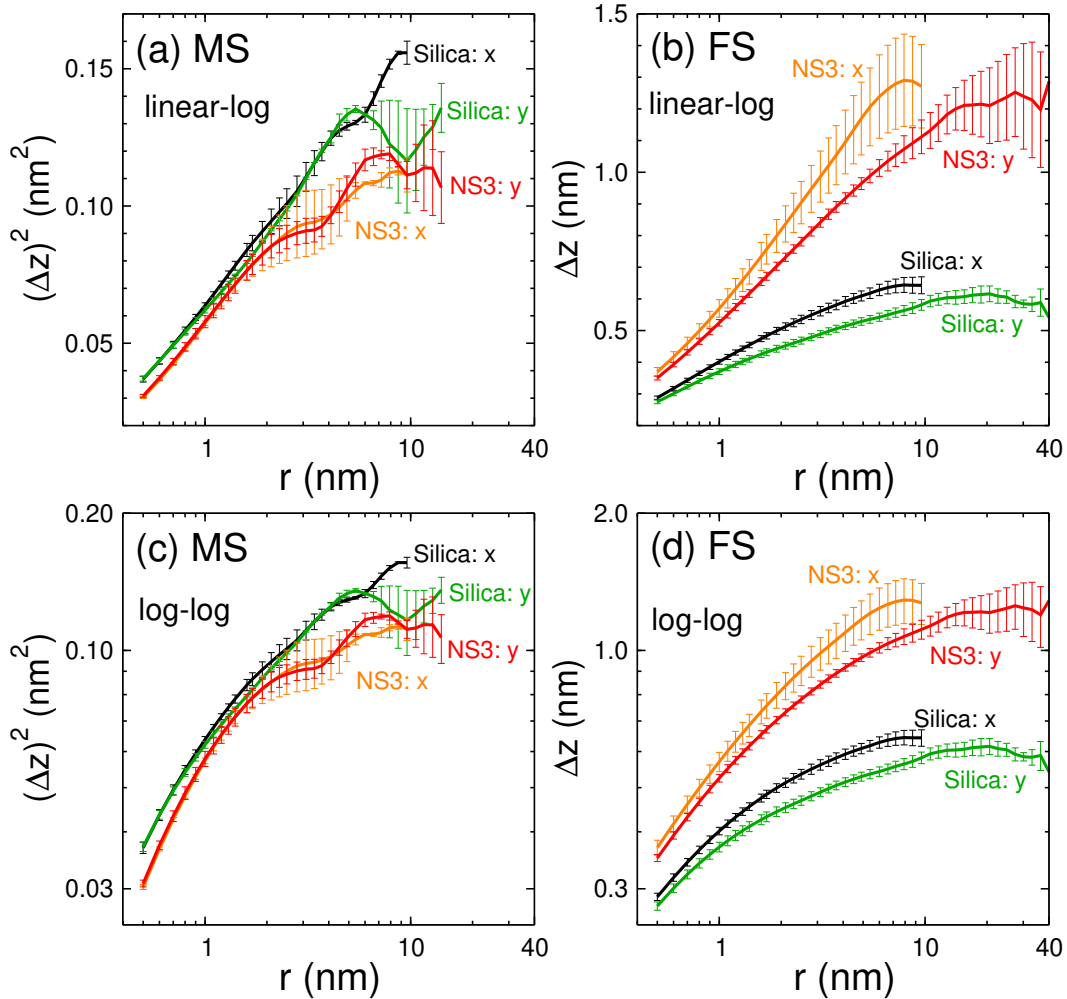


**Figure 4.11:** (a) and (b): Surface height correlation function (linear-log scale) for the MS (a) and FS (b). (c) and (d): Re-plotting the data in (a) and (b) but on log-log scale. Note that the ordinates for the left and right panels are not the same. The labels  $x$  and  $y$  correspond to the direction parallel to the crack front and the direction of crack growth, respectively.

For the scaling property of surfaces, we note that for the MS,  $(\Delta z)^2$  depends logarithmically on  $r$ . The exception is for large  $r$  where the data is affected by insufficient statistics. The observed logarithmic dependence is compatible with the prediction of the frozen capillary wave theory, and agrees with the findings of experimental work [170, 173]. For the FS, we find that the dependence of  $\Delta z$  on  $r$  can be described quite well with a logarithmic scaling (panel(b)) whereas power law scaling does not work (panel (d)), indicating that there is no self-affine behavior at the length scales that we investigated. Our conclusion disagree with previous experimental results which have given evidence that the FS exhibits self-affine property at the nanometer scale with the roughness exponent  $\zeta \sim 0.8$  [171, 179]. A possible explanation to account for this discrepancy will be given a bit later.

Assuming the validity of the observed logarithmic scaling behavior of the surfaces, we then can estimate the rate at which  $\Delta z$  (or  $(\Delta z)^2$ ) changes with  $r$ , i.e., the slope parameter of the height-correlation function. We use expressions  $\Delta z = a \cdot \ln(r/b)$  and  $(\Delta z)^2 = a \cdot \ln(r/b)$  to fit in the range  $r < 1$  nm for the MS and FS, respectively. The two fitting parameters  $a$  and  $b$  are plotted in Fig. 4.12. The slope parameter of the MS, panel (a), depends neither on the composition nor the direction. In contrast, for the FS, panel (b), one sees that  $a$  tends to increase with more Na added. One can also notice that the values for the  $x$ -direction are higher than the  $y$ -direction ones. The parameter  $b$ , panels (c) and (d), shows qualitatively similar compositional and direction dependence as the slope parameter  $a$ . (Panel (c) seems to show an increasing trend of  $b$  as Na concentration increases.)

To understand the difference between our simulation results and the experimental findings, we have investigated the effect of the spatial resolution<sup>2</sup> on the scaling property. Schmittbuhl *et al.* [180] found that local filters may introduce complicated biases in the self-affine analysis. For example, for the measurement of the surface by a mechanical tip, the finite size of the needle may result in distortion in the recorded geometry of the surface. Note that this drawback can not be remedied by just taking more points in the measurement. These artifacts inherent in the experimental data acquisition will inevitably induce biases in the characterization of the surface. Therefore, one would expect that the experimentally measured surface profile loses parts of the geometric features of the real surface and hence may look smoother.

The aforementioned effect is illustrated in Fig. 4.13 for the case of silica. It can be seen that if the spatial resolution is decreased, i.e., more smoothing is applied to the original surface, the curves shift downward, meaning that the surface becomes smoother. Additionally, one also can observe that the slope changes at small  $r$ . The

---

<sup>2</sup>Spatial resolution corresponds to how many spatial details can be captured by the measurement, rather than the number of pixels in an image.

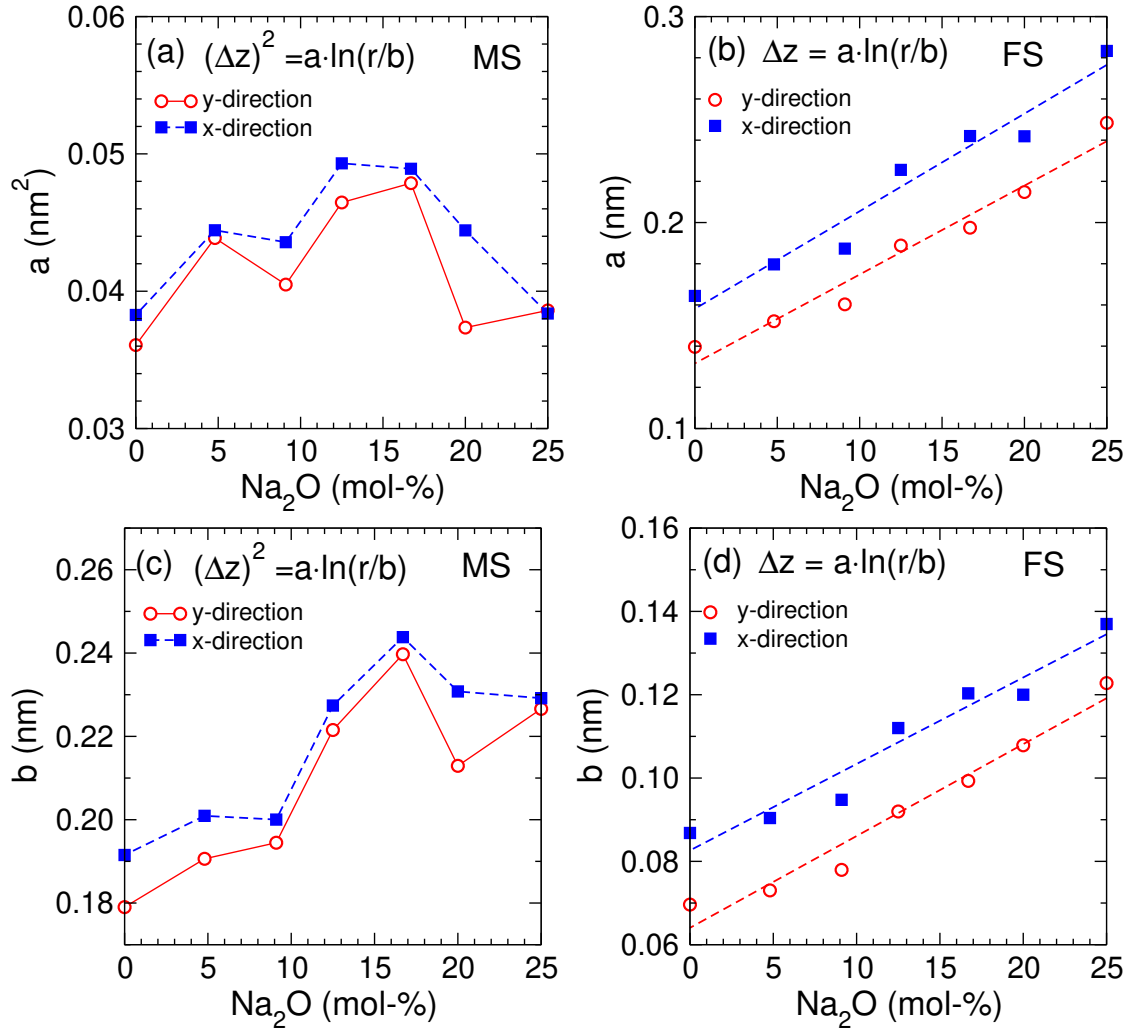


**Figure 4.12:** Parameters of the logarithmic fit to the height correlation function of the surfaces. (a) and (c) are for the MS, and (b) and (d) are for the FS. The fitting was performed only for the data at  $r < 1$  nm, see Fig. 4.11. The expressions used for the fitting are shown in the graphs as well.  $x$  and  $y$  corresponds to the direction parallel to the crack front and the direction of crack growth, respectively. The lines in (d) are linear fits to the data sets.

power law scaling gradually shows up with more smoothing. Eventually the exponent of the power law behavior saturates at a value of  $\approx 0.8$ , which is exactly the roughness exponent reported experimentally for these length scales [171, 179]. Our results also show that a smoothing length scale of 2.8 nm (in radius) can reproduce very well the measurements from experiments, see Fig. 4.13(a). Therefore, we conjecture that the self-affine properties found in experiments on glass surface at the nanometer scale could be an artifact of the insufficient resolution in their measurements. Our results based on the geometric surface with atomic resolution suggest that fracture surface exhibits logarithmic scaling at the nanoscale, thus it can not be treated as a self-affine object.

It is worth noting that previous theoretical studies have already documented that

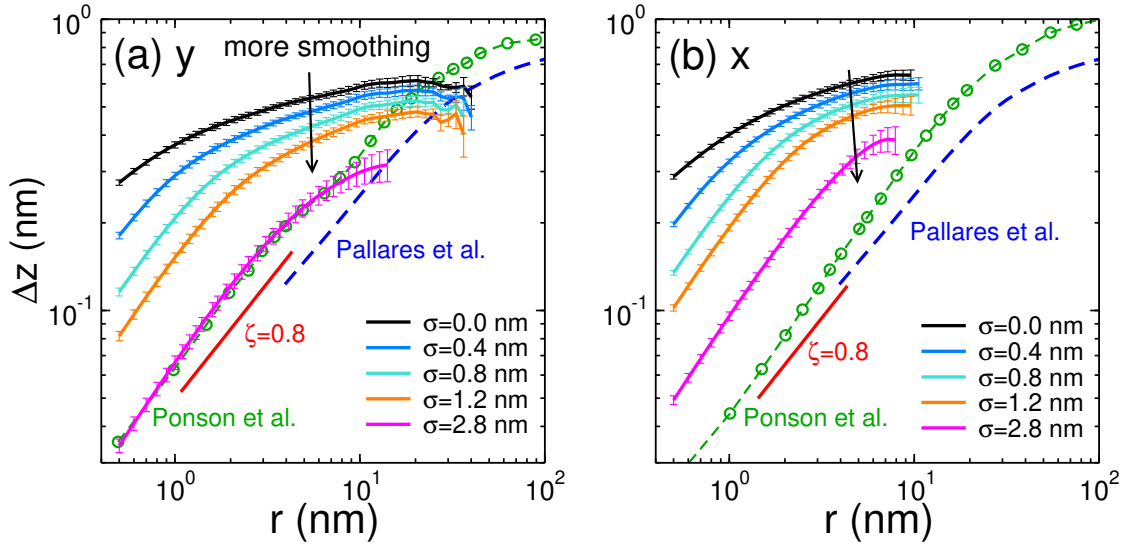


**Figure 4.13:** Evaluating the smoothing effect on the surface height correlation for the FS of silica glass. Panels (a) and (b) are for the direction of crack growth and the direction parallel to the crack front, respectively. The original surface has a resolution of 0.1 nm. A 2D Gaussian filter was applied to smooth the surface. The smoothing operation was applied up to a distance of  $2\sigma$  from the central grid point. The curves labeled  $\sigma = 0$  correspond to the unsmoothed (original) data. Also included are experimental data from AFM measurements of fracture surfaces produced by sub-critical crack propagation [171, 179].

for heterogeneous media, the fracture surface due to mode I (tensile) loading is only logarithmically rough rather than a power law of the length scale [181, 182]. However, these studies are only for simplified model systems. For realistic brittle materials such as silicate glasses, to our knowledge, logarithmic scaling of the fracture surface has not been reported before. Finally, we note that we do not exclude the self-affine behavior of glass surface at larger length scales, but the effect of resolution is certainly something that should be checked.

In chapter 3 we have shown that strain rate  $\dot{\epsilon}$  has a pronounced influence on the failure point of the glass under tension and also on the crack velocity. However, the fracture behavior, i.e., after the failure point, depends only weakly on  $\dot{\epsilon}$  once  $\dot{\epsilon} \leq 0.5$  /ns. In Fig. 4.14 we show the influence of strain rate on the geometrical properties of the FS of silica. Panel (a) shows that decreasing  $\dot{\epsilon}$  from 0.5 /ns to 0.05 /ns (a factor of ten) only results in a  $\approx 4\%$  decrease of the surface roughness. That is to say, the surface roughness is basically converged when  $\dot{\epsilon} \leq 0.5$  /ns. Panel (b) illustrates that the variation in strain rate does not change the logarithmic dependence of  $\Delta z$  on  $r$ . This result seems to suggest that the scaling property that we have found for the fracture surfaces is independent of the applied strain rate.



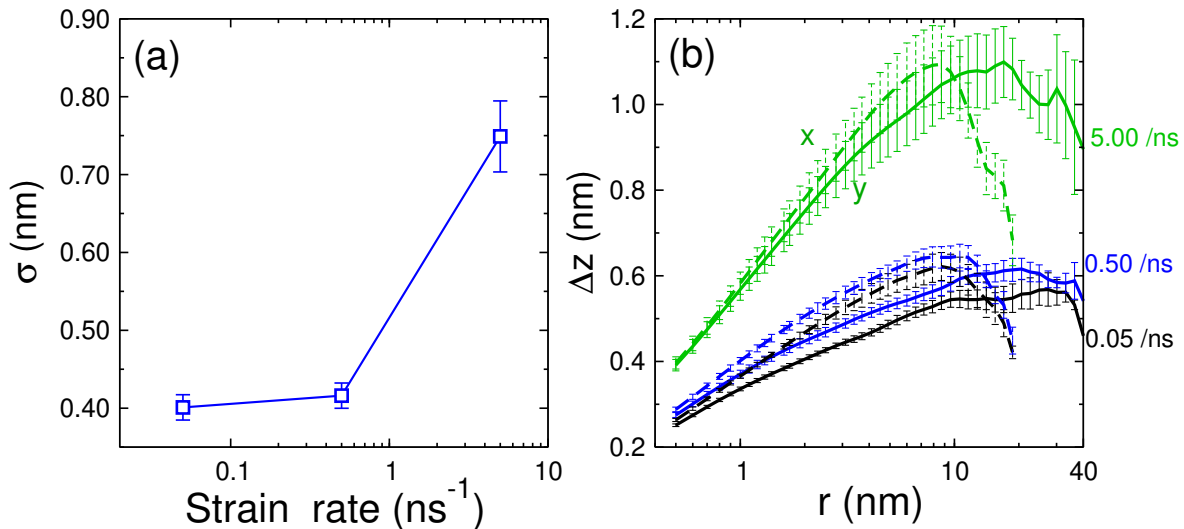


**Figure 4.14:** Influence of strain rate on the roughness and scaling property of the fracture surface for the case of silica. The data are plotted on linear-log scale. In panel (b),  $x$  and  $y$  correspond to the direction parallel to the crack front (dashed lines) and the direction of crack growth (solid lines), respectively.

## 4.5 Temperature dependence of surface properties

So far the surface properties have only been discussed at room temperature (300 K in our simulations). However, the effect of temperature on the surface is also of great interest. In Fig. 4.15 we show such results regarding the influence of temperature on the properties of glass surface. The upper and lower panels show the results for the MS and FS, respectively.

For the MS, panel (a) shows that temperature has a strong effect on the roughness of NS3 surface, i.e.,  $\sigma$  increases with increasing  $T$ , whereas silica is barely affected. In panel (b), it can be seen that the slope of the small-scale scaling region shows a similar  $T$ -dependence. One can also recognize from panel (a) and (b) that the temperature effect is more pronounced for NS3 than for silica, particularly when  $T \geq T_g$ . This result might be related to the fact that NS3 has a more flexible structure due to the presence of Na.

For the case of FS, within the  $T$ -range explored, no noticeable  $T$ -dependence of the surface roughness can be found, independent of the composition, panel (d). The same conclusion can be made for the scaling properties of the surface, panel (e). Therefore, we conclude that at temperatures well below  $T_g$ , fracture surface is insensitive to temperature, but instead strongly depend on the composition and structure of the glass.

Figures. 4.15 (c) and (e) show the skewness of the surfaces at various temperatures.

It can be seen that, for the MS,  $\gamma_1 < 0$  holds for all temperatures, whereas for the FS one finds always  $\gamma_1 > 0$ . These results clearly show that the asymmetric property of the surfaces discussed earlier (Fig. 4.10) is independent of  $T$ .

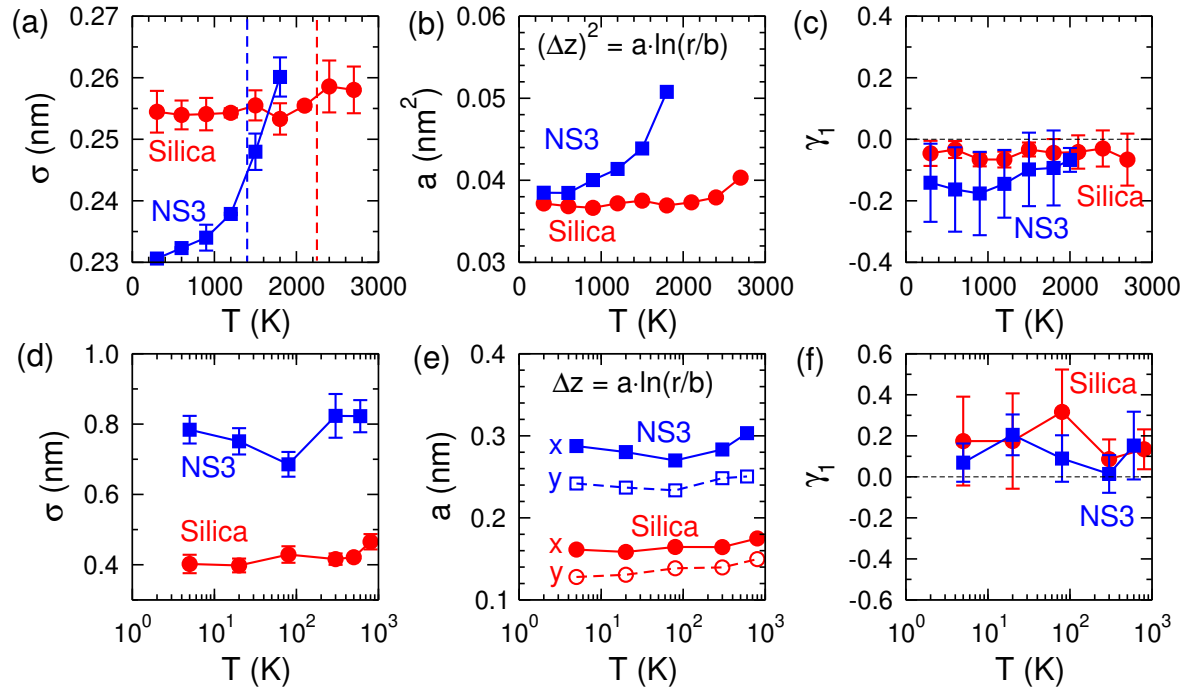


**Figure 4.15:** Effect of temperature on surface properties. Upper and lower panels are for the MS and FS, respectively. (a) and (d):  $T$ –dependence of surface roughness. Vertical dashed lines in (a) indicates the  $T_g$  of the silica and NS3 glasses (also shown in Fig. 3.2). (b) and (e): Slope parameters as estimated from the logarithmic scaling behavior of height correlation function at  $r < 1$  nm. (c) and (f): The skewness indicates the asymmetric property of the surfaces.

## 4.6 Summary

We have presented in this chapter a comparative study of the nanoscale features of the melt-formed surface (MS) and fracture surface (FS) of soda-silicate glasses. The adopted geometric method which is based on the Delaunay triangulation was shown to be able to capture the real features of the glass surfaces with atomic resolution.

We find that both the MS and FS are enriched in Na in comparison with the bulk composition. However, the enrichment of Na is more pronounced in the MS. Additionally, we find that the MS is more abundant in NBO than the FS, which is directly related to the behavior of Na. It is also found that the FS has a non-negligible amount of under coordinated Si,  $\text{Si}^3$ , whereas for MS the concentration of  $\text{Si}^3$  is nearly zero. The differences between the MS and FS can be attributed to their production

history: The MS is created at the liquid state and better relaxed, whereas FS forms as a consequence of nanoscale structural/mechanical heterogeneities. It is also found that both the MS and FS are negatively charged, which could be a driving force for the diffusion of Na from the interior part of the glass to the surface. The depth profile results show that the fluctuations in composition and charge decay quickly with increasing distance  $r$  from the surface, reaching values of the bulk ones when  $r \gtrsim 2$  nm.

Furthermore, we have investigated the morphology and roughness of the two types of surfaces. We find that the MS is relatively smooth and isotropic. Composition has little influence on its roughness. The surface height-height correlation function of the MS exhibits  $\Delta z^2 \propto \ln(r)$ , a result that is compatible with the frozen capillary waves mechanisms. In contrast, the FS is relatively rough and exhibits anisotropy. With increasing Na concentration, the roughness of the MS increases from  $\approx 0.4$  for silica to  $\approx 0.8$  nm for the NS3 glass. In addition, our results show for the FS a logarithmic dependence of  $\Delta z$  on  $r$ . These results indicate that, unlike what was claimed experimentally, fractal description does not work at the nanoscale ( $\lesssim 10$  nm). Furthermore, we have investigated the effect of spatial resolution on the surface scaling property and find that the experimental measurements might be biased by the insufficient resolution on the nano- and Ångstrom scales. Our results, based on geometric surfaces with atomic resolution, suggest that both the MS and FS exhibit logarithmic scaling at the nanoscale.

Finally we note that temperature also plays an important role in determining the properties of glass surfaces. For the MS, we find that surface roughness increases with increasing  $T$ , and this effect is much more pronounced at  $T > T_g$  and for Na-rich glasses. For the FS, no noticeable  $T$ -dependence was found within the  $T$ -range that we have explored, i.e.,  $T < 1000$  K. Also interesting is the finding that the asymmetric properties of the MS and FS are independent of temperature. Therefore, this property can be treated as an intrinsic property of a given type of surface and is mainly related to the production history.

# Chapter 5

## Surfaces of sodium silicate glasses: First principles calculations

This chapter presents the results obtained by using *ab initio* molecular dynamics (AIMD) simulations within the framework of density functional theory (DFT). The main objective is to investigate the surface properties and the nature of chemical bonding in sodium silicate glasses. ( Note that the latter is inaccessible by using classical simulation). We will first introduce the models and simulation procedures for preparing the silica and sodium silicate samples with free surfaces (sandwich geometry) in the liquid and glassy states. Following that, we present results concerning the structural, dynamical, vibrational and electronic properties of the samples. We will focus mainly on the surface layer but the results for the interior (bulk-like) layer and bulk glasses will also be shown for comparison. This work provides information regarding the vibrational and electronic signatures of some structural units such as two-membered ring that are more abundant on the surface. The chemical bonding analysis shed some light on bond strength and may help to understand the fracture of silicate glasses.

### 5.1 Models and simulation details

We performed AIMD simulations for three silica-based compositions, namely pure silica ( $\text{SiO}_2$ ),  $\text{Na}_2\text{O}-5\text{SiO}_2$  (NS5) and  $\text{Na}_2\text{O}-3\text{SiO}_2$  (NS3). A schematic representation of the simulation procedure is shown in Fig. 5.1. Some relevant simulation parameters are summarized in Table 5.1.

For each sample, we placed randomly around 400 atoms into a cubic simulation box with periodic boundary conditions applied. The side length of the simulation box corresponds to the experimental density of the glass at room temperature [112], see Table 5.1. The bulk samples were firstly melted and equilibrated at a high temperature

$T_0$ . Following that, a vacuum layer was inserted at the top and bottom of the bulk sample. The thickness of the vacuum (two sides combined) was chosen to be  $\approx 18 \text{ \AA}$ , a value that ensures that the surfaces from the two sides do not interact with each other. The new configuration thus has a sandwich (or slab) geometry: The middle part is bulk-like and the two ends are empty spaces.

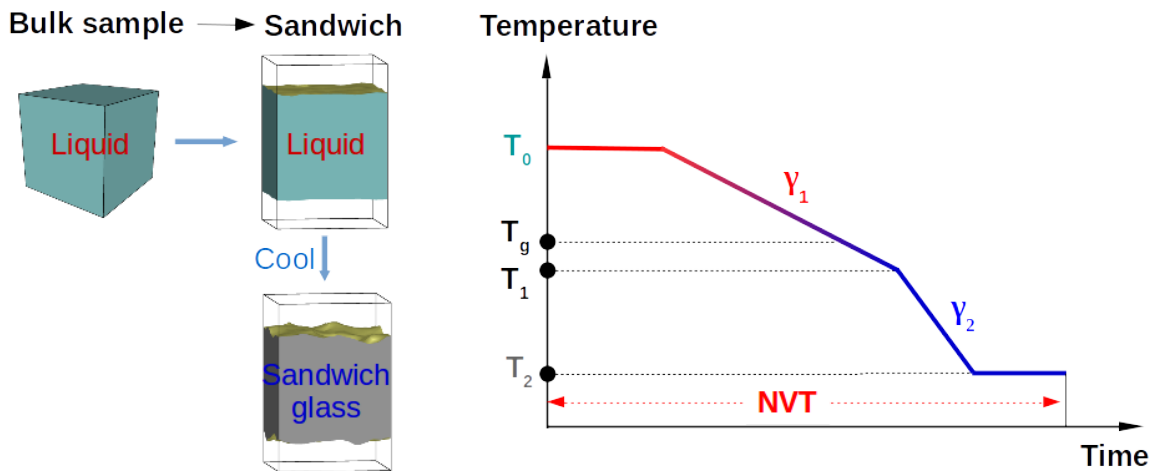


**Figure 5.1:** Schematic drawing of the simulation procedures. See the main text for the definitions of the various temperatures and cooling rates.

	#atoms	Na <sub>2</sub> O-mole%	$L_{\text{bulk}}$ ( $\text{\AA}$ )	$\rho_{\text{bulk}}$ (g/cm <sup>3</sup> )	$T_0$ (K)	$T_1$ (K)
SiO <sub>2</sub>	384	0.0	17.96	2.20	3600	2500
NS5	414	16.7	18.07	2.35	3000	2000
NS3	396	25.0	17.62	2.43	2200	1500

**Table 5.1:** Simulation parameters. The side length ( $L_{\text{bulk}}$ ) of the initial cubic simulation box corresponds to the experimental glass density ( $\rho_{\text{bulk}}$ ) at room temperature. See the main text for the definitions of  $T_0$  and  $T_1$ .

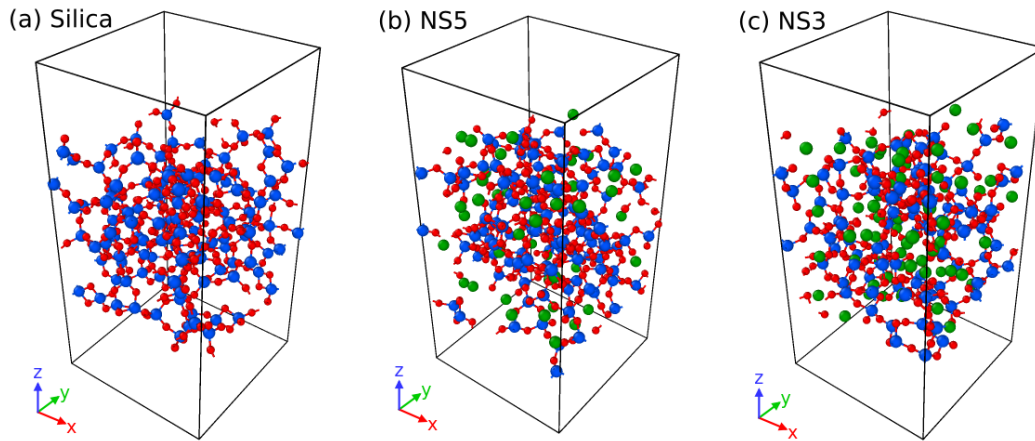
Starting from this sandwich sample, we carried out the conventional melt-and-quench procedure. We note that, in contrast to the simulation of bulk sample, special attention is needed for the equilibration of the sandwich sample at high temperature: On the one hand, the equilibrating temperature should be high enough to allow an adequate diffusion of the atoms within a reasonable amount of computer time. (AIMD is orders of magnitude more computationally expensive than classical MD for simulations with comparable system size and time span, see a more detailed discussion in Chapter 1). On the other hand, a too high temperature may result in a large expansion of the bulk-like region and eventually the connection of the two surfaces. Therefore, we have chosen 3600 K, 3000 K, and 2200 K as the equilibration temperature  $T_0$  for silica, NS5, and NS3, respectively.

The samples were maintained at  $T_0$  for more than 10 ps to allow the reconstruction of the surfaces. After equilibration, the samples were firstly quenched down to an intermediate temperature  $T_1$  using a nominal cooling rate of  $5 \times 10^{14}$  K/s ( $\gamma_1$ ), and then to 300 K using a faster cooling rate of  $2 \times 10^{15}$  K/s ( $\gamma_2$ ).  $T_1$  was chosen to be 2500 K, 2000 K, and 1500 K for silica, NS5, and NS3 respectively. We note that these temperatures are below the glass transition temperature  $T_g$  of the simulated glasses due to the use of fast cooling rates. Finally the samples were relaxed at  $T_2 = 300$  K for another 3 ps. The whole simulation was carried out using the  $NVT$  ensemble and two independent samples were generated for each composition. For the analysis of the properties of the samples, the initial 4 ps and 0.5 ps trajectories were discarded for the runs at  $T_0$  and 300 K, respectively.

The AIMD simulations were performed by using the Vienna *ab initio* package (VASP) [183, 184]. The electronic structure has been calculated by means of the Kohn-Sham (KS) formulation of the density functional theory (DFT) [93, 185] using the generalized gradient approximation (GGA) and the PBEsol functional [97, 99]. The KS orbitals were expanded in a plane-wave basis at the  $\Gamma$  point and the electron-ion interaction was described within the projector-augmented-wave formalism [186, 187]. The plane-wave basis set contained components with energies up to 600 eV. For solving the KS equations, the residual minimization method-direct inversion was used in the iterative space, and the electronic convergence criterion was fixed at  $5 \times 10^{-7}$  eV. The time step was chosen to be 1 fs and a Nosé thermostat [86] was applied to control the temperature in the canonical ensemble. We note that the simulation parameters chosen here are similar to the setup of previous *ab initio* studies of silicate liquids and glasses [83, 84, 188, 189], which have demonstrated that the simulated properties of the liquid and glass compare very well with experimental results.

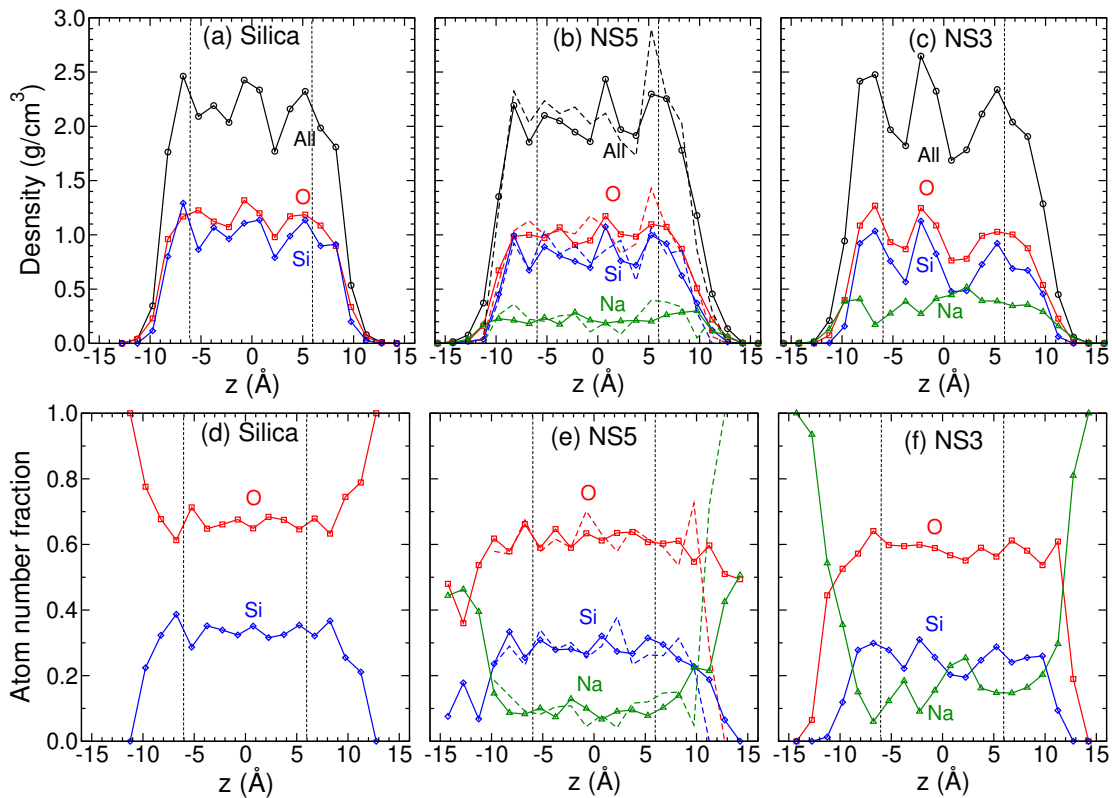
## 5.2 Defining the surface region

Figure 5.2 shows the atomic structure of the three glasses at 300 K. The sandwich geometry of the sample is characterized by a glass network in the middle and vacuum on the two sides. To define the surface and interior regions, we investigate first the atomic distribution of the liquid and glass samples along the direction perpendicular to the surfaces, i.e., the  $z$ -direction, Fig. 5.3. The center of mass of the sample is considered as the origin of the coordinate system. Thus, the plane with  $z = 0$  cuts the sample into two parts with the same mass. For the liquids, one recognizes that the mass density distribution of all three compositions show a relatively flat region for  $|z| \leq 6$  Å, with density around 2.2 g/cm<sup>3</sup>, 2.3 g/cm<sup>3</sup>, 2.4 g/cm<sup>3</sup> for silica, NS5 and NS3, respectively (solid lines in panels (a-c)). These values correspond well to their



**Figure 5.2:** Snapshots of the atomic structure of the three glasses at 300 K. Si, O, and Na atoms are balls in blue, red, and green, respectively. The sticks represent Si-O bonds with bond length smaller than 2 Å.

bulk densities (see Table 5.1).



**Figure 5.3:** Atomic distribution along the  $z$ -direction. Upper panels: (a), (b) and (c) are the mass density profiles for silica, NS5 and NS3, respectively. Lower panels: (d), (e) and (f) are the atomic number fraction along the  $z$ -direction for silica, NS5 and NS3, respectively. In all graphs, the solid lines with symbols are for the liquids at  $T_0$ , see Table 5.1. The dashed lines are for glasses at 300 K and are shown only for NS5 for clarity. The vertical dashed lines in all graphs indicate the boundary between the surface and interior layers.

Also included in Fig. 5.3(b) are the results for the NS5 glass at 300 K (dashed lines). We note that the density distributions for the glass look very similar to ones of their corresponding liquid. The difference between them is due to the contraction during the quenching process. Consequently, the distribution for glass becomes slightly narrower than that of the liquid. Meanwhile the density in the interior is slightly larger than the liquid. These observations hold for all three compositions. For the sake of simplicity, we use the same criteria for defining the different regions for both liquids and glasses: Regions in which  $|z| \leq 6 \text{ \AA}$  belong to the interior part of the sample while regions beyond this range are considered as surface layers.

Figures 5.3(d)-(f) show the profiles of atomic number fraction along the  $z$ -direction. For the case of silica, one observes that the concentration of O in the surface regions is higher than in the interior layer, indicating that the surface layers are enriched in O, and this agrees with previous studies [163, 164, 190]. For the sodium silicate compositions, i.e., NS5 and NS3, the surface layer is clearly rich in Na. Consequently, the fraction of Si and O decreases. The enrichment of Na becomes very pronounced when approaching the interface between the surface and the vacuum, indicating that Na are more likely to locate at the outermost atomic layer of the surface. These results are consistent with the findings from our classical MD simulations (see Fig. 4.5).

### 5.3 Dynamics of the liquids

With the surface regions defined, we can now investigate the properties of the surfaces and compare them with the interior part of the sample. Firstly, we present the results regarding the dynamics of the samples in the liquid states. Figure 5.4 shows the mean squared displacement (MSD, see Eq. (1.35)) of different atomic species at  $T_0$ . Firstly, we observe that the curves for the surface layers are higher than ones for the interiors, showing that the atoms in the surface region are more mobile. This finding makes certainly sense since the atoms close to the surface are less confined by the network and hence have more freedom. Secondly, we recognize that all species show at long time  $r^2(t) \propto t$ , indicating that the system has reached the diffusive region at  $T_0$ . Notably the MSD of Na has reached a value  $100 \text{ \AA}^2$ , i.e., a displacement of more than  $10 \text{ \AA}$ . We thus conclude that the samples, in particular the surface regions have been well reconstructed after their creation.

A further insight into the dynamics of the liquid samples can be obtained by decomposing the total MSD into the contributions from different directions. As an example, we show in Fig. 5.5 the decomposed MSD for the NS5 sample. It can be seen that in the interior, panel (a), the three axial components of the MSD are very close to each other, independent of the atomic species. This result is reasonable since the interior is



similar to the bulk sample, which is supposed to be isotropic. In contrast, we recognize from panel (b) that, in the surface domain, the MSD in the  $z$ -direction is considerably smaller than the other two directions. Notably for Na atoms, at long time the MSD in the  $z$ -direction is only about one tenth of the MSD in the other two directions. The rationale for this finding is that the atoms are restricted to move in the  $z$ -direction due the presence of free surfaces. Obviously the atoms near the surface will be constrained more than the atoms in the interior. This effect is more pronounced for Na since its preferred location is the outermost of the surface layer.

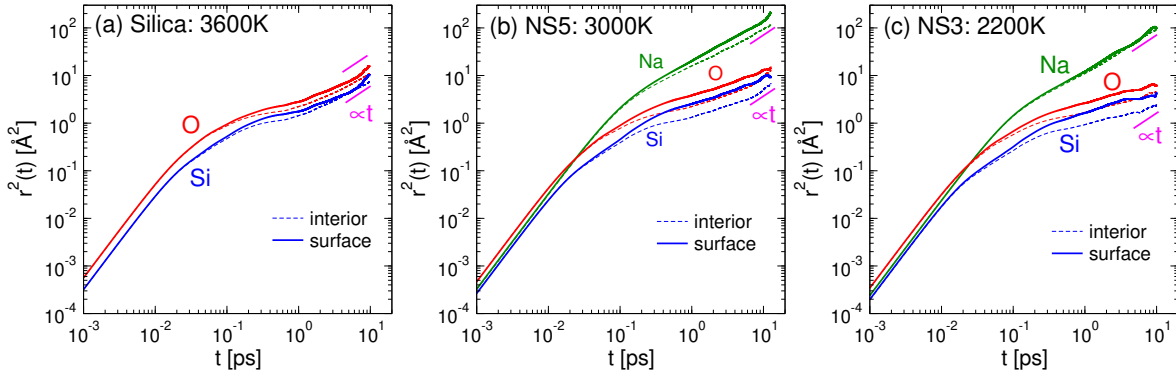


**Figure 5.4:** Mean squared displacement of the liquid samples at their corresponding equilibration temperatures  $T_0$ . Panels (a), (b) and (c) are for silica, NS5 and NS3, respectively. The solid lines are for the surface layer and the dashed lines are for the interior layer.

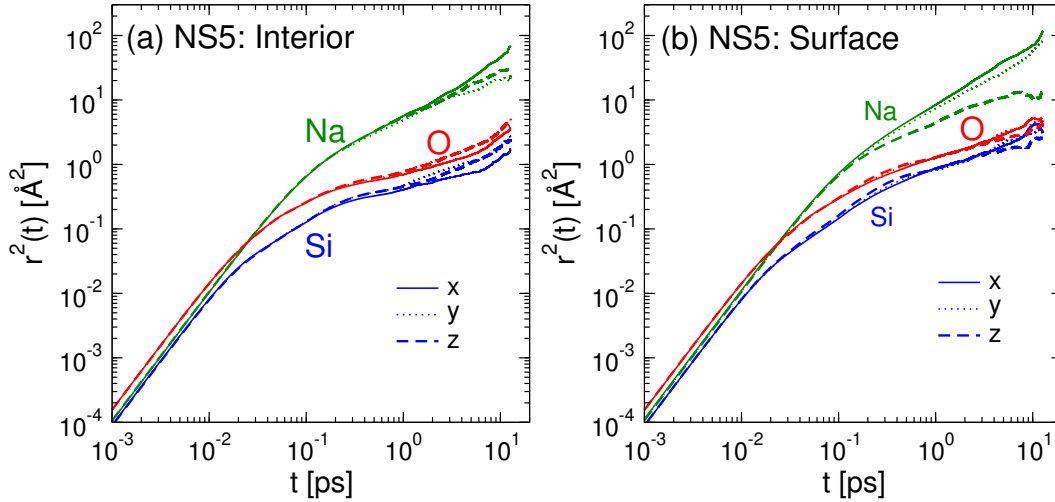


**Figure 5.5:** Decomposition of the total MSD into contributions from the three axial directions. Panels (a) and (b) are for the interior and surface layers of the NS5 sample at  $T_0$ , respectively. The  $z$ -direction is perpendicular to the surfaces.

## 5.4 Structure: Surface vs. interior

We now discuss the structural properties of the silica and sodium silicate samples. The average fractions of different atomic species are summarized in Table 5.2. For both the liquids and glasses, the surface domains are more enriched in non-bridging oxygen (NBO) in comparison with the interior part. This indicates that the surface layer is less polymerized and has more Si-NBO dangling bonds. Sodium atoms will move to the surface for the reason of charge compensation, which is demonstrated in Table 5.2 as well.

	Silica		NS5		NS3	
	liquid	glass	liquid	glass	liquid	glass
%	int. / surf.	int. / surf.	int. / surf.	int. / surf.	int. / surf.	int. / surf.
$N_0$	65.8 / 34.2	66.7 / 33.3	58.6 / 41.4	60.7 / 39.3	58.5 / 41.5	62.9 / 37.1
Si	33.2 / 33.7	33.3 / 33.4	29.1 / 26	29.1 / 25.7	25.5 / 24.4	25.8 / 23.7
Si <sup>3</sup>	2.3 / 3.7	0 / 1.6	0.7 / 1.7	0 / 0	0.1 / 0.8	0 / 0
Si <sup>4</sup>	29.6 / 28.8	32.9 / 31.8	27.2 / 23.6	27.5 / 25.7	24.3 / 23.3	25.4 / 23.7
Si <sup>5</sup>	1.2 / 0.8	0.4 / 0	1.2 / 0.6	1.6 / 0	1.1 / 0.3	0.4 / 0
$Q_2$	0.4 / 0.4	0 / 0	0.3 / 1.6	0.1 / 1.1	2.6 / 3.2	2 / 2.7
$Q_3$	3.6 / 4.8	2.3 / 1.6	7.4 / 11.9	6.9 / 12.6	9.5 / 12.8	10.6 / 14.1
$Q_4$	25.5 / 23.6	30.6 / 30.2	19.4 / 10.1	20.5 / 12	12.1 / 7.3	12.8 / 6.9
O	66.8 / 66.3	66.7 / 66.6	61.9 / 60	62 / 59.7	58.3 / 58.4	58.3 / 58.4
NBO	2.4 / 4.6	0 / 2.3	8.1 / 16.7	6.6 / 15.6	14.3 / 19.7	14.9 / 19
BO	64.4 / 61.7	66.7 / 64.3	53.8 / 43.3	55.4 / 44.1	43.9 / 38.7	43.5 / 39.3
esBO	4.9 / 11.1	1.4 / 12.8	3.4 / 7.5	1.6 / 9.8	1.8 / 4	0.8 / 4.1
esSi	4.6 / 11.3	1.6 / 12.5	3.3 / 7.1	1.2 / 10.5	1.6 / 4.1	0.4 / 4.8
Na	0 / 0	0 / 0	9.1 / 14	8.9 / 14.6	16.3 / 17.2	15.9 / 17.9

**Table 5.2:** Percentages of various atomic species in the interior and surface domains for the silica and sodo-silicate samples. Liquids correspond to  $T_0$  (see Table 5.1). Glasses are at 300 K.  $N_0$  denotes the percentage of atoms in the specific domain relative to the total number of atoms of sample  $N_{tot}$ , whereas the rests are the percentages of specific atomic species relative to  $N_0$ . Si <sup>$n$</sup>  means the Si is bonded to  $n$  oxygen atoms.  $Q_m$  denotes Si<sup>4</sup> connected to  $m$  bridging oxygens (BO, i.e., the O bonded to two Si). NBO denotes non-bridging oxygen, i.e., the O bonded to only one Si. esBO and esSi denote edge-sharing BO and edge-sharing Si, respectively. Note that the edge-sharing atoms form two-membered ring structures.

We note that due to the creation of surface and relatively short time (in comparison with classical MD) for the structural relaxation, structural defects are present in the sample, especially on the surface. Notably we find that there are more under coordinated Si in the surface layer than in the interior, but its concentration decreases

with the addition of Na. Another notable structural defect is two-membered (2M) ring, which consists of two edge-sharing Si (esSi) and bridging oxygen (esBO) atoms. One can notice from Table 5.2 that, there are considerable amount of such defects in the sample, notably in the surface domain. For silica, the presence of such defective structure on the surface has already been documented in previous studies, both in simulations and experiments [164, 165, 191]. We also find that the percentage of the edge-sharing atoms decreases with increasing Na content, indicating that Na plays a critical role in modifying the network and consequently reducing the amount of defective structures: 2M-rings are under strong tension. The presence of Na relieves surface tensile stress by breaking some Si-O bonds. Interestingly, we find a significant reduction of these defects in the interior layer with cooling, whereas the amount of these defects in the surface domain is almost unaffected. The slight increase of the concentrations of the esBO and esSi atoms in the surface layer upon cooling might be simply due to the contraction of the sample, which by definition, leads to a smaller number of atoms in the surface domain. In addition, the fast cooling rate that one usually applies in AIMD may also have an effect.

Figure 5.6 shows top views of the surfaces of silica and NS3 glasses. The surfaces are defined using the Voronoi tessellation method [169] with only the Si atoms being evaluated. (The same method was applied to construct the geometric surface of the classical sandwich samples, see Chapter 3). We show here only one surface layer and leaving out the bulk-like region and the another surface layer on the opposite side of the sample (which is statistically the same as the one shown in Fig. 5.6).

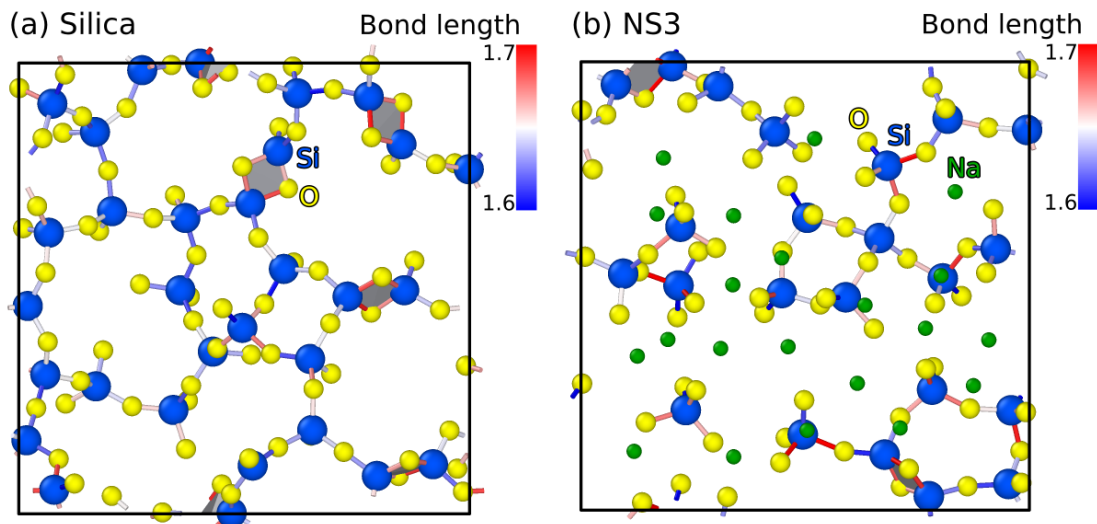


**Figure 5.6:** Top view outlining the structural motifs at the surfaces of (a) silica and (b) NS3 glasses. Only the top most layer of Si and their nearest neighbors O and Na atoms are shown (see the text for the method of construction). Bond length in Å. Two-membered rings (containing four atoms in total) are highlighted with shades.

Firstly, for silica surface, one recognizes the presence of  $[\text{SiO}_4]$ -rings with sizes that vary from two- to nine-members (in terms of number of Si atoms in the ring). Previous *ab initio* investigation of the (0001)  $\alpha$ -quartz surface found the presence of three- and six-membered rings in the most stable reconstruction [192–194]. The greater variation in the ring size of the silica surface found here is likely due to the disordered nature of the glass relative to their crystalline counterparts. Additionally, this top view clearly shows the formation of 2M rings (shaded in grey and with a square-like shape) that are strongly strained (mechanically speaking). As illustrated in panel (b) for NS3, the addition of Na not only breaks the Si-O-Si linkages but also reduce the amount of 2M-rings at the surface, consistent with the results in Table 5.2. These results are also compatible with Pauling’s third rule<sup>1</sup> according to which corner-sharing atom is more preferred [195].

To further understand the local structure of the glass samples, we have investigated structural characteristics such as the interatomic distances and bond angles. For easy comparison, we list in Table 5.3 the mean values of the bond lengths and bond angles as found in the three glasses. The mean Si-Si and Na-O bonds are shorter in the surface domain than the ones in the interior, whereas the Si-O bond is found to be longer in the surface domain. The difference in Na-O bond length between the two domains is related to the change of local environments of the Na atoms. In the interior, a Na atom interacts equally with atoms from all sides. In contrast, a Na atom in the surface domain is more influenced by the atoms below it than the ones above it (see also Fig. 5.3). This is simply due to the fact that Na atoms are enriched in the outer atomic layers of the surface domain. The differences in Si-Si and Si-O bonds between the two domains are mainly due to the 2M-ring structure, which is more enriched in the surface domain.

Further decomposition of the bond pairs shows that the length of the esSi-esSi bond ranges from 2.4 to 2.6 Å (corresponding to the 2M-rings) which is considerably shorter than the csSi-csSi bond which has a length of  $\approx 3.05$  Å. No significant difference between the csSi-csSi and csSi-esSi bonds are found. In addition, we find that the Si-esBO bond is the longest while the Si-NBO bond is the shortest among the Si-O bonds (see also the color coding of bonds in Fig. 5.6). Also interesting is the finding that the Na-NBO bond is about 0.2 Å shorter than the Na-BO bond. The bond length together with the analysis of bond character have implications for bonds strength (see section 5.6).

Figure 5.7 shows the distribution of the nearest neighbor distances for Si-related pairs. For SiO, panels (a-c), one recognizes that in the liquid state the distribution of

---

<sup>1</sup>Pauling’s third rule states that the sharing of edges or faces by two anion polyhedra decreases the stability of an ionic structure. This is due to the fact that sharing edges and faces places cations in closer proximity to each other, so that cation-cation electrostatic repulsion is increased.

Glass	Silica	NS5	NS3
Bond or angle	int. / surf.	int. / surf.	int. / surf.
Si-Si (Å)	3.041 / 2.928	3.041 / 2.927	3.021 / 2.986
csSi-csSi	3.048 / 3.006	3.041 / 3.059	3.023 / 3.024
csSi-esSi	3.055 / 3.058	3.189 / 3.000	2.956 / 3.108
esSi-esSi	2.443 / 2.483	2.370 / 2.616	2.437 / 2.408
Si-O (Å)	1.638 / 1.650	1.648 / 1.651	1.645 / 1.651
Si-NBO	- / 1.563	1.578 / 1.576	1.588 / 1.585
Si-BO	1.638 / 1.652	1.652 / 1.664	1.655 / 1.670
Si-esBO	1.721 / 1.684	1.678 / 1.695	1.704 / 1.695
Na-O (Å)	-	2.423 / 2.362	2.423 / 2.375
Na-NBO	-	2.276 / 2.264	2.347 / 2.315
Na-BO	-	2.526 / 2.531	2.545 / 2.494
Na-esBO	-	2.332 / 2.497	2.542 / 2.423
OSiO (°)	109.4 / 109.5	109.2 / 109.1	109.3 / 109.2
SiOSi*	138.4 / 136.7	136.8 / 135.5	134.1 / 136.4

**Table 5.3:** Average bond lengths and bond angles for the sandwich glass samples at 300 K. csSi and esSi denote corner-sharing and edge-sharing Si, respectively. SiOSi\* denotes the average SiOSi angle without considering 2M-rings.

$r_{\text{SiO}}$  in the interior and surface domain are broad and are very much alike. In contrast, the curves for the glass are much shaper and one can also notice for the surface a slight shift of the distribution to larger distance. This shift in the distribution can be attributed to the enrichment of 2M-ring structures in the surface domain (see also Table 5.3). In addition, the presence of Na leads to broader distributions of  $r_{\text{SiO}}$ , notably for the glasses.

For Si-Si, the distribution of  $r_{\text{SiSi}}$  is shown in Fig. 5.7(d-f). The most noticeable feature is the peak at around 2.4 Å, which originates from the 2M-ring structures as also shown in Table 5.2. For the glasses, the main peak tends to shift to smaller values when more Na is in the network. This is particularly noticeable for the interior domain as the peak position shifted from  $\approx 3.1$  Å for silica to  $\approx 3.0$  Å for NS3. The overall behavior of the surface resembles that of the interior. The reduction of  $r_{\text{SiSi}}$  with increasing Na content can be related to the changes in SiOSi angle, see Table 5.2. For the interior domain, it is clear that increasing Na concentration results in the reduction of the SiOSi angle. Since Si-O bond depends rather very weakly on the composition, we can assume that  $r_{\text{SiO}}$  is a constant ( $\approx 1.64$  Å). Therefore, when adding more Na, geometrically the Si-Si bond will become shorter in order to give a smaller SiOSi angle.

In Fig. 5.8 the bond angle distributions (BAD) for OSiO and SiOSi are shown. For both angles, we observe a noticeable peak at  $\approx 90^\circ$ , which is again a signature of the

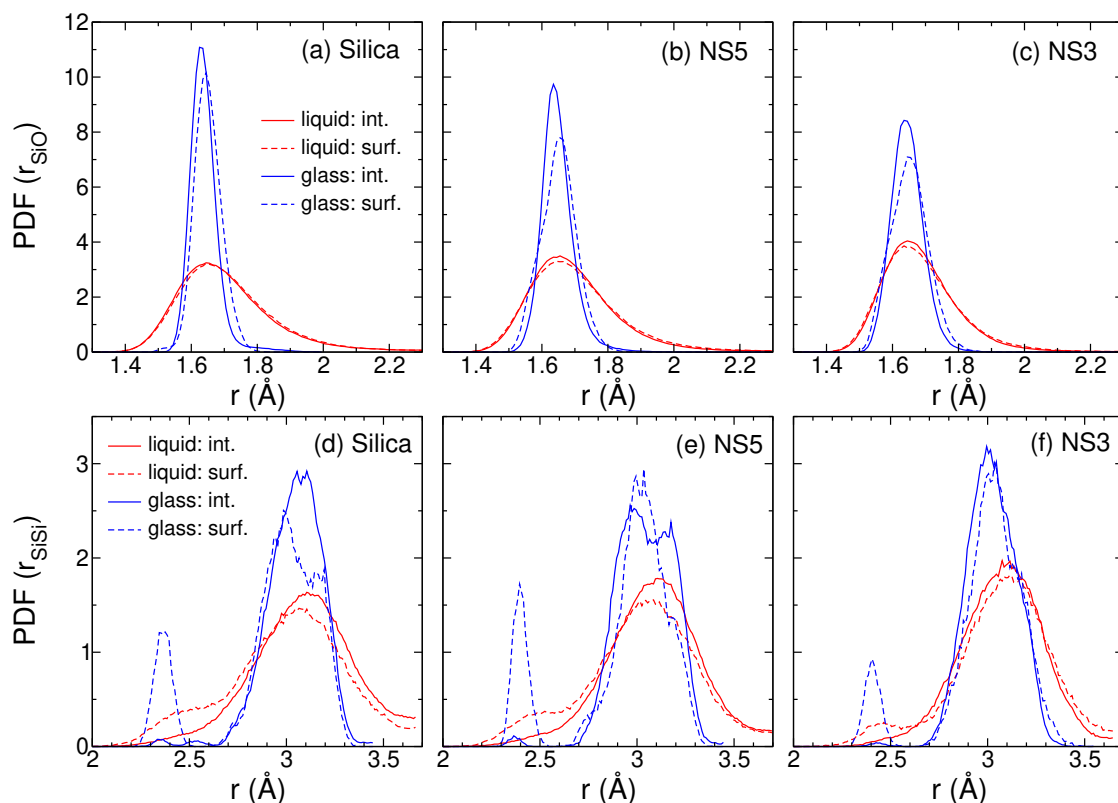


**Figure 5.7:** Probability distribution function (PDF) of nearest neighbor distance. Upper and lower panels are for Si-O and Si-Si pairs, respectively. From left to right the compositions are silica, NS5 and NS3. The PDF are plotted for the interior (solid lines) and surface domains (dashed lines).

2M-ring units (a square-like shape gives rise to  $90^\circ$ , see also Fig. 5.6). The BAD of OSiO is quite stable and only the surface domain shows a slightly wider distribution than the interior.

For the SiOSi angle, the influence of composition is more pronounced. Here we focus only on the main peak which corresponds to the behavior of normal Si-O-Si linkages. For the interior layer, we note that the main peak becomes sharper and shifts toward smaller angle with the addition of Na, consistent with previous studies on the structure of the bulk NSx samples [123]. For silica, the BAD of surface SiOSi is shifted to smaller angle in comparison with the interior one, and thus the mean SiOSi angle of the surface is smaller than that of the interior, see also Table 5.2. Interestingly, with increasing Na concentration, one notices that the BAD of surface SiOSi gradually shifts to larger angle relative to the interior one. Consequently, for the Na-rich NS3 glass, the average SiOSi angle of the surface domain becomes larger than the one of the interior layer.

To summarize, in this section we have discussed in details the structural properties of the silica and sodium silicate samples. It is found that surface domains are more abundant in defective structures such as 2M rings than interior layers. The structural

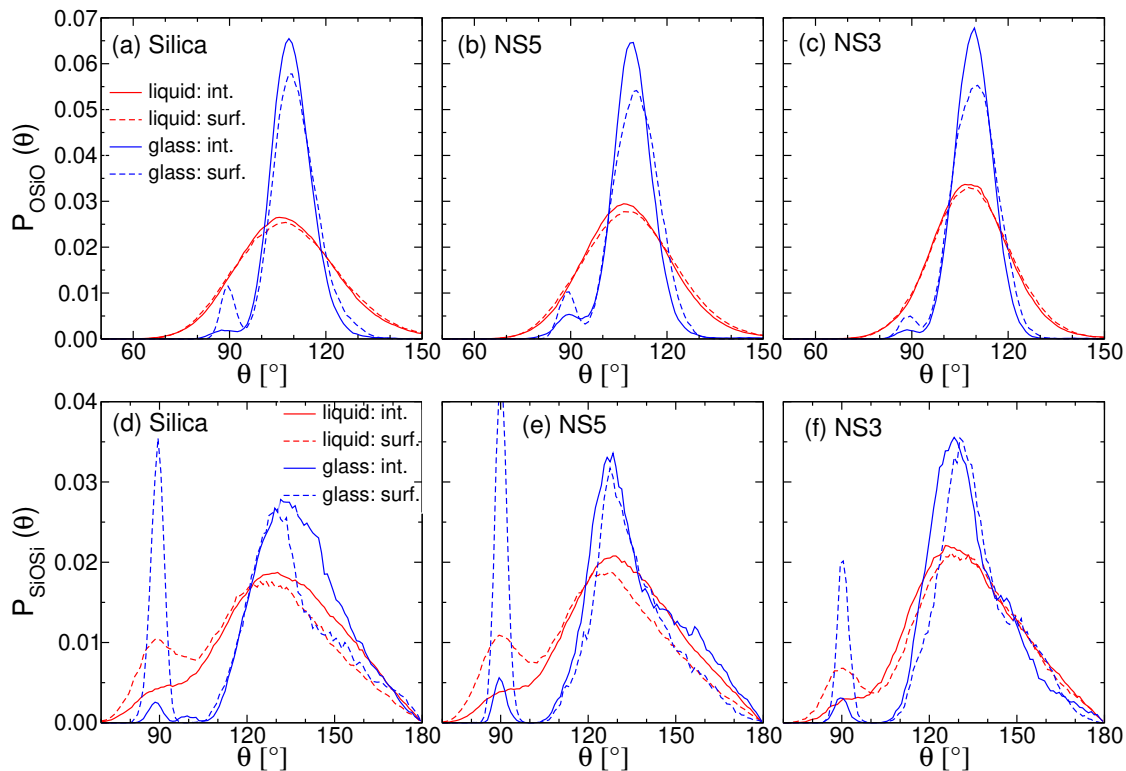


**Figure 5.8:** Bond angle distribution. Upper and lower panels are for OSiO and SiOSi angles, respectively. From left to right the compositions are silica, NS5 and NS3. The BAD are shown for the interior (solid lines) and surface domains (dashed lines).

signatures of the 2M-rings are  $r_{\text{SiO}} \approx 1.70 \text{ \AA}$ ,  $r_{\text{SiSi}} \approx 2.4 \text{ \AA}$ , and  $\theta_{\text{SiOSi}} \approx \theta_{\text{OSiO}} \approx 90^\circ$ . Addition of Na reduces the amount of these defects in the sample by breaking some Si-O bonds, notably those of the 2M-ring structures. The surface Si-Si and Na-O bonds are found to be shorter than their interior counterparts. The relationship between the bond length, bond character and bond strength will be discussed later.

## 5.5 Vibrational properties

A further property that can be explored within the *ab initio* approach is the vibrational spectrum, which is considered as one of the most important quantities for describing atomic dynamics. In this section, we focus on the vibrational density of states (VDOS) of the glass, which in computer simulations can be accessed either through the diagonalization of the dynamical matrix of the glass structure (in a local potential minimum) (method I), or the Fourier transform of the velocity autocorrelation function (method II). In principle, both methods should give essentially the same results for a given simulation technique (i.e., classical or *ab initio* simulations). In practice, computational time and complicity of the algorithm are key factors that need to be

considered. Method I is computationally more complex and expensive but only one atomic configuration (relaxed at 0 K) suffices for the analysis. In contrast, method II is computational easier but it requires a relatively long simulation trajectory. Therefore the former method is usually adopted in *ab initio* calculations, whereas the later is often the choice of simulations using empirical potential. We note that the *ab initio* approach usually reproduces the experimental VDOS much more accurately than the classical approach [196–198].

As we used the *ab initio* approach, the VDOS is thus given by

$$g(\omega) = \frac{1}{3N-3} \sum_{p=4}^{3N} \delta(\omega - \omega_p), \quad (5.1)$$

where  $N$  is the total number of atoms in the sample,  $\omega$  is the frequency and  $\omega_p$  is one of the  $3N$  eigenvalues obtained by direct diagonalization of the dynamical matrix. The VDOS can further be decomposed into the contribution from different species, i.e., the partial-VDOS,

$$g_\alpha(\omega) = \frac{1}{3N-3} \sum_{p=4}^{3N} \sum_{I=1}^{N_\alpha} \sum_{k=1}^3 |\mathbf{e}_{I,k}(\omega_p)|^2 \delta(\omega - \omega_p), \quad (5.2)$$

where  $\alpha = \text{Si, O and Na}$  and  $\mathbf{e}_{I,k}(\omega_p)$  is the part of the  $3N$ -component eigenvector  $\mathbf{e}(\omega_p)$  that contains the three components of the particle  $I$ . The so-obtained discrete spectra have been convoluted with a Gaussian function with a full width at half maximum of  $30 \text{ cm}^{-1}$  in order to obtain smoothed data. The results shown below have been obtained by taking the average of two independent samples.

In Fig. 5.9, we show the total, panel (a), and partial VDOS, panels (b-d), of the three glass samples. Firstly, one recognizes that the VDOS for all samples have three main bands: a low-frequency band with  $\omega < 500 \text{ cm}^{-1}$ , a mid-frequency band with  $500 < \omega < 900 \text{ cm}^{-1}$ , and a high-frequency band with  $\omega > 900 \text{ cm}^{-1}$ . By comparing with the pure bulk silica data [83], we note that the presence of surface results in an intensity decrease of the main peaks. Also noticeable is the disappearance of the double peaks at high-frequency. For the glasses with surfaces, one observes that with increasing Na content, the intensity of the low-frequency band with  $\omega < 300 \text{ cm}^{-1}$  increases which is accompanied by a noticeable decrease in intensity of the bands at  $\approx 400 \text{ cm}^{-1}$  and  $\approx 800 \text{ cm}^{-1}$ . A better understanding of the changes in the total VDOS can be achieved by investigating the contributions from different atomic species. From the three partials, panels (b)-(d), we find that O atoms contribute the most to the total VDOS. The change of intensity below  $300 \text{ cm}^{-1}$  is mainly due the change in Na concentration. This is confirmed by the fact that rescaling the two curves by their corresponding Na fraction results in the collapse of the two curves.



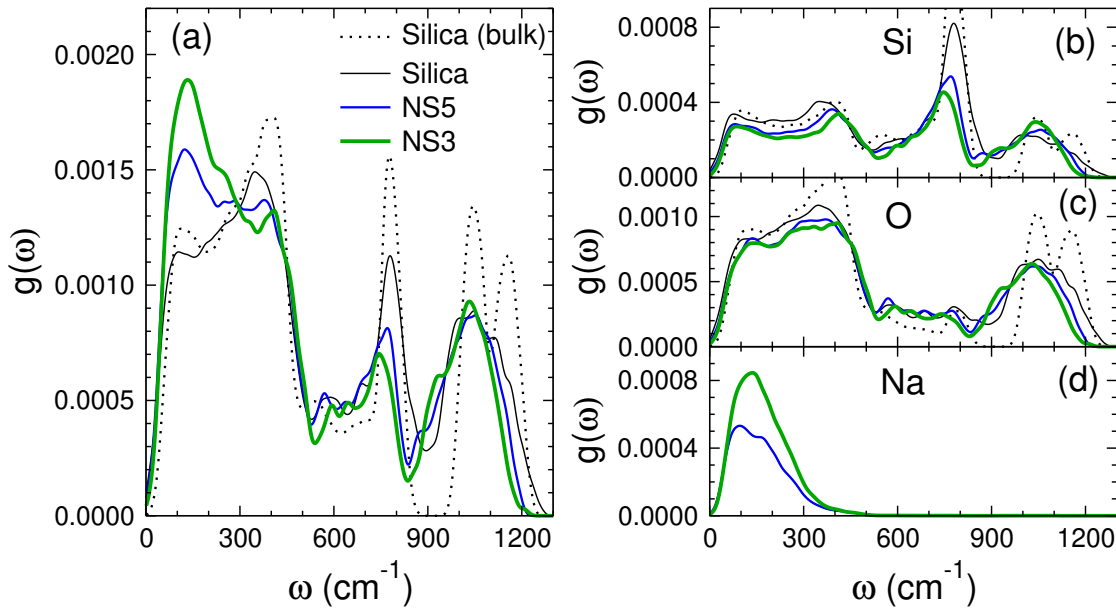


**Figure 5.9:** (a) Total vibrational density of states (VDOS) of the three sandwich glasses. Panels (b)-(d) show the VDOS of Si, O and Na atoms, respectively. Also included in (a) is the total VDOS for a bulk silica from *ab initio* calculations [83]. The total VDOS were normalized to unity, which is equal to the sum of the partials as depicted in (b)-(d).

To better understand the effect of the surface on the vibrational spectra, we further decomposed the VDOS into contributions from the different layers, and the results are shown in Fig. 5.10. We note that the VDOS of the interior layer of the sandwich sample is not equivalent to the one of the bulk sample, as can be inferred from Fig. 5.9. This is not so surprising since atomic vibrations are more sensitive to the presence of surface than the structural features.

For Si, upper panels of Fig. 5.10, we note that the VDOS of surface Si is slightly more pronounced in the low-frequency range while less intense in the mid- and high-frequency ranges. A noticeable feature for the surface Si is the appearance of small peaks or shoulders to the left and right of the main peak at  $\approx 750 \text{ cm}^{-1}$ . For BO, panels (d-f), we observe that the surface BO shows a slight shift of the high-frequency band to lower frequency. Similar to Si, we note for the surface BO the increase of the intensity for the mid-frequency band and the presence of some small peaks in this range. Understanding these features appearing in the mid-frequency range of the VDOS of the surface requires further decomposition. For NBO, panels (g-i), one recognizes that for the sodium silicate glasses the low-frequency bands corresponding to the surface is more pronounced than the interior ones, whereas the high-frequency band for the two domains are almost the same. These results indicate that the vibration of surface NBO is softer than that of the NBO in the interior domain. Finally, we note that for silica, NBO was only found in the surface layer. Still, we find for the surface NBO a

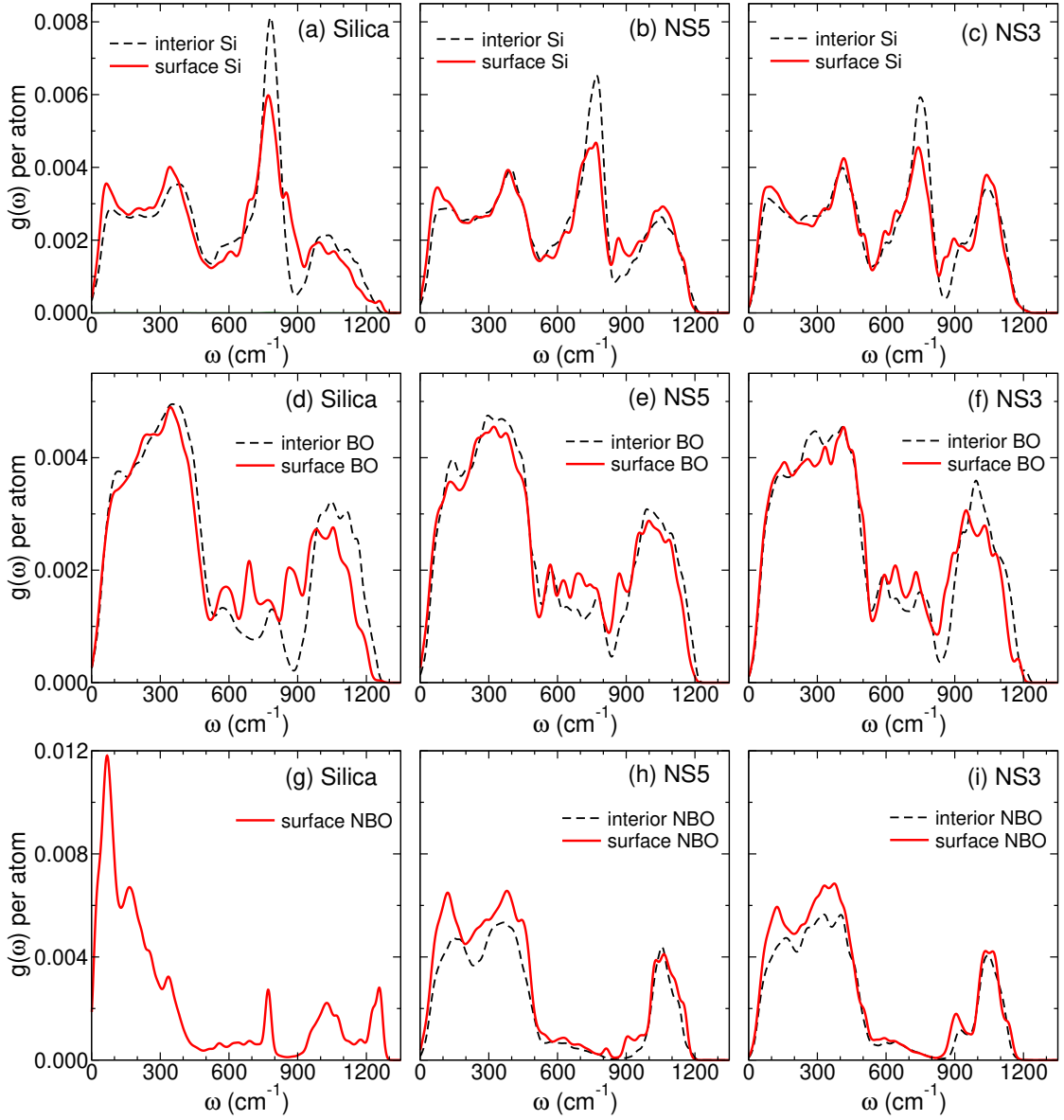


**Figure 5.10:** Decomposition of the partial VDOS into contributions from the interior and surface domains. (a)-(c) Decomposition of the partial VDOS of Si for silica, NS5 and NS3, respectively. (d)-(f) Decomposition of the partial VDOS of bridging oxygen (BO) for silica, NS5 and NS3, respectively. (g)-(i) Decomposition of the partial VDOS of nonbridging oxygen (NBO) for silica, NS5 and NS3, respectively.

very intense peak at  $\omega \approx 100 \text{ cm}^{-1}$ .

Figure 5.11 shows the decomposed VDOS for surface Si and BO. One recognizes from panels (a) and (b) that, the presence of the peak or shoulder at  $\approx 850 \text{ cm}^{-1}$  in the VDOS of the surface Si is due to the presence of edge-sharing Si, which has an unique vibrational signature at this very frequency. As for BO, we recognize from panel (d) for the edge-sharing BO three characteristic vibrational modes, at  $\approx 250 \text{ cm}^{-1}$ ,  $\approx 700 \text{ cm}^{-1}$  and  $\approx 850 \text{ cm}^{-1}$ . The last one is very close to the one for the edge-sharing Si and gives

rise to the peak/shoulder at  $\approx 850 \text{ cm}^{-1}$  in the VDOS of the surface BO. Therefore, we conclude from the decomposed VDOS that the 2M-ring structure has its unique vibrational signature at the frequency  $\approx 850 \text{ cm}^{-1}$ .

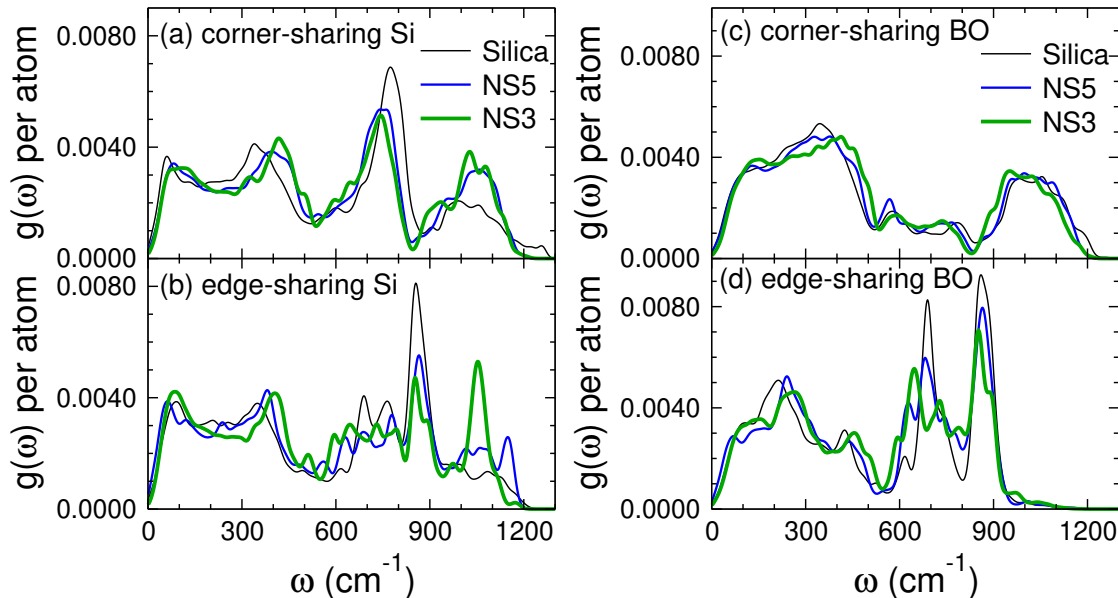


**Figure 5.11:** Decomposition of the partial VDOS of the surface atoms. Panels (a) and (b) are for corner-sharing and edge-sharing Si atoms, respectively. Panels (c) and (d) are for corner-sharing and edge-sharing BO, respectively. Note that corner-sharing atoms constitute 2M-ring structures.

Finally we discuss the anisotropy in the vibrational spectra of the NSx glasses. Figure 5.12 shows, as an example, the partial VDOS for NS3 glass in the three axial directions. As indicated by the arrows in the graphs, the low-frequency band at  $\approx 100 \text{ cm}^{-1}$  is more pronounced in the  $z$ -direction than the ones of the other two directions, whereas for the high-frequency band at  $\approx 1000 \text{ cm}^{-1}$  an opposite trend is found. This finding implies that the creation of surfaces makes the sample anisotropic with respect to the vibrational properties, and the atomic vibration is slightly softer in the  $z$ -direction, i.e., the direction normal to the surfaces.

To summarize, this section discusses the vibrational spectra of the three glasses. By decomposing the total VDOS into contributions from the surface and interior layers, we show that the surfaces show special features with respect to the interior layer and bulk glass sample. Further decomposition of the VDOS identified that the 2M-ring has a unique vibrational signature at frequency  $\approx 850 \text{ cm}^{-1}$ . Finally we have shown that the vibrational motion in the direction perpendicular to the surfaces are softer than the motion in parallel directions.

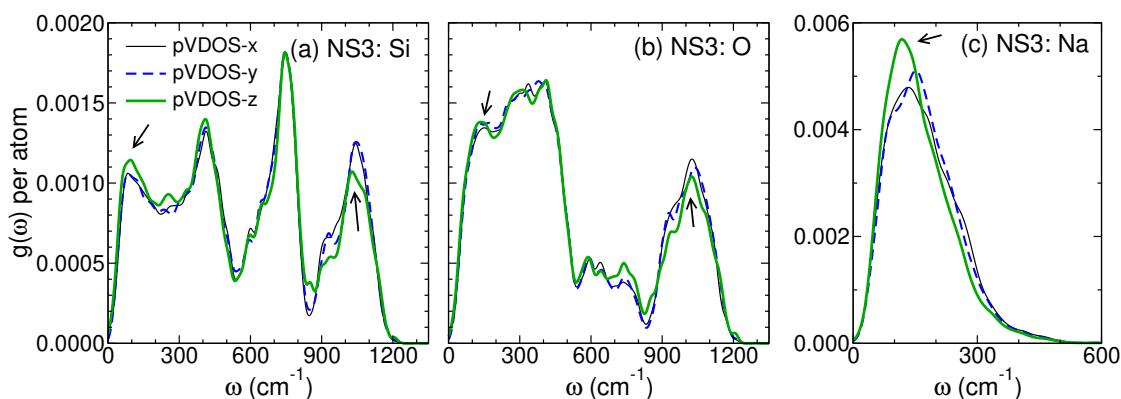


**Figure 5.12:** Decomposition of the partial VDOS into contributions from different directions for the NS3 glass. Panels (a)-(c) are for Si, O and Na, respectively. The arrows indicate the high- and low-frequency ranges where changes of the partial VDOS in the  $z$ -direction can be observed.

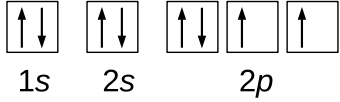
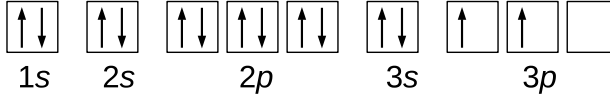
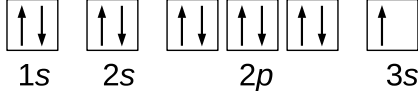
## 5.6 Electronic properties

### 5.6.1 Electronic density of states

Investigating the electronic structure and the nature of chemical bonds in materials is of fundamental importance for a better understanding of their structure-property relationships. To characterize a material’s electronic structure, the most straightforward quantity to look at is probably the electronic density of states (eDOS), which is essentially the electronic “fingerprint” of the entire simulation cell drawn as a histogram along the energy axis. Integrating the eDOS along the energy axis up to the Fermi level yields the number of electrons in the system. The eDOS plot can reveal the location and broadness of the electronic bands. It tells also whether the system is a conductor or a insulator (and the width of the band gap).

We show first in Fig 5.13 the electron configurations and orbital diagrams of the three constituent elements of sodium silicate. This information is important for the discussion below.

Figure 5.14 shows the eDOS for the three glasses as decomposed into the interior and surface domains. For the purpose of comparison, we include in panel (a) also the data for a bulk silica glass. The assignment of various states for the case of silica (crystals and glasses) has been well documented in the literature [199]: (i) the states at about 20 eV are oxygen 2s states; (ii) the states from -10 to -4 eV are bonding states between Si  $sp^3$  hybrids and mainly O 2p orbitals; (iii) the states above -4 eV until the Fermi level are O 2p nonbonding orbitals. The main difference between the eDOS of crystalline and vitreous silica is that the bands for the glass are generally broader than the ones for the crystal, which can be attributed to the structural disorder of the glass.

	Electron configuration	Orbital diagram
<b>O</b>	$1s^2 2s^2 2p^4$	 $1s \quad 2s \quad 2p$
<b>Si</b>	$1s^2 2s^2 2p^6 3s^2 3p^2$	 $1s \quad 2s \quad 2p \quad 3s \quad 3p$
<b>Na</b>	$1s^2 2s^2 2p^6 3s^1$	 $1s \quad 2s \quad 2p \quad 3s$

**Figure 5.13:** Electron configurations and orbital diagrams for the three elements in the sodium silicate.

Previous *ab initio* calculations have predicted a band gap of around 5 eV for silica glass [199–201], and of about 2.8 eV for sodium tetrasilicate glass (i.e., 20 mol-% of  $\text{Na}_2\text{O}$ ) [202]. For the sandwich glasses, the estimated band gaps are 4.1 eV for silica, 2.9 eV for NS5, and 2.7 eV for NS3, compatible with the findings of previous studies. It should be noted that the experimental band gap for silica is about 9 eV [203, 204]. DFT calculations substantially underestimate the band gap, a well-known problem of this technique (see also discussion in Chapter 1). Nevertheless, here we are mainly interested in the valence bands, which are more relevant for chemical bonding.

We discuss first the eDOS for the interior layers which are supposed to be bulk-like. For the case of silica, one recognizes from Fig. 5.14(a) that the eDOS of the interior layer has indeed a shape very similar to the one of the bulk. However, the main bands for the interior layer are shifted to right around 1 eV relative to the bulk. This effect might be attributed to the difference in the production history of the two glasses: The bulk glass was first produced using a classical simulation and a relatively slow quench rate, then further relaxed using the *ab initio* scheme at room temperature [83]. In contrast, the sandwich glasses were prepared using pure *ab initio* simulations with a cooling rate several order of magnitude greater than the classical approach (see 5.1). Therefore, the sandwich silica glass is likely to be at a higher energy state relative to the bulk glass, which may be responsible for the shifting of the eDOS as a whole to a higher energy level. The eDOS for the two sodo-silicate glasses are similar and show common features with the eDOS of silica. However, the influence of Na is clearly seen: 1) The eDOS shifts toward lower energy level with the addition of Na; 2) The intensity of the main peaks and shoulders in the eDOS change, owing to modification of the atomic structure.

The eDOS for the surface layers show similar features as their interior counterparts. A noticeable difference between the two layers is the shifting of the main bands of the

surface eDOS to higher energy level, which might be related to the defective structures in the surface layer. For the case of silica, we note that the splitting between O  $sp$ -Si  $sp^3$  bonding and antibonding states seems to have disappeared in the eDOS of the surface layer.

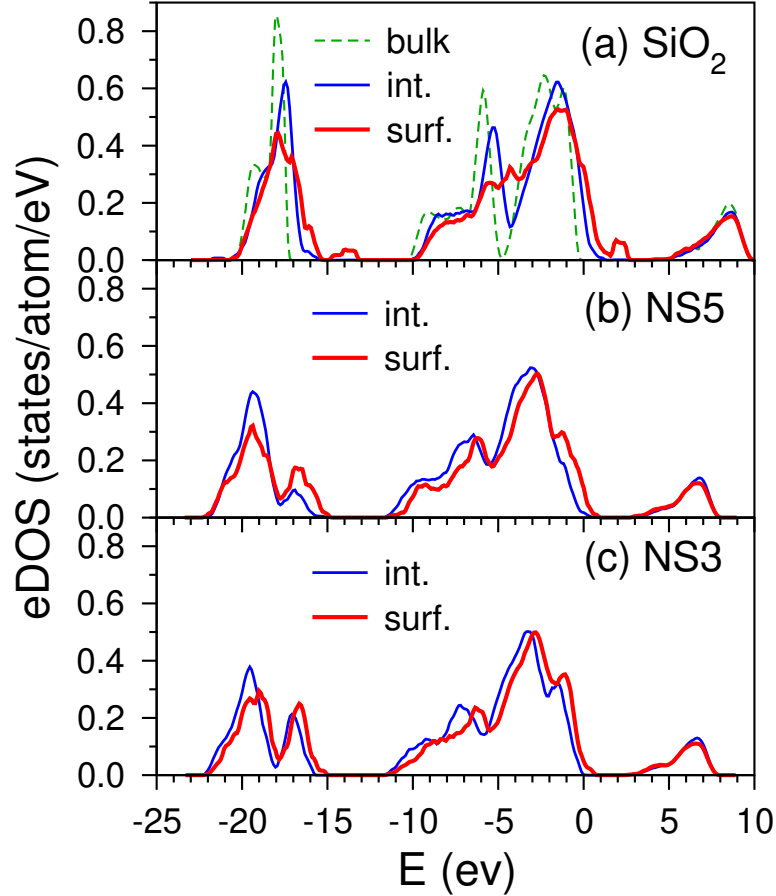


**Figure 5.14:** Electronic density of states (eDOS) of the sandwich glasses at 0 K. (a)-(c) are for silica, NS5, and NS3, respectively. The eDOS are decomposed for the sandwich glasses with respect to the surface (surf.) and interior (int.) layers. The bulk eDOS is also included in the graph for silica glass. The eDOS are normalized with respect to the number of atoms. The Fermi level energy  $E_f$  is at 0 eV.

One of the primary interests of the present work is to better understand the relationship between atomic structure and electronic properties. Therefore, we have decomposed the eDOS of the surface layers, and the results are shown in Fig. 5.15. For the silica surface, panel (a), two small peaks at around -14 and 2 eV are observed. Further decomposition of the O and Si spectra shows that these peaks arise mainly from non-bridging oxygen but also from a contribution of corner-sharing Si (csSi). Thus these two peaks can be attributed to Si-O dangling bonds, in agreement with the findings of previous first principles simulations [205]. The O  $2s$  states (from around -20 eV to -15 eV) can be further assigned to BO and NBO. An additional signature of

the NBO is at around -17 eV, see panel (b) and (e), which gives rise to a shoulder in the eDOS of silica and a pronounced peak in the eDOS of the NS3 glass.

For the silica surface, we note that the main valence bands for the edge-sharing atoms are shifted to higher energy. Consequently, the peaks and valleys of the corner-sharing and edge-sharing atoms cancel out, resulting in the disappearance of the splitting between O  $2p$ -Si  $sp^3$  bonding and O  $2p$  nonbonding states in the total eDOS of silica surface as shown in Fig. 5.14. For the NS3 surface, this effect is less pronounced, which might be attributed to the better relaxed structure of the sample due to the introduction of Na. The contribution of Na is mainly in the near-edge upper valence band and in the conduction band. The results for NS5 are qualitatively similar to that of NS3.

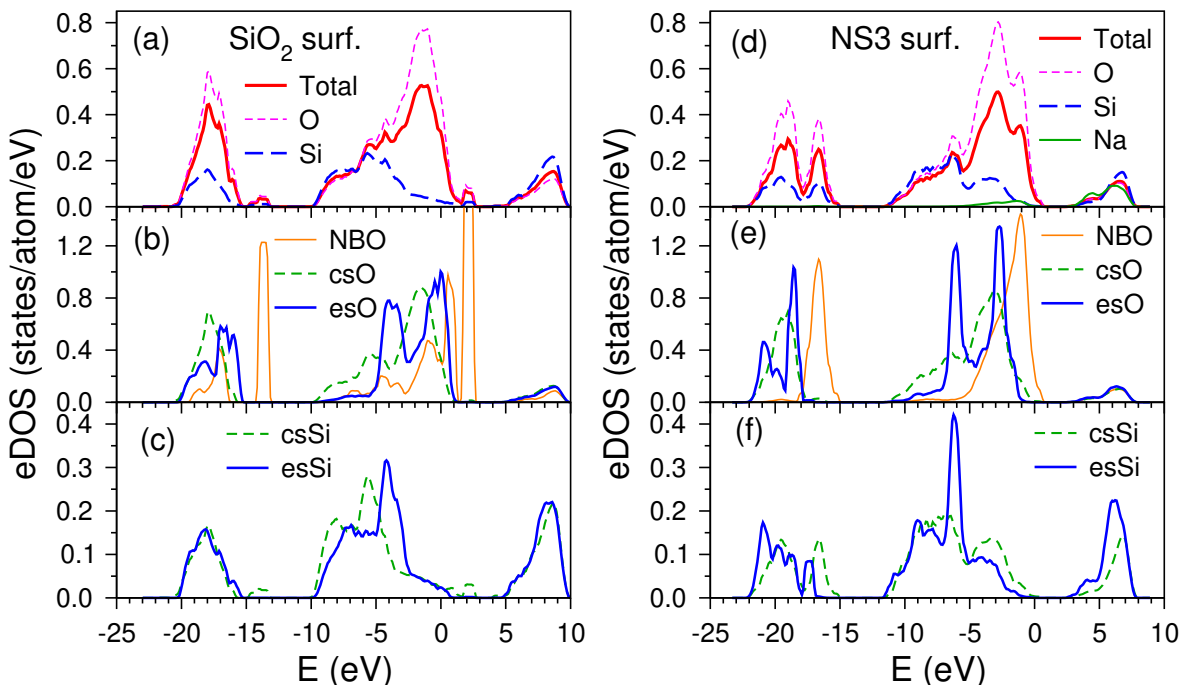


**Figure 5.15:** Decomposition of the surface eDOS of the silica and NS3 glasses. Left panels: Silica. Right panels: NS3. (a) Decomposition with respect to atomic species, i.e., Si, O and Na. (b) Decomposition of O into NBO, csO and esO. (c) Decomposition of Si into csSi and esSi. Panels (d)-(f): The decomposed results for the NS3 glass. The eDOS are normalized with respect to the number of atoms. The Fermi level energy  $E_f$  is at 0 eV.

### 5.6.2 Atomic charge and bond character

The eDOS discussed above has allowed one to see where the electrons and orbitals are, but not on how they engage in bonding. For understanding the later, electron counting is needed since a chemical bond is essentially the attraction between atoms (for a atomic system) due to sharing or transfer of electrons [206]. It is worth noting, however, that

a chemical bond is not a quantum mechanical observable. That is to say, empirical concepts such as ionicity, bond strength and valence do not appear to correspond to anything that is directly measurable. A bonded interaction can only be meaningfully defined within the framework of a given model. For many of the proposed models, measuring and dividing the electron density  $\rho(\mathbf{r})$  is at the center. Both experimental and computational techniques are widely used to obtain electron density maps, based on how atomic charges are usually interpreted.

However, as noted in a recent review article on chemical bonding [207], in the vast majority of cases, there is overlap in the electronic density between atoms, determining the density associated with a particular atom is a non-trivial problem. (The only case in which  $\rho(\mathbf{r})$  uniquely implies ionic charges is the case when the charge distribution do not overlap [208]). Nevertheless, there are several plausible schemes that are well-established and are widely used for partitioning electronic densities among the constitute atoms.

In the present work, we adopt Bader's 'atom in molecule' approach [209], which analyzes topologically the electron density  $\rho(\mathbf{r})$ . The Bader charge is given by

$$Q_{\alpha}^{\text{Bader}} = Z_{\alpha} - \int_{V_{\text{Bader}}} \rho(\mathbf{r}) dV, \quad (5.3)$$

where  $Z_{\alpha}$  is the number of valence electrons of an atom  $\alpha$ , and  $V_{\text{Bader}}$  is the so-called Bader volume around the atom. The Bader volume  $V_{\text{Bader}}$  is enclosed within a surface  $S(\mathbf{r})$ , which exhibits a zero flux property, i.e., the inner product  $\nabla\rho(\mathbf{r}) \cdot \mathbf{n} = 0$ , where  $\mathbf{n}$  is the unit vector oriented perpendicular to  $S(\mathbf{r})$  [209]. In Table 5.4 we list the average Bader charges of various atomic species found in the three glasses. In contrast to the structural analysis, for the charge analysis we did not make distinctions between the surface and interior layers as we found no noticeable differences between the two.

We discuss firstly the Bader charge of Si atoms,  $q_{\text{Si}}$ . The average  $q_{\text{Si}}$  of  $\text{Si}^4$  (i.e. the Si bonded to four O) in the silica glass is about  $+3.18 e$ , in good quantitative agreement with the result found in quartz ( $+3.20 e$ ) [210]. Also the finding that  $q_{\text{Si}}$  increases with increasing coordination number of Si (i.e.,  $n$  in  $\text{Si}^n$  increases) agrees qualitatively with the observation from a high-energy synchrotron-radiation study of stishovite (the high-pressure polymorph of silica) [211]. We note that  $q_{\text{Si}}$  depends also on the character of the tetrahedron,  $Q_m$  (where  $m$  denotes the number of coordinated BO):  $q_{\text{Si}}$  increases with increasing  $m$ . The edge-sharing Si, esSi, has a charge close to the average Si charge in the system.

From Table 5.4, one also notices that  $q_{\text{Si}}$  decreases with increasing Na concentration. To illustrate this point more clearly, we plot in Fig. 5.16(a) the distribution of Si charge and its dependence on  $\bar{n}_{\text{Si}}^{\text{Na}}$ , i.e., the number of Na found in the first coordination shell of the Si-Na pair. The graph shows that  $q_{\text{Si}}$  decreases with increasing  $\bar{n}_{\text{Si}}^{\text{Na}}$ .



Charge ( $e$ )	Silica	NS5	NS3
Si	3.154(0.151)	3.150(0.106)	3.146(0.025)
Si <sup>3*</sup>	2.458(0.469)	1.590	-
Si <sup>4</sup>	3.176(0.018)	3.156(0.024)	3.146(0.025)
Si <sup>5</sup>	3.201(0)	3.178(0.009)	3.158(0.027)
$Q_2$	3.136	3.113(0.007)	3.105(0.017)
$Q_3$	3.142(0.009)	3.133(0.018)	3.134(0.015)
$Q_4$	3.177(0.018)	3.169(0.016)	3.168(0.015)
O	-1.577(0.08)	-1.586(0.055)	-1.588(0.03)
NBO	-1.106(0.243)	-1.529(0.071)	-1.543(0.01)
BO	-1.587(0.014)	-1.599(0.012)	-1.606(0.011)
esBO	-1.563(0.009)	-1.584(0.012)	-1.586(0.011)
esSi	3.144(0.013)	3.13(0.022)	3.119(0.025)
Na	-	0.847(0.015)	0.84(0.016)

**Table 5.4:** Average Bader charge of atoms and various species found in the three glasses at 0 K. Values given in parentheses are the standard deviation of their distributions. Cells without parentheses means that only one such specie is found. Note that Si<sup>3\*</sup> represents all Si atoms with less than four O (not only three) in their nearest neighbor shell.

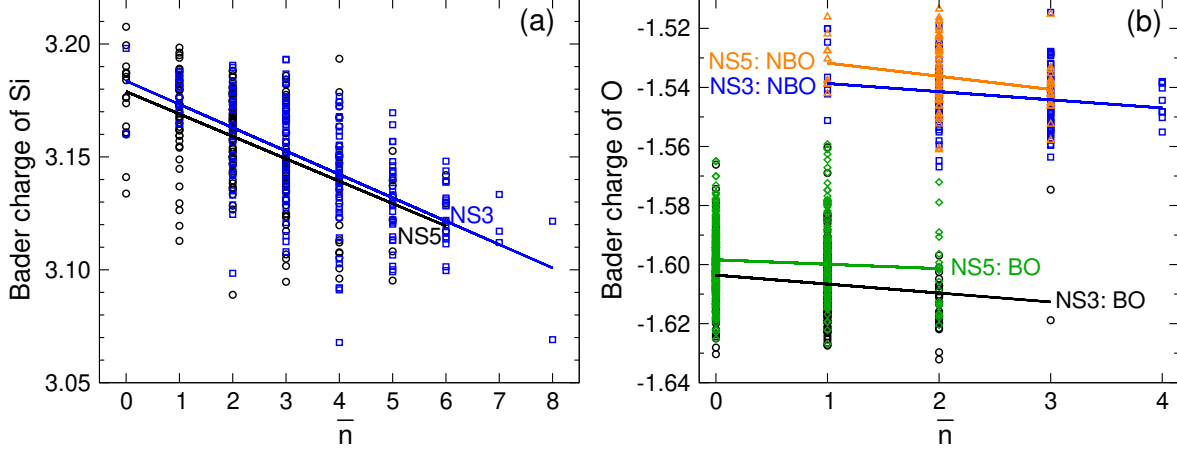


**Figure 5.16:** Dependence of the Bader charge of (a) Si and (b) O on the presence of Na. The A-Na coordination number  $\bar{n}_A^{\text{Na}}$  was obtained by counting the number of Na in the first coordination shell of A, where A denotes O or Si. The cutoff distances for the search are 3.0 Å for O-Na and 4.3 Å for Si-Na, i.e, distances corresponding to the locations of the first minimum of their corresponding pair correlation functions. The symbols show individual values of the charges. The solid lines are linear fits to the data and help to see the overall trend of variation.

For O atoms, the average charge of BO is found to be around  $-1.59 e$ , compared with a value of  $-1.60 e$  in  $\alpha$ -quartz [210]. One notices from Table 5.4 that the charge of BO

is more negative than that of NBO, a deficiency of the Bader charge analysis that has already been found in previous *ab initio* simulations, see for example Refs. [189, 201]. Baring in mind this deficiency, it is still instructive to discuss the atomic charges in different systems using the same description. In particular, we mention that the edge-sharing BO, esBO, has a charge smaller (i.e., less negative) than the one of ordinary BO. Horizontal comparison suggests that the charges of O become slightly more negative with the addition of Na. The same conclusion can be reached from Fig. 5.16, which shows a slight decreasing trend of the charges with increasing  $\bar{n}_O^{\text{Na}}$ .

Finally we note that the Na charge has a value of  $\approx +0.84 e$  and is basically independent of the Na concentration. This result is in good quantitative agreement with a previous *ab initio* simulation of a sodium borosilicate glass, where a Bader charge around  $+0.83 e$  was found for Na ions [188].

Silicate materials are generally considered as covalently bonded networks with some degree of ionicity. However, the degree of ionicity in these materials has been controversial [208]. Based on the results of atomic charge, we further analyzed the ionicity (or covalency) of the bonds in the three glasses. The obtained atomic charges are used to calculate bond ionicity according to the formula [212]

$$\kappa_{A-B} = \frac{1}{2} \left| \frac{Q_A}{\nu_A} - \frac{Q_B}{\nu_B} \right|, \quad (5.4)$$

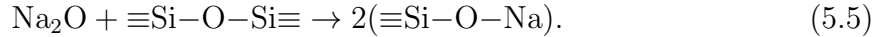
where  $Q_A$  and  $\nu_A$  are the atomic Bader charge and the valence of atom A (i.e., +4 for Si, -2 for O and +1 for Na), respectively. The larger the  $\kappa_{A-B}$  the more ionic the  $A - B$  bond is. It should be noted that this measure of ionicity only depends on the magnitudes of the atomic charge, in line with chemical intuition of the concept of ionicity.

The calculated  $\kappa_{A-B}$  for various types of bonds are listed in Table 5.5. One recognizes that the values vary in a quite large range and are clearly dependent on the bond type and composition. We find that  $\kappa_{\text{Si-NBO}}$  is larger than  $\kappa_{\text{Si-BO}}$  (except for NS3), indicating that the Si-NBO bond is more ionic than the Si-BO bond. However, their difference in ionicity decreases with higher Na concentration. For NS3, the Si-BO becomes even more ionic than the Si-NBO bond. Additionally, one notices that the esSi-esBO bond is less ionic than the usual Si-BO bond, but both of them become more ionic with increasing Na concentration. It should be noted that the character of Si-O bond is an elusive subject for which many contradictory results can be found in the literature [208, 213]. Nonetheless, the analysis of bond ionicity and length (Table 5.3) provide some implications regarding the strength of the Si-O bond. The Si-NBO bond is shorter and more ionic than the Si-BO bond, which implies that Si-NBO bond is stronger than Si-BO bond. With the same logic applied, we thus conclude that the Si-NBO is the strongest type of Si-O bond while the esSi-esO is the weakest one.

	Si-NBO	Si-BO	esSi-esBO	Na-NBO	Na-BO
Silica	0.1178	0.0025	0.0022	-	-
NS5	0.0115	0.0060	0.0048	0.0413	0.0238
NS3	0.0075	0.0082	0.0066	0.0343	0.0185

**Table 5.5:** Bond ionicity  $\kappa_{A-B}$  calculated based on the obtained Bader charges. The larger the  $\kappa_{A-B}$  the more ionic the  $A - B$  bond is.

It is worth noting that the presence of bonding in a given system is not only determined by bond strength but also by the requirement of stoichiometry and charge neutrality. This explains why in silica (crystal or glass) one can only find Si-BO bonds but no Si-NBO bonds. When  $\text{Na}_2\text{O}$  is added to silica, the following reaction is thermodynamically spontaneous:



This reaction is a clear indication that the Si-NBO bond is more stable (i.e., with higher strength) than the Si-BO bond.

Na-O bonds are more ionic in character than the Si-O bond. We also find that the Na-NBO bond is more ionic than the Na-BO bond, and both of their ionicity decrease with the enrichment of Na in the system. Taking into account also the fact that the Na-NBO bond is shorter than the Na-BO bond (Table 5.3), we thus conclude that the Na-NBO bond has higher bond strength. (This might also imply that the Na atoms bonded to NBO are less mobile than the Na atoms around BO, which might have consequences in the VDOS as well).

### 5.6.3 Electron localization function

We have considered a second approach for investigating chemical bonding: The electron localization function (ELF), which was introduced by Becke and Edgecombe in 1990 [214]. The ELF analyzes the probability distribution of electron pairs and is defined as

$$\eta(\mathbf{r}) = \left\{ 1 + \left[ \frac{D(\mathbf{r})}{D_h(\mathbf{r})} \right]^2 \right\}^{-1}. \quad (5.6)$$

The functions  $D(\mathbf{r})$  and  $D_h(\mathbf{r})$  are given by:

$$D(\mathbf{r}) = \frac{1}{2} \sum_i^N |\nabla \psi_i(\mathbf{r})|^2 - \frac{1}{8} \frac{[\nabla \rho(\mathbf{r})]^2}{\rho(\mathbf{r})}, \quad (5.7)$$

$$D_h(\mathbf{r}) = \frac{3}{10} (6\pi^2)^{2/3} \rho^{5/3}(\mathbf{r}), \quad (5.8)$$

where  $D_h$  correspond to the value for a uniform electron gas with spin density  $\rho(\mathbf{r})$  which can be expressed as:

$$\rho(\mathbf{r}) = \sum_{i=1}^N |\nabla\psi_i(\mathbf{r})|^2, \quad (5.9)$$

where the sum is over  $N$  singly occupied Kohn-Sham orbitals  $\nabla\psi_i(\mathbf{r})$ .

By definition,  $\eta$  takes in every point of space a value that lies between 0 and 1. A value of 1 corresponding to perfect localization of electron pairs and a value of 0.5 corresponding to that of a uniform electron gas. The ELF provides a graphical representation of the spatial localization of the probability distribution of electron density as embodied in domains ascribed to localized bond and lone pair electrons.

Previous studies of the ELF of silicates have mainly been devoted to their crystalline phases, whereas this kind of information for amorphous silica or silica-based materials, to our knowledge, is still missing [215]. We are thus motivated in this study to conduct the ELF analysis for silica and sodium silicate glass, which provides valuable insight into the chemical bonding in these amorphous materials.

**Results for silica glass.** Firstly, we discuss the ELF results for the silica glass sample. The structure of bulk silica is known to contain only bridging oxygens which link the neighboring  $[\text{SiO}_4]$  to form a rigid network. In the present study, the presence of free surfaces for our glass samples results in the formation of more types of structural motifs, thus allowing us to explore a broader variety of structures even for the case of silica.

In Fig. 5.17 we show the ELF results for some structural motifs on the surface of the silica glass. Panel (a) shows the ELF isosurface around a  $[\text{SiO}_4]$  tetrahedral unit on the surface. (Note that the isosurface is shown for  $\text{ELF}=0.83$ , which is the same as the value used in a previous study of earth materials [215]). We find for the BO involved linkage, e.g.  $\text{Si1O2Si2}$ , a hemispherical isosurface as a discrete unit along each Si-O bond. This domain is ascribed to a pair of bonding electrons. One also observes that a banana-shaped isosurface is present on the reflex side and which orients perpendicular to the plane of the SiOSi angle. This domain is assigned to two lone pairs of electrons, i.e., the four valence electrons that are not involved in bonding. The banana-shaped nonbonding domains associated with the BO atoms are substantially larger than the bonded hemispherical domains along the Si-O bonds, in agreement with the ELF mapping of the SiOSi linkage in quartz [215].

We now turn our attention to the NBO atoms. NBO is usually absent in bulk silica but do present on the glass surface as it has already been documented in previous studies [164, 190]. A bond pair domain is also observed along the NBO-Si bond vector, i.e.,  $\text{O1Si1}$ . In contrast to the BO, one notices around the NBO a concave hemispherical-shaped domain, which can be ascribed to the nonbonding electrons. One recognizes that the nonbonding electron domain for the NBO has a greater vol-

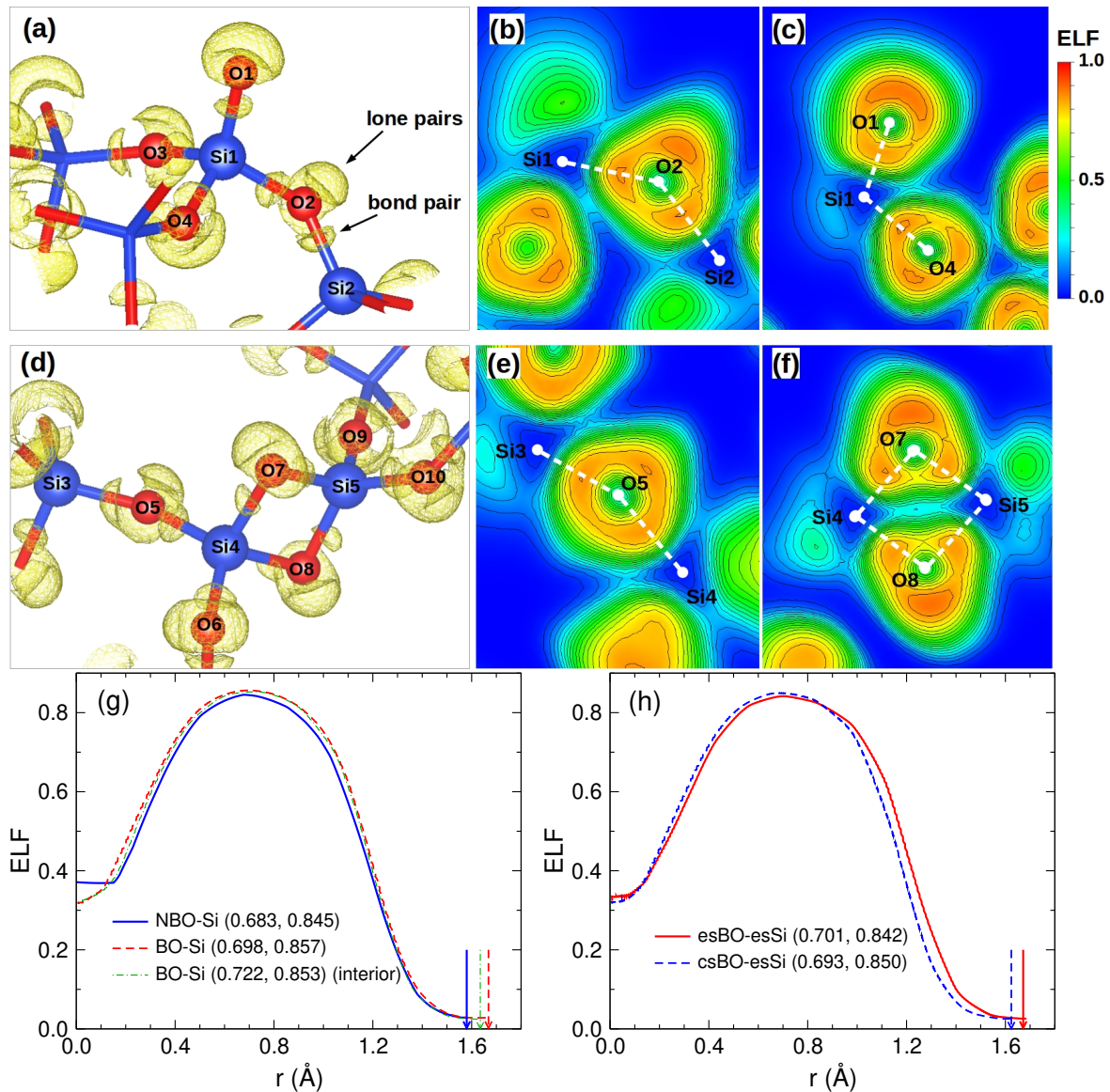


**Figure 5.17:** Analysis of chemical bonding by using the electron localization function (ELF):  $\text{SiO}_2$  surface. (a) The ELF map for a structural motif on the surface, highlighting a  $[\text{SiO}_4]$  tetrahedron bonded to one NBO and three BO atoms. The isosurface (in yellow) represents an ELF value of 0.83. (b) and (c): 2D contour plots for the ELF in the planes defined by three atoms. The increment of the contour plot is equal to 0.05. (d-f): The same representation as in (a-c) but for a two-membered ring structure. (g) and (h): Average line profiles of the ELF along the bond paths as shown in (a) and (d), respectively. Also included in (g) is the average ELF profile of the BO-Si bonds that belong to a Si-BO-Si connection in the interior domain (green line). The O atom is at the origin, i.e.  $r = 0$ . For each bond path the point corresponds to the maximum ELF is indicated in the parenthesis. The arrows correspond to the average Si-O bond length. The visualization of the ELF was realized by VESTA [216].

ume than the one of the BO. This result makes sense because presumably there are five nonbonding electrons for the NBO while only four for the BO.

More quantitatively, we show in Fig. 5.17(b) and (c) the two-dimensional (2D) contour plots of the ELF corresponding to a Si-BO-Si and a NBO-Si-BO connection. The aforementioned bonding and nonbonding domains are clearly visible from the contour plots. In addition, one recognizes that the probability distribution of electron pairs around the NBO is more spread out than that of the BO, panel (c). This observation might be related to the fact that the NBO has more free volume on the vacuum side than the BO atoms.

We now discuss another special structural motif, namely the 2M ring. As depicted in Fig. 5.17(d), the 2M-ring has a square-like shape and consists of four atoms that are almost in the same plane. One notices that the O atoms in the 2M-ring, esBO, have electron pair domains similar to the ordinary BO atoms, e.g., O2 in panel (a).

Figure 5.17 (e) and (f) show the ELF contour plots corresponding to two Si-O-Si linkages associated with the 2M-ring. Note that the Si-O-Si linkage in panel (e) involves an edge-sharing Si, Si4. One sees that the Si3O5Si4 angle is much greater than the one in panel (b), demonstrating that the strong angular constraint in the 2M ring also affects its neighboring linkages. Consequently, the bond and lone pair domains around the BO in panel (e) are not as well developed as the one in panel (b). Panel (f) shows the ELF contour plots of the 2M ring structure. One observes that the bond and lone pair domains are well developed as discrete domains. Another noticeable feature is that the bond paths are no more axes of symmetry for the bond pair domains. This is likely due to the strong repulsion of the electrons from the the two opposing esBO atoms.

For a more quantitative comparison between the bonds, we show in Fig. 5.17(g) and (h) the line profiles of the ELF along the bond paths starting from O atoms. Note that all BO in panel (a) and (g) are the ordinary corner-sharing BO, csBO. From panel (g), one notices that overall the ELF of the NBO-Si bond is smaller than the one of the BO-Si bond, implying that the ELF around the NBO is more spread out, in agreement with the contour plot in panel (c). In addition, as indicated in the parentheses, the BO-Si bond peaks at a higher ELF value and a larger  $r$  relative to the Si-NBO bond.

In order to check if there are differences between the Si-BO-Si linkages in the surface and the interior domains, we have chosen a Si-BO-Si linkage in the interior of the sample and which has a angle close to the Si1O2Si2 linkage shown in panel (a). The corresponding ELF line profiles are included in panel (g) as well. One recognizes that the ELF profiles of the two types of BO-Si bonds are very similar to each other. Nevertheless, we find that the bond length (indicated by the arrows) of interior BO-Si is slightly smaller than the surface BO-Si (see also Table 5.3). This is due to the fact that the bonds on the surface are under stronger tension.

In panel (h) we compare the ELF line profiles of the esBO-esSi and csBO-esSi

bonds. Interestingly, one notices an overall shifting of the ELF of the esBO-esSi bonds to a larger  $r$  relative to the csBO-esSi bonds. Consequently, we observe a slight shift of the maxima location of the ELF from  $r \approx 0.69$  Å for the csBO-esSi to  $r \approx 0.70$  Å for the esBO-esSi.

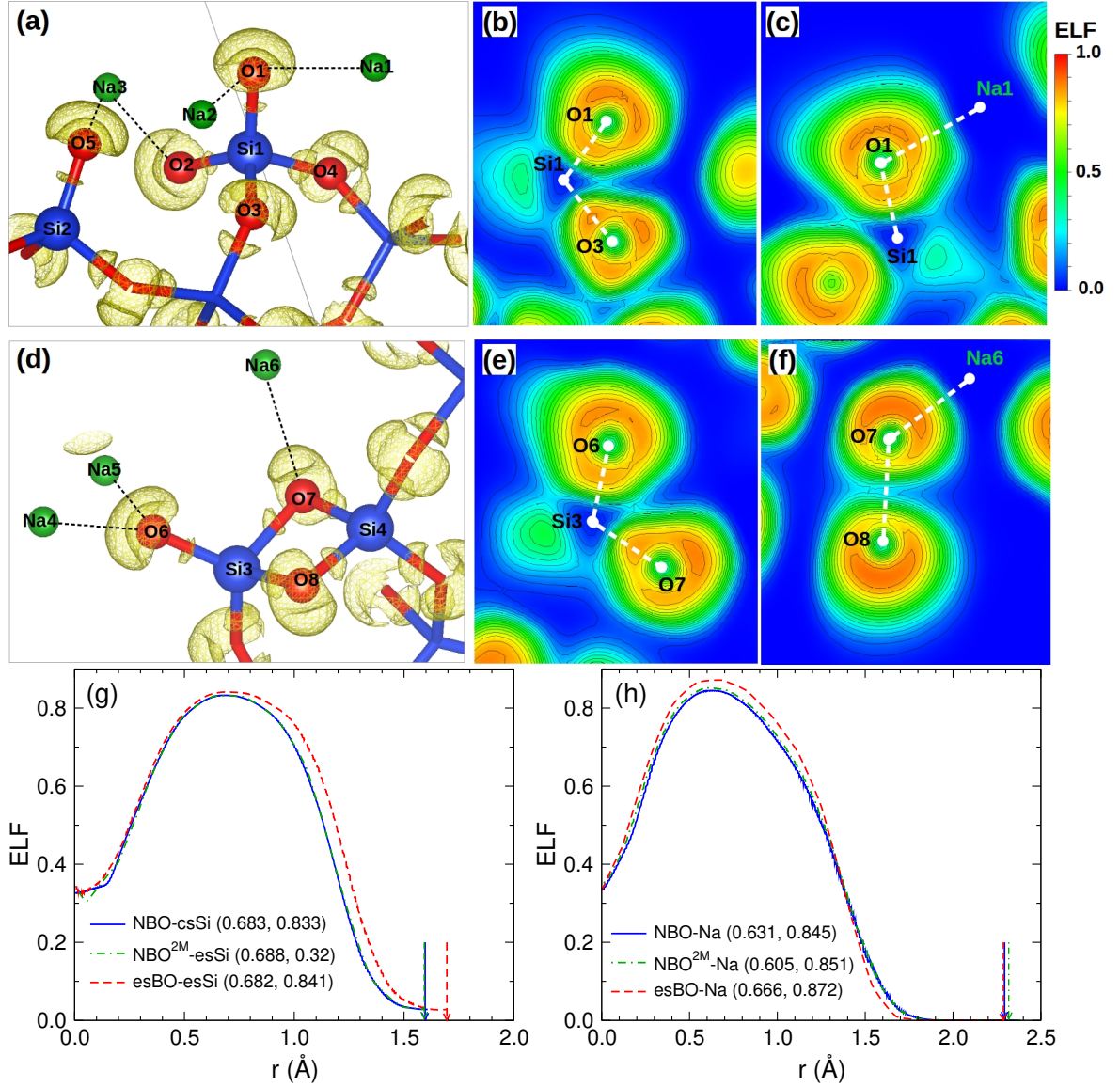
**Results for a sodium silicate glass.** Based on the information obtained for pure silica, we now look at a glass composition containing Na, namely  $\text{Na}_2\text{O}-3\text{SiO}_2$  (NS3). The main objective here is to understand the influence of Na on the bonding of the structures on the surface.

Figure 5.18 shows the ELF data for the NS3 glass surface, which are presented similar to the ones for silica. As can be seen from panel (a), the presence of Na in the neighborhood of the  $[\text{SiO}_4]$  tetrahedra results in the formation of more NBO on the surface. In addition to the structural modification, one can notice that the presence of Na induces changes in bonding as well. Here we focus on the NBO-Si bond. Noticeably, the bond pair domain becomes much smaller relative to the NBO-Si bond with no Na around (Fig. 5.17(a)). From the contour plot in Fig. 5.18 (b), one observes that the presence of Na also makes the lone pair domain of the NBO (i.e. O1) asymmetric. The influence of Na is also seen by using the Na atom for constructing the contour plot, panel (c).

We now turn our attention to the 2M-ring structure. It is worth mentioning that the number of 2M-rings in the NS3 glass is considerably smaller than the silica glass (see section 5.4 for detailed structural analysis). Nevertheless, there are still a few of them present on the surface, allowing to investigate the influence of Na on this type of structure. Figure 5.18(d) shows a NBO linked to the 2M-ring due to the presence of Na. Apart from the bond pair domains that correspond to the O-Si bonds, there are also domains in the directions of the Na atoms, which can be ascribed to the Na-O bond pair interaction superimposed on the lone pair domains, panel (e). Similar results were also found for earth materials containing alkali metals [215]. Figure 5.18(f) clearly shows the banana-shaped lone pair domains. In addition, the effect of Na is also seen as the esBO (O7) bonded to the Na is less spread out than the other esBO (O8).

Fig. 5.18(g) shows the average ELF line profiles of various types of O-Si bonds. Notice that the NBO atom connected to an esSi atom is denoted as  $\text{NBO}^{2\text{M}}$ . One recognizes that the ELF profile of the NBO-csSi bond is very similar to the one of the  $\text{NBO}^{2\text{M}}$ -esSi bond, indicating that the NBO-Si bond character is basically independent of the Si type. Furthermore, we find that the ELF values of the NBO-Si bonds are smaller than that of the esBO-esSi bond, in accordance with the fact that the ELF around the NBO is more spread out. For all the three NBO-Si bonds, the maximum ELF is located at  $r \approx 0.68$  Å, independent of the bond type.

In Fig. 5.18(h) we compare the average ELF line profiles of various types of O-Na



**Figure 5.18:** Analysis of chemical bonding by the electron localization function (ELF): NS3 surface. (a) A map of the ELF for the structures on the surface, highlighting a [SiO<sub>4</sub>] tetrahedron with Na atoms around. The dashed lines are the O-Na bonds with  $r_{\text{O-Na}} < 2.5$  Å. The isosurface represents an ELF value of 0.83. The assignment of different domains are the same as for silica. (b) and (c): 2D contour plots for the ELF in the planes defined by three atoms. The increment of the contour plot is equal to 0.05. (d-f): The same representation as in (a-c) but for a two-membered ring structure. (g) and (h): Average line profiles of the ELF along the bond paths as shown in (a) and (d), respectively. The O atom is at  $r = 0$ . For each bond path the point corresponds to the maximum ELF is indicated in the parenthesis. The arrows correspond to the average Si-O or Na-O bond length. NBO<sup>2M</sup> denotes the NBO bonded to an esSi.

bonds. We find that the maxima of the line profiles are located at  $r \approx 0.61$ , 0.63 and 0.67 Å for the NBO<sup>2M</sup>-Na, NBO-Na, and esBO-Na bonds, respectively. This results



indicate that the character of the O-Na bond is more sensitive to the changes in local environment than the NBO-Si bond. We note that the ELF maxima of the O-Na bonds are closer to the O atoms (at  $r = 0$ ) than the ones of the O-Si bonds. This finding demonstrates the stronger ionic character of the O-Na bonds. Based on the locations of the ELF maxima, it can be deduced that the esBO-Na bond is more covalent than the NBO-Na bonds. This observation may be generalized by saying that the BO-Na bond is more covalent than the NBO-Na bond as also indicated by the bond ionicity in Table 5.5.

We notice that the maximum locations of the ELF profiles found for the NBO-Si and esBO-esSi bonds are very close to the values found for the silica glass. This similarity indicates that the presence of Na only weakly affect the position of the bond pair domains of the O-Si bonds. Comparing with the ionicity results, we thus conclude that the ELF perspective of bond character is less sensitive to compositional change than the ionicity based on atomic charge. But the two methods do show qualitative agreement with each other.

In this section we have explored extensively the electronic properties of silica and sodium silicate glasses, with particular focus on their surfaces. The eDOS of the glass surfaces show noticeable difference from the interior ones. Decomposition of the eDOS reveals the electronic signature of surface structures such as NBO and 2M-rings. The Bader charge analysis shows that the presence of Na affects more on the charge of Si than O. The bond ionicity and the ELF analysis are compatible with each other, showing that the NBO-Si bond is the most ionic type of Si-O bond while the esBO-esSi bond is the most covalent one. Na-O bond is more ionic than the Si-O bonds, but the degree of ionicity also depends on the type of O bonded. Based on the results of bond length and ionicity, we deduce that the bond strength is in the order NBO-Si > BO-Si > esBO-esBO > Na-NBO > Na-BO.

## 5.7 Summary

To summarize, we have investigated systematically the structural, dynamical, vibrational and electronic properties of silica and two sodium silicate samples. The surfaces of the glass samples are of primary interest. We have defined the surface and interior layers for the sandwich samples based on the atomic distribution along the direction perpendicular to the surface (i.e., the  $z$ -direction). It is found that the surface layers are more enriched in O and Na for silica and the sodium silicate glasses, respectively. We also find that in the liquid state, the surface layer has a faster dynamics than the interior layer. In addition, the surface Na atoms are found to be much less mobile in the  $z$ -direction than the other directions, which has been attributed to the constrains

of the surfaces.

Structural analysis shows that the surface layer is less polymerized and has more Si-NBO dangling bonds than the interior layer. In addition, structural defects such as two-membered (2M) ring is more abundant in the surface domain than the interior. The concentration of 2M-ring is found to decrease when more Na is added to the sample. The structural signatures of the 2M-rings are  $r_{\text{SiO}} \approx 1.70 \text{ \AA}$ ,  $r_{\text{SiSi}} \approx 2.4 \text{ \AA}$ , and  $\theta_{\text{SiOSi}} \approx \theta_{\text{OSiO}} \approx 90^\circ$ . The surface Si-Si and Na-O bonds are found to be shorter than their interior counterparts.

The vibrational density of states show that 2M-ring has an unique vibrational signature at frequency  $\approx 850 \text{ cm}^{-1}$ . Besides, it is found that the vibrational motion in the  $z$ -direction is softer than the motion in the other two directions, indicating that the creation of free surfaces results in anisotropic vibrational properties of the glasses.

Furthermore, we have analyzed the electronic properties of the glasses. The signatures of surface structures such as NBO and 2M-rings in the electronic density of states were identified. The Bader charge analysis shows that the charges of O and Si are more sensitive to composition than that of Na. Using the electron localization function (ELF), we have analyzed bonding in the glasses, particularly for surface domains. It is found that the the bond ionicity based on the Bader charge is compatible with the ELF results. We further deduced that the bond strength is in the order NBO-Si > BO-Si > esBO-esBO > Na-NBO > Na-BO. To our knowledge, this is the first time such detailed bonding analysis is conducted for sodium silicate glasses. These knowledge may be helpful for understanding the cracking process of the glasses on the microscopic scales.



## Chapter 6

# Uncovering hidden order in liquids and glasses

Experimental and theoretical investigations indicate that disordered systems such as liquids and glasses have a structural order on the length scale of a few particle diameters but which then quickly vanishes at larger distances. This conclusion is, however, based mainly on the behavior of two-point correlation functions such as the static structure factor,  $S(q)$ , and radial distribution function,  $g(r)$  [13, 217, 218]. These two-point correlations functions are useful for obtaining a basic knowledge of the structure such as the *mean* inter-particle separation and coordination number. However, these functions project the whole three dimensional structural information onto one dimension which inevitably results in a huge loss of the structural information.

In recent years, great efforts have been made to understand the relationship between local structure and macroscopic properties of liquids and glasses. Two types of local structural ordering have been identified for these systems: Energy-driven and entropy-driven<sup>1</sup> [219]. The former is commonly observed in tetrahedral liquids, such as water and SiO<sub>2</sub>. The latter is often found in hard-sphere-like liquids (whose free energy is only composed of an entropic term), such as the Kob-Andersen Lennard-Jones mixture [220].

Tens of local structural measures incorporating many-body effects have been proposed to probe the structure in liquids and glasses (For a comprehensive list, the reader is referred to a review article [219]). These structural quantities can be divided into two categories, depending on whether or not they rely on local geometry of the structure. One of the most well-known geometrical structural descriptors is the bond-orientational order (BOO), which measures the local orientational order between a particle and its nearest neighbors [221, 222]. It has been shown that the BOO parameters are able

---

<sup>1</sup>This classification is based on the fact that the influence of the free energy on local structures can be decomposed into energy and entropy contributions.

to distinguish between disordered (liquid-like) and ordered (crystal-like) environments in hard-sphere-like glass-forming liquids. For tetrahedral liquids, the tetrahedrality of the local structure (formed by a particle and its four nearest neighbors) is often evaluated [223]. The extension of this idea has allowed to identify the spatial correlation between the polytetrahedral order and the slow dynamics in granular materials [224]. On the other hand, non-geometrical structural descriptors such as the local structural entropy<sup>2</sup> has recently been used as a local structural indicator in glass-forming systems [225, 226]. The local structural ordering as given by these structural descriptors has frequently been connected to the slow glassy dynamics and glass-forming ability [219, 227].

It is worth noting that these local structural descriptors were proposed for specific applications (i.e., for a given type of system and property). Therefore, one can hardly tell which one of them is most efficient. These descriptors, particularly the ones based on local geometry, have enabled us to obtain deeper insights into the local structural ordering in disordered systems relative to what  $g(r)$  and  $S(q)$  can provide. However, the structural information beyond the second coordination shell<sup>3</sup> can hardly be inferred from these local structural measures. This is the primary reason for the fact that the knowledge regarding the structure of liquids and glasses beyond short range is still very limited. Whether or not disordered systems have a structural order that extends beyond a few particle diameters is therefore still an open question.

In this work, we extend the idea of many-body (higher order) correlation to a much larger length scale which allows to reveal that liquids and glasses do have highly non-trivial correlations up to distances well beyond the first few coordination shells. In order to show the generality of our results, we consider two systems that have a very different structure: A binary mixture of Lennard-Jones particles (BLJM) and silica. The former liquid has a close packed local structure that is similar to the one of a hard sphere system while the latter is a paradigm for an open network liquid with local tetrahedral symmetry.

## 6.1 Simulation details

**Silica.** We perform molecular dynamics simulations for silica. The cubic simulation box, with periodic boundary condition applied, contains around 120000 atoms. The sample was firstly melted at 4500 K for 80 ps in the canonical ensemble ( $NVT$ ) to

---

<sup>2</sup>Local structural entropy is essentially a local version of the two-body excess entropy which can be derived from the radial distribution function [219].

<sup>3</sup>The spherical shell corresponding to the distances between the first and second minima of the radial distribution function.

completely remove the memory of the initial configuration. The liquid sample was then equilibrated at various temperatures ranging from 2600 K to 4400 K in the isothermal-isobaric ensemble ( $NPT$ ) and at zero pressure. The equilibration time of the sample is temperature dependent. Therefore, we have carefully monitored the dynamics of the system at each temperature and ensured that the system have become diffusive before taking configurations for subsequent structural analysis. In order to compare the structure of the glass with the one of the liquid, we have also quenched the equilibrated liquid sample at 3000 K to 300 K with a cooling rate of 1 K/s. The temperature and the pressure of the system are controlled by using a Nosé-Hoover thermostat and barostat [87–89]. Throughout the simulations, we use a well-established two-body effective potential named SHIK [83] which has already been introduced in chapter 2. All simulations were realized using the LAMMPS package [116] with a time step of 1.6 fs.

**Binary Lennard-Jones mixture.** We study the equilibrium properties of the BLJM in a temperature range in which the system changes from a very fluid state to a moderately viscous one, i.e.  $5.0 \geq T \geq 0.4$ . The system is a 80:20 mixture of Lennard-Jones particles (type A and B) with interactions given by

$$V_{\alpha\beta}(r) = 4\epsilon_{\alpha\beta}[(\sigma_{\alpha\beta}/r)^{12} - (\sigma_{\alpha\beta}/r)^6], \quad (6.1)$$

where  $\alpha, \beta \in \{A, B\}$ ,  $\sigma_{AA} = 1.0$ ,  $\epsilon_{AA} = 1.0$ ,  $\sigma_{AB} = 0.8$ ,  $\epsilon_{AB} = 1.5$ ,  $\sigma_{BB} = 0.88$ , and  $\epsilon_{BB} = 0.5$  [220]. Here we use  $\sigma_{AA}$ ,  $\epsilon_{AA}$  as the units of length and energy. We set the mass of all particles equal to  $m = 1.0$  and the Boltzmann constant is  $k_B = 1.0$ . Using the LAMMPS package we simulate a total of  $10^5$  particles at constant volume and temperature. The cubic simulation box has a side length of 43.68 which corresponds to a density of 1.2. At the lowest temperature,  $T = 0.4$ , the run was  $1.4 \cdot 10^8$  time steps (step size 0.005) for equilibration and the same length for production, time spans that are sufficiently large to completely equilibrate the system.

## 6.2 Model construction

To probe the three dimensional (3D) structure of the system we introduce a local coordinate system as follows:

- $\text{SiO}_2$ : Take any Si atom as the origin and its bonding to a nearest neighbor O (i.e.,  $\overrightarrow{\text{SiO}}$ ) defines the  $z$ -direction. We then find another nearest neighbor O of the Si and define the plane containing the three atoms as the  $z-x$ -plane. The  $y$ -axis is thus normal to the  $z-x$ -plane.

- BLJM: Take any three A particles that are nearest neighbors, i.e., they form a triangle with sides that are less than the location of the first minimum in the radial distribution function  $g(r)$ . We define the position of particle #1 as the origin, the direction from particle #1 to #2 as the  $z$ -axis, and the plane containing the three particles as the  $z-x$ -plane. The  $y$ -axis is thus normal to the  $z-x$ -plane.

This local reference frame allows to introduce a spherical coordinate system  $\theta, \phi, r$  and to measure the probability to find any other atom at a given point in space, i.e. to measure a four point correlation function (Fig. 6.1). Since this coordinate system is adapted to the configuration by the three particles it allows to detect angular correlations that are not visible in  $g(r)$ .

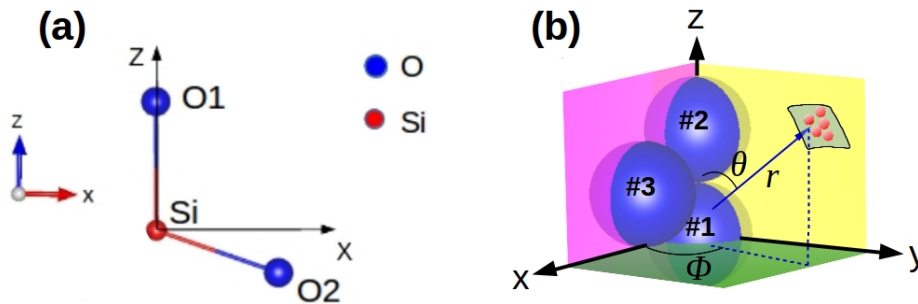


**Figure 6.1:** The definition of the local coordinate system involves three atoms/particles that are representatives of the local structure. (a)  $\text{SiO}_2$ . (b) BLJM.

### 6.3 Radial distribution function

To establish a base for the subsequent discussion of the three dimensional structural information, we show first the radial distribution functions  $g(r)$  (RDFs) of the two considered systems. Figure 6.2 shows the partial RDFs of silica at three different temperatures. The first peak for the SiO and SiSi correlations are located at  $r \approx 1.65 \text{ \AA}$  and  $r \approx 3.10 \text{ \AA}$ , respectively. These distances correspond to the first nearest neighbor distances of the two pairs and are only weakly dependent on temperature. With increasing  $T$ , the most noticeable feature is the broadening of the peaks at varied distances, indicating that the structure becomes less ordered.

Similarly, in Fig. 6.3 we show the partial RDFs of the BLJM system at various temperatures. The temperature varies from a very fluid state ( $T = 2.0$ ) to a moderately viscous one ( $T = 0.4$ ). For all four partials, one observes a slight shift of the main peaks and also the decrease in peak intensity with increasing temperature. Note that the N

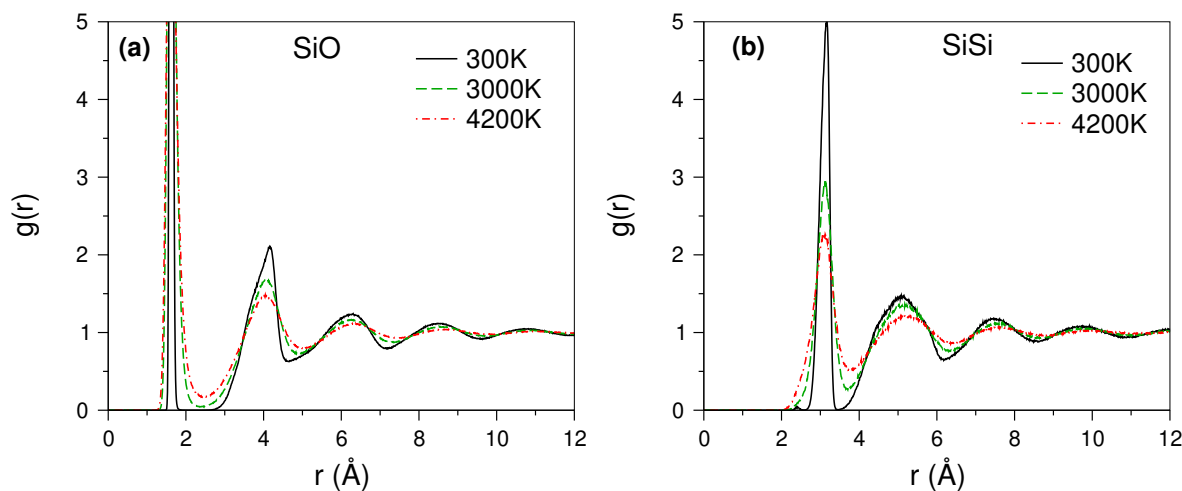


**Figure 6.2:** Radial distribution functions of silica at different temperatures. (a) and (b) are for SiO and SiSi correlations, respectively. 300 K is in the glass state and the other temperatures are in the liquid state. The curves were obtained by averaging over 8 samples.

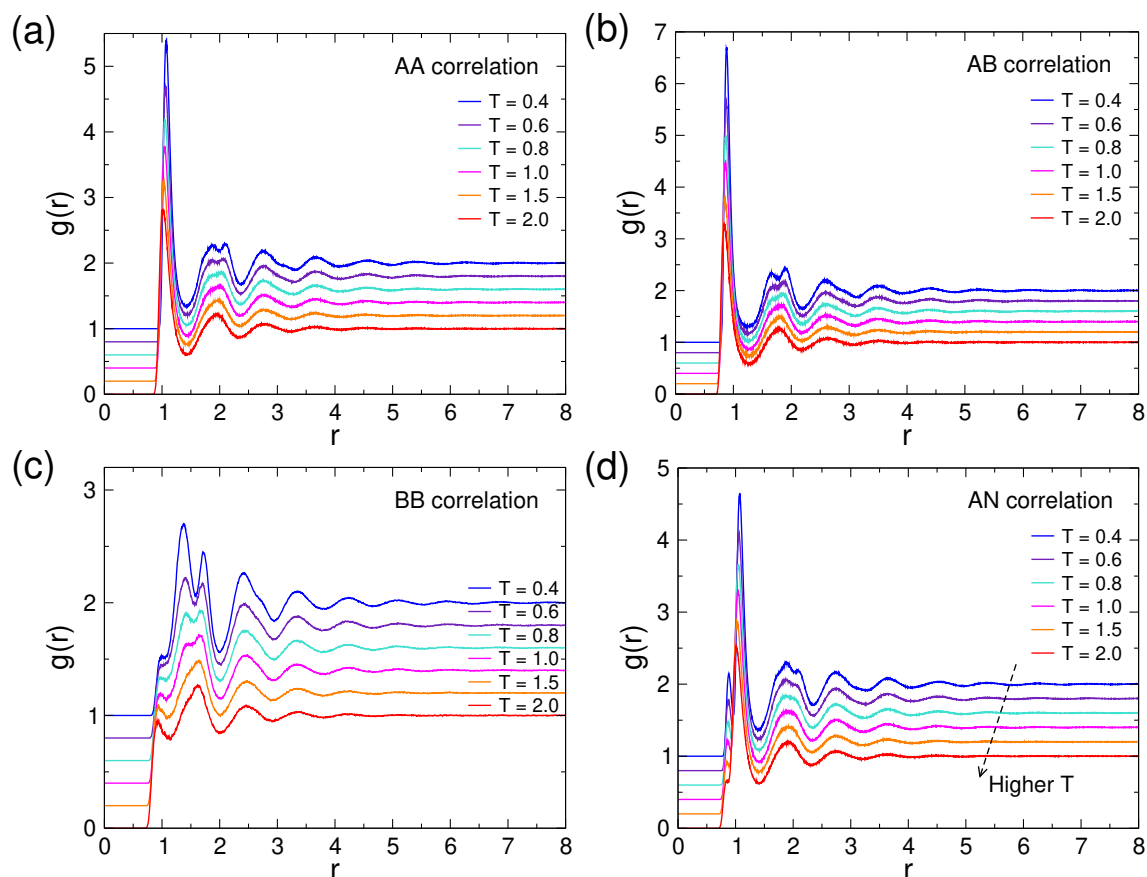


**Figure 6.3:** Radial distribution functions of the BLJM system at different temperatures. All temperatures are in the liquid state. The AA, AB, BB, and AN (N denotes A+B) correlations are shown in panel (a)-(d), respectively. The different curves have been shifted vertically by multiples of 0.2 for clarity. The curves were obtained by averaging over 20 configurations.



represents the sum of A and B, i.e., all particles in the system. For the sake of simplicity, we consider in the following only the AN correlation for the BLJM system.

Figure 6.2 and Fig. 6.3 illustrate that the  $T$ -dependence of  $g(r)$  is very smooth, indicating that both systems are good glass-formers. Therefore, crystallization is unlikely to happen either in the liquid or the quenched state (300 K for silica glass).

## 6.4 Three dimensional distribution of particles

Since  $g(r)$  is the spherical average of particle-particle correlations, the angular dependence of the structural information is lost. As mentioned earlier, by introducing a local reference frame we can explore angular correlations that are not visible in  $g(r)$ . Here we show first the 3D distribution of particles for the two systems.

Figure 6.4 shows the three dimensional normalized distribution  $\rho(\theta, \phi, r)$  of Si and O atoms on the sphere of radius  $r$  from the origin (i.e., a Si atom by construction). We recognize that  $\rho(\theta, \phi, r)$  has a noticeable angular dependence and which extends to large distances, e.g. 14 Å at 300 K. Furthermore we notice that these density maps all show pronounced tetrahedral symmetry. This observation is reasonable as  $[\text{SiO}_4]$  tetrahedron is the basic building block which forms the network of  $\text{SiO}_2$  structure. In addition, both the O and Si density maps show noticeable temperature dependence, i.e., the signal becomes more pronounced when temperature is decreased, implying that the structure of the system becomes more ordered. This finding is in accordance with the conventional knowledge that the glass state is more ordered than the corresponding liquid state.

Similarly, for the BLJM system, based on the introduced local reference frame, the three dimensional distribution of the particles can be probed. In Fig. 6.5 we show firstly the distribution of the particle density for a distance that corresponds to the first coordination shell of the central particle. The figure clearly shows that the density distribution is anisotropic and has an icosahedral-like symmetry (as indicated by the dashed line in (a)). We note that the icosahedral symmetry is due to the presence of large proportion of icosahedra-like local structure that one would find for a hard-sphere-like simple liquid. However, the icosahedral symmetry is not perfect since at these small distances many local motifs coexist and the most favorable structure is a bit different from icosahedron [228].

With the knowledge of the packing of particles in the nearest neighbor shell, we now can explore the particle distribution at larger distances. Figures 6.6(a-c) show the distribution  $\rho(\theta, \phi, r)$  for the BLJM at three temperatures. We recognize that  $\rho(\theta, \phi, r)$  has a strong angular dependence not only at small distances but also at intermediate

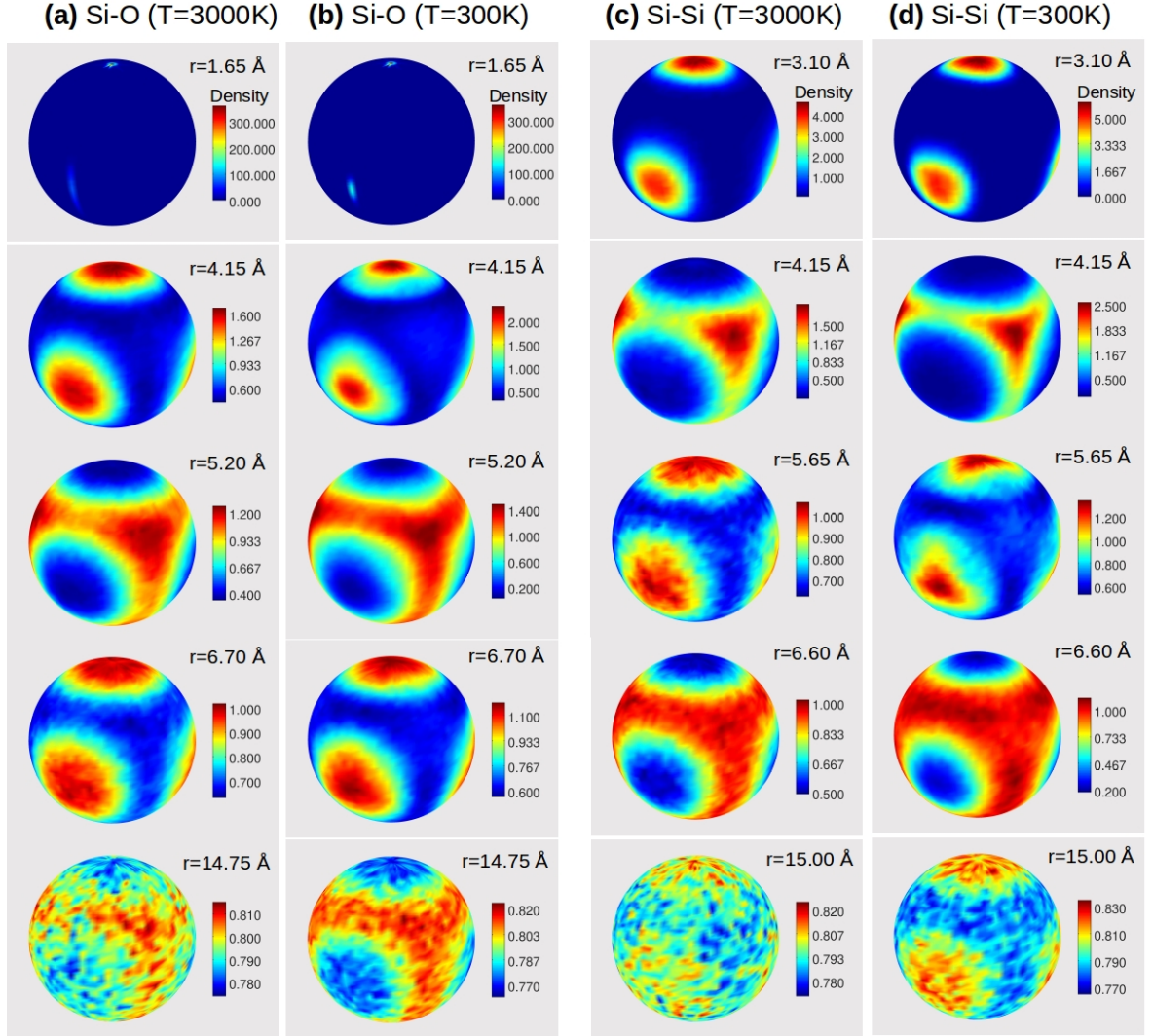


**Figure 6.4:** Distribution of particles in 3D for silica. Density distribution  $\rho(\theta, \phi, r)$  for different values of  $r$ , i.e., the distribution of the particles that are in a spherical shell of radius  $r$  and thickness  $1.0 \text{ \AA}$  around the central particle. (a) and (b) are for SiO correlations at 3000 and 300 K, respectively. (c) and (d) are for SiSi correlation at 3000 and 300 K, respectively.

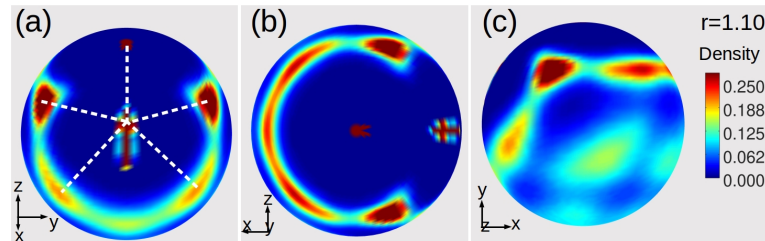


**Figure 6.5:** Distribution of the particles in 3D in the nearest neighbor shell for the BLJM at  $T = 0.4$ . Density distribution  $\rho(\theta, \phi, r)$  for  $r = 1.1$ . (a-c) are different perspectives of the density distribution on the sphere (see orientation of the coordinate system). The dashed lines indicate the connection between neighboring particles.

ones, e.g., at  $r = 4.5$ , and at low  $T$  even at large ones, e.g.,  $r = 8.0$ . Furthermore, for  $r = 1.65$ , corresponding to the distance between the first minimum and the second nearest neighbor peak in  $g(r)$ , one finds a dodecahedral-like symmetry. This result can be rationalized by recalling that a dodecahedron is the dual of an icosahedron, and vice versa, see Fig. 6.6(d), and hence the local dip formed by three neighboring particles in the first shell will be occupied by particles forming part of the second shell, thus giving rise to a dodecahedral symmetry. The fact that this “duality mechanism” works even at large distances is surprising since it is at odds with the standard view that in liquids correlations are quickly washed out at large distances.

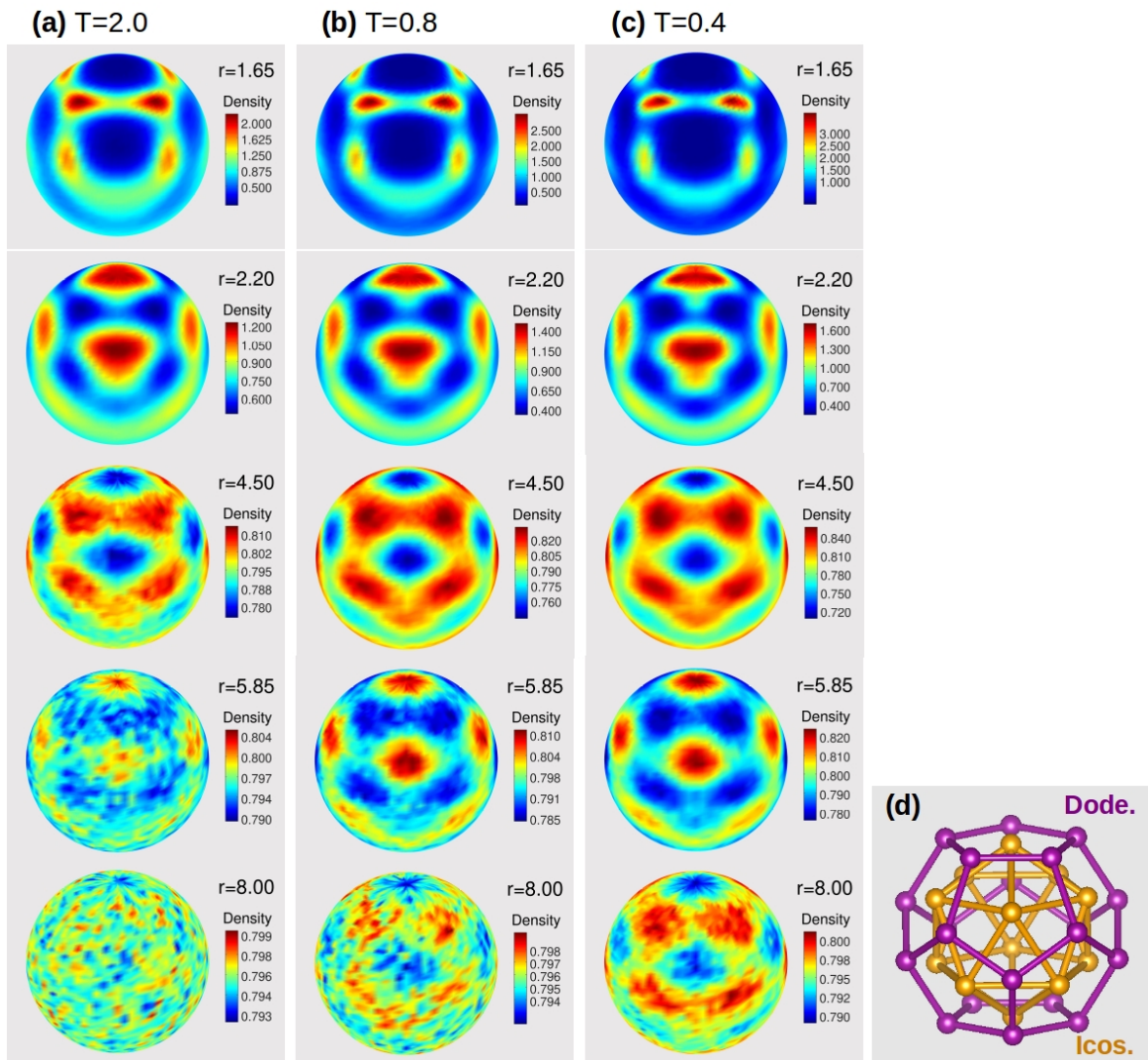


**Figure 6.6:** Distribution of particles in three dimensions for the BLJM system. In practice, the density distribution  $\rho(\theta, \phi, r)$  represents the distribution of particles that are in a spherical shell of radius  $r$  and thickness 0.4 around the central particle. (a), (b) and (c) are for  $T = 2.0$ , 0.8 and 0.4, respectively. Depending on the distance  $r$  the high density regions show an icosahedral or dodecahedral symmetry. (d) illustrates that an icosahedron is the dual polyhedron of a dodecahedron and vice versa.

Finally, we note that for geometrical reasons, at large  $r$  a region with high  $\rho(\theta, \phi, r)$  is *not* a single particle, but a structure that grows linearly with  $r$  and hence is a whole collection of particles, i.e., at a given distance the structure is given by patches with a high density of particles that alternate with patches with low density.

## 6.5 Quantitative characterization

The standard way to characterize in a quantitative manner the structural order on a sphere is to decompose the signal, here the normalized density distribution, into spherical harmonics  $Y_l^m$ ,

$$\rho(\theta, \phi, r) = \sum_{l=0}^{\infty} \sum_{m=-l}^l \rho_l^m(r) Y_l^m(\theta, \phi), \quad (6.2)$$

where the expression for the expansion coefficients  $\rho_l^m$  are given by

$$\rho_l^m = \int_0^{2\pi} d\phi \int_0^\pi d\theta \sin \theta \rho(\theta, \phi, r) Y_l^{m*}(\theta, \phi) \quad , \quad (6.3)$$

where  $Y_l^{m*}$  is the complex conjugate of the spherical harmonic function of degree  $l$  and order  $m$  [229]. In practice, this integration was done for silica by sampling the integrand over up to  $10^8$  points for each shell of width 1.0 Å. The corresponding numbers for the BLJM are  $2 \cdot 10^9$  and 0.4. One can thus consider the angular power spectrum

$$S_\rho(l, r) = (2l + 1)^{-1} \sum_{m=-l}^l |\rho_l^m(r)|^2. \quad (6.4)$$

For  $\text{SiO}_2$ , the component with  $l = 3$  is the most prominent one, see Fig. 6.7(a), a result that is reasonable in view of the tetrahedral symmetry that we find in the density distribution. In contrast to the case of silica, we find that for the BLJM system, the component with  $l = 6$  is the most prominent one, independent of  $r$ , Fig. 6.7(b). This result is reasonable since  $S_\rho(6, r)$  represents well both icosahedral and dodecahedral symmetries, which are also the symmetries that we find in the density plots.

In the following we will focus on the behavior of  $S_\rho(l, r)$  for its strongest mode in particular, and discuss the structural order encoded in this quantity. Unless otherwise specified, the results shown below will be for the SiSi correlation in silica and the AN correlation in the BLJM. For the other particle-particle correlations qualitatively the same conclusions can be made.

In Fig. 6.8 we show the  $r$ -dependence of  $S_\rho(l, r)$  for silica, panel (a), and the BLJM, panel (b). One observes that for both systems  $S_\rho(l, r)$  decays in an exponential manner with increasing  $r$ . Despite the smallness of the value of  $S_\rho(l, r)$  at large  $r$ , the function

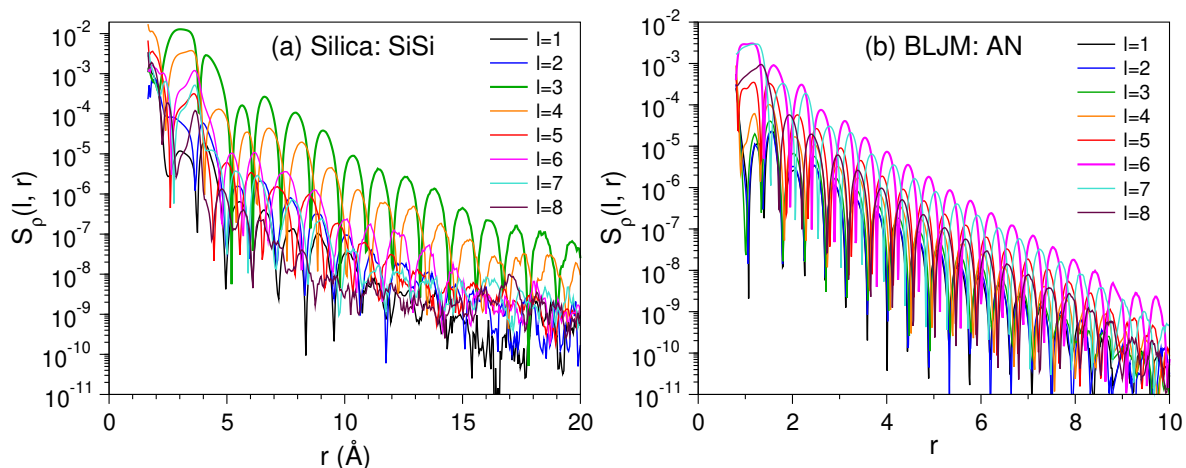


**Figure 6.7:** The angular power spectrum  $S_\rho(l, r)$  for (a) the SiSi correlation in silica and (b) the AN correlation in the BLJM. The temperature is 3000 K for silica and 0.5 for the BLJM. One recognizes that the signal for  $l = 3$  and  $l = 6$ , are the most pronounced modes for silica and the BLJM, respectively.

can be determined with good accuracy up to large distances, in agreement with the visual observation from the density plots. In order to probe the symmetry properties of the density field, we consider also a *normalized* density field  $\eta(\theta, \phi, r)$ , defined as

$$\eta(\theta, \phi, r) = \frac{\rho(\theta, \phi, r) - \rho_{\min}(r)}{\rho_{\max}(r) - \rho_{\min}(r)}, \quad (6.5)$$

where  $\rho_{\max}(r)$  and  $\rho_{\min}(r)$  are the maximum and minimum of  $\rho(\theta, \phi, r)$ , respectively. The angular power spectrum of  $\eta(\theta, \phi, r)$ ,  $S_\eta(r)$ , is included in Fig. 6.8(a-b) as well.

For the case of silica, panel (a),  $S_\eta(r)$  is high for small and intermediate distances, but even in this range it decreases slowly, indicating that for this network liquid the orientational symmetry is gradually lost with increasing  $r$ . For the BLJM,  $S_\eta(r)$  oscillates around a constant value before reaching a threshold  $\xi_\eta(T)$ . For distances larger than  $\xi_\eta(T)$ ,  $S_\eta(r)$  decays quickly and soon reaches at large  $r$  a value that is determined by the noise of the data. We will discuss the definition and the  $T$ -dependence of  $\xi_\eta(T)$  a bit later.

Very interestingly, we find for the BLJM the height of the local maxima in  $S_\eta(r)$  shows a periodic behavior in that a high maximum is followed by a low one. A visual inspection of  $\rho(\theta, \phi, r)$  reveals that these high/low maxima correspond to distances at which the distribution has an icosahedral/dodecahedral symmetry demonstrating that these two geometries are not only present at short distances but also at large ones, in agreement with the snapshots in Fig. 6.6. One thus concludes that the distribution of the particles in three dimensions is given by shells in which the particles are arranged in a pattern with alternating icosahedral/dodecahedral symmetry.

For distances larger than  $r \approx 4$  one finds that the radial position of these two

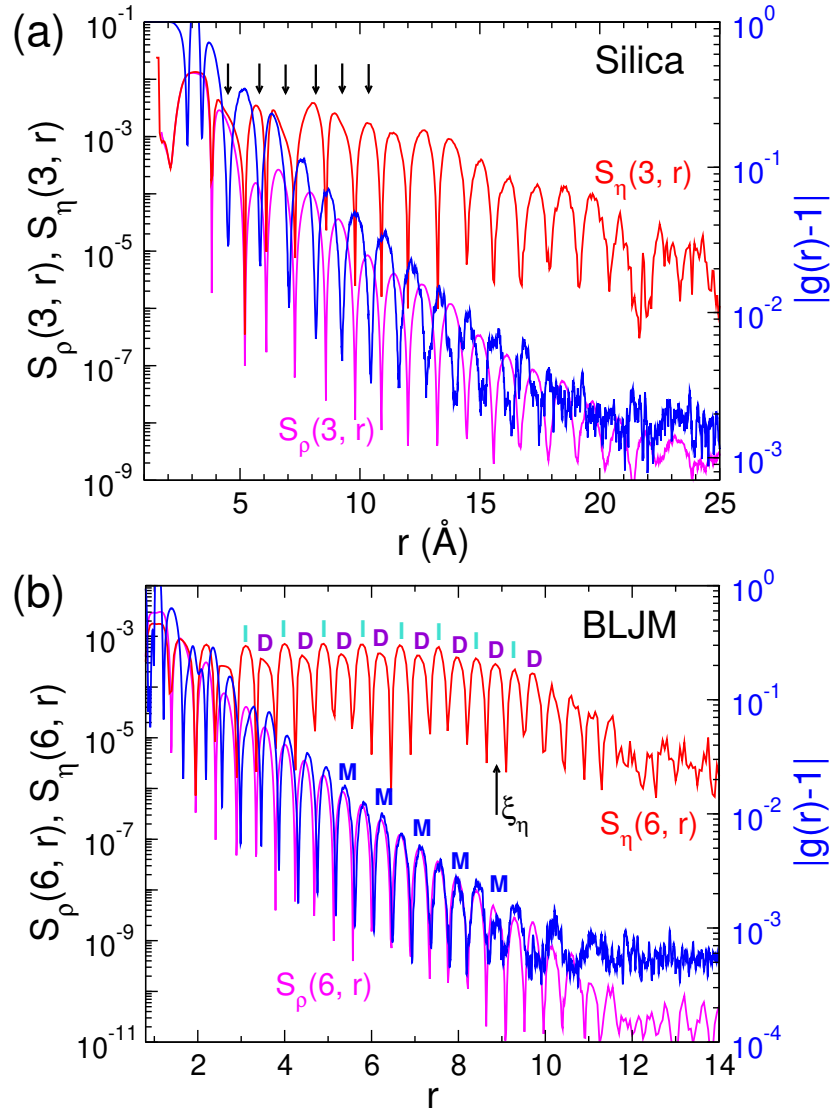


**Figure 6.8:** The angular power spectra and radial distribution function for (a) the SiSi correlation in silica at  $T = 3000$  K and (b) the AN correlation in the BLJM at  $T = 0.4$ . For  $\text{SiO}_2$  the arrows indicate the distances at which  $g_{\text{SiSi}}(r) = 1$ . For the BLJM and  $r > 4.0$  the high/low maxima in  $S_\eta(r)$ , labeled I and D, coincide with the minima/maxima (labeled M) in  $|g(r) - 1|$  (blue line, right ordinate). This up-down behavior is related to the alternating icosahedral/dodecahedral symmetry in the distribution of the particles when  $r$  is increased.

geometrical arrangements match well the locations of the minima/maxima in  $g(r)$ . This observation can be rationalized by the fact that a dodecahedron has 20 vertices (i.e., regions in which  $\rho(\theta, \phi, r)$  has high values) and an icosahedron only 12, thus making that the former structure corresponds to the *maxima* of  $g(r)$  and the latter to the *minima*. In contrast to this one finds no noticeable correspondence between the peaks in  $S_\eta(r)$  and  $g(r)$  for  $r < 3$ , indicating that the packing in the first few shells around the central particle has not just a pure icosahedral or dodecahedral symmetry but a more complex structure that is determined by steric and energetic considerations,

a result that is in agreement with previous studies of similar systems that have probed the geometry of the packing on small length scales [228, 230–232].

In contrast to the BLJM, we find that for silica, Fig. 6.8(a), the locations of the maxima in  $S_\rho(3, r)$  do not correspond to the ones in  $|g_{\text{SiSi}}(r) - 1|$  but are instead close to distances at which  $g_{\text{SiSi}}(r) = 1$  (as indicated by the arrows in the graph), i.e. at a distance at which one expects *no* structural order. This shows that for liquids which have an open network structure, the distances at which one finds the highest orientational symmetry is *not* associated with a dense packing of particles, in contrast to hard sphere like systems.

The 3D arrangement of these ordered zones extending to large distances are depicted in Fig 6.9 for  $\text{SiO}_2$ , panel (a), and the BLJM, panel (b), respectively. The BLJM system is characterized by alternating icosahedral/dodecahedral symmetry, whereas silica is dominated by four-fold tetrahedral symmetry.

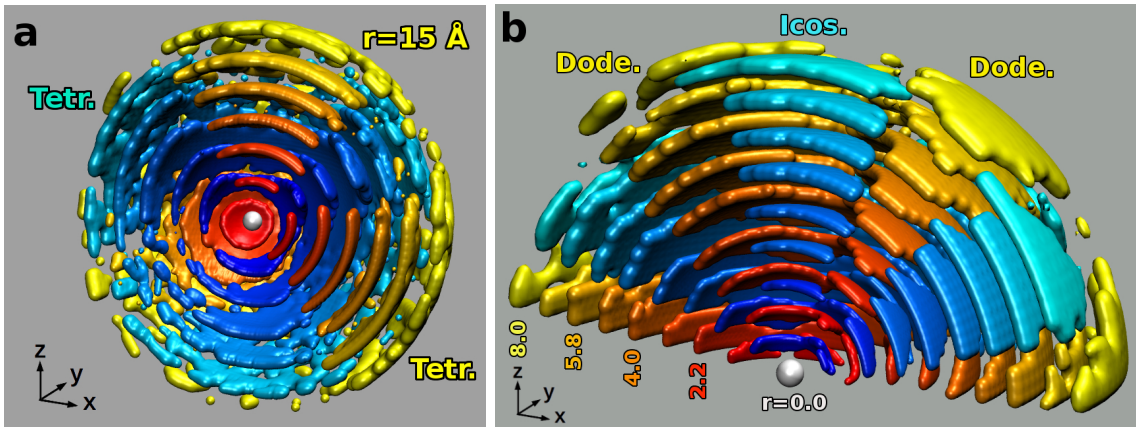


**Figure 6.9:** Three dimensional representation of the layered structure extending to large distances. (a) Silica at  $T = 3000$  K. The high density regions form interlocked zones with a tetrahedral symmetry. (b) BLJM at  $T = 0.4$ . The bluish/reddish colors correspond to the locations of the high/low maxima in  $S_\eta(r)$  and thus to shells with icosahedral/dodecahedral symmetry. The shown layers correspond to distances at which  $S_\rho(r)$  has a local maximum. Only regions with high density (covering 35% area of the sphere) are depicted.

For  $\text{SiO}_2$ , Fig 6.10(a) shows that  $S_\rho(3, r)$  strongly depends on temperature. At the highest  $T$ , i.e., 4200 K, the signal decays rapidly and survives only up to a distance of around 15  $\text{\AA}$ , indicating that the structure vanishes very quickly at such a high temperature. With decreasing  $T$ , the intensity of these peaks increases considerably, and at 2600 K (still in liquid state) the signal can survive beyond 20  $\text{\AA}$ . With further cooling below the glass transition temperature (around 2000 K), the system becomes even more ordered. At 300 K, the structural order can even be detected at distance larger than 25  $\text{\AA}$ . For comparison, in Fig. 6.10(c) we show the  $T$ -dependence of  $|g(r) - 1|$  for the SiSi correlation. Clearly, the  $T$ -dependence of this quantity is weaker than

that of  $S_\rho(3, r)$ , and the signal of the curves can only survive at smaller distances.

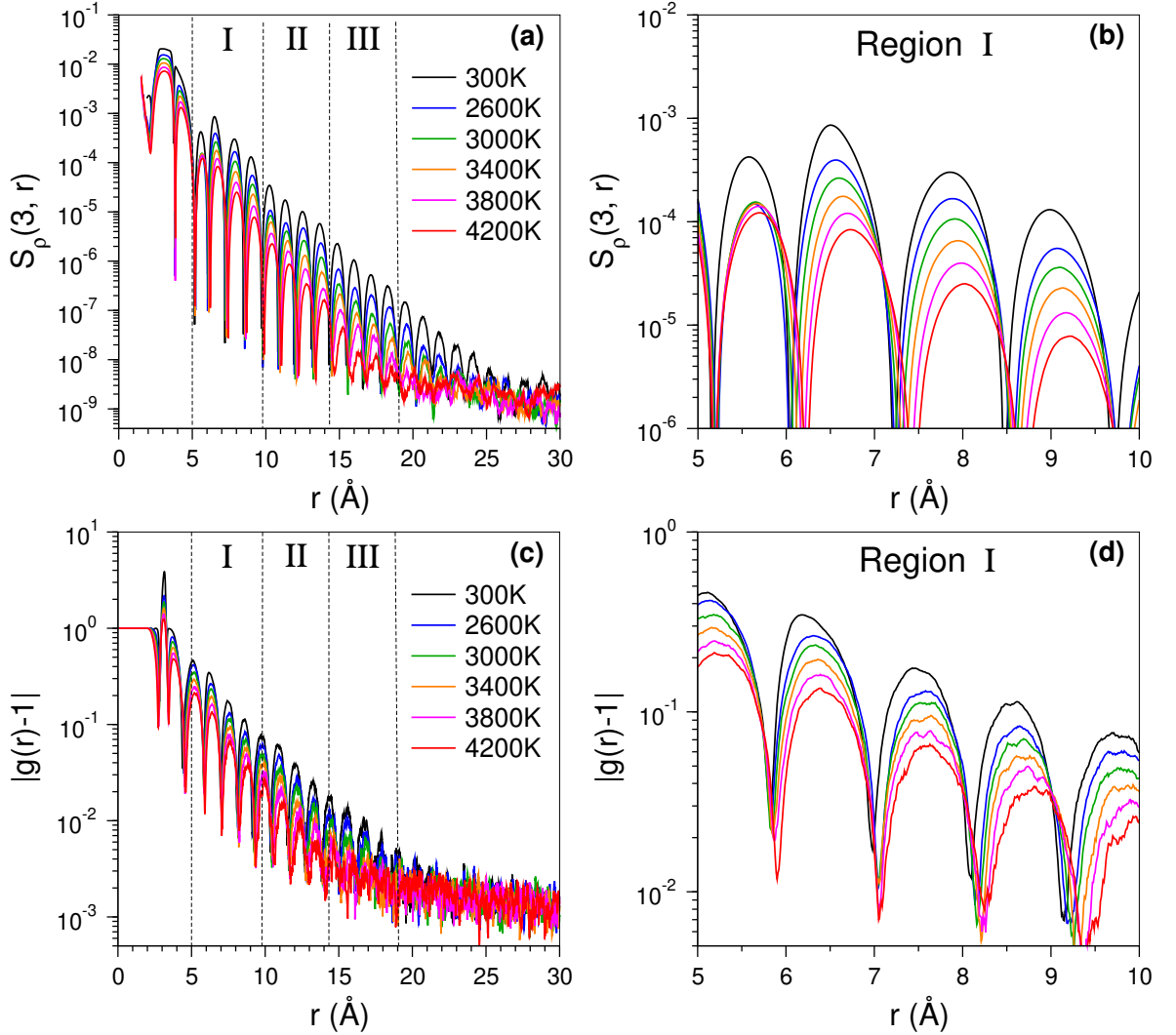


**Figure 6.10:** Temperature dependence of (a-b)  $S_\rho(3, r)$  and (c-d)  $g(r)$  of silica. Regions I, II, and III are obtained based on the  $T$ -dependence of the peaks of  $S_\rho(3, r)$ . (b) and (d) are close-up views of the peaks in region I for  $S_\rho(3, r)$  and  $|g(r) - 1|$ , respectively.

In addition, we note that  $S_\rho(3, r)$  exhibits an interesting  $T$ -dependence in the range  $5 \text{ \AA} < r < 10 \text{ \AA}$  (region I). The first peak in this range seems independent of temperature in the liquid state (from 4200 K to 2600 K), but a big jump shows up when the system becomes glass, see the close-up view in panel (b). The rest of the peaks in this distance range show a stronger dependence on temperature relative to the first peak. The distinct behavior of the peaks at different distances implies that the medium range structure changes in a complicated manner when varying temperature. This temperature effect seems to propagate to larger distances (region II and III) but becomes less and less pronounced with increasing  $r$ . The function  $|g(r) - 1|$ , by contrast, does not show such  $T$ -dependence in the medium and long ranges, see Fig 6.10(c-d).



**Extracting length scales.** For the BLJM, we have realized from Fig. 6.8(b) that one can define a length scale  $\xi_\eta$  based on the decaying behavior of  $S_\eta$ . To determine  $\xi_\eta$  we have calculated the integral  $I(r, T) = \int_0^r S_\eta(r', T) dr'$  and in Fig. 6.11(a) we plot this quantity as a function of  $r$ . For small and intermediate  $r$  the integral shows a basically linear increase with  $r$  since the integrand  $S_\eta(r)$  is essentially a constant. Once  $S_\eta(r)$  starts to decay  $I(r, T)$  becomes a constant. Using a fit with two straight lines this cross-over point can be determined accurately, giving thus  $\xi_\eta(T)$ .

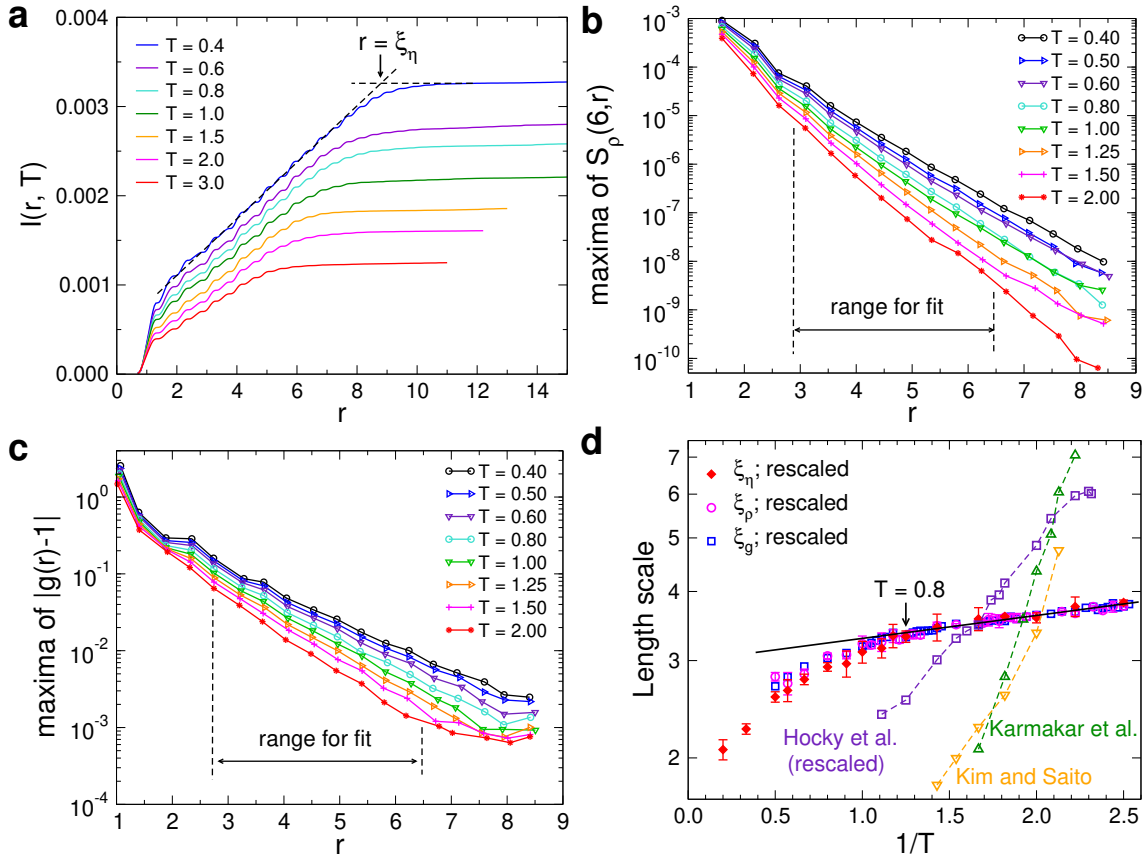


**Figure 6.11:** Extracting length scales in the BLJM system. (a):  $I(r, T)$ , the integral of  $S_\eta(r)$ . (b) and (c): Local maxima of  $S_\rho(6, r)$  and  $|g(r) - 1|$ , respectively. For both quantities, the data in the range  $2.8 < r < 6.5$  are fitted with an exponential function to extract the corresponding length scales. (d): Different length scales (on log scale) as a function of inverse temperature. See the text for the definitions of the various length scales.  $\xi_\eta$ ,  $\xi_\rho$ , and  $\xi_g$  have been multiplied by a scaling factor of 0.43, 2.58, and 1.29. Error bars are the standard error of the mean of eight samples. The solid line is a guide to the eye and the arrow indicates the location where  $T = 0.8$ . Also included are the dynamical length scale as obtained in previous studies [233–235]. The data from Hocky *et al.* have been multiplied by a factor of three.

In addition, one can also extract length scales based on the behavior of  $S_\rho(r)$  and  $g(r)$ . In 6.11(b) we show the  $r$ –dependence of  $S_\rho$  for different temperatures. Note that we plot only the local maxima of the function since these have been used to fit the data

at intermediate and large distances with an exponential function (see below). From the graph one recognizes that the slopes of the curves decrease with lowering temperature, indicating that the associated length scale increases. We thus obtain the length scale  $\xi_\rho$  by making a fit with an exponential of the form  $S_\rho(r, T) \propto \exp(-r/\xi_\rho(T))$ . In 6.11(c) we show the  $r$ -dependence of  $|g(r) - 1|$ . (Again only the location of the maxima are shown). We see that also this dependence can be fitted well by an exponential function, thus allowing to define a length scale  $\xi_g(T)$ .

Figure 6.11(d) shows the three (rescaled) length scales  $\xi_\eta$ ,  $\xi_\rho$  and  $\xi_g$  as a function of inverse temperature and one recognizes that, after appropriate rescaling, the three length scales collapse onto each other quite well. In the  $T$ -range considered, the scales change by about a factor of two, i.e. a relatively modest value. From the graph one recognizes two regimes: At high  $T$  the length scales increase quickly with decreasing  $T$  whereas at low temperatures one finds a weaker  $T$ -dependence and which is compatible with  $\ln(\xi) \propto T^{-1}$ . Hence one concludes that a decreasing temperature leads to an increasing static length scale, in agreement with previous studies that have documented a weak increase of static length scales in glass-forming systems [227]. Surprisingly the crossover between the two regimes occurs at around  $T = 0.8$ , thus very close to the so-called “onset temperature”  $T_o$  [220] at which the relaxation dynamics of the system crosses over from a normal dynamics to a glassy one [3]. The fact that also  $\xi_\eta$  and  $\xi_g$  exhibit this crossover behavior in their  $T$ -dependence further support the existence of  $T_o$ . This result shows that the change in the dynamical properties of the system has a counterpart in the statics, giving hence support to the idea that the latter allows to understand the former [236].

For the sake of comparison, we included in Fig. 6.11(d) also the results for the dynamic length scales that have been obtained in previous works for exactly the same model [233–235]. One observes that these dynamic length scales show a significantly stronger  $T$ -dependence than the static ones that we have considered here, a result that is consistent with earlier studies on this question [231].

**Structure factor and compressibility.** Since the  $T$ -dependence of  $\xi_g$  is very similar to the one of  $\xi_\eta$ , Fig. 6.11(d), one can expect that also the intensity of the static structure factor  $S(q)$  at small wave-vectors has the same  $T$ -dependence. Figure 6.12(a) shows the  $q$ -dependence of  $S(q)$  for different temperatures. Because of the finite size of the box, the smallest accessible wave-vector is  $2\pi/L \approx 0.144$  and one has only three independent wave-vectors with this modulus. In order to estimate with good accuracy the  $T$ -dependence of  $S(q)$  at small wave-vectors we have averaged  $S(q)$  over the range  $1 \leq q \leq 2$  (see the inset). The so obtained averaged data for  $S(q)$ , denoted as  $S_0$ , is plotted in Fig. 6.11(c). The straight line is a power-law fit to the low- $T$  data. (At this stage this functional form should be considered just as a parameterization of the data

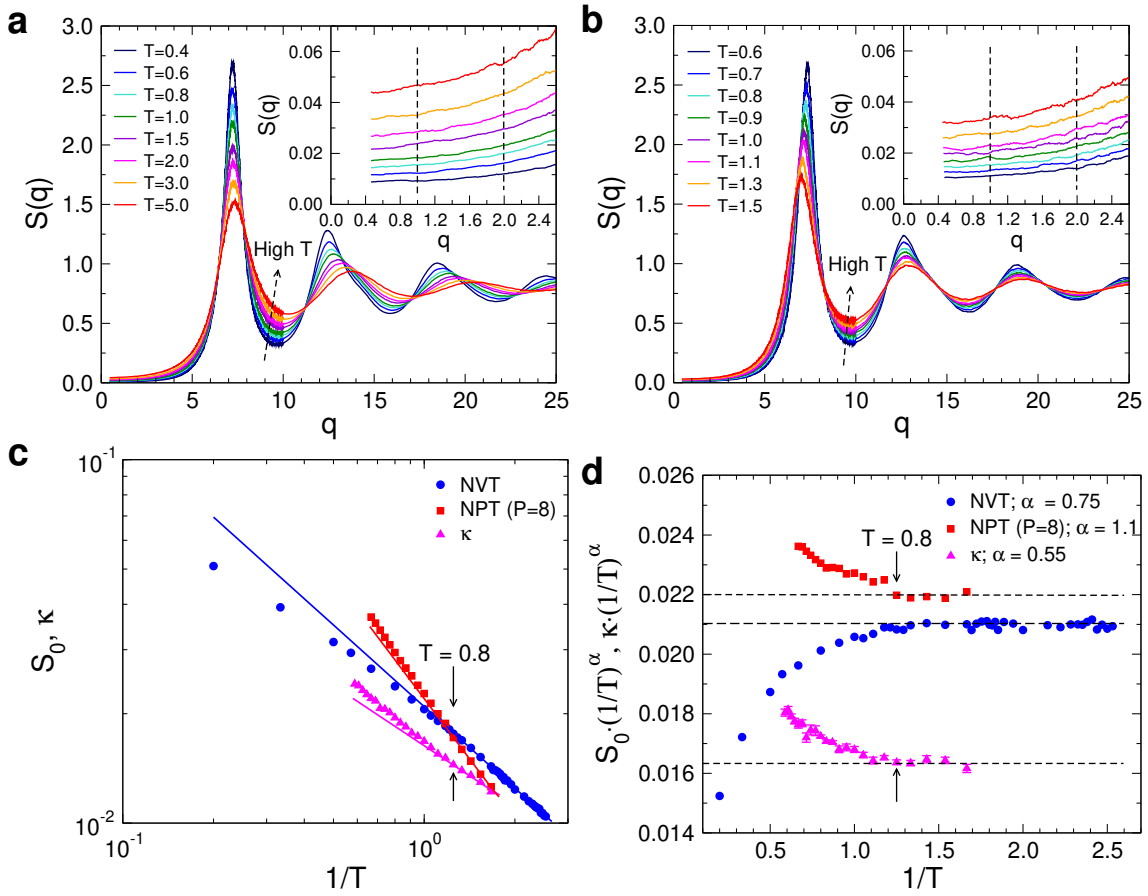


**Figure 6.12:** (a) and (b): Partial static structure factor  $S(q)$  for the AA pairs for the simulations at constant volume ( $NVT$ ) and constant pressure ( $NPT$ ), respectively. The insets show  $S(q)$  at small  $q$ . The two vertical dashed lines indicate the interval over which  $S(q)$  was averaged. (c)  $S_0(T)$  as obtained for the two ensembles as a function of inverse temperature. (d) Same data as in panel (c), now multiplied by  $(1/T)^\alpha$ , where the value of  $\alpha$  is given in the legend. The horizontal dashed lines are guides to the eye.

since we do not have a theoretical basis for it). In order to see better the  $T$ -range in which this fit works well, we shown in Fig. 6.11(d) the ratio between  $S_0$  and this power-law. One recognizes that this ratio shows a crossover at around the onset  $T_o \approx 0.8$ , a result that is coherent with the  $T$ -dependence of the extracted length scales.

The aforementioned results are obtained from constant volume ( $NVT$ ) simulations. In order to confirm that the observed  $T$ -dependence is independent of the simulation ensemble, we have also performed simulations at constant pressure ( $NPT$ ). The chosen pressure was  $P = 8.0$  since this corresponds to the pressure at the onset temperature in the constant volume ensemble and hence it can be expected that the onset temperature in the two ensembles are very similar. The resulting static structure factor is presented in Fig. 6.11(b) and the corresponding  $S_0$  is included in Figs. 6.11(c-d) as well. One observes from panel (d) that the data from the  $NPT$  simulations also show

at  $T \approx 0.8$  a change in its temperature dependence. This result demonstrates that the  $T$ -dependence of the large scale structure (i.e., at small wave-vectors) shows at the onset temperature a marked change which is independent of the considered ensemble.

For the  $NPT$  simulations we have determined also the compressibility

$$\kappa = \frac{(\Delta V)^2}{k_B TV}, \quad (6.6)$$

where  $(\Delta V)^2$  is the variance of the volume fluctuation and  $k_B$  the Boltzmann constant. The obtained  $\kappa(T)$  are presented in Figs. 6.11(c-d) as well. As expected, this quantity shows a similar temperature dependence as  $S_0$ , i.e., the description with the power-law starts to break down at around  $T \approx 0.8$ .

Based on the results shown in Fig. 6.11, one can conclude that a careful measurement of the structure factor or compressibility allows to estimate the onset temperature  $T_0$  with good accuracy, without referring to any probe of the *dynamics*.

**Anisotropic radial distribution function.** Since we have found that the distribution of particles in 3D is anisotropic, Figs 6.4 and 6.6, it is of interest to consider also the radial distribution functions in which one probes the correlations in a specific direction with respect to the local coordinate system. We note that this type of information is also accessible in experimental studies, e.g., confocal microscopy or scattering experiments [237]. For both the BLJM and silica, the directions of particular interest are the ones correspond to the vertices of the polyhedra that we have identified earlier, see the snapshots in Figs. 6.13(a-b). Also interesting is the direction corresponding to the mid-point of two neighboring vertices of the polyhedra, which is supposed to have a smaller signal relative to other directions.

Quantitatively, Figs. 6.13(c-d) show for the BLJM this angular dependent correlation function for the directions that correspond to the vertices of the icosahedra ( $g_D(r)$ ) and of the dodecahedra ( $g_D(r)$ ). We recognize that for intermediate and large distances,  $g_D(r)$  has oscillations that are in phase with  $g(r)$  whereas  $g_I(r)$  has oscillations that are in anti-phase. The amplitudes of the oscillations in  $g_I(r)$  and  $g_D(r)$  are significantly larger than the ones found in  $g(r)$ , a result that is reasonable since the latter function is a weighted average of the two former ones and hence will be affected by cancellation effects. We also show in the same graph the distribution function in the direction that corresponds to the mid-point of the line connecting two neighboring vertices of an icosahedron and a dodecahedron,  $g_0(r)$ . It shows significantly smaller oscillations than  $g(r)$ , a result that is expected since one probes the structure in a direction which does not pass close to the locations that correspond to the vertices of the icosahedra/dodecahedra. Panel (b) shows that the decaying behavior of  $g(r)$ ,  $g_I(r)$ , and  $g_D(r)$  is basically independent of the function considered, demonstrating that they are indeed closely related to each other.

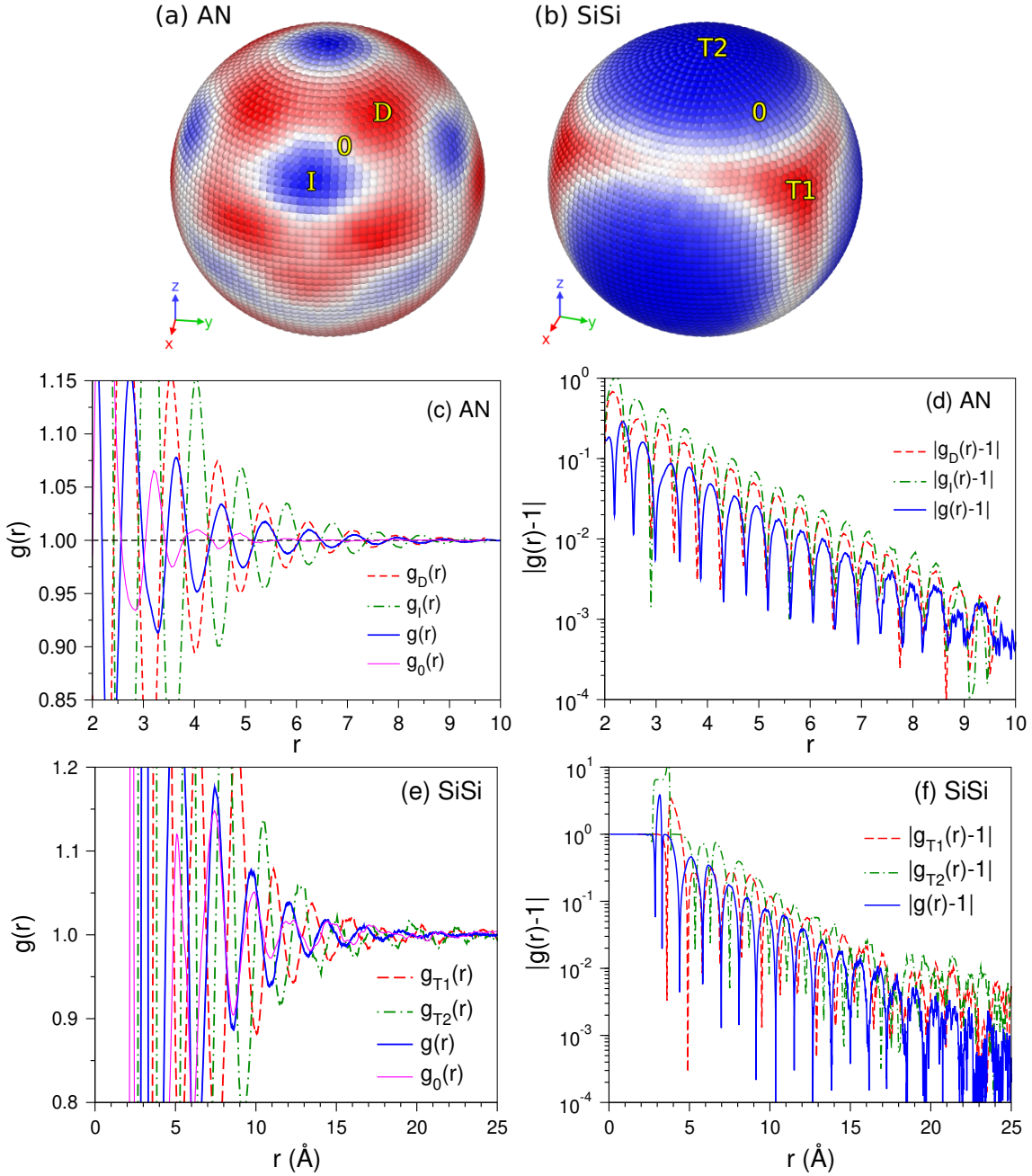


**Figure 6.13:** Anisotropic radial distribution function. (a) and (b): Two density maps showing the selected directions of probing for the AN correlation in the BLJM and ( $r = 4.5$ ) the SiSi correlation in silica ( $r = 4.15$  Å), respectively. (c) and (d): The BLJM at  $T = 0.4$ . Radial distribution function as measured in the direction of the vertices of the icosahedra,  $g_I(r)$  and the direction of the vertices of the dodecahedra,  $g_D(r)$ . The function  $g_0(r)$  probes the structure in the direction corresponding to the mid-point of the line connecting two neighboring vertices of an icosahedron and a dodecahedron. Also included is the conventional  $g(r)$ , i.e., averaged over all directions. (e) and (f): Silica at  $T = 300$  K. The function  $g_{T1}(r)$  and  $g_{T2}(r)$  probe the structure in the two directions corresponding to vertices of the interlocked tetrahedral symmetry.  $g_0(r)$  is similar to  $g_0(r)$  for the BLJM. (c) and (e) show these functions on linear-linear scale, whereas (d) and (f) on log-linear scale.

Figs. 6.13(e-f) show for the case of  $\text{SiO}_2$  the angular-dependent  $g(r)$  in three directions:  $T1$  and  $T2$  correspond to two directions of the vertices of the interlocked tetrahedral symmetry (see the snapshot in Fig. 6.4(d) when  $r = 4.15 \text{ \AA}$ );  $T_0$  represents the direction corresponding to mid-point of the line connecting  $T1$  and  $T2$ . Similar to the findings for the BLJM, one observes that also for this open-network system the angular-dependent  $g(r)$  can be much more pronounced than the conventional  $g(r)$ .

## 6.6 Summary

We have demonstrated firstly the fact that conventional  $g(r)$  (which takes spherical average of the particle distribution) allows only a very basic understanding of the structure of disordered systems. More insights into the structure, particularly beyond the short range distances, require more than two-point correlation functions.

Our approach which takes into account the angular dependence of the structure reveals that liquids and glasses have non-trivial structural symmetries that extend to distances well beyond the first few nearest neighbors and which have gone unnoticed so far. This conclusion is reached by looking at the 3D particle distribution and the angular power spectrum of the density field for two very different glass-forming systems, i.e., silica and the BLJM. We find that silica is dominated by a tetrahedral symmetry whereas the BLJM system shows an interesting alternating icosahedral/dodecahedral symmetries.

In addition, we find that, for silica, the  $T$ -dependence of  $S_\rho(3, r)$  shows the signature of complex structural changes that are invisible from  $g(r)$ . For the BLJM, by looking at the  $T$ -dependence of various length scales, we find two regimes which cross at around the onset temperature  $T_o$ , suggesting that the change in the dynamical properties of the system has a counterpart in the statics. This finding is further supported by the fact that the static structure factor and compressibility of the system also show a crossover in their  $T$ -dependence at around the  $T_o$ . We thus conclude that the  $T_o$  can also be determined from careful experimental measurements.

Furthermore, based on the spherical density map, we have probed the structural correlations in specific directions. We find that depending on the selected direction, the anisotropic  $g(r)$  can be much more pronounced than the conventional  $g(r)$ , thus highlighting the importance of considering the angular dependence of the structure.



# Summary and outlook

## Summary

This thesis aimed at obtaining microscopic insights into the properties, notably the fracture behavior, of oxide glasses. Taking advantage of atomistic simulation techniques, we have explored systematically the properties of silica and sodium silicate in the liquid and glass states. Figure S1 summarizes the major research topics that have been covered in this thesis. The results documented in this manuscript have brought several new insights into the structure, surface, deformation and fracture of oxide glasses.

In chapter 1, we briefly introduced the structure and mechanical properties of oxide glasses. We also presented a comparative review of recent experimental and simulation studies of glass fracture. A brief introduction of the fundamentals of atomistic simulation techniques is included as well.

In chapter 2, we presented the results concerning the importance of interaction potential and simulation protocol on a realistic description of glass properties. It is found that the mechanical properties of the glasses are considerably more sensitive to the interaction potential than the structural properties. In addition, as the deformation and fracture of glass involve strongly non-local processes, simulations with relatively large system size are required to minimize the finite size effects. Regarding the simulation protocol, this study emphasizes that (Mode I) fracture simulation should be performed under constant pressure, rather than constant volume.

In chapter 3, we investigated systematically the deformation and fracture of glasses with bulk and sandwich geometries. The latter represents the glasses with surface flaws. For the bulk glasses, both the stress-strain behavior and elastic constants are in good agreement with the experimental results, indicating the reliability of the adopted potential and simulation setup. To investigate the fracture process, the sandwich glasses are notched on the surface. The stress-strain responses of the two types of glasses show qualitatively the same compositional dependence, and exhibit an interesting transition behavior in the macroscopic stiffness (given by the tangent modulus) as the  $\text{Na}_2\text{O}$



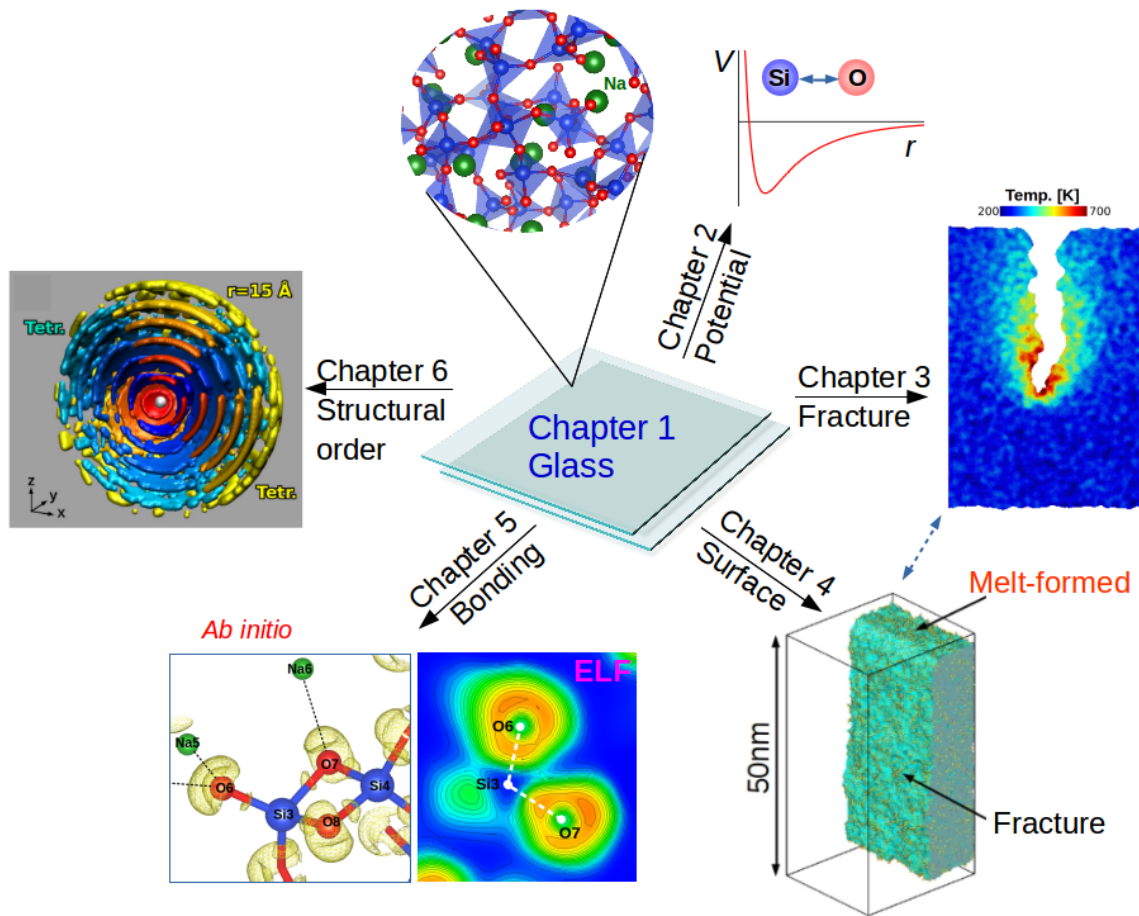


**Figure S1:** Schematic summary of the research topics covered in this thesis. The structure and properties of sodium silicate glasses are explored by using atomistic simulation techniques.

concentration reaches  $\approx 10$  mole%. Further exploration of the microscopic properties reveals that this transition behavior originates from the nonaffine part of the atomic displacement.

In addition, the cavitation analysis shed light on the fracture mechanism at the microscopic scale. Voids with radius  $R \approx 4 \text{ \AA}$  are detected in the unstrained glasses, weakly depending on the composition. Fracture of silica glass is attributed to pure rupturing of bonds at the crack tip, whereas fracture of the Na-rich NS3 glass is accompanied by the growth and coalesce of voids ahead of the crack tip. The estimated crack velocities and various sound wave speeds are compatible with experimental measurements and the theoretical predictions from linear elastic fracture mechanics.

Following chapter 3, we focused in chapter 4 on the nanoscale features of the two types of surfaces of soda-silicate glasses, namely the melt-formed surface (MS) and fracture surface (FS). It is found that the MS is more abundant in Na and NBO than the FS, whereas the FS has more under-coordinated Si than the FS. The differences between

---

the MS and FS are attributed to their production history. In addition, we find that the fluctuations in composition and charge quickly wash out and become unnoticeable when the distance from the surface is larger than  $\approx 2$  nm. Further analysis of the roughness of the surfaces show that the MS is relatively smooth (with a RMS roughness  $\approx 0.25$  nm) and isotropic, whereas the FS is relatively rough (RMS roughness ranges from  $\approx 0.4$  to  $\approx 0.8$  nm) and anisotropic. Finally, our results regarding the scaling property of the FS suggest that fractal description does not work at the nanoscale. We have also given evidence to demonstrate that insufficient spatial resolution of the surface measurement can lead to the wrong conclusion that the FS exhibits power-lawing scaling at the nanoscale.

In chapter 5, we have used *ab initio* simulations to explore glass surface properties that are otherwise less accurate or even inaccessible in classical simulations, i.e., vibrational and electronic properties. For the first time, the vibrational and electronic signatures of the structural units that are more abundant on the surface, e.g., two-membered ring, have been identified for silica and sodosilicate glasses. The analysis of electronic property shows that the bond ionicity as calculated from the Bader atomic charge is compatible with the conclusions from the electronic localization functions. Together with the knowledge of bond length, we have deduced qualitatively the bond strengths of various kinds of Si-O and Na-O bonds in sodium silicate glasses. These information may facilitate the understanding of crack propagation in oxide glasses.

In chapter 6, we dealt with a fundamental question regarding the hidden structural order in liquids and glasses. We have introduced a new approach for probing the structure of disordered systems and demonstrated its versatility by applying it to silica (open network) and a binary Lennard-Jones mixture (hard-sphere-like). It is found that both silica and the BLJM have non-trivial structural symmetries that extend to distances well beyond the short range. More specifically, silica is dominated by a tetrahedral symmetry, whereas for the BLJM alternating icosahedral/dodecahedral symmetries are found. The obtained results highlight the importance of considering angular-dependent measures for probing the structure of liquids and glasses.

## Outlook

This thesis opens many interesting prospects that can be pushed further to gain more insights into the properties of glasses (or disordered materials in general). Several directions are highlighted below.

Firstly, this work concentrates on the properties of silica and sodo-silicate systems, i.e., simplified compositions for oxide glasses. However, the methodologies proposed in this manuscript are certainly applicable to glass compositions of more commercial

interests, e.g., soda-lime-silica (window glass), sodium borosilicate (kitchenware). From a simulation point of view, such extension requires the usage of reliable interatomic potentials. For the aforementioned ternary systems, there are a few options that are currently available [84, 238–242].

Secondly, further extension of this work can be done by introducing chemical-mechanical interactions into the simulations, e.g. the interaction between the glass network and water molecules. In fact, such simulations have been performed since decades, but the considered system sizes are relatively small even with the current available computational power. A proper evaluation of finite size effects and simulation protocol is needed before one can gain useful insights from these simulations.

In chapter 3, the correlation analysis between various microscopic properties were conducted for the Na-rich NS3 glass at 300 K. A very natural extension of this work would be the exploration of how the correlations evolve with varying glass composition (e.g.,  $\text{Na}_2\text{O}$  concentration or different types of alkali oxides). Also, one may want to understand the thermal effects during the deformation of the glasses. Therefore, further studies of these local properties at very low temperatures (minimizing the thermal effects) or elevated temperatures will be interesting.

The method for structural characterization as introduced in chapter 6 is also applicable to other disorder systems such as colloidal and granular systems for which the particle coordinates are accessible. The application of this method to other disordered systems will provide useful insights regarding the nature of these systems. In addition to exploring the static structural features of a system, it is also worthwhile to monitor the time-dependence of the proposed correlation functions. With this type of information, one can elucidate better the relationship between statics and dynamics of disordered systems.

To conclude, we believe that this work not only bring several original insights into the properties of oxide glasses on the microscopic scales, but also paves the way for further investigation on the properties of other disordered materials under various environments.

# Résumé en français

## Motivations

Les matériaux vitreux tels que les verres à vitre, la verrerie de cuisine et les fibres optiques sont une partie intégrante de notre vie quotidienne. Parfois, nous ne remarquons même plus leur présence en raison de leur transparence. La fiabilité mécanique est devenue une exigence cruciale dans les utilisations diverses des matériaux vitreux modernes. En effet, les verres d'oxydes sont des matériaux fragiles et cassants, ce qui représente leur défaillance majeure caractérisée par l'apparition et la propagation de fissures. La compréhension du comportement à la fissuration du verre est donc d'une importance fondamentale pour la conception de produits en verre aux performances mécaniques améliorées.

La complexité de la fissuration des verres d'oxydes réside principalement dans le fait que la fracture est un phénomène multi-échelle, c'est-à-dire que des mécanismes différents se produisent sur plusieurs échelles de longueur, voir Fig. S2. Cependant, tout processus de fissuration implique en fin de compte la rupture des liaisons atomiques. Ce processus à l'échelle atomique influence donc de manière critique la ténacité et comportement global à la fissuration de ces matériaux. La compréhension fondamentale de la fracture du verre nécessite des connaissances approfondies à l'échelle atomique. Ceci représente ainsi est la motivation première de ce travail de thèse.

Une motivation supplémentaire de cette thèse concerne une compréhension plus approfondie de la structure du verre et des systèmes désordonnés en général. Dans les études expérimentales et les de simulations, la structure des liquides et des verres est principalement caractérisée par des fonctions de corrélation à deux points telles que le facteur de structure statique et la fonction de distribution radiale. Cependant, ce type de mesure structurelle est loin d'être suffisante pour fournir une connaissance complète spectre complet des caractéristiques structurelles de ces systèmes. Nous avons donc été motivés à proposer de nouvelles approches pour obtenir plus d'information sur la structure de ces systèmes désordonnés. Ce travail de thèse vise l'obtention d'une compréhension fondamentale de la structure et du comportement à la fissuration

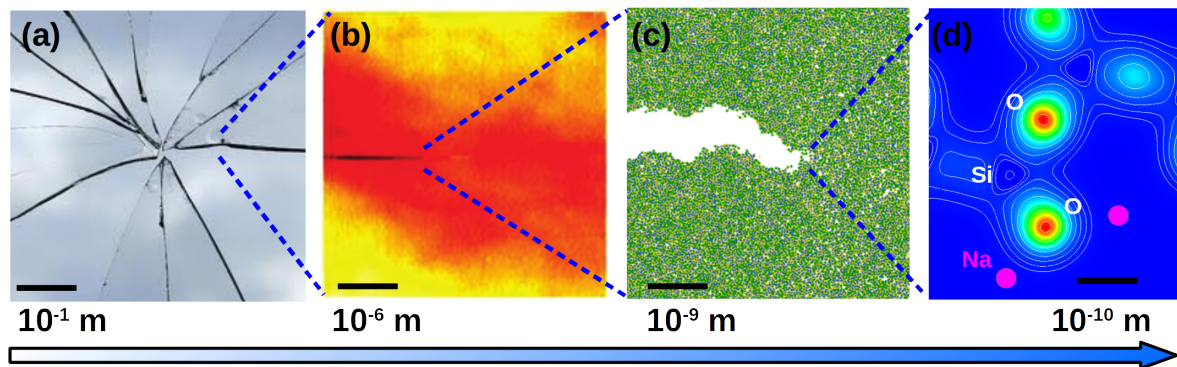


**Figure S2:** Fracture multi-échelle du verre. La fissuration qui se propage dans des solides tels que les verres d'oxyde implique des mécanismes qui s'étendent sur plusieurs gammes d'échelles de longueur. (a) Fissuration macroscopique d'une vitre provoquée par un impact. (b) Évolution à l'échelle micrométrique d'une fissure telle que mesurée par microscopie à force atomique. Image adaptée de Pallares *et al.* [12]. (c) Détails à l'échelle nanométrique de la géométrie de la fissure obtenue par modélisation atomistique (ce travail). (d) Visualisation à l'échelle atomistique de la densité de charge volumique autour des liaisons Si-O cassées. (ce travail).

des verres d'oxydes à l'échelle microscopique. À cette fin, nous combinons plusieurs techniques de simulation atomistique et analyse. Les systèmes étudiés sont la silice et des silicates de sodium, qui sont des compositions représentatives pour des verres d'oxydes complexes.

## Résultats

En utilisant des techniques de simulation atomistique, nous avons donc exploré systématiquement les propriétés de la silice et des silicates de sodium à l'état liquide et vitreux. La figure S3 résume les travaux de recherche principaux effectués durant cette thèse. Les résultats présentés dans ce manuscrit apportent de perspectives nouvelles sur la structure, la surface, la déformation et la fracture des verres d'oxydes.

**Potentiel interatomique.** Dans le chapitre 2, nous avons présenté les résultats concernant l'importance du potentiel d'interaction et du protocole de simulation pour une description réaliste des propriétés du verre. On constate que les propriétés mécaniques des verres dépendent fortement du potentiel, ce qui n'est pas le cas pour leurs propriétés structurales. De plus, comme la déformation et la fissuration du verre impliquent des processus fortement non locaux, des simulations avec des tailles de système relativement grandes sont nécessaires pour minimiser les effets de taille finie. En ce qui concerne le protocole de simulation, cette étude souligne que la simulation de la fracture (Mode I) doit être effectuée à pression constante plutôt qu'à volume constant.

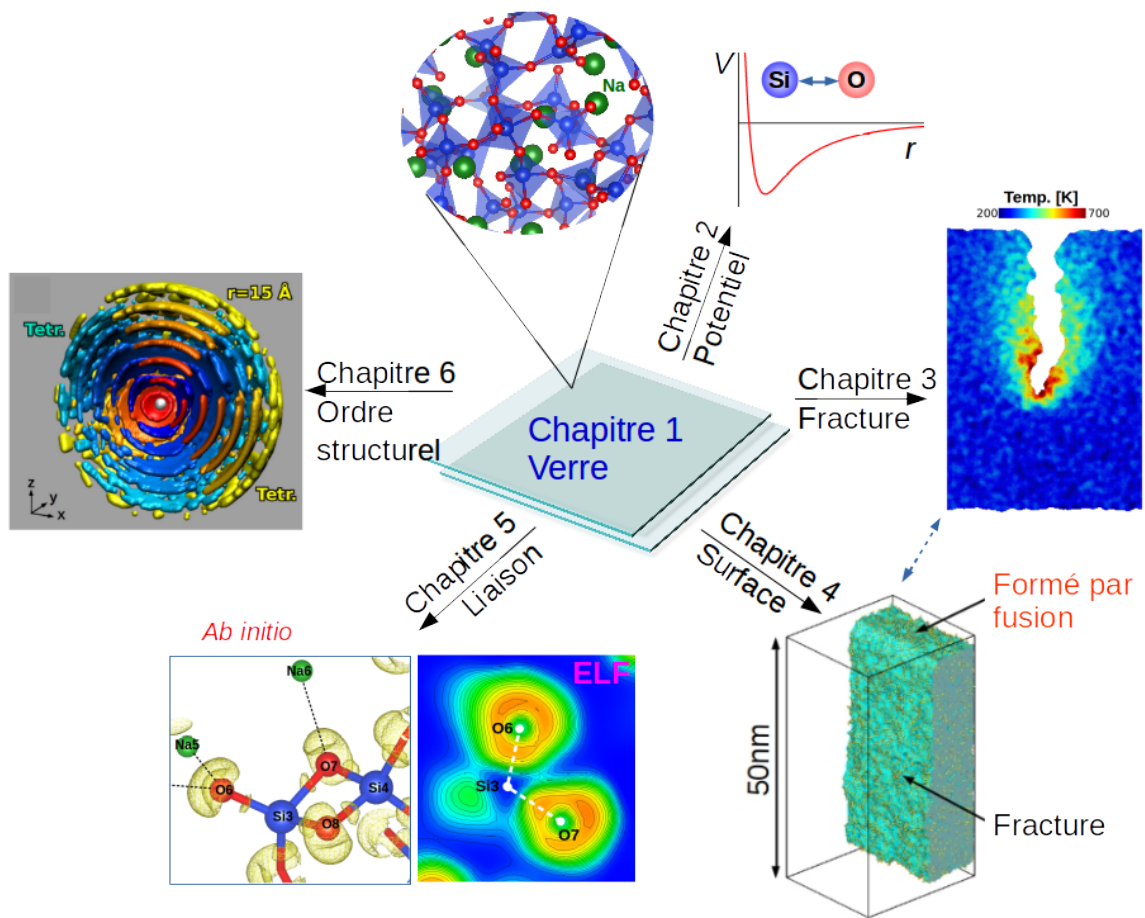


**Figure S3:** Représentation schématique des études effectuées durant cette thèse. La structure et les propriétés de verres de silicate de sodium sont explorées en utilisant des techniques de simulation atomistique.

**Déformation et fracture.** Dans le chapitre 3, nous avons étudié systématiquement la déformation et la fracture des verres avec 2 géométries: une massive et une de type sandwich (voir Fig. S4). La deuxième géométrie est plus appropriée pour des verres présentant des défauts de surface. Pour les verres massives, le comportement contrainte-déformation et les constantes élastiques sont en bon accord avec les données expérimentales, ce qui confirme la fiabilité du potentiel adopté et la configuration de simulation. Pour étudier le processus de fracture, les verres avec une géométrie sandwich sont entaillés à la surface. Les réponses contrainte-déformation des deux types de verres montrent qualitativement la même dépendance en fonction de la composition et présentent un comportement de transition intéressant pour la rigidité macroscopique (donnée par le module tangent) lorsque la concentration en  $\text{Na}_2\text{O}$  atteint  $\approx 10$  mole%. Une exploration plus approfondie des propriétés microscopiques révèle que ce comportement est dû aux déplacements atomiques non-affines des atomes constituants. De plus, une analyse des cavités a mis en lumière le mécanisme de fracture à l'échelle microscopique. Des cavités de rayon  $R \approx 4 \text{ \AA}$  sont détectées pour les verres non con-

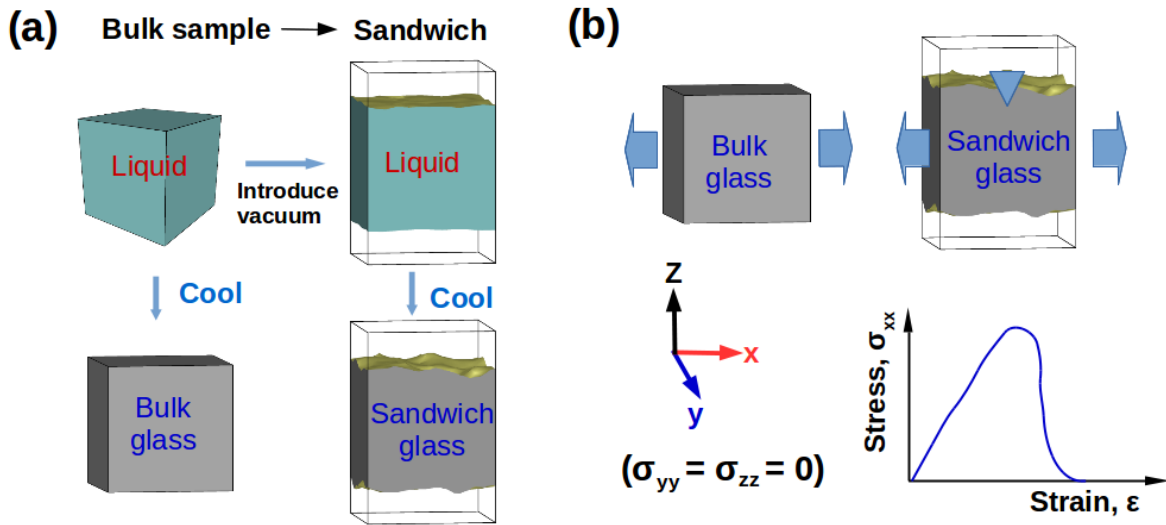


**Figure S4:** Schéma des protocoles de simulation. (a) Préparation des échantillons de verre massif et sandwich. (b) Fracture du verre par tension uni-axiale. La courbe contrainte-déformation correspond à la direction de traction. Les taux de refroidissement appliqués sont respectivement de 0,25 et 0,125 K/ps pour les échantillons massif et sandwich. Le taux de déformation est de 0,5 /ns.

traints, en fonction de la composition. La fracture du verre de silice est attribuée à la rupture des liaisons à la pointe de la fissure, tandis que celle du verre NS3 riche en Na s'accompagne de la croissance et de la fusion des cavités en amont de la pointe de fissure. Les vitesses de fissuration estimées et les différentes vitesses d'ondes sonores sont compatibles avec les données expérimentales et les prédictions théoriques de la mécanique de la fissuration élastique linéaire.

**Caractéristiques des surfaces.** Dans le chapitre 4, nous nous sommes concentrés sur les caractéristiques à l'échelle nanométrique des deux types de surfaces des verres de silicate de sodium, à savoir la surface formée par fusion (MS) et la surface formée lors de la fracture (FS). On constate que la surface MS contient plus de Na et NBO que la surface FS, alors que la surface FS a plus de Si sous-coordonné. Les différences entre ces deux surfaces sont attribuées à leur historique de fabrication. De plus, nous constatons que les fluctuations de composition et de charge disparaissent rapidement et deviennent négligeables lorsque la distance par rapport à la surface est supérieure à  $\approx 2$  nm. Une analyse plus approfondie de la rugosité des surfaces montre que la surface MS est relativement lisse (avec une rugosité RMS  $\approx 0.25$  nm) et isotrope, tandis que la surface FS est relativement rugueuse (la rugosité RMS varie de  $\approx 0.4$  à  $\approx 0.8$  nm) et anisotrope. Enfin, nos résultats pour la surface FS suggèrent que une description fractale ne fonctionne pas à l'échelle nanométrique, et qu'un comportement en loi logarithmique est plus approprié. Nous avons également fourni des éléments qui mettent en évidence qu'une résolution spatiale insuffisante des mesures à la surface

---

peut conduire à la conclusion erronée que la surface FS présente un comportement en loi de puissance à l'échelle nanométrique.

**Une liaison chimique.** Dans le chapitre 5, nous avons utilisé des simulations *ab initio* pour explorer les propriétés de la surface du verre qui sont autrement moins précises ou même inaccessibles dans les simulations classiques, c'est-à-dire les propriétés vibrationnelles et électroniques. Pour la première fois, les signatures vibrationnelle et électroniques des unités structurales abondantes à la surface, par exemple un anneau de taille 2, ont été identifiées pour les verres de silice et sodosilicatés. L'analyse des propriétés électroniques montre que l'ionicité de la liaison obtenue à partir de la charge atomique Bader est compatible avec les conclusions des fonctions de localisation électronique. En utilisant la connaissance des longueurs de liaison, nous avons obtenu qualitativement les forces des liaisons Si-O et Na-O dans les verres de silicate de sodium. Ces informations peuvent faciliter la compréhension de la propagation des fissures dans les verres d'oxydes.

**Ordre structurel.** Dans le chapitre 6, nous avons traité une question fondamentale concernant l'ordre structurel caché des liquides et des verres. Nous avons introduit une nouvelle approche pour sonder la structure des systèmes désordonnés et démontré sa polyvalence en l'appliquant à la silice (réseau ouvert) et à un mélange binaire de Lennard-Jones (semblable à des sphères dures, BLJM). On constate que la silice et le BLJM ont des symétries structurales non triviales qui s'étendent sur des distances bien au-delà de la courte portée. Plus précisément, la silice est dominée par une symétrie tétraédrique, tandis que le système BLJM, présente des symétries icosaédriques/dodécaédriques alternées. Les résultats obtenus mettent en évidence l'importance de considérer des mesures dépendant des angles pour sonder la structure des liquides et des verres.

## Perspectives

Cette thèse ouvre de nombreuses perspectives intéressantes qui peuvent permettre d'acquérir plus de connaissance sur les propriétés des verres (ou des matériaux désordonnés en général). Plusieurs directions sont mises en évidence ci-dessous.

Tout d'abord, ce travail se concentre sur les propriétés des verres de silice et sodosilicatés, c'est-à-dire les compositions simplifiées pour les verres d'oxydes. Cependant, les méthodologies proposées dans ce manuscrit sont certainement applicables aux compositions plus complexes utilisées dans les applications, par exemple pour les verres sodo-calcaïque (verre à vitre), les borosilicates de sodium (verrerie de cuisine). Du point de vue de la simulation, une telle extension nécessite l'utilisation de potentiels



interatomiques fiables. Pour les systèmes ternaires mentionnés ci-dessus, des potentiels sont actuellement disponibles [84, 238–242].

Deuxièmement, une extension supplémentaire de ce travail peut être effectuée en introduisant des interactions chimio-mécaniques dans les simulations, par ex. l'interaction du réseau vitreux avec des molécules d'eau. En fait, de telles simulations ont été effectuées depuis des décennies, mais les tailles de système considérées restent relativement petites, même avec la puissance de calcul disponible actuellement. Une évaluation appropriée des effets de taille finie et du protocole de simulation est donc nécessaire avant de pouvoir tirer des renseignements utiles à partir de ces simulations.

Dans le chapitre 3, l'analyse des corrélations entre plusieurs propriétés microscopiques a été réalisée pour le verre NS3 riche en Na à 300 K. Une extension très naturelle de ce travail serait l'exploration de l'évolution des corrélations en variant la composition du verre (par exemple, la concentration en  $\text{Na}_2\text{O}$  ou différents types d'oxydes alcalins). Aussi, on peut vouloir comprendre les effets thermiques lors de la déformation des verres. Par conséquent, d'autres études de ces propriétés locales à des températures très basses (minimisant les effets thermiques) ou à des températures élevées seront intéressantes.

La méthode de caractérisation structurale décrite au chapitre 6 peut être également utilisée pour d'autres systèmes désordonnés tels que les systèmes colloïdaux et granulaires pour lesquels les coordonnées des particules sont accessibles. L'application de cette méthode devra fournir des informations utiles sur la nature de ces systèmes. Au delà de l'exploration des caractéristiques structurelles statiques d'un système, il est également utile d'étudier l'évolution temporelle de ces fonctions de corrélation. Avec ce type d'information, on peut mieux élucider le lien entre les propriétés statiques et dynamiques des systèmes désordonnés.

Pour conclure, nous pensons que ce travail comporte non seulement résultats originaux sur les propriétés des verres d'oxydes aux échelles microscopiques, mais ouvre également la voie à des recherches plus approfondies sur les propriétés d'autres matériaux désordonnés dans des environnements divers.

# Bibliography

- [1] C. A. Angell. “Formation of glasses from liquids and biopolymers.” *Science*, **267**, 1924–1935, 1995.
- [2] J. E. Shelby. *Introduction to glass science and technology*. Royal Society of Chemistry, 2005.
- [3] K. Binder and W. Kob. *Glassy materials and disordered solids: An introduction to their statistical mechanics*. World Scientific, 2011.
- [4] A. A. Griffith. “The phenomena of rupture and flow in solids.” *Philosophical Transactions of the Royal Society A: Mathematical, Physical and Engineering Sciences*, **221**, 163–198, 1921.
- [5] G. R. Irwin. “Analysis of stresses and strains near the end of a crack transversing a plate.” *Trans. ASME, Ser. E, J. Appl. Mech.*, **24**, 361–364, 1957.
- [6] T. L. Anderson. *Fracture mechanics: Fundamentals and applications, Fourth Edition*. CRC Press, 2017.
- [7] G. D. Quinn. “Fractography of ceramics and glasses: A NIST recommended practice guide.” *Special Publication 960-16. Washington, DC: National Institute of Standards and Technology*, 2007.
- [8] R. C. Bradt. “The Fractography and Crack Patterns of Broken Glass.” *Journal of Failure Analysis and Prevention*, **11**, 79–96, 2011.
- [9] C. L. Rountree, R. K. Kalia, E. Lidorikis, A. Nakano, L. V. Brutzel, and P. Vashishta. “Atomistic Aspects of Crack Propagation in Brittle Materials: Multimillion Atom Molecular Dynamics Simulations.” *Annual Review of Materials Research*, **32**, 377–400, 2002.
- [10] F. Célarié, S. Prades, D. Bonamy, L. Ferrero, E. Bouchaud, C. Guillot, and C. Marlière. “Glass Breaks like Metal, but at the Nanometer Scale.” *Physical Review Letters*, **90**, 075504, 2003.

- [11] J.-P. Guin and S. Wiederhorn. “Fracture of Silicate Glasses: Ductile or Brittle?” *Physical Review Letters*, **92**, 215502, 2004.
- [12] G. Pallares, M. George, L. Ponson, S. Chapuliot, S. Roux, and M. Ciccotti. “Multiscale investigation of stress-corrosion crack propagation mechanisms in oxide glasses.” *Corrosion Reviews*, **33**, 501–514, 2015.
- [13] J.-P. Hansen and I. R. McDonald. *Theory of simple liquids: with applications to soft matter*. Academic Press, 2013.
- [14] M. P. Allen and D. J. Tildesley. *Computer simulation of liquids*. Oxford University Press, 2017.
- [15] H. Scholze. *Glass: nature, structure, and properties*. Springer Science & Business Media, 2012.
- [16] E. D. Zanotto and J. C. Mauro. “The glassy state of matter: Its definition and ultimate fate.” *Journal of Non-Crystalline Solids*, **471**, 490–495, 2017.
- [17] J. Schmelzer and T. Tropin. “Glass transition, crystallization of glass-forming melts, and entropy.” *Entropy*, **20**, 103, 2018.
- [18] L. Berthier and G. Biroli. “Theoretical perspective on the glass transition and amorphous materials.” *Reviews of Modern Physics*, **83**, 587–645, 2011.
- [19] M. D. Ediger, C. A. Angell, and S. R. Nagel. “Supercooled liquids and glasses.” *The Journal of Physical Chemistry*, **100**, 13200–13212, 1996.
- [20] P. Badrinarayanan, W. Zheng, Q. Li, and S. L. Simon. “The glass transition temperature versus the fictive temperature.” *Journal of Non-Crystalline Solids*, **353**, 2603–2612, 2007.
- [21] S. Kasap, J. Málek, and R. Svoboda. “Thermal Properties and Thermal Analysis: Fundamentals, Experimental Techniques and Applications.” In *Springer Handbook of Electronic and Photonic Materials*. Springer International Publishing, 2017.
- [22] C. A. Angell. “Structural instability and relaxation in liquid and glassy phases near the fragile liquid limit.” *Journal of Non-Crystalline Solids*, **102**, 205–221, 1988.
- [23] N. A. Mauro, M. Blodgett, M. L. Johnson, A. J. Vogt, and K. F. Kelton. “A structural signature of liquid fragility.” *Nature Communications*, **5**, 4616, 2014.
- [24] F. C. Kracek. “The System Sodium Oxide-Silica.” *The Journal of Physical Chemistry*, **34**, 1583–1598, 1930.

- 
- [25] O. Mazurin, M. Streltsina, and T. Shvaiko-Shvaikovskaya. *Handbook of glass data. part a. silica glass and binary silicate glasses*. Elsevier Science Publishers, 1983.
- [26] W. H. Zachariasen. “The atomic arrangement in glass.” *Journal of the American Chemical Society*, **54**, 3841–3851, 1932.
- [27] M. Hasanuzzaman, A. Rafferty, M. Sajjia, and A. G. Olabi. “Properties of glass materials.” *Reference Module in Materials Science and Materials Engineering*, 2016.
- [28] C. A. Angell, P. A. Cheeseman, and S. Tamaddon. “Computer simulation studies of migration mechanisms in ionic glasses and liquids.” *Le Journal de Physique Colloques*, **43**, C9–381–C9–385, 1982.
- [29] G. N. Greaves. “EXAFS and the structure of glass.” *Journal of Non-Crystalline Solids*, **71**, 203–217, 1985.
- [30] H. Lammert, M. Kunow, and A. Heuer. “Complete Identification of Alkali Sites in Ion Conducting Lithium Silicate Glasses: A Computer Study of Ion Dynamics.” *Physical Review Letters*, **90**, 215901, 2003.
- [31] A. Meyer, J. Horbach, W. Kob, F. Kargl, and H. Schober. “Channel formation and intermediate range order in sodium silicate melts and glasses.” *Physical Review Letters*, **93**, 027801, 2004.
- [32] R. Knoche, D. B. Dingwell, F. A. Seifert, and S. L. Webb. “Non-linear properties of supercooled liquids in the system  $\text{Na}_2\text{O}-\text{SiO}_2$ .” *Chemical Geology*, **116**, 1–16, 1994.
- [33] L. Wondraczek, J. C. Mauro, J. Eckert, U. Kühn, J. Horbach, J. Deubener, and T. Rouxel. “Towards Ultrastrong Glasses.” *Advanced Materials*, **23**, 4578–4586, 2011.
- [34] M. A. Meyers and K. K. Chawla. *Mechanical behavior of materials*. Cambridge University Press, 2008.
- [35] L. Wondraczek. “Overcoming glass brittleness.” *Science*, **366**, 804–805, 2019.
- [36] C. Kurkjian, P. Gupta, R. Brow, and N. Lower. “The intrinsic strength and fatigue of oxide glasses.” *Journal of Non-Crystalline Solids*, **316**, 114–124, 2003.
- [37] R. E. Mould. “The strength of inorganic glasses.” In *Fracture of Metals, Polymers, and Glasses*. Springer, 1967.

- [38] R. O. Ritchie. “The conflicts between strength and toughness.” *Nature Materials*, **10**, 817–822, 2011.
- [39] M. F. Ashby. *Materials Selection in Mechanical Design*. Pergamon Press, 1992.
- [40] T. Rouxel and S. Yoshida. “The fracture toughness of inorganic glasses.” *Journal of the American Ceramic Society*, **100**, 4374–4396, 2017.
- [41] A. K. Varshneya. “Stronger glass products: Lessons learned and yet to be learned.” *International Journal of Applied Glass Science*, **9**, 140–155, 2018.
- [42] M. Tomozawa. “Fracture of glasses.” *Annual Review of Materials Science*, **26**, 43–74, 1996.
- [43] J. Fineberg and M. Marder. “Instability in dynamic fracture.” *Physics Reports*, **313**, 1–108, 1999.
- [44] M. Ciccotti. “Stress-corrosion mechanisms in silicate glasses.” *Journal of Physics D: Applied Physics*, **42**, 214006, 2009.
- [45] S. M. Wiederhorn, T. Fett, J.-P. Guin, and M. Ciccotti. “Griffith Cracks at the Nanoscale.” *International Journal of Applied Glass Science*, **4**, 76–86, 2013.
- [46] E. Bouchbinder, T. Goldman, and J. Fineberg. “The dynamics of rapid fracture: instabilities, nonlinearities and length scales.” *Reports on Progress in Physics*, **77**, 046501, 2014.
- [47] S. M. Wiederhorn, J.-P. Guin, and T. Fett. “The Use of Atomic Force Microscopy to Study Crack Tips in Glass.” *Metallurgical and Materials Transactions A*, **42**, 267–278, 2011.
- [48] S. M. Wiederhorn, J. M. López-Cepero, J. Wallace, J.-P. Guin, and T. Fett. “Roughness of glass surfaces formed by sub-critical crack growth.” *Journal of Non-Crystalline Solids*, **353**, 1582–1591, 2007.
- [49] M. Ciccotti and M. George. “In Situ AFM Investigations and Fracture Mechanics Modeling of Slow Fracture Propagation in Oxide and Polymer Glasses.” In W. Andreoni and S. Yip, editors, *Handbook of Materials Modeling: Applications: Current and Emerging Materials*. Springer International Publishing, Cham, 2018.
- [50] K. Muralidharan, J. Simmons, P. Deymier, and K. Runge. “Molecular dynamics studies of brittle fracture in vitreous silica: Review and recent progress.” *Journal of Non-Crystalline Solids*, **351**, 1532–1542, 2005.

- 
- [51] R. Ochoa, T. P. Swiler, and J. H. Simmons. “Molecular dynamics studies of brittle failure in silica: effect of thermal vibrations.” *Journal of Non-crystalline Solids*, **128**, 57–68, 1991.
- [52] B. Wang, Y. Yu, Y. J. Lee, and M. Bauchy. “Intrinsic Nano-Ductility of Glasses: The Critical Role of Composition.” *Frontiers in Materials*, **2**, 11, 2015.
- [53] M. Bauchy, B. Wang, M. Wang, Y. Yu, M. J. Abdolhosseini Qomi, M. M. Smedskjaer, C. Bichara, F.-J. Ulm, and R. Pellenq. “Fracture toughness anomalies: Viewpoint of topological constraint theory.” *Acta Materialia*, **121**, 234–239, 2016.
- [54] S. C. Chowdhury, E. A. Wise, R. Ganesh, and J. W. Gillespie. “Effects of surface crack on the mechanical properties of Silica: A molecular dynamics simulation study.” *Engineering Fracture Mechanics*, **207**, 99–108, 2019.
- [55] T. P. Swiler, J. H. Simmons, and A. C. Wright. “Molecular dynamics study of brittle fracture in silica glass and cristobalite.” *Journal of Non-crystalline Solids*, **182**, 68–77, 1995.
- [56] A. Pedone, G. Malavasi, M. C. Menziani, U. Segre, and A. N. Cormack. “Molecular Dynamics Studies of Stress-Strain Behavior of Silica Glass under a Tensile Load.” *Chemistry of Materials*, **20**, 4356–4366, 2008.
- [57] A. Pedone, M. C. Menziani, and A. N. Cormack. “Dynamics of Fracture in Silica and Soda-Silicate Glasses: From Bulk Materials to Nanowires.” *The Journal of Physical Chemistry C*, **119**, 25499–25507, 2015.
- [58] S. C. Chowdhury, B. Z. Haque, and J. W. Gillespie. “Molecular dynamics simulations of the structure and mechanical properties of silica glass using ReaxFF.” *Journal of Materials Science*, **51**, 10139–10159, 2016.
- [59] T. Hao and Z. M. Hossain. “Atomistic mechanisms of crack nucleation and propagation in amorphous silica.” *Physical Review B*, **100**, 014204, 2019.
- [60] G. Molnár, P. Ganster, J. Török, and A. Tanguy. “Sodium effect on static mechanical behavior of MD-modeled sodium silicate glasses.” *Journal of Non-Crystalline Solids*, **440**, 12–25, 2016.
- [61] J. M. Rimsza, R. E. Jones, and L. J. Criscenti. “Crack propagation in silica from reactive classical molecular dynamics simulations.” *Journal of the American Ceramic Society*, **101**, 1488–1499, 2018.
- [62] J. M. Rimsza, R. E. Jones, and L. J. Criscenti. “Chemical effects on subcritical fracture in silica from molecular dynamics simulations.” *Journal of Geophysical Research: Solid Earth*, **123**, 9341–9354, 2018.

- [63] J. M. Rimsza, R. Jones, and L. Criscenti. “Mechanisms of Silica Fracture in Aqueous Electrolyte Solutions.” *Frontiers in Materials*, **6**, 79, 2019.
- [64] H. Mei, Y. Yang, A. C. van Duin, S. B. Sinnott, J. C. Mauro, L. Liu, and Z. Fu. “Effects of water on the mechanical properties of silica glass using molecular dynamics.” *Acta Materialia*, **178**, 36–44, 2019.
- [65] S. Prades, D. Bonamy, D. Dalmas, E. Bouchaud, and C. Guillot. “Nano-ductile crack propagation in glasses under stress corrosion: spatiotemporal evolution of damage in the vicinity of the crack tip.” *International Journal of Solids and Structures*, **42**, 637–645, 2005.
- [66] D. Bonamy, S. Prades, C. L. Rountree, L. Ponsen, D. Dalmas, E. Bouchaud, K. Ravi-Chandar, and C. Guillot. “Nanoscale damage during fracture in silica glass.” *International Journal of Fracture*, **140**, 3–14, 2006.
- [67] R. Ochoa and J. H. Simmons. “High strain rate effects on the structure of a simulated silica glass.” *Proceedings of the International Conference on the Theory of the Structures of Non-Crystalline Solids*, **75**, 413–418, 1985.
- [68] R. K. Kalia, A. Nakano, P. Vashishta, C. L. Rountree, L. Van Brutzel, and S. Ogata. “Multiresolution atomistic simulations of dynamic fracture in nanostructured ceramics and glasses.” *International Journal of Fracture*, **121**, 71–79, 2003.
- [69] C. Rountree, S. Prades, D. Bonamy, E. Bouchaud, R. Kalia, and C. Guillot. “A unified study of crack propagation in amorphous silica: Using experiments and simulations.” *Journal of Alloys and Compounds*, **434-435**, 60–63, 2007.
- [70] B. Wang, Y. Yu, M. Wang, J. C. Mauro, and M. Bauchy. “Nanoductility in silicate glasses is driven by topological heterogeneity.” *Physical Review B*, **93**, 064202, 2016.
- [71] K. Han, M. Ciccotti, and S. Roux. “Measuring nanoscale stress intensity factors with an atomic force microscope.” *Europhysics Letters*, **89**, 66003, 2010.
- [72] D. S. Dugdale. “Yielding of steel sheets containing slits.” *Journal of the Mechanics and Physics of Solids*, **8**, 100–104, 1960.
- [73] G. I. Barenblatt. “The mathematical theory of equilibrium cracks in brittle fracture.” In *Advances in applied mechanics*. Elsevier, 1962.
- [74] B. R. Lawn, K. Jakus, and A. C. Gonzalez. “Sharp vs blunt crack hypotheses in the strength of glass: a critical study using indentation flaws.” *Journal of the American Ceramic Society*, **68**, 25–34, 1985.

- [75] S. M. Cox. “Glass strength and ion mobility.” *Physics and Chemistry of Glasses*, **10**, 226, 1969.
- [76] A. R. C. Westwood and R. D. Huntington. “Adsorption-sensitive flow and fracture behavior of sodalime glass.” In *Mechanical Behavior of Materials: Proceedings of the International Conference on Mechanical Behavior of Materials*. The Society of Materials Science Japan, 1972.
- [77] S. M. Wiederhorn, H. Johnson, A. M. Diness, and A. H. Heuer. “Fracture of Glass in Vacuum.” *Journal of the American Ceramic Society*, **57**, 336–341, 1974.
- [78] J. F. Kelso, C. G. Pantano, and S. H. Garofalini. “A comparison of ion scattering spectra and molecular dynamics simulations at the surface of silicate glasses.” *Surface Science Letters*, **134**, L543–L549, 1983.
- [79] F. Cleri, S. R. Phillpot, D. Wolf, and S. Yip. “Atomistic Simulations of Materials Fracture and the Link between Atomic and Continuum Length Scales.” *Journal of the American Ceramic Society*, **81**, 501–516, 2005.
- [80] L. V. Woodcock, C. A. Angell, and P. Cheeseman. “Molecular dynamics studies of the vitreous state: Simple ionic systems and silica.” *The Journal of Chemical Physics*, **65**, 1565–1577, 1976.
- [81] J. C. Mauro, A. Tandia, K. D. Vargheese, Y. Z. Mauro, and M. M. Smedskjaer. “Accelerating the Design of Functional Glasses through Modeling.” *Chemistry of Materials*, **28**, 4267–4277, 2016.
- [82] A. Carré, S. Ispas, J. Horbach, and W. Kob. “Developing empirical potentials from ab initio simulations: The case of amorphous silica.” *Computational Materials Science*, **124**, 323–334, 2016.
- [83] S. Sundararaman, L. Huang, S. Ispas, and W. Kob. “New optimization scheme to obtain interaction potentials for oxide glasses.” *The Journal of Chemical Physics*, **148**, 194504, 2018.
- [84] S. Sundararaman, L. Huang, S. Ispas, and W. Kob. “New interaction potentials for alkali and alkaline-earth aluminosilicate glasses.” *The Journal of Chemical Physics*, **150**, 154505, 2019.
- [85] A. Pedone, G. Malavasi, M. C. Menziani, A. N. Cormack, and U. Segre. “A New Self-Consistent Empirical Interatomic Potential Model for Oxides, Silicates, and Silica-Based Glasses.” *The Journal of Physical Chemistry B*, **110**, 11780–11795, 2006.



- [86] S. Nosé. “A molecular dynamics method for simulations in the canonical ensemble.” *Molecular Physics*, **52**, 255–268, 1984.
- [87] S. Nosé. “A unified formulation of the constant temperature molecular dynamics methods.” *The Journal of Chemical Physics*, **81**, 511–519, 1984.
- [88] W. G. Hoover. “Canonical dynamics: Equilibrium phase-space distributions.” *Physical Review A*, **31**, 1695–1697, 1985.
- [89] W. G. Hoover. “Constant-pressure equations of motion.” *Physical Review A*, **34**, 2499–2500, 1986.
- [90] J. Kohanoff. *Electronic structure calculations for solids and molecules: theory and computational methods*. Cambridge University Press, 2006.
- [91] D. Marx and J. Hutter. *Ab initio molecular dynamics: Basic theory and advanced methods*. Cambridge University Press, 2009.
- [92] P. Hohenberg and W. Kohn. “Inhomogeneous Electron Gas.” *Physical Review*, **136**, B864–B871, 1964.
- [93] W. Kohn and L. J. Sham. “Self-Consistent Equations Including Exchange and Correlation Effects.” *Physical Review*, **140**, A1133–A1138, 1965.
- [94] W. Kohn. “Nobel Lecture: Electronic structure of matter—wave functions and density functionals.” *Reviews of Modern Physics*, **71**, 1253–1266, 1999.
- [95] R. Jones. “Density functional theory: Its origins, rise to prominence, and future.” *Reviews of Modern Physics*, **87**, 897–923, 2015.
- [96] K. Burke. “Perspective on density functional theory.” *The Journal of Chemical Physics*, **136**, 150901, 2012.
- [97] J. P. Perdew, K. Burke, and M. Ernzerhof. “Generalized Gradient Approximation Made Simple.” *Physical Review Letters*, **77**, 3865–3868, 1996.
- [98] A. D. Becke. “Density-functional exchange-energy approximation with correct asymptotic behavior.” *Physical Review A*, **38**, 3098–3100, 1988.
- [99] J. P. Perdew, A. Ruzsinszky, G. I. Csonka, O. A. Vydrov, G. E. Scuseria, L. A. Constantin, X. Zhou, and K. Burke. “Restoring the Density-Gradient Expansion for Exchange in Solids and Surfaces.” *Physical Review Letters*, **100**, 136406, 2008.

- 
- [100] A. D. Becke. “Density-functional thermochemistry. I. The effect of the exchange-only gradient correction.” *The Journal of Chemical Physics*, **96**, 2155–2160, 1992.
- [101] A. D. Becke. “A new mixing of Hartree–Fock and local density-functional theories.” *The Journal of Chemical Physics*, **98**, 1372–1377, 1993.
- [102] W. Kob and S. Ispas. “First-principles simulations of glass-formers.” *arXiv:1604.07959*, 2016.
- [103] J. Habasaki and I. Okada. “Molecular dynamics simulation of alkali silicates based on the quantum mechanical potential surfaces.” *Molecular Simulation*, **9**, 319–326, 1992.
- [104] A. N. Cormack, J. Du, and T. R. Zeitler. “Alkali ion migration mechanisms in silicate glasses probed by molecular dynamics simulations.” *Physical Chemistry Chemical Physics*, **4**, 3193–3197, 2002.
- [105] B. Guillot and N. Sator. “A computer simulation study of natural silicate melts. Part I: Low pressure properties.” *Geochimica et Cosmochimica Acta*, **71**, 1249–1265, 2007.
- [106] B. W. H. van Beest, G. J. Kramer, and R. A. van Santen. “Force fields for silicas and aluminophosphates based on *ab initio* calculations.” *Physical Review Letters*, **64**, 1955–1958, 1990.
- [107] D. Wolf, P. Keblinski, S. R. Phillpot, and J. Eggebrecht. “Exact method for the simulation of Coulombic systems by spherically truncated, pairwise r-1 summation.” *The Journal of Chemical Physics*, **110**, 8254–8282, 1999.
- [108] A. Carré, L. Berthier, J. Horbach, S. Ispas, and W. Kob. “Amorphous silica modeled with truncated and screened Coulomb interactions: A molecular dynamics simulation study.” *The Journal of Chemical Physics*, **127**, 114512, 2007.
- [109] Z. Zhang, S. Ispas, and W. Kob. “The critical role of the interaction potential and simulation protocol for the structural and mechanical properties of sodosilicate glasses.” *Journal of Non-Crystalline Solids*, **632**, 119895, 2020.
- [110] K. Vollmayr, W. Kob, and K. Binder. “Cooling-rate effects in amorphous silica: A computer-simulation study.” *Physical Review B*, **54**, 15808–15827, 1996.
- [111] R. W. Hockney and J. W. Eastwood. *Computer simulation using particles*. CRC Press, 1988.

- [112] N. P. Bansal and R. H. Doremus. *Handbook of glass properties*. Orlando: Academic Press, 1986.
- [113] J. M. D. Lane. “Cooling rate and stress relaxation in silica melts and glasses via microsecond molecular dynamics.” *Physical Review E*, **92**, 012320, 2015.
- [114] X. Li, W. Song, K. Yang, N. M. A. Krishnan, B. Wang, M. M. Smedskjaer, J. C. Mauro, G. Sant, M. Balonis, and M. Bauchy. “Cooling rate effects in sodium silicate glasses: Bridging the gap between molecular dynamics simulations and experiments.” *The Journal of Chemical Physics*, **147**, 074501, 2017.
- [115] A. P. Thompson, S. J. Plimpton, and W. Mattson. “General formulation of pressure and stress tensor for arbitrary many-body interaction potentials under periodic boundary conditions.” *The Journal of Chemical Physics*, **131**, 154107, 2009.
- [116] S. Plimpton. “Fast parallel algorithms for short-range molecular dynamics.” *Journal of computational physics*, **117**, 1–19, 1995.
- [117] M. Hemmatti and C. Angell. “Comparison of pair potential models for the simulation of liquid SiO<sub>2</sub>: Thermodynamic, angular-distribution, and diffusional properties.” *Physics Meets Mineralogy: Condensed Matter Physics in the Geosciences*, 2000.
- [118] <https://www.ncnr.nist.gov/resources/n-lengths/>.
- [119] S. Susman, K. J. Volin, D. G. Montague, and D. L. Price. “Temperature dependence of the first sharp diffraction peak in vitreous silica.” *Physical Review B*, **43**, 11076–11081, 1991.
- [120] M. Pöhlmann. *Structure and dynamics of hydrous silica(tes) as seen by molecular dynamics computer simulations and neutron scattering*. PhD thesis, Technische Universität München and Université Montpellier 2, 2005.
- [121] W. J. Malfait, W. E. Halter, and R. Verel. “<sup>29</sup>Si NMR spectroscopy of silica glass: T1 relaxation and constraints on the Si–O–Si bond angle distribution.” *Chemical Geology*, **256**, 269–277, 2008.
- [122] F. Angeli, O. Villain, S. Schuller, S. Ispas, and T. Charpentier. “Insight into sodium silicate glass structural organization by multinuclear NMR combined with first-principles calculations.” *Geochimica et Cosmochimica Acta*, **75**, 2453–2469, 2011.

- [123] D. Kilymis, S. Ispas, B. Hehlen, S. Peugnet, and J.-M. Delaye. “Vibrational properties of sodosilicate glasses from first-principles calculations.” *Physical Review B*, **99**, 054209, 2019.
- [124] A. Tilocca and N. H. de Leeuw. “Structural and electronic properties of modified sodium and soda-lime silicate glasses by Car–Parrinello molecular dynamics.” *Journal of Materials Chemistry*, **16**, 1950–1955, 2006.
- [125] H. W. Nesbitt, G. M. Bancroft, G. S. Henderson, R. Ho, K. N. Dalby, Y. Huang, and Z. Yan. “Bridging, non-bridging and free (O<sup>2-</sup>) oxygen in Na<sub>2</sub>O–SiO<sub>2</sub> glasses: An X-ray Photoelectron Spectroscopic (XPS) and Nuclear Magnetic Resonance (NMR) study.” *Journal of Non-Crystalline Solids*, **357**, 170–180, 2011.
- [126] H. Maekawa, T. Maekawa, K. Kawamura, and T. Yokokawa. “The structural groups of alkali silicate glasses determined from <sup>29</sup>Si MAS-NMR.” *Journal of Non-Crystalline Solids*, **127**, 53–64, 1991.
- [127] F. Yuan and L. Huang. “Molecular dynamics simulation of amorphous silica under uniaxial tension: From bulk to nanowire.” *Journal of Non-Crystalline Solids*, **358**, 3481–3487, 2012.
- [128] J. Horbach, W. Kob, and K. Binder. “Dynamics of Sodium in Sodium Disilicate: Channel Relaxation and Sodium Diffusion.” *Physical Review Letters*, **88**, 125502, 2002.
- [129] W. Griffioen. *Optical fiber mechanical reliability*. PhD thesis, Eindhoven University of Technology, 1995.
- [130] J. T. Krause, L. R. Testardi, and R. N. Thurston. “Deviations from linearity in the dependence of elongation on force for fibers of simple glass formers and of glass optical lightguides.” *Physics and Chemistry of Glasses*, **20**, 135–9, 1979.
- [131] P. K. Gupta and C. R. Kurkjian. “Intrinsic failure and non-linear elastic behavior of glasses.” *Journal of Non-Crystalline Solids*, **351**, 2324–2328, 2005.
- [132] K. Januchta, T. To, M. S. Bødker, T. Rouxel, and M. M. Smedskjaer. “Elasticity, hardness, and fracture toughness of sodium aluminoborosilicate glasses.” *Journal of the American Ceramic Society*, **102**, 4520–4537, 2019.
- [133] N. P. Lower, R. K. Brow, and C. R. Kurkjian. “Inert failure strain studies of sodium silicate glass fibers.” *Journal of Non-Crystalline Solids*, **349**, 168–172, 2004.
- [134] C. R. Kurkjian and P. K. Gupta. “Intrinsic strength and the structure of glass.” *Proc. Int. Congr*, pages 11–18, 2001.

- [135] W. A. Smith and T. M. Michalske. “DOE contract# DEAC040DPOO789.” 1990.
- [136] Q. Zhao, M. Guerette, G. Scannell, and L. Huang. “In-situ high temperature Raman and Brillouin light scattering studies of sodium silicate glasses.” *Journal of Non-Crystalline Solids*, **358**, 3418–3426, 2012.
- [137] W. E. S. Turner and F. Winks. “The thermal expansion of glass, Part II. Glasses of the series sodium metasilicate-silica.” *Journal of the Society of Glass Technology*, **14**, 110–126, 1930.
- [138] J. E. Shelby. “Thermal expansion of mixed-alkali silicate glasses.” *Journal of Applied Physics*, **47**, 4489–4496, 1976.
- [139] P. Richet and Y. Bottinga. “Glass transitions and thermodynamic properties of amorphous  $\text{SiO}_2$ ,  $\text{NaAlSi}_n\text{O}_{2n+2}$  and  $\text{KAlSi}_3\text{O}_8$ .” *Geochimica et Cosmochimica Acta*, **48**, 453–470, 1984.
- [140] W. Haller, D. H. Blackburn, and J. H. Simmons. “Miscibility Gaps in Alkali-Silicate Binaries-Data and Thermodynamic Interpretation.” *Journal of the American Ceramic Society*, **57**, 120–126, 1974.
- [141] F. Yuan and L. Huang. “Brittle to ductile transition in densified silica glass.” *Scientific Reports*, **4**, 5035, 2014.
- [142] R. C. Bradt. “Applying fractography and fracture mechanics to the energy and mass of crack growth for glass in the mirror region.” *Journal of the European Ceramic Society*, **34**, 3255–3262, 2014.
- [143] A. J. Rosakis. “Intersonic shear cracks and fault ruptures.” *Advances in Physics*, **51**, 1189–1257, 2002.
- [144] L. Bergmann. *Ultrasonics and their scientific and technical applications*. Wiley, 1948.
- [145] J. D. Achenbach. *Wave Propagation in elastic solids*. Elsevier, 1973.
- [146] M. A. Meyers. *Dynamic behavior of materials*. John wiley & sons, 1994.
- [147] G. D. Quinn. “On terminal crack velocities in glasses.” *International Journal of Applied Glass Science*, **10**, 7–16, 2019.
- [148] L. E. Kinsler, A. R. Frey, A. B. Coppens, and J. V. Sanders. *Fundamentals of acoustics, 4th Edition*. Wiley-VCH, 1999.
- [149] H. Schardin. “Velocity effects in fracture.” In *ICF0, Swampscott-MA (USA)*, 1959.

- 
- [150] S. R. Anthony, J. P. Chubb, and J. Congleton. “The crack-branching velocity.” *Philosophical Magazine*, **22**, 1201–1216, 1970.
- [151] A. Polian, D. Vo-Thanh, and P. Richet. “Elastic properties of a-SiO<sub>2</sub> up to 2300 K from Brillouin scattering measurements.” *Europhysics Letters*, **57**, 375–381, 2002.
- [152] F. Leonforte, R. Boissiere, A. Tanguy, J. P. Wittmer, and J.-L. Barrat. “Continuum limit of amorphous elastic bodies. iii. three-dimensional systems.” *Physical Review B*, **72**, 224206, 2005.
- [153] F. Shimizu, S. Ogata, and J. Li. “Theory of shear banding in metallic glasses and molecular dynamics calculations.” *Materials Transactions*, **48**, 2923–2927, 2007.
- [154] M. L. Falk and J. S. Langer. “Dynamics of viscoplastic deformation in amorphous solids.” *Physical Review E*, **57**, 7192, 1998.
- [155] A. Stukowski. “Visualization and analysis of atomistic simulation data with OVITO—the Open Visualization Tool.” *Modelling and Simulation in Materials Science and Engineering*, **18**, 015012, 2010.
- [156] J. A. Zimmerman, E. B. WebbIII, J. J. Hoyt, R. E. Jones, P. A. Klein, and D. J. Bammann. “Calculation of stress in atomistic simulation.” *Modelling and Simulation in Materials Science and Engineering*, **12**, S319–S332, 2004.
- [157] C. Spearman. “The proof and measurement of association between two things.” *The American Journal of Psychology*, **15**, 30, 1901.
- [158] G. W. Corder and D. I. Foreman. *Nonparametric statistics: A step-by-step approach*. John Wiley & Sons, 2014.
- [159] J. F. Kelso and C. G. Pantano. “Spectroscopic examination of clean glass surfaces at elevated temperatures.” *Journal of Vacuum Science & Technology A: Vacuum, Surfaces, and Films*, **3**, 1343–1346, 1985.
- [160] R. M. Almeida, R. Hickey, H. Jain, and C. G. Pantano. “Low-Energy Ion Scattering spectroscopy of silicate glass surfaces.” *Journal of Non-Crystalline Solids*, **385**, 124–128, 2014.
- [161] R. M. Almeida, H. Jain, and C. G. Pantano. “Low-Energy Ion-Scattering Spectroscopy of Modified Silicate Glasses.” *Journal of the American Ceramic Society*, **99**, 1259–1265, 2016.

- [162] F. Lechenault, G. Pallares, M. George, C. Rountree, E. Bouchaud, and M. Ciccotti. “Effects of finite probe size on self-affine roughness measurements.” *Physical Review Letters*, **104**, 025502, 2010.
- [163] S. H. Garofalini. “A molecular dynamics simulation of the vitreous silica surface.” *The Journal of Chemical Physics*, **78**, 2069–2072, 1983.
- [164] A. Roder, W. Kob, and K. Binder. “Structure and dynamics of amorphous silica surfaces.” *The Journal of Chemical Physics*, **114**, 7602–7614, 2001.
- [165] M. Rarivomanantsoa, P. Jund, and R. Jullien. “Classical molecular dynamics simulations of amorphous silica surfaces.” *Journal of Physics: Condensed Matter*, **13**, 6707, 2001.
- [166] P. Ganster, M. Benoit, J.-M. Delaye, and W. Kob. “Surface of a calcium aluminosilicate glass by classical and ab initio molecular dynamics simulations.” *Surface Science*, **602**, 114–125, 2008.
- [167] H. Edelsbrunner and E. P. Mücke. “Three-dimensional alpha shapes.” *ACM Transactions on Graphics*, **13**, 43–72, 1994.
- [168] B. Delaunay. “Sur la sphère vide. A la mémoire de Georges Voronoï.” *Bulletin de l’Académie des Sciences de l’URSS. Classe des sciences mathématiques et naturelles*, **6**, 793, 1934.
- [169] A. Stukowski. “Computational analysis methods in atomistic modeling of crystals.” *JOM*, **66**, 399–407, 2014.
- [170] P. K. Gupta, D. Inniss, C. R. Kurkjian, and Q. Zhong. “Nanoscale roughness of oxide glass surfaces.” *Journal of Non-Crystalline Solids*, **262**, 200–206, 2000.
- [171] G. Pallares, F. Lechenault, M. George, E. Bouchaud, C. Ottina, C. L. Rountree, and M. Ciccotti. “Roughness of oxide glass subcritical fracture surfaces.” *Journal of the American Ceramic Society*, **101**, 1279–1288, 2018.
- [172] J. Jäckle and K. Kawasaki. “Intrinsic roughness of glass surfaces.” *Journal of Physics: Condensed Matter*, **7**, 4351, 1995.
- [173] T. Sarlat, A. Lelarge, E. Søndergård, and D. Vandembroucq. “Frozen capillary waves on glass surfaces: an AFM study.” *The European Physical Journal B*, **54**, 121–126, 2006.
- [174] J. Fineberg, S. P. Gross, M. Marder, and H. L. Swinney. “Instability in dynamic fracture.” *Physical Review Letters*, **67**, 457, 1991.

- 
- [175] J. J. Mecholsky, R. W. Rice, and S. W. Freiman. “Prediction of Fracture Energy and Flaw Size in Glasses from Measurements of Mirror Size.” *Journal of the American Ceramic Society*, **57**, 440–443, 1974.
- [176] N. M. Parikh. “Effect of atmosphere on surface tension of glass.” *Journal of the American Ceramic Society*, **41**, 18–22, 1958.
- [177] A.-L. Barabási and H. E. Stanley. *Fractal concepts in surface growth*. Cambridge University Press, 1995.
- [178] B. B. Mandelbrot, D. E. Passoja, and A. J. Paullay. “Fractal character of fracture surfaces of metals.” *Nature*, **308**, 721–722, 1984.
- [179] L. Ponson, D. Bonamy, and E. Bouchaud. “Two-dimensional scaling properties of experimental fracture surfaces.” *Physical Review Letters*, **96**, 035506, 2006.
- [180] J. Schmittbuhl, J.-P. Vilotte, and S. Roux. “Reliability of self-affine measurements.” *Physical Review E*, **51**, 131–147, 1995.
- [181] S. Ramanathan, D. Ertaş, and D. S. Fisher. “Quasistatic Crack Propagation in Heterogeneous Media.” *Physical Review Letters*, **79**, 873–876, 1997.
- [182] J. Barés, M. Barlet, C. L. Rountree, L. Barbier, and D. Bonamy. “Nominally brittle cracks in inhomogeneous solids: from microstructural disorder to continuum-level scale.” *Frontiers in Physics*, **2**, 70, 2014.
- [183] G. Kresse and J. Furthmüller. “Efficiency of ab-initio total energy calculations for metals and semiconductors using a plane-wave basis set.” *Computational Materials Science*, **6**, 15–50, 1996.
- [184] G. Kresse and J. Furthmüller. “Efficient iterative schemes for *ab initio* total-energy calculations using a plane-wave basis set.” *Physical Review B*, **54**, 11169–11186, 1996.
- [185] R. M. Martin. *Electronic structure: basic theory and practical methods*. Cambridge University Press, 2004.
- [186] P. E. Blöchl. “Projector augmented-wave method.” *Physical Review B*, **50**, 17953–17979, 1994.
- [187] G. Kresse and D. Joubert. “From ultrasoft pseudopotentials to the projector augmented-wave method.” *Physical Review B*, **59**, 1758–1775, 1999.
- [188] L. Pedesseau, S. Ispas, and W. Kob. “First-principles study of a sodium borosilicate glass-former. I. The liquid state.” *Physical Review B*, **91**, 134201, 2015.



- [189] L. Pedesseau, S. Ispas, and W. Kob. “First-principles study of a sodium borosilicate glass-former. II. The glass state.” *Physical Review B*, **91**, 134202, 2015.
- [190] A. Rimola, D. Costa, M. Sodupe, J.-F. Lambert, and P. Ugliengo. “Silica Surface Features and Their Role in the Adsorption of Biomolecules: Computational Modeling and Experiments.” *Chemical Reviews*, **113**, 4216–4313, 2013.
- [191] D. Ceresoli, M. Bernasconi, S. Iarlori, M. Parrinello, and E. Tosatti. “Two-membered silicon rings on the dehydroxylated surface of silica.” *Physical Review Letters*, **84**, 3887, 2000.
- [192] G.-M. Rignanesse, A. De Vita, J.-C. Charlier, X. Gonze, and R. Car. “First-principles molecular-dynamics study of the (0001)  $\alpha$ -quartz surface.” *Physical Review B*, **61**, 13250, 2000.
- [193] T. P. M. Goumans, A. Wander, W. A. Brown, and C. R. A. Catlow. “Structure and stability of the (001)  $\alpha$ -quartz surface.” *Phys. Chem. Chem. Phys.*, **9**, 2146–2152, 2007.
- [194] Y.-W. Chen, C. Cao, and H.-P. Cheng. “Finding stable  $\alpha$ -quartz (0001) surface structures via simulations.” *Applied Physics Letters*, **93**, 181911, 2008.
- [195] L. Pauling. “The principles determining the structure of complex ionic crystals.” *Journal of the American Chemical Society*, **51**, 1010–1026, 1929.
- [196] S. N. Taraskin and S. R. Elliott. “Nature of vibrational excitations in vitreous silica.” *Physical Review B*, **56**, 8605–8622, 1997.
- [197] M. Benoit and W. Kob. “The vibrational dynamics of vitreous silica: Classical force fields vs. first principles.” *Europhysics Letters*, **60**, 269, 2002.
- [198] L. Huang and J. Kieffer. “Challenges in modeling mixed ionic-covalent glass formers.” In *Molecular Dynamics Simulations of Disordered Materials*. Springer, 2015.
- [199] J. Sarnthein, A. Pasquarello, and R. Car. “Model of vitreous SiO<sub>2</sub> generated by an *ab initio* molecular-dynamics quench from the melt.” *Physical Review B*, **52**, 12690–12695, 1995.
- [200] M. Benoit, S. Ispas, P. Jund, and R. Jullien. “Model of silica glass from combined classical and *ab initio* molecular-dynamics simulations.” *The European Physical Journal B*, **13**, 631–636, 2000.

- 
- [201] J. Du and L. R. Corrales. “Structure, dynamics, and electronic properties of lithium disilicate melt and glass.” *The Journal of Chemical Physics*, **125**, 114702, 2006.
- [202] S. Ispas, M. Benoit, P. Jund, and R. Jullien. “Structural and electronic properties of the sodium tetrasilicate glass  $\text{Na}_2\text{Si}_4\text{O}_9$  from classical and ab initio molecular dynamics simulations.” *Physical Review B*, **64**, 214206, 2001.
- [203] F. J. Himpsel and D. Straub. “Inverse photoemission as a probe for unoccupied electronic states.” *Surface Science*, **168**, 764–772, 1986.
- [204] F. J. Grunthaner and P. J. Grunthaner. “Chemical and electronic structure of the  $\text{SiO}_2/\text{Si}$  interface.” *Materials Science Reports*, **1**, 65–160, 1986.
- [205] M. Benoit, M. Pöhlmann, and W. Kob. “On the nature of native defects in high OH-content silica glasses: A first-principles study.” *Europhysics Letters*, **82**, 57004, 2008.
- [206] R. P. Feynman. “Forces in Molecules.” *Physical Review*, **56**, 340–343, 1939.
- [207] A. Walsh, A. A. Sokol, J. Buckeridge, D. O. Scanlon, and C. R. A. Catlow. “Oxidation states and ionicity.” *Nature Materials*, **17**, 958–964, 2018.
- [208] C. R. A. Catlow and A. M. Stoneham. “Ionicity in solids.” *Journal of Physics C: Solid State Physics*, **16**, 4321–4338, 1983.
- [209] R. F. Bader. *Atoms in Molecule: A Quantum Theory*. Oxford University Press, 1985.
- [210] G. V. Gibbs, K. M. Rosso, D. M. Teter, M. B. Boisen Jr, and M. S. T. Bukowinski. “Model structures and properties of the electron density distribution for low quartz at pressure: a study of the SiO bond.” *Journal of Molecular Structure*, **485**, 13–25, 1999.
- [211] A. Kirfel, H.-G. Krane, P. Blaha, K. Schwarz, and T. Lippmann. “Electron-density distribution in stishovite,  $\text{SiO}_2$ : a new high-energy synchrotron-radiation study.” *Acta Crystallographica Section A: Foundations of Crystallography*, **57**, 663–677, 2001.
- [212] N. D. Chuvylkin and G. M. Zhidomirov. “Semi-empirical quantum-chemical calculations on intermediary complexes in catalytic reactions. 9. Step of hydrogen adsorption on sodium forms of zeolites.” *Kinetics and Catalysis*, **18**, 749–752, 1977.

- [213] P. J. Heaney, C. T. Prewitt, and G. V. Gibbs. *Silica: Physical behavior, geochemistry, and materials applications*. Walter de Gruyter GmbH & Co KG, 2018.
- [214] A. D. Becke and K. E. Edgecombe. “A simple measure of electron localization in atomic and molecular systems.” *The Journal of Chemical Physics*, **92**, 5397–5403, 1990.
- [215] G. V. Gibbs, D. F. Cox, N. L. Ross, T. D. Crawford, J. B. Burt, and K. M. Rosso. “A mapping of the electron localization function for earth materials.” *Physics and Chemistry of Minerals*, **32**, 208–221, 2005.
- [216] K. Momma and F. Izumi. “VESTA 3 for three-dimensional visualization of crystal, volumetric and morphology data.” *Journal of Applied Crystallography*, **44**, 1272–1276, 2011.
- [217] P. S. Salmon. “Decay of the pair correlations and small-angle scattering for binary liquids and glasses.” *Journal of Physics: Condensed Matter*, **18**, 11443–11469, 2006.
- [218] P. S. Salmon and A. Zeidler. “Ordering on different length scales in liquid and amorphous materials.” *Journal of Statistical Mechanics: Theory and Experiment*, **2019**, 114006, 2019.
- [219] H. Tanaka, H. Tong, R. Shi, and J. Russo. “Revealing key structural features hidden in liquids and glasses.” *Nature Reviews Physics*, **1**, 333–348, 2019.
- [220] W. Kob and H. C. Andersen. “Testing mode-coupling theory for a supercooled binary Lennard-Jones mixture I: The van Hove correlation function.” *Physical Review E*, **51**, 4626, 1995.
- [221] P. J. Steinhardt, D. R. Nelson, and M. Ronchetti. “Bond-orientational order in liquids and glasses.” *Physical Review B*, **28**, 784–805, 1983.
- [222] W. Lechner and C. Dellago. “Accurate determination of crystal structures based on averaged local bond order parameters.” *The Journal of Chemical Physics*, **129**, 114707, 2008.
- [223] P.-L. Chau and A. Hardwick. “A new order parameter for tetrahedral configurations.” *Molecular Physics*, **93**, 511–518, 1998.
- [224] C. Xia, J. Li, Y. Cao, B. Kou, X. Xiao, K. Fezzaa, T. Xiao, and Y. Wang. “The structural origin of the hard-sphere glass transition in granular packing.” *Nature Communications*, **6**, 8409, 2015.

- 
- [225] P. M. Piaggi and M. Parrinello. “Entropy based fingerprint for local crystalline order.” *The Journal of Chemical Physics*, **147**, 114112, 2017.
- [226] X. Yang, R. Liu, M. Yang, W.-H. Wang, and K. Chen. “Structures of local rearrangements in soft colloidal glasses.” *Physical Review Letters*, **116**, 238003, 2016.
- [227] C. P. Royall and W. Kob. “Locally favoured structures and dynamic length scales in a simple glass-former.” *Journal of Statistical Mechanics: Theory and Experiment*, **2017**, 024001, 2017.
- [228] D. Coslovich and G. Pastore. “Understanding fragility in supercooled Lennard-Jones mixtures. I. Locally preferred structures.” *The Journal of Chemical Physics*, **127**, 124504, 2007.
- [229] W. H. Press, S. A. Teukolsky, W. T. Vetterling, and B. P. Flannery. *Numerical recipes 3rd edition: The art of scientific computing*. Cambridge University Press, 2007.
- [230] Y. Q. Cheng and E. Ma. “Atomic-level structure and structure–property relationship in metallic glasses.” *Progress in Materials Science*, **56**, 379–473, 2011.
- [231] C. P. Royall and S. R. Williams. “The role of local structure in dynamical arrest.” *Physics Reports*, **560**, 1–75, 2015.
- [232] D. B. Miracle. “A structural model for metallic glasses.” *Nature Materials*, **3**, 697–702, 2004.
- [233] S. Karmakar, C. Dasgupta, and S. Sastry. “Length scales in glass-forming liquids and related systems: a review.” *Reports on Progress in Physics*, **79**, 016601, 2016.
- [234] K. Kim and S. Saito. “Multiple length and time scales of dynamic heterogeneities in model glass-forming liquids: A systematic analysis of multi-point and multi-time correlations.” *The Journal of Chemical Physics*, **138**, 12A506, 2013.
- [235] G. M. Hocky, L. Berthier, W. Kob, and D. R. Reichman. “Crossovers in the dynamics of supercooled liquids probed by an amorphous wall.” *Physical Review E*, **89**, 052311, 2014.
- [236] W. Götze. *Complex dynamics of glass-forming liquids: A mode-coupling theory*, volume 143. OUP Oxford, 2008.
- [237] P. Wochner, C. Gutt, T. Autenrieth, T. Demmer, V. Bugaev, A. D. Ortiz, A. Duri, F. Zontone, G. Grübel, and H. Dosch. “X-ray cross correlation analysis uncovers hidden local symmetries in disordered matter.” *Proceedings of the National Academy of Sciences*, **106**, 11511–11514, 2009.

- [238] S. Sundararaman, L. Huang, S. Ispas, and W. Kob. “New interaction potentials for borate glasses with mixed network formers.” *arXiv:1912.08943*, 2019.
- [239] L. Deng and J. Du. “Development of boron oxide potentials for computer simulations of multicomponent oxide glasses.” *Journal of the American Ceramic Society*, **102**, 2482–2505, 2019.
- [240] B. Stevansson, Y. Yu, and M. Edén. “Structure–composition trends in multicomponent borosilicate-based glasses deduced from molecular dynamics simulations with improved B–O and P–O force fields.” *Physical Chemistry Chemical Physics*, **20**, 8192–8209, 2018.
- [241] M. Wang, N. A. Krishnan, B. Wang, M. M. Smedskjaer, J. C. Mauro, and M. Bauchy. “A new transferable interatomic potential for molecular dynamics simulations of borosilicate glasses.” *Journal of Non-Crystalline Solids*, **498**, 294–304, 2018.
- [242] M. Fortino, A. Berselli, N. Stone-Weiss, L. Deng, A. Goel, J. Du, and A. Pedone. “Assessment of interatomic parameters for the reproduction of borosilicate glass structures via DFT-GIPAW calculations.” *Journal of the American Ceramic Society*, **102**, 7225–7243, 2019.



# Zhen Zhang

---

## Personal information

Gender Male

Nationality Chinese

Born April 21, 1991, Chongqing, China

E-mail zhen.zhang@etu.umontpellier.fr

Address Laboratoire Charles Coulomb, cc069 University of Montpellier  
34095 Montpellier Cedex 05, France

## Research interest

Revealing and understanding the the processing-structure-properties relationship of materials through multi-scale modeling and computer simulations.

## Education

May 2020 **Doctor of Philosophy (Ph.D.)**, *University of Montpellier, France.*

- Supervised by Dr. Simona Ispas and Prof. Walter Kob, Physics department and Charles Coulomb Laboratory
- Thesis: "Fracture, surface, and structure of silicate glasses: Insights from atomistic computer simulations"

June 2016 **Master of Engineering (M.E.)**, *Chongqing University, China.*

- Supervised by Prof. Bing Xie, College of Materials Science and Engineering
- Thesis: "Molten Structure and Viscous Flow Properties of Vanadium Slag"

June 2013 **Bachelor of Engineering (B.E.)**, *Chongqing University, China.*

- Supervised by Prof. Mingmei Zhu, College of Materials Science and Engineering
- Thesis: "Modeling of steelmaking process based on artificial neural network"

## Awards and Honors

June 2019 Poster contest winner by the American Ceramic Society

2016-2020 Doctoral fellowship by the China Scholarship Council

## Publications

- [1] Zhen Zhang and Walter Kob. Revealing the three-dimensional structure of liquids using four-point correlation functions. Proc. Natl. Acad. Sci. U.S.A. (accepted) (2020).
- [2] Zhen Zhang, Simona Ispas, and Walter Kob. The critical role of the interaction potential and simulation protocol for the structural and mechanical properties of sodosilicate glasses. Journal of Non-Crystalline Solids **532**, 119895 (2020).

- [3] Zhen Zhang, Bing Xie, Wang Zhou, Jiang Diao, and Hongyi Li. Structural characterization of FeO-SiO<sub>2</sub>-V<sub>2</sub>O<sub>3</sub> slags using molecular dynamics simulations and FTIR spectroscopy. *ISIJ International* **56**, 828 (2016).
- [4] Zhen Zhang, Simona Ispas, and Walter Kob. Morphology and roughness of oxide glass surfaces at the nanoscale. (In preparation) (2020).
- [5] Zhen Zhang, Simona Ispas, and Walter Kob. Structural, vibrational and electronic properties of silicate glass surfaces from first-principles simulations. (In preparation) (2020).
- [6] Zhen Zhang, Simona Ispas, and Walter Kob. Stiffness anomalies in silica and alkali silicate glasses: Viewpoint of atomic dynamics. (In preparation) (2020).

## Workshops and conferences

- September 2019 **4th International Workshop on Glass & Entropy and 9th International Otto Schott Colloquium**, Jena, Germany.
  - o Poster: Characteristics of oxide glass surfaces at the nanoscale
- June 2019 **25th International Congress on Glass**, Boston, USA.
  - o Oral: MD simulation of sodium silicate glasses: The critical role of interaction potential
  - o Poster: Characteristics of oxide glass surfaces at the nanoscale
- July 2018 **15th International Conference on the Physics of Non-Crystalline Solids, simulation and modeling**, Saint-Malo, France.
  - o Oral: Fracture of sodium-silicate glasses: Insights from atomistic computer simulations
- August 2017 **Hands-on Workshop Density-Functional Theory and Beyond**, Berlin, Germany.
  - o Poster: Detecting structural order in glasses
- March 2015 **TMS Annual Meeting & Exhibition, Computational Thermodynamics and Kinetics**, Orlando, USA.
  - o Poster: Molecular Dynamics Study of Structural and Transport Properties of FeO-SiO<sub>2</sub>-V<sub>2</sub>O<sub>3</sub> System

## Computer skills

- OS Linux, Microsoft Windows
- Simulation LAMMPS, VASP
- Others Efficient at using several programming languages and graphic tools (Fortran, Python, Bash script, OVITO, VESTA, ParaView, GNU Octave, Xmgrace, Gnuplot, etc.)

## Languages

- Chinese**, *Mother tongue.*
- English**, *Intermediate to fluent.*
- French**, *Basic to intermediate.*

## Hobbies

- Guitar
- Cooking